

Elucidating the Structural Dynamics of Alpha-Synuclein by Structural Mass Spectrometry



Emily Jane Byrd

School of Molecular and Cellular Biology
Astbury Centre for Structural Molecular Biology
University of Leeds

Submitted in accordance with the requirements for the degree of

Doctor of Philosophy

December 2023

This thesis is dedicated to my loving parents Vivienne and Andrew Byrd.

Declaration

The candidate confirms that the work submitted is her own. The candidate confirms that appropriate credit has been given within the thesis where reference has been made to the work of others. This copy has been supplied on the understanding that it is copyright material and that no quotation from this thesis may be published without proper acknowledgement. Throughout this thesis the work directly attributable to the candidate is as follows:

(i) Literature research and compilation of the manuscript stated above. (ii) The candidate performed all the experimental work and data analysis unless otherwise stated.

Chapter 3 includes work from the following publications:

Byrd, E. J., Wilkinson, M., Radford, S. E., and Sobott, F. (2023). Taking charge: Metal ions accelerate amyloid aggregation in sequence variants of α -Synuclein. *J. Am. Soc. Mass Spectrom.*, 34(3):493–504.

Ulamec, S. M., Maya-Martinez, R., Byrd, E. J., Dewison, K. M., Xu, Y., Willis, L. F., Sobott, F., Heath, G. R., van Oosten Hawle, P., Buchman, V. L., Radford, S. E., and Brockwell, D. J. (2022). Single residue modulators of amyloid formation in the n-terminal p1-region of α -synuclein. *Nat. Commun.*, 13(1):4986.

Chapter 5 includes work from the following submitted manuscript:

Santos, J., Cuellar, J., Pallarès, I., Byrd, E. J., Lends, A., Moro, F., Abdul-Shukkoor, M. B., Pujols, J., Velasco-Carneros, L., Sobott, F., Otzen, D. E., Calabrese, A. N., Muga, A., Pedersen, J. S., Loquet, A., Valpuesta, J. M., Radford, S. E., and Ventura, S. *BioRxiv* (2023). The structural architecture of an α -synuclein toxic oligomer.

Emily Jane Byrd

December 2023

Acknowledgements

Firstly, a huge thank you goes to my supervisors professor Sheena Radford and Frank Sobott. I have been extremely fortunate to have received such dedicated mentorship throughout my PhD. Sheena, after giving you many heart attacks (...Sorry, the reviewers comments were fine) I will be forever grateful for your tireless support, advice and your constant belief in me. Your passion for science and your enthusiasm for all of your students and staff is inspiring. Thank you to Frank for the fantastic opportunities you made me a part of, I am so grateful for your support to get us to Asilomar and many other conferences.

I would like to acknowledge the BBSRC White Rose DTP for funding and to ASMS and BMSS for travel grants towards international conferences; I have been so lucky! I am grateful to Dr Salvador Ventura and Dr Jaime Santos for collaborating and providing oligomer samples for HDX-MS experiments.

Thank you to Dr Anton Calabrese for always supporting me and helping me whenever I got stuck, listening to ALL of my pointless rants and having me look after Barry! I cannot go without thanking Dr James Ault our MS facility manager and HDX genius! I'll never forget our constant rants and rarely mentioning the lack of Qreserve requests submitted... Thank you so much Anton and James for never making me feel like a burden. To Dr Rachel George and Dr Sri Ranjani Ganji, thank you for bringing joy to stressful lab times. Thanks to Dr Tim Minshull, TDP whizz and MS facility manager, thank you for all the support and laughs.

I don't know where to start when it comes to my partner in crime, double act and fellow assistant TO the facility manager, Alice Colyer. THANK YOU for being my best pal, my cafe nero date always, making my HDX buffers for me whilst I cried, quoting summer heights high and referencing things that no one else understands. We are just being our own dogs. To my California road trip gals Alice, Mel and Sammy, I had the best trip with such great friends. And Mel, hitting the hospitality suites in Houston was so memorable, thanks for being such a wonderful friend. To the star of the show in Minneapolis: Jake, please NEVER change.. and cheers for the absurd anecdotes.

There are many people I am grateful to have met during my PhD. Emily P for the pre-covid laughs. Katy, for laughing at the things no one else notices with me. Sabine, for teaching me all things α S. The rest of the dream team: Paul, Jess and Anna! James, Leon, Conor and Ben for always bringing joy to the lab. Sophie for saving the day with PCRs. Romany, a crafty genius and such a great friend, and Jim for always solving science problems. Alex P, for the GM and JC preps! A heartfelt thank you to Roberto, Nicolas and Yong, I was lucky to learn from each of you. And to Helen McAllister for unbreakable positivity. Kyle, thanks for being a great flat-mate and supportive friend, Owen for teaching me lots in a short space of time, and Emma for being such a joy to be around. Dr Patrick Knight, for setting up my PIPs and being a sound source of advice. I cannot forget Dr David Smith and Dr Danny Allwood from my undergraduate at Sheffield Hallam University, particularly David for starting my fascination with mass spec and amyloid. I am grateful to have met Dr Kiani Jeacock at Asilomar who became a great friend. And Thank you to Dr Dale Cooper-Shepherd at Waters for hosting our visit. And my pals at JD gym!

Finally, a huge thank you to my family for supporting me, Mum, Dad, Kelly, Lauren, Karl, Paul, Nigel, Sharon and Nan thank you for your support and love always. Of course, I cannot go without thanking Dr Joel Crossley for always pushing me, guiding me, making amazing soups and so much more. You mean the world to me! ...Un-acknowledgments: AerLingus.

Abstract

Parkinson's disease (PD) is characterised by the deposition of insoluble Lewy Bodies (LBs) in dopaminergic neurons in the brain. LBs are primarily composed of α -Synuclein (α S), a 140-residue, intrinsically disordered protein which can self-associate and undergo a transition from disordered monomers into ordered β -sheet rich amyloid fibril architectures. Characterising the structural properties of early intermediates in α S amyloid assembly is crucial towards elucidating amyloid assembly mechanisms.

This thesis presents the development and application of structural mass spectrometry (MS) based techniques to study the structure and dynamics of N-terminally acetylated α S (α SNTA). Findings capture how the conformation of α S correlates with its amyloid propensity. The conformational ensemble of α S along with variants which decrease/abolish amyloid assembly is shown. Ion mobility MS shows that monomeric α SNTA exists as a conformational ensemble populating partially compact conformational families in equilibrium with extended conformational families and this thesis explores the effect of perturbing the α S conformational ensemble on its amyloid assembly kinetics. α S is negatively charged under physiological conditions and is known to bind divalent metal ions. Upon addition of Ca^{2+} , Mn^{2+} or Zn^{2+} , multiple binding events occur and the conformational ensemble of α SNTA is shifted to compact conformations and the rate of amyloid assembly is increased. Oligomeric species populated during α S amyloid assembly are considered toxic drivers of neurodegeneration in PD but are difficult to study due to

their transient form and heterogeneity. In this thesis, hydrogen-deuterium exchange MS is used to characterise the role of the N-terminal region in trapped oligomer assembly.

Overall, this thesis aims to shine light on the use of structural MS to investigate the structure and dynamics of transient, heterogeneous proteinaceous species. Evidence is provided for the accelerating role of α S compaction in amyloid propensity and provides a foundation for the further development of structural MS based methodologies.

Table of contents

List of figures	xvi
List of tables	xxiii
1 Introduction	1
1.1 Mass Spectrometry for Protein Structure Determination	1
1.2 Electrospray Ionisation	3
1.3 Mass analysers	7
1.3.1 Quadrupole	8
1.3.2 Time of flight	10
1.3.3 Linear ion trap	14
1.3.4 Orbitrap	16
1.3.5 Astral	18
1.4 Detectors	18
1.5 Ion mobility mass spectrometry	19
1.5.1 Drift tube ion mobility	20
1.5.2 Traveling wave ion mobility	22
1.5.3 Cyclic ion mobility	23
1.6 Tandem mass spectrometry	25
1.6.1 Electron capture dissociation	27
1.6.2 Electron transfer dissociation	29
1.6.3 Ultraviolet photodissociation	29

1.7	Liquid-chromatography mass spectrometry	30
1.8	Cross linking-mass spectrometry	32
1.9	Hydrogen-deuterium exchange mass spectrometry	36
1.10	Amyloid proteins and disease	39
1.10.1	Protein folding, misfolding and aggregation	39
1.10.2	Mechanisms of amyloid assembly	41
1.10.3	The amyloid fold and fibril architectures	52
1.10.4	Seeding potential and mechanisms of disease progression	54
1.11	Introduction to α -Synuclein	55
1.11.1	Structural properties of α S	55
1.11.2	Physiological properties of α S	57
1.11.3	Current treatments/therapeutics towards Parkinson's disease	60
1.12	Mass spectrometry analysis of amyloid	61
1.12.1	Monomers	61
1.12.2	Oligomers	63
1.12.3	Fibrils	65
1.13	Aims of this thesis	66
2	Materials and Methods	69
2.1	Materials	69
2.2	Molecular biology, protein expression and purification	71
2.2.1	NatB competent cells preparation	71
2.2.2	Protein expression and purification	72
2.3	Biochemistry	73
2.3.1	Sodium dodecyl sulphate - polyacrylamide gel electrophoresis (SDS-PAGE)	73
2.3.2	ThT assays	74
2.3.3	Transmission electron microscopy (TEM)	75

2.3.4	Fibril yields	75
2.3.5	Circular dichroism	75
2.4	Biophysics	76
2.4.1	NMR	76
2.5	smFRET	76
2.5.1	Site directed mutagenesis	76
2.5.2	Labelling of FRET construct	79
2.6	Intact mass analysis	79
2.7	Native nESI-IM-MS	80
2.7.1	Nanospray tip pulling and coating	80
2.7.2	Native nESI-IM-MS	80
2.7.3	Calculation of CCS	81
2.7.4	Zn ²⁺ titration by IM-MS	81
2.7.5	Collision induced unfolding	82
2.7.6	Dimer abundance analysis	82
2.8	Cross-linking-MS	83
2.8.1	Cross-linking-MS experimental	83
2.8.2	Cross linking-MS S-Trap digestion	83
2.8.3	Cross linking-MS peptide mapping	84
2.8.4	Cross linking-MS data processing	84
2.9	ETD fragmentation	85
2.10	UVPD fragmentation	86
2.11	Cyclic IM-MS	86
2.12	K _d determination	87
2.13	HDX-MS	87
2.13.1	HDX-MS experimental	87
2.13.2	HDX-MS data processing	88
2.14	Mass photometry	88

3 Probing the Conformational Dynamics of Monomeric α-Synuclein and How it Relates to Amyloid Assembly	91
3.1 Introduction	91
3.2 Objectives	96
3.3 N-terminal acetylation of α -synuclein	96
3.3.1 Protein production of acetylated α -synuclein	96
3.3.2 Effect of N-Terminal acetylation on α S amyloid assembly	100
3.3.3 Native MS of α SNTA identifies similarities	101
3.3.4 Native nESI-IM-MS of α SNTA identifies the same conformational families	104
3.4 The addition of metal ions affects amyloid kinetics and conformational dynamics	110
3.4.1 Metal ions on α SNTA increase the rate of amyloid assembly	110
3.4.2 Multiple metal ion binding events revealed by nESI-MS	115
3.4.3 Metal ion binding causes compaction of α SNTA by Native nESI-IM-MS	119
3.4.4 Collision Induced Unfolding of α S probes the stability of the compact conformational family	125
3.4.5 Secondary structure of α SNTA by circular dichroism is not induced by metal ion binding	128
3.5 P1 Peptide binding to α S	129
3.5.1 Native nESI-MS of the P1 peptide bound to α S and collision induced dissociation to map binding stability	132
3.6 C-terminal truncation of α S: residues 1-119	134
3.6.1 1-119 α SNTA rate of amyloid assembly increases with metal ions	135
3.6.2 Native nESI-MS and IM-MS of 119 α SNTA confirms compaction upon metal ion binding	137
3.7 Dimer abundance correlates with amyloid propensity	140

3.8	Discussion	143
3.9	Conclusion	147
4	Understanding the molecular mechanisms that govern αS compaction	149
4.1	Introduction	149
4.2	Objectives	150
4.3	Correlating ion mobility with the rate of amyloid formation	151
4.3.1	Fitting binding curves to obtain Zn^{2+} binding affinities to α SNTA	155
4.4	Cyclic ion mobility mass spectrometry reveals hidden conformational families	159
4.5	Long range intramolecular interaction increase in the presence of Zn^{2+} . .	166
4.6	Zn^{2+} titration with α SNTA by NMR	173
4.7	Revealing conformational sensitivity with native top-down intact fragmentation	178
4.7.1	Investigating α SNTA structure using ETD	178
4.7.2	Investigating α SNTA structure using UVPD	186
4.7.3	Comparing ETD and UVPD for α SNTA structure interrogation . .	188
4.8	smFRET	189
4.9	Discussion	193
4.10	Conclusion	195
5	Defining the structural assembly of toxic type B* oligomers of αS	197
5.1	Introduction	197
5.2	The N-terminal and NAC regions are important for α S oligomer assembly	204
5.3	G51D and A30P alter the α S oligomer architecture	210
5.4	Oligomers constitute a thirty-mer arrangement	217
5.5	Discussion	220
5.6	Conclusion	221

6	Concluding remarks	223
6.1	Final overall conclusion	223
6.2	Future work	228
6.2.1	The role of dimers and small oligomers	228
6.2.2	Using top-down fragmentation to identify metal ion binding sites	229
	References	231
	Appendix A Appendix	271
A.1	Appendix A: Related information for Chapter 3	271
A.2	Appendix B: Related information for Chapter 4	275
A.3	Appendix C: Related information for Chapter 5	287

List of figures

1.1	Schematic of a mass spectrometer.	2
1.2	The electrospray ionisation process.	5
1.3	Mass resolution.	8
1.4	Schematic of a quadrupole mass analyser.	9
1.5	A schematic of the orthogonal arrangement of a ToF cell in a quadrupole-time of flight (QToF) mass spectrometer.	13
1.6	A schematic of the reflectron ToF mass analyser.	14
1.7	Linear ion trap.	16
1.8	The Orbitrap mass analyser.	17
1.9	Schematic of an electron multiplier detector.	19
1.10	Drift tube ion mobility spectrometry	22

1.11	Traveling wave ion mobility spectrometry	23
1.12	Cyclic ion mobility	25
1.13	Product ion scan	26
1.14	Fragment ions generated through peptide bond dissociation.	27
1.15	Fragmentation mechanisms.	29
1.16	DMTMM reaction mechanism.	35
1.17	HDX labelling reaction	38
1.18	Protein folding and aggregation.	40
1.19	The process of <i>de novo</i> and seeded amyloid assembly.	46
1.20	Structural characterisation of type A and type B oligomers.	48
1.21	Thioflavin T.	49
1.22	Amyloid assembly pathways.	50
1.23	Liquid-liquid phase separation.	51
1.24	The amyloid cross- β structure.	53
1.25	Monomeric α S sequence.	56
1.26	The role of α S in synaptic vesicle exocytosis and recycling.	59
1.27	α -Synuclein interacts with lipid nanodiscs.	63
1.28	A heat map of deuterium uptake in peptides from α S oligomers.	64
1.29	FPOP reaction.	65
3.1	The P1 and P2 regions in α S.	93
3.2	The role of the P1 and the P2 region in amyloid assembly.	94
3.3	α S is predicted to bind metal ions primarily in the negatively charged C-terminal region.	95
3.4	Purification of α S.	98
3.5	Denatured LC-MS of purified WT α SNTA.	99
3.6	Denatured LC-MS of purified α S variants.	100

3.7 Amyloid assembly ThT fluorescence kinetics of α S with and without N-terminal acetylation.	101
3.8 Native nESI-MS comparing N-terminal acetylation of WT and $\Delta\Delta$ α S.	102
3.9 Native nESI-MS comparing N-terminal acetylation of Δ P1 and Δ P2 α S.	103
3.10 Log-log calibration plot for nESI-IM-MS ^{TW} CCS _{N2} calculation.	104
3.11 Three dimensional nESI-IM-MS plot of WT α S NTA.	106
3.12 Optimisation of Waters Synapt G1 tuning parameters.	108
3.13 Native nESI-IM-MS spectra of acetylated α S.	109
3.14 WT α SNTA amyloid assembly is faster in the presence of metal ions.	111
3.15 Deletion variants of α SNTA form amyloid faster in the presence of metal ions.	113
3.16 Metal ions decrease the t_{50} values for all variants.	114
3.17 Aggregate yields determined through pelleting and densitometry.	115
3.18 Native nESI-MS identifies binding of metal ions to WT α SNTA.	116
3.19 Native nESI-MS identifies binding of metal ions to Δ P1 α SNTA.	117
3.20 Native nESI-MS identifies binding of metal ions to Δ P2 α SNTA.	118
3.21 Native nESI-MS identifies binding of metal ions to $\Delta\Delta$ α SNTA.	119
3.22 Native nESI-IM-MS spectra.	121
3.23 Native nESI-IM mass spectra showing compaction of WT and $\Delta\Delta$ α SNTA when Zn ²⁺ ions bind.	122
3.24 Zn ²⁺ ions selectively modulate compaction of low charge states of α S.	124
3.25 Collision induced unfolding with metal ions.	126
3.26 Collision induced unfolding of WT α SNTA bound to Zn ²⁺	127
3.27 Zn ²⁺ binding does not induce secondary structure by far UV circular dichroism.	129
3.28 Amyloid formation kinetics of WT, Δ P1 and $\Delta\Delta$ - α S in the presence of the P1 peptide.	131

3.29	The interaction between WT α S, Δ P1 and the P1 peptide characterised by native nESI-MS.	133
3.30	LC-MS of purified 119 α SNTA.	135
3.31	Metal ion binding modulates the rate of 119 α SNTA amyloid assembly.	136
3.32	t_{50} values and fibril yields for 119 α SNTA amyloid assembly.	137
3.33	Native nESI mass spectrum of 119 α SNTA.	138
3.34	Native nESI-MS identifies binding of metal ions to 119 α SNTA.	139
3.35	Native nESI-IM-MS spectra show compaction of 119 α SNTA when metal ions bind.	140
3.36	Dimer abundance versus t_{50}	141
3.37	Dimer abundance versus t_{50} with the addition of Zn^{2+} to WT α SNTA.	142
3.38	Dimer abundance versus the molar excess of Zn^{2+} when added to WT α SNTA.	143
3.39	Schematic of the resulting conformational effects when metal ions bind to α SNTA.	147
4.1	ThT fluorescence showing a titration of α SNTA with Zn^{2+}	152
4.2	Correlating CCS with t_{50} directly links compaction with amyloid propensity in the presence of Zn^{2+}	153
4.3	Correlating CCS with t_{50} directly links compaction with amyloid propensity of 119 α SNTA in the presence of Zn^{2+} for 119 α SNTA.	154
4.4	Determination of K_d values of Zn^{2+} binding events to WT α SNTA acquired using the Waters Synapt G1 HDMS.	156
4.5	Determination of K_d values of Zn^{2+} with WT α SNTA acquired using the ThermoFisher Orbitrap Eclipse Tribrid MS.	158
4.6	Mass spectrum of WT α S measured on the Waters SELECT series cyclic ion mobility mass spectrometer.	160
4.7	Cyclic IM-MS of the 8+ charge state of WT α SNTA.	161

4.8	Cyclic IM-MS of the 8+ charge state of WT α SNTA for the maximum number of passes.	162
4.9	Gaussian fitting of cIM-MS for the 8+ charge state of α SNTA.	163
4.10	Cyclic IM-MS of slice <i>a</i> of the 8+ charge state of WT α SNTA.	164
4.11	Gaussian fitting of cIM-MS of slice <i>a</i> for the 8+ charge state of α SNTA.	165
4.12	Optimisation of DMTMM cross-linking of WT α SNTA.	167
4.13	DMTMM cross-linking of WT α SNTA with Zn^{2+}	168
4.14	XL-MS of α SNTA in the presence of Zn^{2+} identifies an increase in long range intramolecular interactions.	170
4.15	Quantification channels for precursor ion quantification of cross-linked peptides which increase in the presence of Zn^{2+}	171
4.16	Quantification channels for precursor ion quantification of cross-linked peptides which decrease in the presence of Zn^{2+}	172
4.17	^{15}N - 1H HSQC NMR spectra showing a Zn^{2+} titration with α SNTA.	174
4.18	Chemical shift perturbations and fitting of α SNTA Zn^{2+} binding from 1H - ^{15}N HSQC spectra.	175
4.19	Minor peaks observed in ^{15}N - 1H HSQC NMR spectra.	177
4.20	Native and denaturing nESI mass spectra of α SNTA recorded on a ThermoFisher Orbitrap Eclipse instrument.	179
4.21	α SNTA ETD fragmentation spectra for denaturing solution conditions.	180
4.22	Denaturing solution conditions α SNTA ETD example fragment ion spectra.	182
4.23	α SNTA ETD fragmentation spectra for native solution conditions.	183
4.24	ETD sequence coverage of terminal fragment ions α SNTA using the TD validator node in ProSight Native by Proteinaceous.	184
4.25	ETD sequence coverage of terminal and internal fragment ions α SNTA using the TD validator node in ProSight Native by Proteinaceous.	185
4.26	UVPD sequence coverage of terminal fragment ions α SNTA using the TD validator node in ProSight Native by Proteinaceous.	187

4.27	Comparing ETD versus UVPD on the fragmentation of α SNTA.	188
4.28	α SNTA _{G7C-A140C} smFRET construct.	190
4.29	Time trace of α SNTA _{G7C-A140C} in 20 mM Tris HCl, pH 7.5 at 50 pM protein concentration.	191
4.30	Lifetime analysis of α SNTA _{G7C-A140C}	192
4.31	Lifetime analysis of α SNTA _{G7C-A140C} with 1 mM Ca ²⁺	193
5.1	The cross- α amyloid structure of PSM α 3.	198
5.2	PSM α 3 binds to type B* α S oligomers.	199
5.3	solid state NMR of type B* oligomers.	201
5.4	Characterisation of type B* oligomers.	203
5.5	Sequence coverage of α S monomers, oligomers and oligomers with PSM α 3 used to detect deuterium uptake.	204
5.6	HDX-MS of type B* α S oligomers compared to α S monomers.	205
5.7	A schematic showing PSM α 3 binding sites to α S oligomers revealed by XL-MS.	206
5.8	HDX-MS of type B* α S oligomers with PSM α 3 compared to α S monomers.	207
5.9	HDX-MS of type B* α S oligomers with PSM α 3 compared to apo type B* α S oligomers.	208
5.10	Uptake plots identify significant protection from deuterium uptake in the N-terminal and NAC regions for α S type B* oligomers by HDX.	209
5.11	Sequence coverage of G51D α S oligomers and WT α S oligomers used to detect deuterium uptake.	211
5.12	HDX-MS of type B* G51D α S oligomers compared to type B* WT α S oligomers.	212
5.13	Uptake plots identify significant deprotection from deuterium uptake in the N-terminal region for G51D type B* α S oligomers by HDX.	213

5.14	Sequence coverage of A30P α S oligomers and WT α S oligomers used to detect deuterium uptake.	214
5.15	HDX-MS of type B* A30P α S oligomers compared to type B* WT α S oligomers.	215
5.16	Uptake plots identify significant protection from deuterium uptake in the N-terminal region for A30P α S oligomers by HDX.	216
5.17	Molecular weight histograms obtained from mass photometry measurements of WT, WT-PSM α 3, G51D and A30P α S type B* oligomers.	218
6.1	Cluster analysis of α S MD guided by smFRET and validated by XL-MS.	226
6.2	Factors that influence α S self-assembly.	227
A.1	SDS-PAGE showing fibril yields of WT, Δ P1, Δ P2 and $\Delta\Delta\alpha$ SNTA.	271
A.2	Native nESI-MS identifies binding of metal ions to WT α SNTA 17+ dimer.	272
A.3	SDS-PAGE showing fibril yields of of 119 α SNTA.	272
A.4	Native nESI-MS showing dimer abundance with metal ions	273
A.5	Native nESI-MS showing dimer abundance for variants	274
A.6	cIM-MS of the 8+ charge state for WT α SNTA with total ion counts.	275
A.7	Cross-linking sequence coverage.	275
A.8	NMR intensity changes.	276
A.9	Calculation of the K_D of Zn^{2+} binding to different α S residues by NMR.	277
A.10	Calculation of the K_D of Zn^{2+} binding to different α S residues by NMR.	278
A.11	Calculation of the K_D of Zn^{2+} binding to different α S residues by NMR.	279
A.12	Calculation of the K_D of Zn^{2+} binding to different α S residues by NMR.	280
A.13	Uptake plots for the N-terminal and NAC regions of α S monomers, WT oligomers and WT oligomer + PSM α 3 by HDX.	287
A.14	Uptake plots for the C-terminal region of α S monomers, WT oligomers and WT oligomer + PSM α 3 by HDX.	288

A.15 Uptake plots for the N-terminal and NAC regions of G51D α S oligomers and WT oligomers by HDX.	289
A.16 Uptake plots for the C-terminal region of G51D α S oligomers and WT oligomers by HDX.	290
A.17 Uptake plots of A30P α S oligomers and WT oligomers by HDX.	291
A.18 Amino acids summary.	292

List of tables

1.1 Common cross-linkers and their characteristics.	36
1.2 Amyloid Proteins. Precursor amyloid proteins are listed with their species of origin, known structure, and disease or function associated. APO: apolipoprotein, polyQ: poly-glutamine, TBP: TATA-binding protein. Adapted from [156–158].	42
2.1 Materials	69
2.2 SDS-PAGE recipe	74
2.3 Primer Sequences for the generation of G7C_A140C α S.	77
2.4 Components and volumes for a 25 μ l Q5 PCR reaction.	77
2.5 Thermocycling conditions.	77
2.6 Components and volumes for KLD reaction.	78
2.7 Nanospray needles	80
3.1 Denatured calibrants used for nESI-IM-MS ^{TW} CCS _{N2} calculation.	105
A.1 Fragment ions detected for ETD of denatured α SNTA.	281
A.2 Fragment ions detected for ETD of native α SNTA.	285

Chapter 1

Introduction

1.1 Mass Spectrometry for Protein Structure Determination

Mass spectrometry (MS) is an analytical technique used to determine the mass of an analyte through measurement of the mass to charge ratio (m/z) of ionic species in the gas phase [1–3]. Although initially MS was limited to studying volatile, small compounds, the advent of new methods of sample ionisation and mass sorting has extended the breadth of amenable samples for analysis. Tractable samples now range from complex biological systems such as ribosomes and viral particles, to metabolites, RNA and protein complexes [4, 5]. The study of proteins, using different MS-based methods are the focus of this thesis in a manner that explores how the structure and dynamics of an amyloid-prone protein can be elucidated.

A mass spectrometer consists of three main components: ionisation, m/z analyser and detection (Figure 1.1). Firstly, the sample containing the analyte(s) of interest must be liberated from its typically liquid state into a gaseous phase of charged ionic species. Once

ionised, a plume of gas phase ions enters one or more mass analysers where they are separated based on their m/z . A plethora of mass analysers currently exist for specific sorting and analyses, a topic that is to be later discussed. Finally, separated ions enter a detection region. Detection commonly occurs through the measurement of the impact of charged ions on a detector plate or by measuring an image current. Such signals are amplified and converted into a digital format [6]. The advent of structural MS techniques which conjugates MS to hybrid/orthogonal methodologies such as hydrogen-deuterium exchange and cross linking has enabled the structural characterisation, stoichiometry and conformational heterogeneity of many complex samples to be further explored [7–12]. MS of proteins can be native or denatured, intact or digested depending on the information required. For structural analysis, native MS, that is, maintaining the native structure of proteins from solution as they enter the gas phase, is key to understanding factors such as compaction, conformational ensembles, stoichiometry of ligand binding and oligomeric states for example [13, 14]. The conditions of the ionisation process play a significant role in keeping proteins in their native conditions, such as using low temperatures and low voltages to prevent unfolding [15].

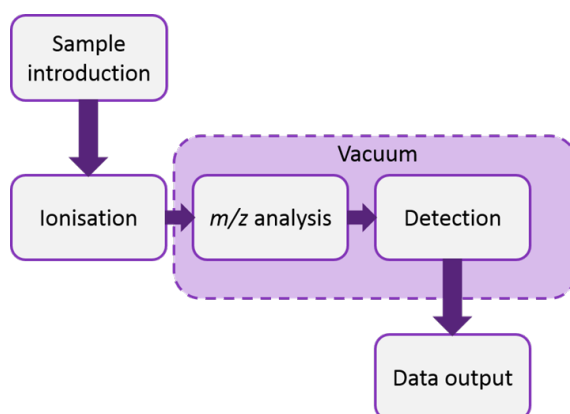


Figure. 1.1 Schematic of a mass spectrometer. Samples are introduced to the ion source where analytes are converted into a plume of gaseous ions. Gaseous ions are directed into one or multiple mass analysers for subsequent m/z sorting under vacuum. Separated ions are detected also under vacuum for signal amplification and downstream processing.

1.2 Electrospray Ionisation

In the beginning of MS development, the production of charged gas phase species relied upon harsh techniques such as electron ionisation (EI). The EI process consists of bombarding a heated sample already in the gas phase at high impact with a plume of high energy electrons generated from a heated filament. The high impact collisions needed for EI fragments analyte molecules and is limited to samples which are volatile and stable in the gas phase, ruling out large, native biomolecules which require gentle transfer into the gas phase [16]. The development of “soft” ionisation techniques in 1984 by John Fenn brought life to the prospect of biomolecule analysis in their native state by MS, facilitated by electrospray ionisation (ESI) whereby protein structures can be ionised in near native conditions so that gaseous ions retain their conformation(s) adopted in solution using non denaturing, volatile buffers such as ammonium acetate (AmAc) [17].

During the ESI process shown in Figure 1.2, samples are ionised at atmospheric pressure. The solution containing protein analytes is emitted through a thin borosilicate glass capillary coated typically in palladium metal to become electrically charged [16]. A voltage is applied to the capillary containing $\mu\text{M}/\text{nM}$ concentrations of protein creating a fine charged spray of droplets from a Taylor cone formation. The polarity of the emitter, which essentially becomes an electrode, determines the supply of positive or negative ions in the solution. Droplets are desolvated through gentle heating (typically around 30°C for native analyses) resulting in reduction of the droplet hydrodynamic radius, and an increase in the charge density of droplets. As a result, droplet fission occurs due to coulombic repulsion when the Rayleigh limit by excess charge carriers such as H^+ and NH_4^+ is reached [18]. Proteins and peptides can acquire multiple charges as many protonation sites are available along the protein backbone and side chain groups including lysine, arginine, histidine and the N-terminal amino group [19]. The mass spectrum generated contains multiple charge states in the case of ESI such that $[\text{M}+\text{nH}]^{n+}$ where M is the molecular

weight of the analyte and n is the number of charges acquired. Inevitably, the surface charges on a protein differs between the solution and gas phase [19]. For positive mode ESI, typically used for protein analyses, the number of charges that a protein acquires is related to its solvent accessible surface area (SASA). However, the maximum observable number of charges acquired is usually less than the number of basic residues (lysine, arginine, histidine and the N-terminal amino group) from charging in solution and de-protonated acidic groups (aspartic acid, glutamic acid and the C-terminal group) in the gas phase in the protein chain due to the stochastic nature of protein charging and charge repulsion [20].

The formation of ions can occur through three potential ionisation mechanisms (Figure 1.2). The charge residue model (CRM) which generally occurs for larger, folded and globular proteins, suggests that through continued droplet fission and solvent evaporation ions eventually become completely desolvated and acquire charges from the droplet [18]. The ion ejection model (IEM) proposes that analytes acquire their charges before becoming ejected from the droplet surface once a certain droplet radius has been achieved, IEM is predicted to be favoured for low molecular weight species, inorganic ions or a specifically niche range of proteins which are tightly folded with a high solution net charge [21, 22]. The third potential mechanism, the chain ejection model (CEM), is suggested to describe the ionisation of unfolded proteins or proteins containing intrinsically disordered regions (IDRs). In this proposed mechanism, the solvent exposed hydrophobic chain is migrated to the droplet surface to protrude outwards through ejection of the chain terminus driven by electrostatic repulsion [23]. Mobile H^+ present in the droplet undergo charge equilibration between the droplet and the protein chain protruding out of the droplet surface, many H^+ can be accommodated by the disordered, accessible protein chain resulting in highly charged ions [22].

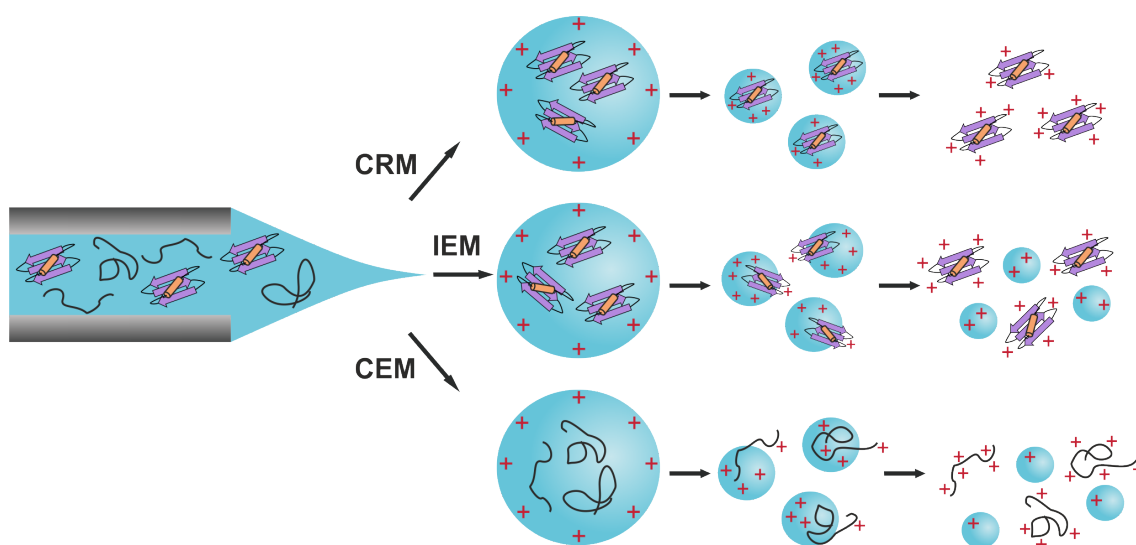


Figure. 1.2 The electrospray ionisation process. The three proposed models for the ESI process including the charge residue model (CRM), the ion ejection model (IEM) and the chain extension model (CEM).

For folded, globular proteins, the positive ESI charging process is thought to be dependent on SASA regardless of the distribution of preferred basic protonation sites. A larger number of basic residues allows for better distribution of charged sites which, in turn, minimises charge repulsion resulting in more stable compact states in the gas phase. For unfolded and disordered proteins, charging depends on the number of basic residues [19]. Conformationally heterogeneous protein samples produce multimodal charge state distributions which represent coexisting conformational families which were present at the moment of transfer from solution into the gas phase. The former mentioned conformational families might be present transiently with rapid interconversion which become locked when desolvated into the gas phase. Native ESI-MS offers a powerful approach to structurally characterise subtle differences in IDP conformation [24].

Once a mass spectrum of ion intensity versus m/z is generated for multiply charged species in positive ion mode, the molecular weight of analytes can be calculated by

determining the charge states of two adjacent spectral peaks applying Equation 1.1 where n is the charge state (number of charges acquired) and 1.0072 Da is the mass of a proton.

$$n_2 = \frac{m/z_{(1)} - 1.0072}{m/z_{(2)} - m/z_{(1)}} \quad \therefore \quad n_{(1)} = n_{(2)} - 1.0072 \quad (1.1)$$

Equation 1.3 Adjacent spectral peaks must be either $n+1$ (lower m/z) or $n-1$ (higher m/z). n is calculated for a given peak where $n_{(2)}$ is larger than $n_{(1)}$.

Once the charge states of two adjacent peaks are established, the analyte mass is calculated (Equation 1.2).

$$Mass = m/z_{(1)} \quad n - \quad z_{(1)} - 1.0072 \quad (1.2)$$

Equation 1.2 Calculation of the molecular weight of an analyte from adjacent spectral peaks in a charge state distribution by correcting for the number of protons acquired.

When sufficient resolution is achieved, another method to determine the charge state of an unknown species in the mass spectrum uses the isotope envelope. The isotopic distribution of C^{13} in a protein ion dominates the isotopic envelope, since the difference between isotopic peaks should be 1 Da from the lighter carbon isotope C^{12} , the charge state would be equal to the reciprocal of the distance between two adjacent isotopic peaks for each charge state.

ESI development has continued since its advent, into nano ESI (nESI) which takes advantage of electrospray capillaries with smaller orifices (1-4 μm inner diameter) enabling lower flow rates (20-50 nL/min) and minimal sample consumption; around 10-20 μL [16]. Nanospray capillaries are capable of producing a finer spray of smaller initial droplet sizes which encourages the desolvation process, reducing the degree of fission events needed to occur and therefore reducing the energy needed for desolvation. Therefore, nESI offers an even gentler technique for proteins and protein complexes to reach the gas phase [25]. The

application of ESI and nESI unlocked a unique versatility of analytes applicable to MS analysis, maintaining native structural arrangements, non-covalent complexes and ligand interactions; essential in the study of proteins and protein complexes.

1.3 Mass analysers

Ions, now in their gaseous phase, enter a high vacuum at the mass spectrometer interface for separation depending on their mass to charge ratio (m/z) using a mass analyser. An electric field accelerates ions out of the source and into the mass analyser [26]. This low pressure environment prevents collisions between ions enabling high ion transmission. There are different types of established mass analysers that are characterised by their amenable mass transmission, analysis range (by way of m/z), mass resolving power of the spectral output (the smallest mass difference between two fully resolved m/z peaks; Equation 1.3), mass accuracy and the rate of spectral acquisition (sensitivity).

$$R = \frac{m/z}{\Delta m/z} \quad (1.3)$$

Equation 1.3 Mass resolution. Resolution (R) is equal to the mass to charge ratio of an ion (m/z) divided by the difference in m/z either by the valley between two peaks or the full-width at half maximum (FWHM) of one peak.

There are two possible ways that resolution can be calculated. For a single peak, resolution is defined at the peak width at half of the maximum peak height, or simply the FWHM (Figure 1.3a). Two separated peaks are said to be resolved from one another if the valley between the peaks is below a threshold percentile such as 50 % for time of flight instruments (ToF) and 10 % for Orbitrap instruments which offer greater resolution (Figure 1.3b) [26].

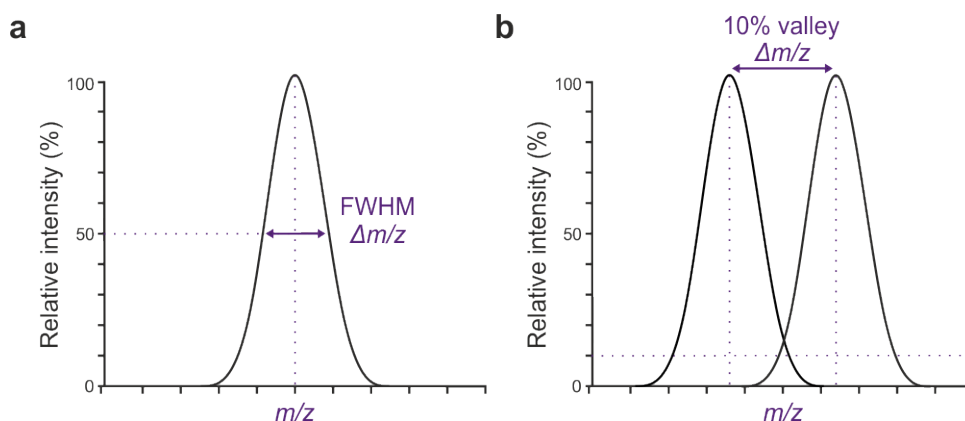


Figure. 1.3 Mass resolution. (a) Resolution for a single peak is defined by the FWHM (50% valley). (b) The resolution between two peaks is the difference in m/z between two overlapping peaks at 10% relative intensity.

Mass accuracy defines how far the mass measured conforms to the theoretical mass value, measured in parts per million (PPM), where a smaller PPM means minimal divergence of the experimental mass measurement. Mass accuracy is determined from Equation 1.4. For mass analysers such as the Orbitrap, sub 1-ppm mass accuracy can be achieved.

$$\text{Mass accuracy} = \left(\frac{\text{Theoretical mass} - \text{Measured mass}}{\text{Theoretical mass}} \right) \times 10^6 \quad (1.4)$$

Equation 1.4 Mass accuracy. The divergence of the measured mass from the theoretical mass defines the mass accuracy of the observed mass in ppm.

1.3.1 Quadrupole

Quadrupole mass analysers can be arranged as single instruments or in tandem with multiple quadrupoles or other mass analysers. In the latter arrangement, quadrupoles often serve as m/z filters for selecting ions of a particular m/z for further reactions and analysis [27]. However quadrupole mass analysers alone can serve as m/z analysers. For m/z sorting, filtering or detection the geometry of the quadrupole consists of four cylindrical metal rods

to which a direct current (DC) polarity is applied as opposite pairs, such that opposite rods possess the same charge, whilst adjacent rods possess opposite charges (Figure 1.4). A radio frequency (RF) alternating current (AC) with an amplitude greater than that of the DC current is applied so that the waveforms of adjacent rods are 180° out of phase to one another. The result is periodic switching of the polarity of rod pairs simultaneously to transmit ions of a certain m/z [28]. This oscillating field operates as a bandpass filter. Ions will be attracted to, and then repelled by, each rod pair which creates a helical or spiral trajectory through the trapping path. A given m/z resonates with the selected RF value enabling a stable, central trajectory. The amplitude of this three-dimensional wave-like trajectory depends on the m/z of an ion. For an m/z oscillating below or above the RF the ions trajectory is lost and these ions strike the electrodes to become electrically discharged or exit between them.

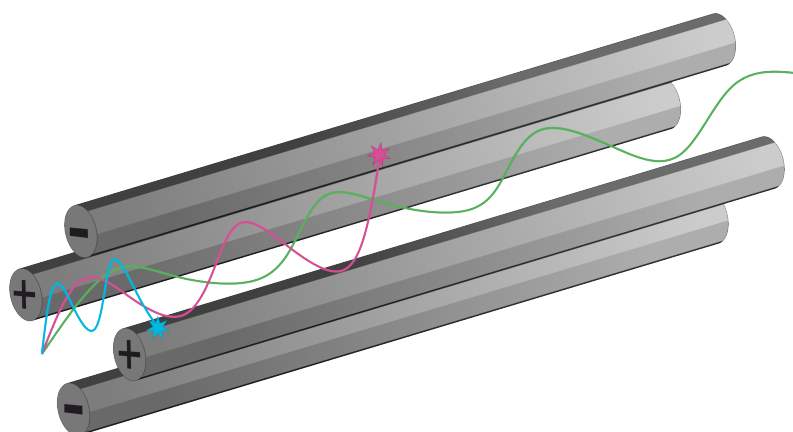


Figure. 1.4 Schematic of a quadrupole mass analyser. Metal rod electrodes are arranged as opposite pairs of potentials. An oscillating radio frequency with an alternating current enables ions of a certain m/z to pass through with a stable, helical trajectory (green trace). Unstable ions (blue and pink traces) collide with the metal rods resulting in electrical discharge.

Operating as a high pass filter, high m/z ions are transmitted, whilst the amplitude of low m/z ions becomes too great due to acceleration resulting in collision with the electrode, the m/z cut-off is defined by the RF. By adding a DC voltage high m/z ions cannot refocus

within the RF cycle and become influenced by the DC potential resulting in drifting from the central trajectory [29]. For a quadrupole acting as an ion guide, the DC component is switched off, enabling a defined range of ion transmission simultaneously through the centre of the quadrupole. In this operation mode, quadrupole mass analysers are coupled to other mass analysers to guide ions, reduce the m/z range or remove neutral molecules. The upper m/z limit of standard quadrupole mass analysers is generally 4000 m/z [30]. In this thesis, mass spectrometers containing quadrupole mass analysers are the Waters Synapt G1 HDMS, XEVO G2-XS and the Select Series Cyclic and the ThermoFisher Scientific Q-Exactive UHMR and Orbitrap Eclipse.

1.3.2 Time of flight

Time of flight (ToF) mass analysers accelerate ions using an electric potential through a field free flight tube. Ions are separated according to their time taken to travel to the detector which is dependent on their m/z . Ions accumulate as packets in the "pusher region", where a pusher voltage is applied to accelerate ions orthogonally by providing, ideally, a uniform initial kinetic energy (E_k) to all ions. Ions traverse through the flight tube in a vacuum towards a detector. Since all ions theoretically receive the same E_k , separation occurs due to the difference in flight time influenced by the mass of an ion (as velocity is inversely proportional to the square root of m/z) [31]. Essentially, the infinite time limit for an ion to reach the detector means that there is no upper mass detection limit, facilitating the detection of large biomolecules, however in reality, scanning frequency and other factors ultimately introduce limits. Heavier ions with a lower charge are accelerated less than lower mass ions or more highly charged ions. Thus, the velocity (v) of ions carrying the same number of charges (z) will be dependent on their mass value. (E_k) is proportional to the charge (z) and the applied potential (eV) where e is the elementary charge of an electron (1.601×10^{-19}) and V is the acceleration potential. This relationship is described in the following Equations.

$$E_k = \frac{mv^2}{2} = ze \quad (1.5)$$

Equation 1.5 The relationship between kinetic energy (E_k), mass (m), velocity (v) and charge (ze).

This relationship can be rearranged in order to determine v .

$$v^2 = \frac{2E_k}{m} = \frac{2zeV}{m} \quad (1.6)$$

Equation 1.6 rearrangement of Equation 1.5 to make velocity (v) the subject.

The time taken (t) for an ion to reach the detector during ToF analysis also depends on the length (L) of the field free flight tube and this relationship is described as follows.

$$t = \frac{L}{v} \quad \therefore \quad t^2 = \frac{m}{z} \left(\frac{L^2}{2eV} \right) \quad (1.7)$$

Equation 1.7 The time taken for an ion to reach the detector is equal to the length of the flight tube (L) divided by the velocity of the ion (v).

Since many components of the Equation are constant, including L , e and V the resulting Equation 1.8 is a proportional relationship between time taken and the square root of m/z .

$$t \propto \sqrt{m/z} \quad (1.8)$$

Equation 1.8 Flight time is proportional to the square root of an ions m/z .

Ions are separated based on their differing m/z values as they reach the detector at different times. ToF tubes are typically 1-2 m in length in order to maintain ion transmission so that ion flight times are on the μs timescale, within a vacuum in the 10e^{-6} to 10e^{-7} range, ion losses are minimised. Therefore, the scan speed of ToF instruments is particularly high enabling higher duty cycles of the instrument with multiple scans acquired rapidly (around

1000 spectra per second to capture flight times of about 10-100 μ seconds). Combining over multiple scans reduces the signal to noise ratio (S/N) of spectra significantly, improving the resolution. In a linear ToF arrangement, the ion beam enters the ToF cell directly and ions are immediately accelerated via the pusher voltage into the flight tube [32].

ToF is a pulsed analysis technique, which consists of the accumulation of ion packets in the pusher region which acts as a trapping region so that ions start their flight ideally in the same position relative to the pusher voltage. This means that ions of the same m/z receive the same E_k . Nonetheless, the spatial distribution of ions in the pusher region results in a variable distribution of voltage picked up from the acceleration voltage, leading to uneven E_k distributions. Ions of the same m/z therefore would receive varied acceleration forces to one another, reaching the detector at different times, broadening the arrival time to the detector and thus broadening spectral peaks, reducing the instrument resolution. With the continuous inlet of ions from an ESI source, this is highly problematic as broad peaks make differing m/z species indistinguishable [33]. The issue of ion spatial dispersion was initially addressed in the implementation of orthogonal ToF. Orthogonal ToF utilises a geometry whereby the flight tube of the ToF cell is arranged orthogonally to the ion beam direction (Figure 1.5).

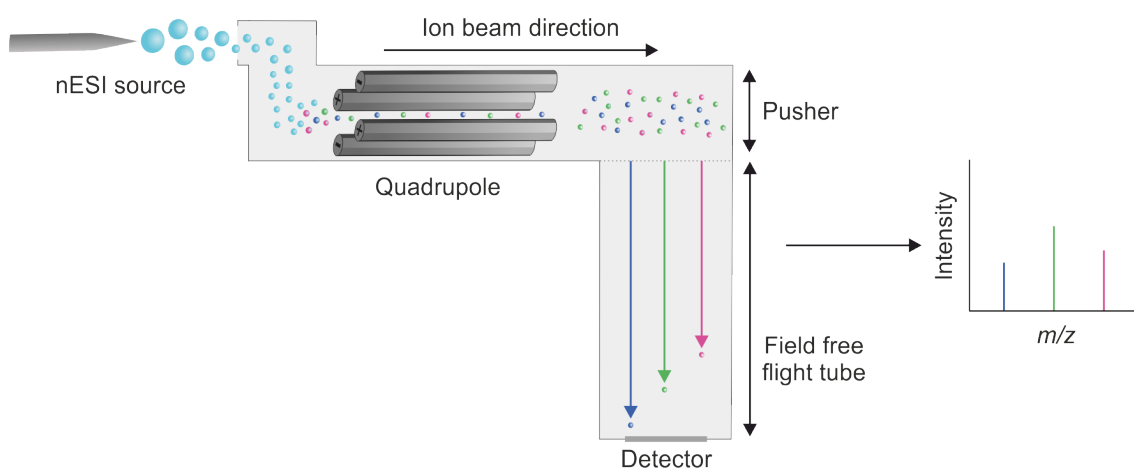


Figure. 1.5 A schematic of the orthogonal arrangement of a ToF cell in a quadrupole-time of flight (QToF) mass spectrometer. Ions are ionised at the nESI source, and are directed through a quadrupole mass analyser, the ion beam enters the pusher region and is trapped as an ion packet. The pusher voltage accelerates ions orthogonal to their initial ion path down the flight tube towards the detector. Ions with lower m/z values represented by the blue arrow reach the detector first followed by green ions and then the pink ions which are increasing in m/z respectively. The resulting spectrum on the right shows separated ions based on m/z .

Orthogonal ToF enables efficient ion accumulation in the pusher region and subsequent successive pushes of ion packets. The sudden change in direction of the ion beam enables tighter ion packets, minimising spatial dispersion so that ions of the same m/z should receive the same E_k and arrive at the detector together to give a sharper spectral peak. Although the orthogonal geometry improved the instrument resolution, some E_k dispersion still remains. The later development of the reflectron ToF largely addressed the issue of E_k dispersion. In the reflectron ToF model, the ion trajectory through the ToF flight tube is essentially doubled, and this occurs due to the arrangement of stacked ring electrodes which reflect ions backwards onto a detector plate creating a bell shaped ion path. Ions of a particular m/z that enter the ToF path with differing E_k values penetrate the stacked ring of electrodes to differing degrees resulting in refocusing of the ion packet [34]. Ions

with greater E_k travel deeper into the ring electrodes, a mirroring effect occurs which slows the ions down and propels them backwards. Since ions with lower E_k travel less into the ring electrodes, ions of the same m/z become refocussed together. The higher energy ions catch up with the lower energy ions upon reflection. Not only does this result in an improvement in resolution by minimising peak broadening, the doubled flight path also enables much more efficient separation of ions with differing m/z values [34]. A schematic of the reflectron ToF is depicted in Figure 1.6. Instruments used in this thesis containing ToF mass analysers are the Waters Synapt G1 HDMS, XEVO G2-XS and the Select Series Cyclic.

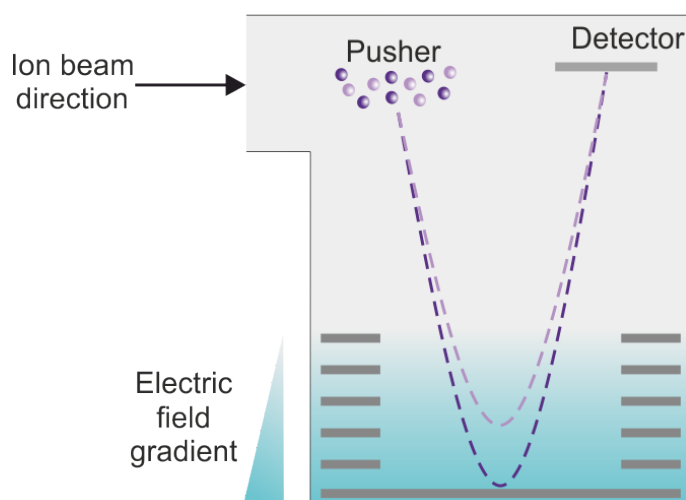


Figure. 1.6 A schematic of the reflectron ToF mass analyser. Ions with the same m/z but differing E_k , where dark purple ions have higher energy and light purple ions have lower energy are refocussed by the electrodes creating the electric field gradient. Ions with higher E_k penetrate deeper into the electrodes so that ions of the same m/z reach the detector simultaneously for sharper spectral peaks.

1.3.3 Linear ion trap

Similarly to quadrupole mass analysers, the linear ion trap (LIT) consists of four parallel rods shown in Figure 1.7. These rods are split into three sections referred to as a segmented

quadrupole. An RF field is applied to the central section of the LIT much like in the quadrupole geometry, whereby adjacent rods are 180 ° out of phase. The front and back sections are controlled by DC potentials. Ions are confined to all three dimensions by the central electrode and repelled back and forth axially between the front and back sections. Varying the DC and RF amplitudes in the centre section enables selection or scanning of m/z ranges. Ions are detected through an operation mode known as dipolar resonance ejection whereby supplemental AC potentials are applied to both x axis rod pairs [35]. Trapped ions oscillate around the central section, and when this oscillation frequency resonates with that of the AC field frequency, the ion trajectory linearly increases in amplitude for each oscillation until it becomes ejected through slits in the x axis rods to eventually hit detector plates placed outside of each x axis rod [29].

LITs can be used as stand alone mass analysers due to their comparable scan speeds and resolution to quadrupole instruments. However, more commonly LITs are used in commercial instruments as ion storage cells for collision based techniques prior to detection enabling MS^n . Collisional activation for precursor ion fragmentation is discussed later in this thesis. The ThermoFisher Scientific Orbitrap Eclipse instrument used in this thesis contains a LIT.

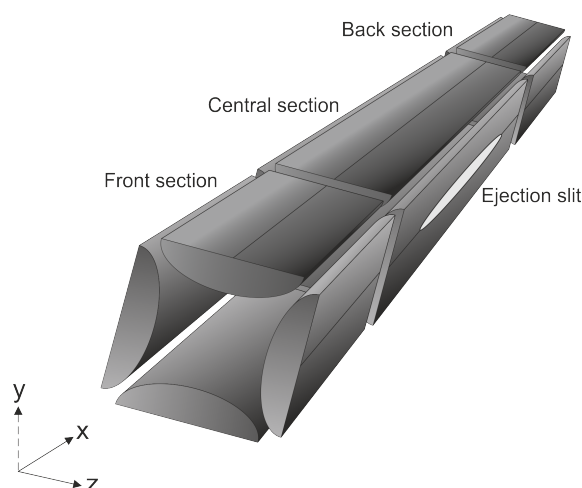


Figure. 1.7 Linear ion trap. Separated into the front, central and back sections, four rods are arranged in parallel. DC confinement potentials are applied to both the front and the back sections. RF-AC potentials are applied to the central section for ion trapping. Ions are ejected through ejection slits.

1.3.4 Orbitrap

The Orbitrap mass analyser was developed by Alexander Makarov in 2000 and operates as an orbital ion trap. Orbitrap instruments consist of a central spindle shaped electrode encased in outer electrodes (Figure 1.8) [36, 37]. The outer electrodes are typically held at ground potential whilst a voltage is applied to the central electrode, so that when ions are injected into the Orbitrap they begin to form stable orbits around the central electrode. Each ions oscillation frequency is dependent on its E_k and inversely proportional to m/z , resulting in orbits which are out of phase. Ions are required to undergo multiple orbits to effectively "find their orbit frequency" for more accurate detection which does reduce the scanning speed of the Orbitrap compared to the quadrupole, ToF and LIT. The scanning speed of the Orbitrap is typically around 10 Hz [29]. The difference in oscillation frequencies for differing m/z values is distinguished in a read out generated through current detection from the outer electrodes. This initial signal is recorded in the time domain for oscillations (known as a free induction decay; FID), which is converted through fourier transform into

the frequency domain versus intensity. This frequency spectrum is then further converted into m/z versus intensity [38].

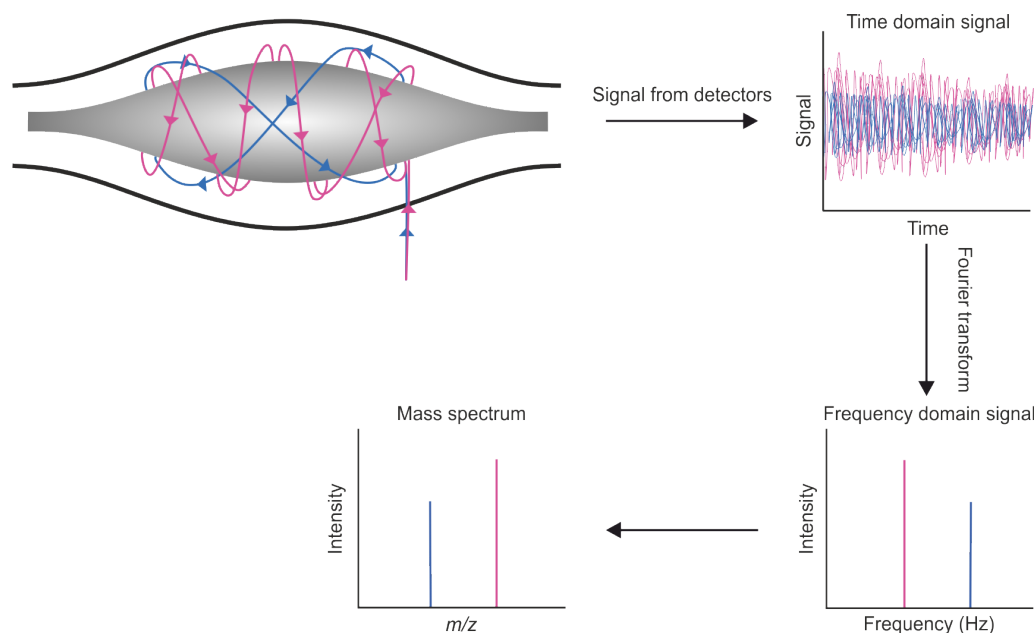


Figure. 1.8 The Orbitrap mass analyser. Ions are injected into the Orbitrap to begin their orbit. Ions orbit with an oscillation frequency inversely proportional to their m/z . Oscillations are measured as a current signal over time, which is converted through fourier transform into a frequency spectrum. A mass spectrum is generated by converting frequency into m/z .

The resolution of Orbitrap measurements decreases as a factor of $(m/z)^{0.5}$. Nonetheless, Orbitraps function as high resolution instruments achieving 500,000 (FWHM) at m/z 200 for the ThermoFisher Scientific Orbitrap Eclipse instrument. Much like ToF instruments, Orbitrap mass analysers use a pulsed analysis technique where packets of ions are pulsed into the Orbitrap region for analysis from a curved linear ion trap called a C-trap. Therefore, the Orbitrap is suitably coupled to continuous ionisation sources as ions can accumulate in the C-trap which is filled with collision gas molecules for ion cooling and rapid injection of packets of ions with minimal spatial spreading [39]. The Orbitrap offers high mass analysis

capabilities enabled by high resolution [36]. The ThermoFisher Scientific Orbitrap Eclipse instrument is used in this thesis.

1.3.5 Astral

The most recent mass analyser is the Astral developed by Alexander Makarov *et al* and commercialised by ThermoFisher Scientific [40]. The astral mass analyser is coupled to both a quadrupole for precursor ion selection and an Orbitrap mass analyser for high dynamic range single ion detection. The Astral offers unique sensitivity, as well as high dynamic range, acquiring spectra at a rate of 200 Hz. To enter the astral mass analyser, ions are first trapped in an ion routing multipole and can be fragmented using a collision gas. Ions are ejected through sequential ion optics which align the ion packet to improve instrument sensitivity. The packet of ions is accelerated into an open electrostatic trap and guided through a thirty meter long track of asymmetric ion mirrors to be focussed in three dimensions for nearly lossless ion transmission. The extended asymmetric track enables enhanced spectral resolution which can resolve overlapping ions [40, 41]. The extremely short scanning time of the Astral reduces the duty cycle which could revolutionise the rapid analysis of complex samples such as those in the clinical research field.

1.4 Detectors

Ion signals are detected after separation on the basis of m/z in the mass analyser. One of the most common detector systems used is the electron multiplier. Ions collide with a conversion dynode which results in the emission of electrons. The electron emission is then amplified to generate a current (Figure 1.9) [42]. Detection in the ToF mass analyser uses a microchannel plate detector due to its rapid response time (sub ns) matching the fast μ second scan speed achieved by ToF analysers with narrow pulse width and separation based on time measurements [42].

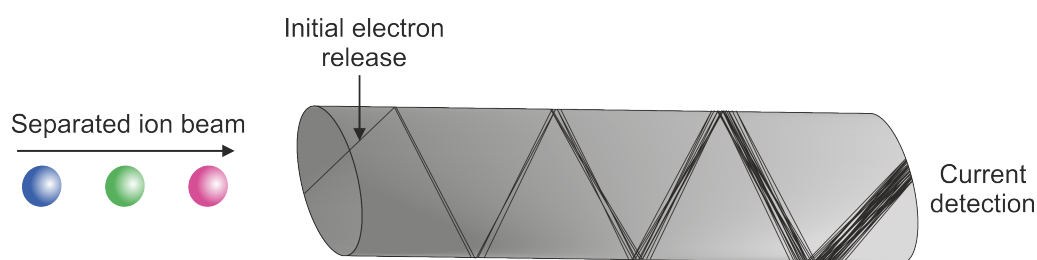


Figure. 1.9 Schematic of an electron multiplier detector. Ions are separated by a mass analyser and strike the detector made of semiconducting glass such as lead oxide, to release an electron beginning a cascade effect where electrons continually strike the detector to release more electrons for signal amplification to generate a current.

In the Orbitrap mass analyser, the outer electrodes surrounding the central spindle electrode (Figure 1.8) which act as the detectors. The ion orbit generates an image current from the oscillation frequency and amplitude which is related to an ions m/z value. In the case of the Orbitrap, image-current detection is undisturbed and the overlapping image current signals from ions with differing m/z are processed through the fourier transform algorithm to generate a frequency signal, converted into a spectrum of m/z versus intensity [36].

1.5 Ion mobility mass spectrometry

Separating species by their m/z is a useful biological tool for identifying biomolecules present in complex mixtures. In some cases, adding another dimension of orthogonal separation offers more detailed characterisation that may benefit the understanding of molecular mechanisms. Ion mobility (IM) spectrometry separates ionic species orthogonally to MS which can differentiate between ions with overlapping m/z values but are conformationally distinct in space [43]. Therefore, when IM is coupled with MS (IM-MS) a direct read out of a proteins conformation can be achieved. IM separates ionic species in the gas phase after ionisation based on their mobility when moving through a drift tube that is filled

with neutral buffer gas [44]. Under conditions where the pressure and temperature of the drift tube are controlled, the mobility that each ion exhibits is dependent on its rotationally averaged collision cross section (CCS) as well as the number of charges acquired. IM separates ionic species on the ms timescale which makes this technique adequately suited to coupling with ToF analysis which scans ions on the μ second timescale. A variety of IM separation technologies currently exists, the most common IM methodologies are summarised below.

1.5.1 Drift tube ion mobility

The simplest, original method of IM separation is drift tube IM (DTIM; Figure 1.10). Ions are accumulated in a trap cell which is positioned prior to the drift tube for pulsed entry of ion packets. A weak electric field is applied across the drift tube so that ions migrate from one end to the other [45]. It is crucial that this electric field is weak so that ions do not gain too high E_k and therefore unfold or fragment upon energetic collisions with buffer gas, such that E_k is converted into internal energy. The drift tube itself is filled with a neutral buffer gas such as He or N₂ which do not chemically interact with protein molecules but can initiate gentle collisions as ions travel through so that they reach a constant velocity [44]. Ionic species which occupy a larger, exposed structure, such as unfolded proteins, experience more frequent collisions with the buffer gas molecules and therefore possess a lower mobility resulting in a longer drift time (t_d). Ions with a smaller surface area however experience less collisions with the buffer gas and travel with a greater mobility to reach the end of the tube first. The result is an array of "arrival time distributions" (ATDs) [46].

Additionally, ions carrying a greater number of charges are more influenced by the weak electric field and are pulled through the tube faster than ions carrying fewer charges. Separation is therefore also dependent on charge state [46]. This enables instrument users to gain better clarity on how far the charge state distribution of a protein reflects its native conformational ensemble, for example for higher charge states, the arrival time distribution

IM may not be accurate. This arises due to two reasons: i. acquiring too many like-charges will result in charge repulsion and therefore over-expansion of the protein chain and ii. quicker mobility through the drift tube can result in more energetic collisions and potential unfolding [47]. Both of these considerations would lead to an over-estimation of the arrival time distribution of a protein and selecting charge states requires careful consideration. Lower charge states are considered to be more native-like [48]. With precise control of instrument parameters, IM can be used to calculate CCS (denoted ^{DT}CCS for drift time measurements) or a measurement of the shape of an ion (Ω) in a given buffer gas of known pressure, tube length and temperature using the Mason-Schamp Equation [46].

$$CCS = \frac{(18\pi)^{1/2}}{16} \frac{ze}{(k_b T)^{1/2}} \left(\frac{1}{\mu}\right)^{1/2} \frac{760}{P} \frac{T}{273.2} \frac{1}{N} \frac{t_d E}{L} \quad (1.9)$$

Equation 1.9 The Mason-Schamp Equation. Where e is the charge on an electron, z is the charge state of the analyte ion, K_b is the Boltzmann constant, N is the number density for the drift gas, T is the temperature in the drift tube, P is the drift gas pressure, t_d and μ is the reduced mass of the ion and neutral defined by $(m_{neutral}m_{ion})/(m_{neutral}+m_{ion})$ where $m_{neutral}$ is the molecular mass of the drift gas and m_{ion} is the molecular mass of the analyte ion. E is the electric field and L is the length of the drift tube.

Ions separated by their CCS leave the mobility cell and are subsequently detected on the basis of their m/z in a tandem IM-MS approach. As a result, each peak in the mass spectrum has a drift time profile attached to it, called an arrival time distribution where the x-axis is t_d . The sensitivity of DTIM is hindered due to the low duty cycle such that ion species can reach the detector and reduce current detection. DTIM technology has since been improved for better separation by an alternative technique of IM separation known as traveling wave IM spectrometry (TWIMS).

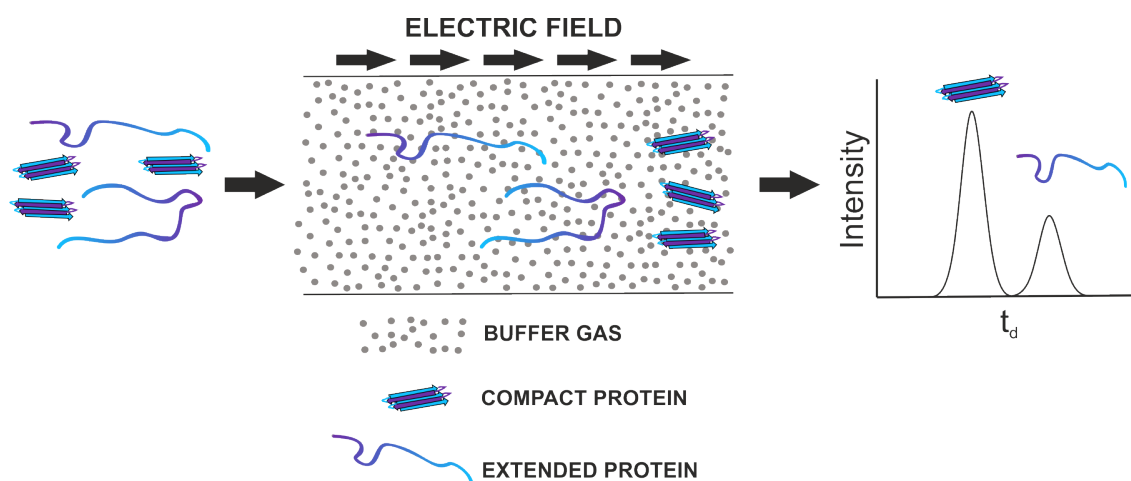


Figure. 1.10 Drift tube ion mobility spectrometry. A weak electric field causes ions to migrate through a controlled tube filled with neutral buffer gas molecules resulting in collisions. Ions with larger conformers undergo more frequent collisions with the buffer gas and take longer to traverse the tube than ions with smaller conformers.

1.5.2 Traveling wave ion mobility

Developed by Waters corporation, TWIMS adopts the principles outlined in DTIM, with the addition of a stacked ring ion guide (SRIG) of electrodes (Figure 1.11) [49, 50]. An RF voltage is applied to the SRIG which traps ions centrally in the drift tube region whilst ions migrate through the cell. A DC potential is superimposed over the RF voltage onto adjacent pairs or sequences of electrode rings which are 180° out of phase. The DC potential is set in an alternating fashion through the length of the SRIG to create an alternating waveform [51]. This secondary wave propagates through the drift tube so that ions with higher mobility (those with smaller CCS) experience fewer rollover events and, as they experience less collisions, are propelled through the drift tube. Ions with lower mobility (larger CCS) roll over the wave and rely on the next wave to pick them up again. This mechanism improves the resolution of separation of ions and increases the speed of the process therefore, increasing the duty cycle. Manipulating the voltage applied to the SRIG affects the wave amplitude and velocity, allowing control of the degree of ion separation,

as well as modifying the gas pressure in the cell [52, 49]. Due to the now non uniform electric field in the drift tube in TWIMS, CCS cannot be directly calculated (denoted as ^{TW}CCS for traveling wave measurements). ^{TW}CCS is instead calculated by calibrating the drift tube against calibrants measured in DTIM which correct for the non-uniform electric field [51]. The calibrants selected must be fine tuned for the analyte of interest, for a disordered protein for example, it would be suitable to select calibrants of a similar molecular weight and charge states measured in denaturing conditions [53].

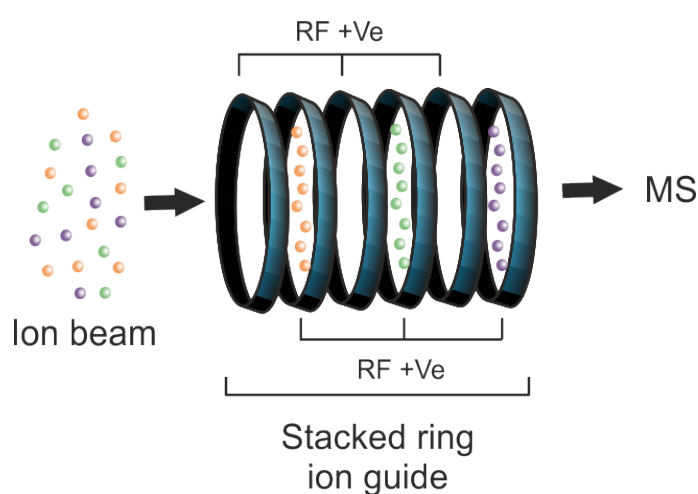


Figure. 1.11 Traveling wave ion mobility spectrometry. Across the stacked ring ion guide, adjacent rings are 180° out of phase. Ions are centrally focussed for a radial propagation. The sweeping DC potential separates ions based on their mobility.

1.5.3 Cyclic ion mobility

The resolving power of IM instruments is highly dependent on the length of the drift tube, also known as the path length [54]. Efforts to increase the resolving power of IM have therefore involved increasing path length. Recently Waters corporation advanced their TWIMS device into a commercially available cyclic ion mobility spectrometry device (cIM). The geometry of the cIM device consists of a TWIMS cell extended into a closed loop called a racetrack which runs perpendicular to the ion beam direction through the MS system (Figure 1.12) [54]. The racetrack loop is also situated between two ion guides

called the pre- and post-array stores. At the entry junction into the racetrack after the pre-array store, there is a multifunctional array which consists of multiple electrodes to generate a traveling wave. By changing the direction of this wave, ions can be moved between the racetrack and the pre- or post-array stores, which facilitates the ability to isolate ions based on their drift time for further analysis [55].

The cIM-MS system offers IM^n , where the initial ATD from one pass of the cyclic loop can be "sliced" into separated peaks, to then pass one "conformational family" under one t_d peak for multiple passes for further separation. Ions are stored as packets in the trap cell which precedes the IM separation region. Packets of ions are injected into the pre-array electrodes where the DC potential applied is held below that of the cIM region to prevent ions separating prematurely [55]. The voltage applied is increased and the direction of the travelling wave matches that of the cIM cell so that ions are propelled around the cyclic separator for a single pass. The path length of the cyclic device is 98 cm, which improves the separation of ions observed in a standard linear TWIMS device with a path length of 25.4 cm [54]. Therefore, with a single pass, the resolving power of IM separation is increased. For IM^n , a slice of around a few milliseconds of the separation phase can be ejected back into the pre-array store so that a segment set manually can be excised from the single-pass ATD. The remainder of the ions in the ATD are ejected in the opposite direction through the post-array and towards the ToF mass analyser preceding IM separation but without triggering data acquisition [55, 56]. The ions stored in the pre-array can be reinjected into the cIM cell and passed as many times as manually set around the closed loop. The number of passes however is not infinite, as the high mobility ions will catch up with low mobility ions resulting in overlap of separated peaks known as "wrap-around".

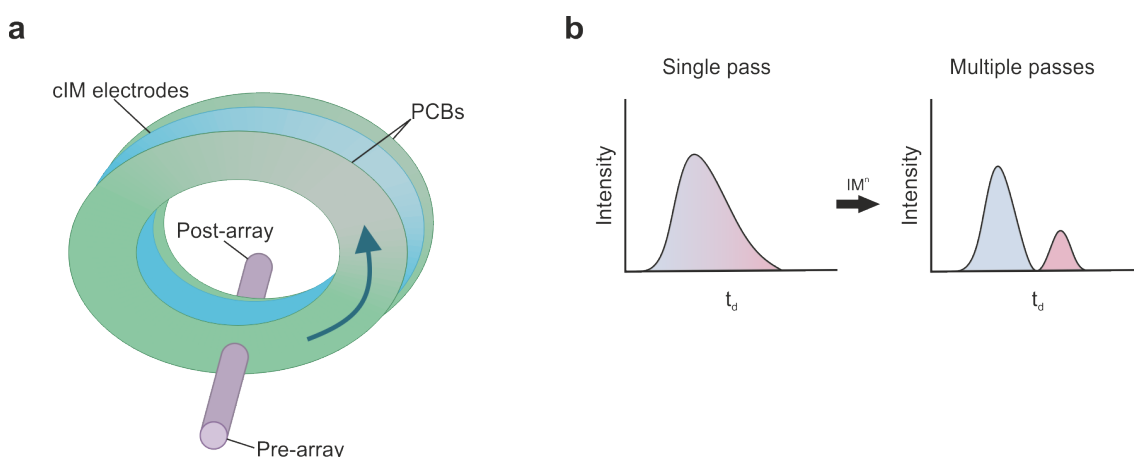


Figure. 1.12 Cyclic ion mobility. (a) The geometry of the instrument includes a pre-array store, ions are injected into the cIM electrodes which are encased in printed circuit boards (PCBs) which provide the voltage connections. Ions then migrate through the cyclic and exit to the post-array. (b) The resolution of the shoulder peak observed at a single pass is resolved into a separate conformational family after multiple passes in the t_d domain [56].

1.6 Tandem mass spectrometry

Mass analysers can be arranged in tandem (MS/MS) with one another enabling MS^n where mass analysers are separated by a collision cell for precursor ion selection (MS^1) and fragment ion detection (MS^2). This method of analysis is commonly used in proteomics [57]. Known as a product ion scan (Figure 1.13), one ion or a particular m/z is isolated usually by a quadrupole in the (MS^1). There are various methods for fragmentation, one of the most common is collisionally induced dissociation (CID). CID relies on a collision gas such as Ar, N_2 or He which fills the collision cell. Ions undergo energetic collisions with the gas molecules where there is a transfer of E_k into internal energy, this heating effects results in fragmentation of covalent bonds in an ergodic reaction [58]. Similarly, higher energy dissociation (HCD) which is carried out in the C-trap prior to the Orbitrap mass analyser described in Section 1.3.4, relies on rapid injection of collision gas for

fragmentation [59]. CID and HCD are not native techniques, as bond heating does not maintain native protein structures, CID is known as a slow-heating activation method [60].

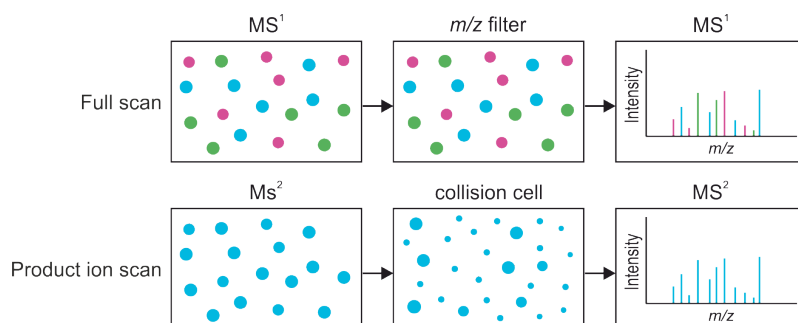


Figure. 1.13 Product ion scan. A multiply charged ion of a specific m/z (blue) is selected in the MS^1 cell and is subjected to fragmentation. Fragment ions are detected in the MS^2 cell.

Fragmentation occurs in the linear backbone of multiply charged protein (top-down) or peptide (bottom-up) molecules. Adding energy by CID and HCD causes cleavage of the amide bond between neighbouring amino acid residues in a peptide bond yielding b - and y - type ions which are N- and C- terminal directed respectively (Figure 1.14) for *de novo* protein sequencing [61]. Internal fragments can also be generated by internal bond fragmentation in two places causing two or more residue length fragments, however, internal ions are generally large and assigning peaks becomes ambiguous. Nonetheless, internal ions do increase the sequence coverage possible [57]. For native fragmentation of intact proteins, also called native top-down fragmentation, other methodologies exist such as electron capture dissociation (ECD), electron transfer dissociation (ETD) and ultra-violet photo-dissociation (UVPD). The advent of top-down proteomics involves directly infusing intact proteins for dissociation in order to sequence the protein backbone and this has largely facilitated MS detection of proteins in complex mixtures [61–65].

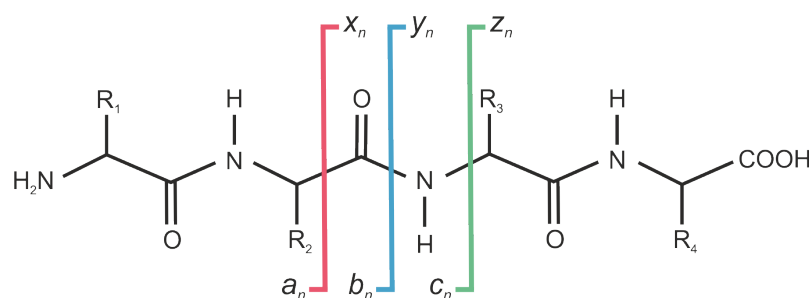
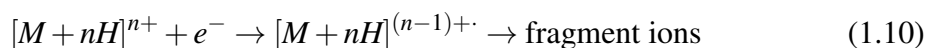


Figure. 1.14 Fragment ions generated through peptide bond dissociation. Type x , y and z ions are formed when the positive charge is retained at the C-terminal end of the peptide. Type a , b and c ions are formed when the positive charge is retained at the N-terminal end of the peptide. Subscript n defines the amino acid residue number in the peptide ion sequence.

1.6.1 Electron capture dissociation

Developed in around 1988 by Roman Zubarev, Neil Kelleher and Fred McLafferty, the process of low-energy ECD involves the capture of an electron by a multiply charged cation to produce cationic dissociation product ions [61]. ECD is an electron initiated, radical driven method used in MS/MS. Cleavage of the protein backbone occurs primarily at N-C $_{\alpha}$ bonds. Labile bonds such as non-covalent interactions and post-translational modifications (PTMs) remain intact and can be identified as mass shifts of a single residue [66]. The protein backbone chain is built up of amino acids H₂N-C $_{\alpha}$ RH-COOH (where R is one of the twenty common amino acid side chains; Figure A.18) joined sequentially by peptide bonds through removal of H₂O for N-C bonding. Cleavage of the N-C bond yields b - and y - type ions achieved by vibrational activation of the peptide bond. The capture of a low energy electron (1 eV) results in cleavage of the N-C $_{\alpha}$ bond producing N-terminally generated c - and C-terminally generated z - type ions (Equation 1.10 and Figure 1.15) [61].



Equation 1.10 Charge reduction due to electron capture results in radical generation before fragmentation where M is the molecular weight of the protein analyte, n is the number of proton charges, e^- is an electron, and \cdot represents a radical.

Low energy electrons are generated by a heated filament usually composed of tungsten which heats as an electric current is passed through it. Electrons in the filament material gain enough energy to overcome the minimum energy required to release an electron from the surface (thermionic emission). Emitted electrons create a low energy electron cloud or reservoir of which gaseous protein ions pass through for electron capture [67]. ECD has been applied to identify phosphorylation sites on protein chains, identify a dimer interface and has been coupled to cIM to identify conformation sensitive fragmentation patterns for carbonic anhydrase [68, 69]. Electron capture does not always result in bond dissociation, referred to as electron capture without dissociation or ECnoD. This results in the production of charge reduced ionic species appearing to the right of the isolated protein ion on the m/z spectrum. It is thought that charged reduced species represent adjacent c - and z - ions held together by non-covalent bonds. One potential weakness of ECD, which became apparent due to the development of newer fragmentation techniques is the abundance of b - and y - type ions which can be generated due to heating of the ECD cell from the tungsten filament. As the cell heats, this energises gaseous protein ions prior to fragmentation and results in higher energy fragmentation of the N-C bond from energetic electrons which reduces the extent of how native ECD really is in comparison to ETD developed in around 2004 [70].

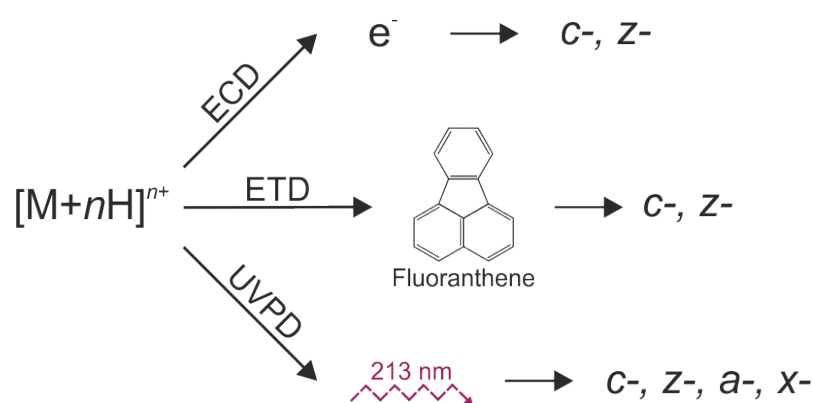


Figure 1.15 Fragmentation mechanisms. All three processes highlighted: ECD, ETD and UVPD result in primarily the production of $c-$ and $z-$ ions with the exception of UVPD which also generates $a-$ and $x-$ ions.

1.6.2 Electron transfer dissociation

ETD relies on a similar mechanism to ECD. The difference between the two processes is that in ETD, multiple charged protein ions interact with a reagent anion such as fluoranthene (Figure 1.15) which transfers an electron to the protein cation [60]. A radical forms and dissociates into $c-$ and $z-$ ions. ETD can be used in combination with HCD supplemental activation in order to improve *de novo* sequencing by way of generating more fragment ions [71], in a hybrid approach called EThcD however, the generation of $b-$ and $y-$ ions makes this approach highly energetic [57]. ETD is carried out in ion traps held at lower pressure for ion collisional cooling, reducing the internal energy of the electron attachment. The Kelleher group at Northwestern University showed the true potential of ECD in the structural elucidation of 5000 proteoforms from the human lung cancer cell line H1299 [72].

1.6.3 Ultraviolet photodissociation

UVPD offers an orthogonal fragmentation approach which does not involve electron attachment, but instead utilises photons (around 6 eV per photon) generated from a UV

laser source [73]. Energetic photons with a wavelength of 213 nm are absorbed by the amide bond (N-C) on the microsecond timescale resulting in fragmentation via electronic excitation [74]. Cleavage of the C-C_α yields the less common *a*- and *x*- type ions (Figure 1.14). Each amino acid residue moiety is composed of the mass of the residue minus a water molecule which is lost during peptide bond formation, enabling sequencing. A key benefit to UVPD is that it is not dependent on the precursor ion charge state. The only parameter that requires optimisation is the activation time which is the duration of the UV laser pulse (usually around 50-100 ms) [75]. The high energy photons are absorbed by chromophores within the protein, *a*- type ions are formed when cleavage occurs between the C_α and the COOH group in the N-terminal direction, *x*- type ions are formed from cleavage of the carboxyl group and the internal amino acid in the C-terminal direction [76]. Both *c*- and *z*- ions also arise [73] which is discussed further in Section 4.7.2. UVPD has been used to dissociate oligomers of streptavidin, transthyretin and haemoglobin into dimers and monomers for backbone sequencing to yield information about the quaternary structures of protein complexes [77].

1.7 Liquid-chromatography mass spectrometry

The analyses of complex biological samples, such as cell lysates or peptide mixtures which contain many analytes and PTMs, results in complex overlapping *m/z* spectra. Liquid chromatography (LC) is a separation technique used prior to sample ionisation and MS analysis. LC is generally used in bottom-up proteomics approaches which includes enzymatic digestion of proteins into peptides using common protease enzymes such as trypsin (see also Section 1.8) [78]. LC separates proteins (top-down) and peptides (bottom-up) in their aqueous phase through an analytical column packed with a specific material for defined separation chemistries. The physicochemical properties of analytes are utilised for separation in LC, this can be their size, charge or hydrophobicity. The most commonly adopted LC approach in biological MS is reverse phase LC (RP-LC)

which separates molecules based on their hydrophobicity. For RP-LC, the inner surface of the analytical column is coated with alkyl chains bonded to silica. The length of the alkyl chain is an important determinant in the degree of analyte separation. Longer alkyl chains are more hydrophobic. Analyte separation follows the "like likes like" principle, where hydrophobic molecules will interact more with a hydrophobic surface [79]. Thus, separation occurs based on how well an analyte interacts with the surface coating which is called the stationary phase, and therefore how little an analyte is found in the flowing aqueous liquid called the mobile phase. Analytes which interact well with the stationary phase reside on the column for longer, and have a longer retention time. Typically a C18 chain is used (composed of 18 alkyl moieties in series). Hydrophilic analytes exit the column with the shortest retention time. The polarity of the analyte (in the case of proteins) is defined by its amino acid composition [80]. Other columns such as C4 alkyl chains offer retention mechanisms based on ionic interactions.

So that hydrophobic analytes do not get stuck interacting with the stationary phase indefinitely, the polarity of the mobile phase is gradually decreased by mixing a non-polar buffer (buffer B) usually acetonitrile, into buffer A which is usually water doped with around 0.1-5% acetonitrile or formic acid so that non polar analytes begin interacting with the mobile phase, after their more polar counterparts have eluted from the column [81]. The development of high pressure liquid chromatography (HPLC) using thinner diameter columns and higher flow rates, leading to higher column pressures, have offered improved resolution of separation and increased speed of the column run times [82]. The buffers used in LC separation are compatible with ESI sources to enable direct sample ionisation once an analyte has eluted off of the column with a defined retention time, so that an m/z can be attached to each LC peak, amenable buffers include formic or trifluoroacetic acid for denatured analysis.

Each analyte offers a brief elution peak and this must be accompanied by rapid mass analysis of the intact precursor ion in the MS¹ cell prior to fragmentation and rapid

detection of fragment ions in the MS² cell. For data acquisition there are two dominating modes: data-dependent acquisition (DDA) and data-independent acquisition (DIA) [83–85]. In DDA, after the first full mass spectrum scan, the most intense or abundant precursor ions are selected for fragmentation where spectra are acquired until the LC elution protocol finishes. A dynamic exclusion parameter can be manipulated in order to prevent the same *m/z* precursor being repeatedly fragmented in a time frame so that other, less intense ion species can be selected for [86]. DDA cycles must be finely tuned to be short enough to improve the duty cycle, but also be long enough to thoroughly analyse elution peaks (around 30-90s). In DIA, there is no pre-selection of precursor ions, so that co-eluting precursor ions are fragmented together, using MSe developed by Waters Corporation and more recently using windows in other instruments. The resulting fragmentation spectra are complex and crowded, but the depth of analyte detection is more thorough. DIA is unbiased towards ion abundance and ionisation efficiency, acquiring a mass spectrum for all precursor ions within a defined mass range [87]. Recently, ThermoFisher Scientific have developed a workflow called AcquireX, a modified version of DDA, which requires iterative sample injections to create "inclusion and exclusion lists". This protocol enables exclusion of background ions and commonly fragmented ions so that lower intensity ions are fragmented.

1.8 Cross linking-mass spectrometry

Chemical cross linking (XL) has emerged as a versatile and indispensable technique in structural biology [88, 4, 89–92]. XL-MS provides unique information about the three-dimensional architecture and interactions between complex biomolecules by capturing dynamic processes and transient interactions in solution [93]. The basis of XL involves the formation of covalent bonds between amino acid residues in close proximity within a protein structure in solution, or between proteins within a complex or between interacting partners. XL therefore provides information on the structural arrangement of proteins

either to themselves or to other proteins [94]. By covalently linking proximal residues, XL-MS essentially provides a frozen snapshot of the most abundant conformations with optimal cross-linking efficiency present at once in an ensemble.

Following the XL reaction, proteins or their complexes are digested using proteolytic enzymes which retain these native linkages. These peptides are analysed by MS/MS to map the global protein sequence by matching tagged peptide m/z values with spectral peaks. A range of proteolytic enzymes are widely used for the digestion of proteins such as trypsin, a serine protease which consists of a nucleophilic serine at the active site and cleaves peptide bonds specifically at the carboxyl side of lysine and arginine residues (unless followed by a proline residue) with high efficiency through a hydrolysis reaction [95]. Trypsin is well established for protein digestion in bottom up proteomics approaches. Engineered trypsin carry methylation modifications at lys and arg residues in order to prevent autolysis/self digestion for cleaner MS analysis [96]. Although trypsin is widely established and accepted as the gold-standard enzyme for bottom-up proteomics, one limitation is that for proteins which do not contain numerable lys or arg residues, or contain clustered lys and arg sequences, tryptic digestion results in poor sequence coverage. The peptides produced would either be too long for accurate MS/MS sequencing, or too short for adequate MS detection respectively and also prove difficult for LC separation [97, 98]. Many other enzymes with different peptide bond cleavage specificities are commonly used such as GluC which cleaves at the carboxyl side of glutamic acid residues. Different enzymes can also be used in tandem for either a sequential series of digests in order for a primary enzyme to cleave the protein into peptides, followed by primary enzyme removal and then addition of a secondary enzyme to further target longer peptides for digestion into smaller peptides of optimal length for MS detection and sequencing. This workflow has been shown to improve the sequence coverage for proteome analysis, improving the number of proteins detected [97]. A second workflow involves partitioning the protein mixture into separate reaction tubes, and adding for example trypsin to one tube and an

alternative enzyme to the other and allowing each reaction to proceed, targeting specific regions of the protein. The separate reactions are then analysed by MS/MS and the resulting sequences are pooled to increase coverage [99].

Various XL methodologies exist with the exhaustive development of different XL chemistries [100]. Proteins are cross-linked through the chemical reaction of homo- or hetero-bifunctional cross linkers and the reactive functional groups present on the side chains of amino acids. Reactive functional groups include amino groups (lysine, N-terminus), thiols (cysteine) and carboxyl groups (aspartic acid, glutamic acid, C-terminus). Specifically, N-hydroxysuccinimide (NHS) esters react with primary amines present on lysine side chains forming a covalent link and are frequently used in cross-linking reactions [101, 102, 90, 103]. The chemical reaction consists of acylation of a nucleophile which in this case is the positive amine group. However, a lack of accessible lysine residues in some cases has been shown to induce non-specific cross-linking to hydroxyl groups on serine, threonine and tyrosine [100]. The linker length of a cross linker defines the maximum distance restraint achieved, much like a molecular 'ruler'. Linkers can range from 'zero-length' to tens of angstroms [104]. Examples of 'zero-length' cross linkers are 1-ethyl-3-(3-dimethylaminopropyl)carbodiimide hydrochloride (EDC) and 4-(4,6-dimethoxy-1,3,5-triazin-2-yl)-4-methyl-morpholinium chloride (DMTMM), which promote the reaction between carboxylic acids on acidic residues and amine groups on basic residues by first attacking acidic residues and then acting as a good leaving group so that the XL group is removed by the incoming amine group (Figure 1.16). Whilst EDC is only sufficiently active at relatively low pH (5.5), DMTMM is efficient at physiological pH [103]. Zero-length cross linkers have the lowest possible distance constraint, but present challenges for MS/MS cleavability and peptide identification and produce less rich data by capturing fewer cross-links.

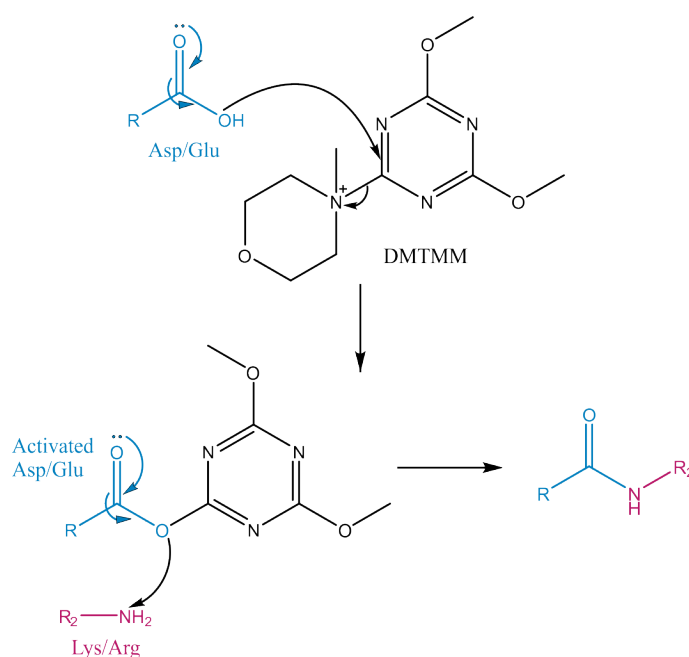


Figure. 1.16 DMTMM reaction mechanism. Adapted from [103].

XL-MS proved powerful in the identification of protein subunit arrangements in complexes [88, 93, 92, 105, 106]. XL could contribute to the study of intrinsically disordered proteins (IDPs) and their elusive roles in cellular function and disease [93, 102]. XL-MS is a useful platform for complementing molecular dynamic (MD) modelling, but often requires a resolved structure to begin with. The length of the linker used in the XL reaction is an important determining factor for constraints. Shorter linkers refine the MD search space, reducing conformational possibilities for an ensemble [107, 108]. IDPs explore a large conformational space and an ensemble of conformations, which limits the accuracy of force fields used to generate MD simulations [102]. Henceforth using orthogonal data to restrain MD simulations of an IDP is a powerful approach to help to define their conformational ensemble. Brodie. et al., [89] have probed the structure of monomeric α -synuclein through ‘short distance cross-linking constraint-guided discrete molecular dynamics’ (CL-DMD). This method uses short distance constraints achieved by cross-linking to reduce the possible conformational space visited during an MD simulation, enabling simulations of ensembles to be calculated. Using CL-DMD, their research showed that a distinct topology

appears to be present in α -synuclein where the C-terminal region of the protein is in close proximity to the N-terminal region consistent with long-range electrostatic interactions [89]. Table 1.1 highlights some common cross-linkers and their characteristics.

Table 1.1 Common cross-linkers and their characteristics [109, 104].

Cross-linker	Spacer-length	Reactive group	Reactive residues	Advantages/ Disadvantages
BS3	11.4Å	NHS ester	Primary amines	Not membrane permeable or cleavable
DSBU	12.5Å	NHS ester	Primary amines	Cleavable, membrane permeable
DSSO	10.1Å	NHS ester	Primary amines	Cleavable, membrane permeable
PhoX	4.8Å	NHS ester, phosphonic acid enrichment	Primary amines	Enrichable
Azide-A-DSBSO	12.9Å	NHS ester, azide enrichment	Primary amines	Enrichable, cleavable, membrane permeable
DMTMM	Zero-length	Hetero-bifunctional, coupling reagent	Lys, N- and C-termini, glu/asp	Active at physiological pH
EDC	Zero-length	Hetero-bifunctional, coupling reagent	Lys, N- and C-termini, glu/asp	Not active at physiological pH
DHSO	12.4Å	Hydrazide, coupling reagent	Glu/asp, C-termini	Cleavable, membrane permeable

1.9 Hydrogen-deuterium exchange mass spectrometry

Hydrogen-deuterium exchange MS (HDX-MS) is a non-covalent labelling technique used in structural biology [110–115, 7, 115, 8, 9, 116–118]. HDX-MS offers insights into the

dynamics, secondary structure and conformational changes of biomolecules in solution by probing the solvent accessible surface area (SASA) and hydrogen bonding network [119]. This is achieved by the exchange of liable hydrogen atoms on the protein backbone with deuterium atoms (a heavy isotope of hydrogen with an additional neutron in the nucleus resulting in +1 Da mass increase) from the solvent. This mass addition from the incorporation of deuterium atoms is detectable by MS [120].

The information achieved using HDX-MS includes protein stability, folded/unfolded structure, folding/unfolding kinetics, protein-protein interactions and protein-ligand interactions by comparing at least two different conditions and mapping differences in local hydrogen bonding at the peptide level [111, 112, 114, 115, 7, 115, 8, 9, 116–118]. The HDX reaction begins through the dilution of the protein sample into a deuterated buffer solution which is left to equilibrate over a fixed time period. Solvent accessible hydrogen atoms on the amide nitrogen on the protein backbone are exchanged against deuterium through acid or base catalysis on a detectable timescale [121]. The exchange reaction is quenched by reducing the pH to 2.5 and the temperature to 4°C followed by an on-column digest of the protein(s) into peptides. Enzymes required for proteolysis must be active at low pH and low temperature for efficient peptide bond cleavage, typically this involves the use of pepsin immobilised on a column [119]. Coupling HDX to MS enables the identification of hydrogen protection and deprotection on the peptide level, mapping binding sites and regions of conformational change. Peptides are separated using rapid on-line liquid chromatography (LC) and analysed by ESI-MS-MS (Figure 1.17).

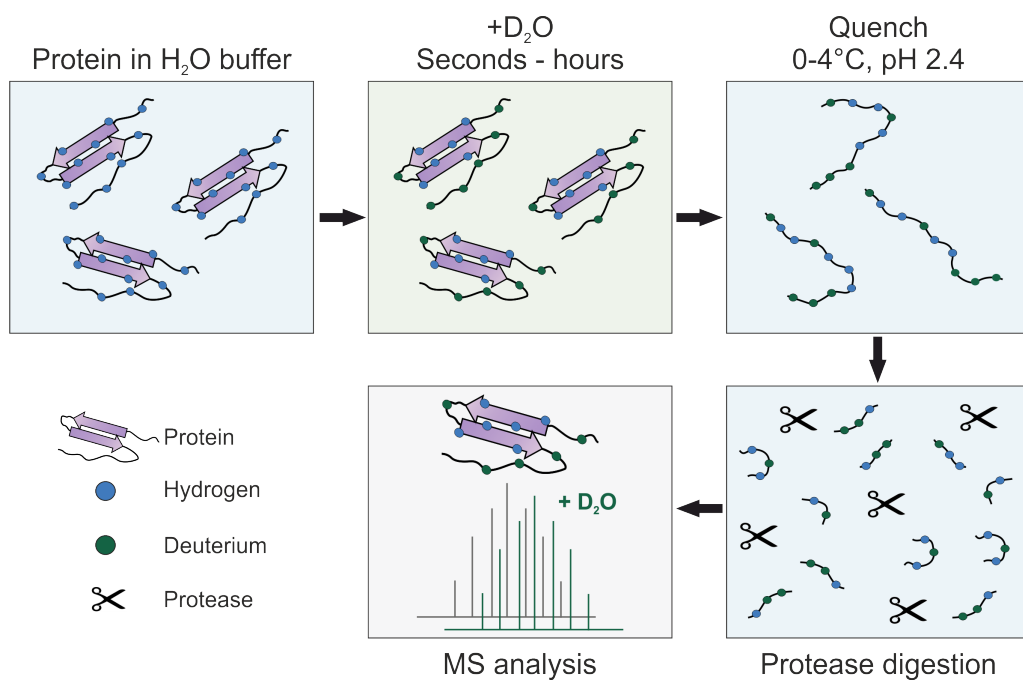


Figure. 1.17 HDX labelling reaction.

Any proton is liable to deuterium exchange, but, in practice only backbone deuterium incorporation occurs on the timescale (> ms) of experimental procedures without being lost entirely to back exchange, meaning that each amino acid with its backbone amine group can be probed for exchange, except for proline residues which do not contain an exchangeable amide group. HDX is a common foot-printing technique for investigating protein dynamics in solution and for characterising protein-protein/ligand interactions, and identifying regions prone to aggregation [116, 9, 122, 123]. However, due to the non-covalent labelling technique used in HDX-MS, back exchange of deuterium atoms back to hydrogen atoms can occur which has contributed to the popularisation of covalent labelling foot-printing techniques such as XL-MS and fast photochemical oxidation of proteins (FPOP) [8].

1.10 Amyloid proteins and disease

1.10.1 Protein folding, misfolding and aggregation

Proteins are the most abundant bio-macromolecules which carry out essential functions to sustain life. The proteome defines the complete set of proteins found in living cells, each of which plays a key role in biochemical processes. Remarkably, there are just twenty common, natural amino acids, as well as two rare natural amino acids, selenocysteine and pyrrolysine which polymerise into a vast array of linear sequences forming the primary structure of proteins. Most primary protein sequences fold (via various inter- and intra-molecular interactions) into precise three-dimensional conformations in order to achieve a functional form, ranging from enzymatic catalysis to cellular signalling. The journey of a protein from its initial disordered state to a well-defined structure can be an intricate, multi-step process where missteps could lead to consequences with profound implications for cellular health [124].

The process of protein folding is guided by sequence-specific interactions between amino acid residues, driven by non-covalent interactions such as hydrogen bonding, hydrophobic interactions and electrostatic bonding, as well as covalent bonding such as disulphide bridging between cysteine residues [125–129]. Through exploration of the former mentioned bonding mechanisms, a protein can adopt a plethora of intermediate conformations known as partially folded intermediates or molten globule states before achieving its final "native state". This is an energetically and entropically driven process, where proteins tumble downhill from high energy conformations to lower energy states (Figure 1.18) and often requires the assistance of chaperones such as the heat shock protein family to prevent off pathway interactions such as aggregation [124]. The earliest experiments to determine how a protein folds were performed in the early 1960's and led to the idea of folding funnels from studies in the 1980's which highlight the role of partially folded intermediates in the energetic search for the native state [129–135].

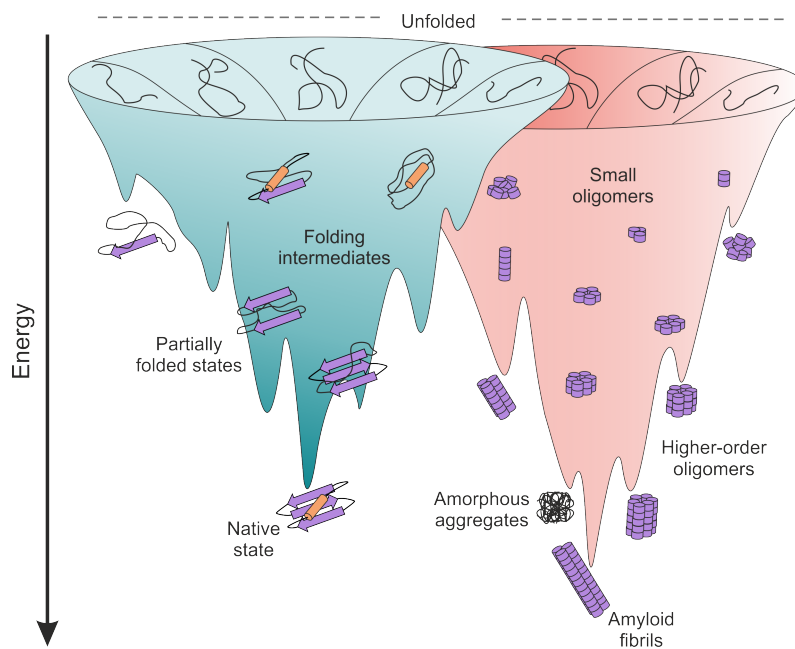


Figure. 1.18 Protein folding and aggregation. An illustration of an intramolecular protein folding energy landscape in blue where unfolded protein chains are funnelled downwards through folded intermediates into the lowest energy native state. Intermolecular aggregation is shown in the red funnel where ordered fibril structures are even lower energy states. The two funnels overlap which identifies the interconversion from folding to an aggregation landscape under certain conditions [136].

Nonetheless, misfolding can occur, resulting in kinetic trapping of partially folded protein conformations. Misfolding can be a result of changes in the sequence (such as familial mutations [137]) or changes in the environment such as pH, ionic strength, temperature, mechanical forces, and the presence/absence of ligands. Therefore, for environments dissimilar to physiological conditions, the misfolded conformation of a protein may in fact be highly populated if not at the energy minimum. For example, proteins entering lysosomes will experience a pH decrease from physiological pH in the cytoplasm (pH 7.4) to a low, acidic pH in lysosomes (pH 4.5) resulting in potential conformational changes. The exposure of regions with low solubility in a partially folded state can lead to interactions with neighbouring misfolded monomers or with various

ligands and molecules which can give rise to aberrant folding and associated misfolding diseases [138]. The imperfect, yet fascinating occurrence of protein misfolding is of high biological importance *in vivo*. The consequences of incorrect protein folding include protein aggregation, fibrillation, loss of function or toxic gain of function, often resulting in disease [139–142].

1.10.2 Mechanisms of amyloid assembly

The aggregation of a particular class of proteins into amyloid fibrils is the hallmark of a number of diseases such as Alzheimer's disease (AD), type II diabetes and Huntington's disease [143, 144]. These proteins, called amyloid proteins possess an increased propensity to self-assemble into insoluble β -sheet rich, highly ordered structures known as amyloid fibrils which can form insoluble deposits [145]. Fibrils can accumulate over time within cells or tissues, in the extracellular space or *in vitro* and are exceedingly difficult to degrade through cellular mechanisms [146, 147]. The most common amyloid-related disease is AD characterised by the amyloid assembly of the proteins amyloid- β and tau which contribute to neurodegeneration [141].

In 1639, Nicolaus Fontanus reported the autopsy of an unusual specimen, a deceased young man with severe jaundice, with large white stones deposited in his spleen which may have been the first observation and description of the sago spleen amyloidosis [148]. Amyloid was first openly defined in 1854 by Rudolf Virchow, a German physician who identified that iodine turned blue when added to cerebral corpora amylacea macroscopic structures of the nervous system. He postulated that this was due to their carbohydrate based structures built of cellulose or starch [149]. Later, these deposits were classified as proteinaceous by Friedrich and Kekulé in 1859 through the discovery of their high nitrogen content and "amyloid degeneration" was exemplified by Samuel Wilks in 1856, who collected over 60 cases of the white stony visceral material detected by autopsy [148, 149]. The introduction of dyes such as the aniline dye; congo red, which was initially

designed for staining textiles, but was later discovered to bind to amyloid by Bennhold in 1922, helped to associate amyloid deposits with disease [150].

Beyond the category of neurodegeneration, amyloidosis encompasses a spectrum of disease pathologies affecting various tissues/ organs. Cardiac amyloidosis is an example of localised amyloidosis where amyloid fibrils primarily composed of antibody light chains (AL) are deposited in the heart tissue [151]. AL is an immunoglobulin light chain produced by plasma cells in the bone marrow and, when in excess, can assemble into amyloid fibrils [152, 153]. Amyloid proteins can, however, have positive roles in cellular function, such as the eosinophil major basic protein 1 which is stored in eosinophils as a toxic protein which binds to, and disrupts, pathogenic infectious cell membranes driven by amyloid assembly [144, 154]. Amyloid fibrils can also be found in organisms other than humans, such as bacteria and fungi (see Table 1.2), and are useful structural components in biofilm formation such as CsgA (curli) and FapC [155, 144]. Overall, amyloid is present across life and how fibrils assemble is of paramount importance in tackling devastating diseases, but they can also find use in the development of strong bio-materials. Most of the known amyloid precursor proteins are listed in Table 1.2.

Table 1.2 Amyloid Proteins. Precursor amyloid proteins are listed with their species of origin, known structure, and disease or function associated. APO: apolipoprotein, polyQ: poly-glutamine, TBP: TATA-binding protein. Adapted from [156–158].

Protein Name	Domain of Life	Native Structure	Associated Diseases or Functions
Chaplins and Rodlin	Bacteria	α -helical	Aerial hyphae formation and spores
Curli proteins (CsgA)	Bacteria	β -sheet rich	Biofilm formation
Phenol-Soluble Mod- ulins	Bacteria	α -helical and β - strand	Produced by <i>Staphylococcus aureus</i> for biofilm formation
HET-s	Fungi	α -helical	Prion protein in <i>Podospora anserina</i>

Protein Name	Domain of Life	Native Structure	Associated Diseases or Functions
Sup35	Fungi	α -helical (soluble) and β -sheet (prion form)	Prion protein in <i>Saccharomyces cerevisiae</i>
Ure2	Fungi	α -helical	Prion protein in <i>Saccharomyces cerevisiae</i>
British and Danish amyloid	Humans	IDP	Familial dementia
Actin	Humans	Mostly α , some β	Actin-related neurodegenerative disorders
Amyloid-beta ($A\beta$)	Humans	IDP, β hairpin	AD, hereditary cerebral hemorrhage with amyloidosis
PolyQ containing proteins (Huntingtin)	Humans	Mostly IDP	Huntington disease
ApoCII, ApoCIII	Humans	α -helix, IDP	ApoCII amyloidosis, ApoCIII amyloidosis
Atrial natriuretic peptide (ANP)	Humans	IDP	Atrial amyloidosis
Calcitonin	Humans	IDP	Medullary carcinoma of the thyroid
Cystatin C	Humans	α -helical, antiparallel β -strands	Icelandic hereditary cystatin C amyloid angiopathy
Enfuvirtide	Humans	IDP	Injection-localized amyloidosis
Ferritin	Humans	α -helical	Neuroferritinopathy
Fibrinogen	Humans	Multisubunit	Hereditary renal amyloidosis, fibrinogen amyloidosis
Gelactin 7	Humans	All β -strand	Localized cutaneous amyloidosis
Gelsolin	Humans	IDP	Finnish-type familial amyloidosis
Immunoglobulin light chains (AL amyloidosis)	Humans	β -strand	Systemic light chain amyloidosis

Protein Name	Domain of Life	Native Structure	Associated Diseases or Functions
Insulin	Humans	α -helical	Injection-localized amyloidosis
Islet amyloid polypeptide (IAPP or amylin)	Humans	Random coil	Type 2 diabetes
Keratins	Humans	Unknown	Cutaneous lichen amyloidosis
Lactadherin C2 domain	Humans	IDP	Aortic media amyloidosis
Lactoferrin	Humans	$\alpha + \beta$	Corneal amyloidosis
Leukocyte cell-derived chemotaxin 2	Humans	Unknown	LECT2 amyloidosis
Lung surfactant protein C	Humans	Unknown	Pulmonary alveolar proteinosis
Lysozyme	Humans	α/β lysozyme fold	Hereditary non-neuropathic systemic amyloidosis
Kerato-epithelin	Humans	Unknown	Hereditary lattice corneal dystrophy
Medin	Humans	Unknown	Aortic medial amyloidosis
Neuroserpin	Humans	$\alpha + \beta$	Familial encephalopathy with neuroserpin inclusion bodies
ApoAI, ApoAII, ApoAIV	Humans	IDP	ApoAI amyloidosis, ApoAII amyloidosis, ApoAIV amyloidosis
Odontogenic ameloblast-associated protein	Humans	Unknown	Calcifying epithelial odontogenic tumors
Prion protein (PrP)	Humans	α -helix, IDP	Prion diseases (e.g., Creutzfeldt-Jakob disease)
Prolactin	Humans	All α -helical	Pituitary prolactinoma
Semenogelin 1	Humans	Unknown	Senile seminal vesicle amyloidosis
Serum amyloid A	Humans	α -helical bundles	Secondary amyloidosis
Superoxide dismutase	Humans	All β -strands	Amyotrophic lateral sclerosis
Tau	Humans	IDP	AD and tauopathies, Frontotemporal dementia with Parkinsonism

Protein Name	Domain of Life	Native Structure	Associated Diseases or Functions
TAR DNA-binding protein 43	Humans	IDP	Amyotrophic lateral sclerosis, Frontotemporal dementia
Transthyretin	Humans	Four β -strands, two α -helices	Familial amyloid polyneuropathy, senile systemic amyloidosis
α -synuclein	Humans	IDP	PD, Dementia with Lewy bodies
β 2 Microglobulin	Humans	β -sandwich	Dialysis-related amyloidosis
γ -Crystallins	Humans	All β -strand	Cataract
Fused in sarcoma (FUS)	Humans	IDP	RNA and DNA metabolism
Orb2	Drosophila	α -helical, IDP	Memory formation

Amyloid precursor proteins typically, but not exclusively, contain IDRs, hydrophobic clusters and/ or low complexity domains (LCD; where amino acid variation is low) [159–161]. The fibril assembly process is complex and the exact mechanisms can vary between specific amyloid proteins. Despite immense efforts towards the study of the mechanism of amyloid assembly, the molecular mechanisms that govern amyloid formation remain largely unresolved [157, 162]. Indeed, the biological question regarding how amyloid assembly occurs is highly important in order to advance our understanding of various devastating diseases. The general amyloid assembly process is outlined in Figure 1.19 and is described by a sigmoidal growth curve as monitored using the amyloid specific dye thioflavin T [163].

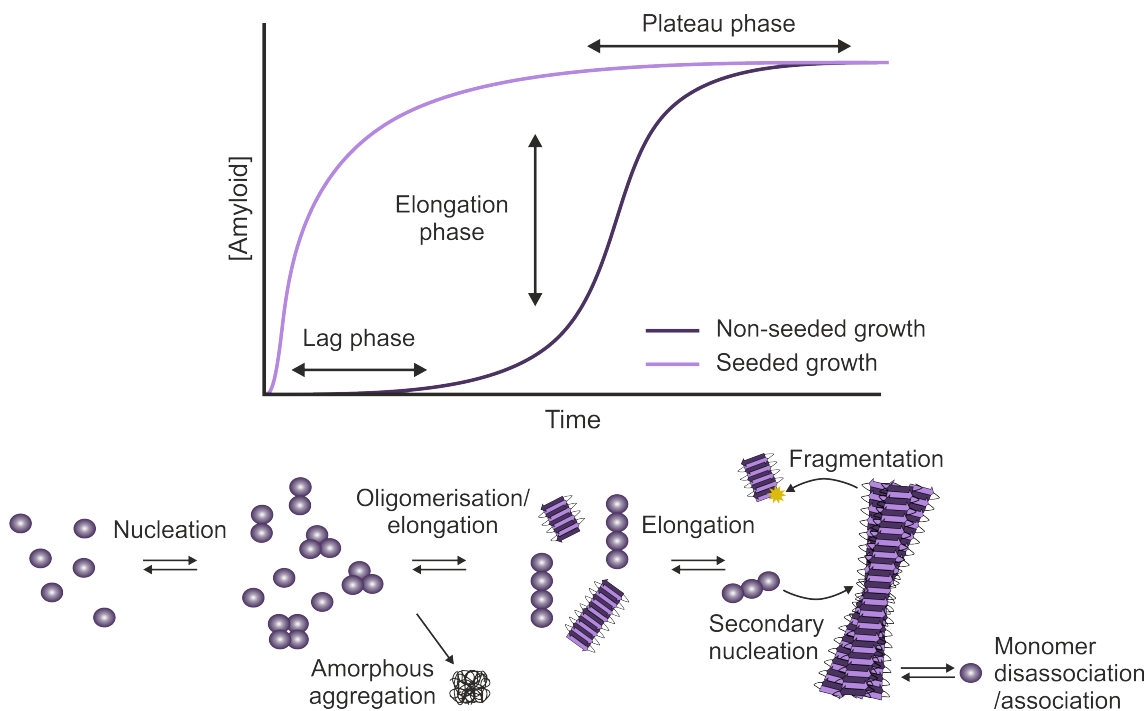


Figure. 1.19 The process of *de novo* and seeded amyloid assembly. In *de novo* amyloid assembly (light purple sigmoidal curve) the process begins with the lag phase whereby thermodynamically disfavoured nucleation events occur, also known as primary nucleation. The elongation phase consists of rapid, thermodynamically favoured growth by addition of monomers to fibril ends reversibly or by secondary nucleation along the fibril axis. Fragmentation of fibrils can occur which replenishes the pool of fibril ends. The plateau phase is eventually achieved, reaching an equilibrium of monomer association and disassociation. The addition of seeds (pre-formed fibrils; dark purple sigmoidal curve) dramatically shortens the lag phase of fibril assembly by overcoming thermodynamically disfavoured events. Off-pathway intermediates involve the assembly of amorphous aggregates.

Initially, monomers form small oligomers through primary nucleation. This stage is dependent on monomer concentration and the ability of monomers to nucleate which can depend on their conformation, sequence mutations, modifications and the environment [164]. Monomer association is thermodynamically unfavourable and is therefore called the lag phase [165, 166]. The lag phase can be eliminated by the addition of pre-formed

fibrils (seeds) which offer fibril ends to act as surfaces for rapid monomer recruitment. Small oligomers are held together by intermolecular interactions including hydrophobic shielding, electrostatic interactions and pi-pi stacking [167]. Monomers are continually recruited to the nuclei in the elongation phase.

Higher-order oligomers begin to form and an increase in secondary structure can be observed as the disorder to order transition begins [168]. This shift involves the assembly of β -sheets achieved through hydrogen bonding increasing stability. Oligomers can have annular structures, with a pore-like centre hinting to a potential toxic mechanism of pore formation in membranes [169, 170]. Kinetically trapped oligomers with differing toxicities (type A*: non toxic and type B*: toxic) have been identified for α -synuclein (α S) and these are described further in Chapter 5 (Figure 1.20) [169–172]. Type A* and B* oligomers showed subtle differences in structure to one another and type B* oligomers induced a release of calcein from small unilamellar vesicles which suggest disruption of acidic lipid bilayers, 10 times greater than that of type A [171, 172]. Similarly, for the amyloid precursor protein A β , the proposal of a β -barrel pore forming oligomer for A β ⁴² has helped to understand the potential toxic mechanism exhibited by oligomeric species [173–175, 14]. A combination of IM-MS measurements with molecular dynamics simulations revealed the possible structure of a pore forming, β -barrel oligomer of A β ⁴² with an internal diameter of 9Å to 17Å which could insert into membranes resulting in Ca²⁺ release [176].

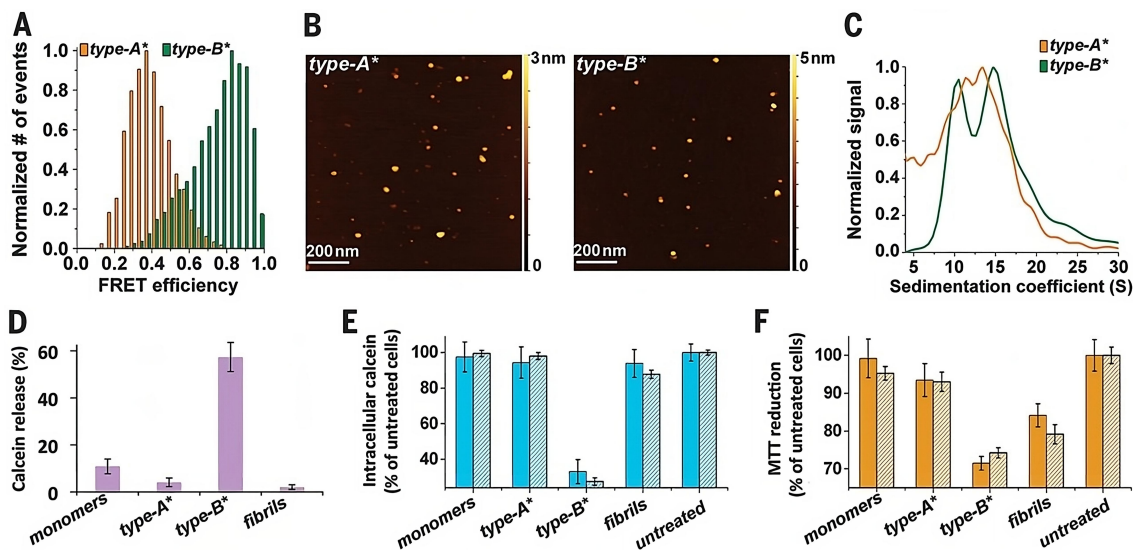


Figure. 1.20 Structural characterisation of type A grown with EGCG and type B oligomers of α -synuclein. (a) Intermolecular Förster resonance energy transfer (FRET) efficiencies for measurements of Type A* (orange) and Type B* (green) α S oligomers reveal differences in structure. (b) Atomic force microscopy images with a scale bar of 200 nm identify annular species. (c) Differences observed in sedimentation coefficients through analytical ultracentrifugation. (d) *In vitro* calcein release in percentage from small unilamellar vesicles. (e) Intracellular calcein-induced fluorescence under different conditions for human neuroblastoma cell line (SH-SY5Y; solid bars) and rat primary cortical neurones (striped bars) and (f) a measure of mitochondrial activity by the reduction of MTT (3-(4,5-Dimethylthiazol-2-yl)-2,5-Diphenyltetrazolium Bromide) for SH-SY5Y cells (solid bars), and rat primary cortical neurones (striped bars) after incubation with defined α S species. Figures taken from [172].

The increase in cross β -sheet content can be tracked by the addition of a fluorescent molecule called Thioflavin-T (ThT) to the reaction (Figure 1.21). ThT consists of a C-C bond connecting a benzothiazole ring and aniline ring. When ThT intercalates into the hydrogen bond network of stacked β -sheets, rotational freedom about this bond is immobilised resulting in increased fluorescence [177, 178]. Amyloid growth generally

follows a similar overall process, but at the molecular level for different amyloid proteins listed in Table 1.2, and different environmental factors such as pH, ligand presence/absence and monomer concentration, differences can be observed resulting in a variation of sigmoid curves observed in Figure 1.19.

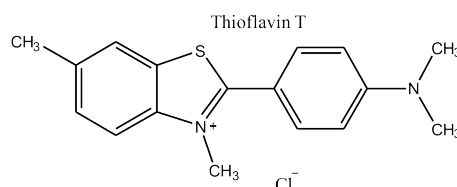


Figure. 1.21 Thioflavin T. The chemical structure of Thioflavin T created using ChemDraw.

Elongation continues, resulting in the assembly of long, highly ordered, twisted amyloid fibrils with a characteristic cross- β structure (Figure 1.22 [179]). Eventually monomers are converted into fibril structures stabilised by hydrogen bonding and π - π stacking [180]. At this stage, secondary events can also play a significant role in the amyloid formation kinetics. For instance, fragmentation events can create free fibril ends which act as seeds for further amyloid assembly, and fibril surfaces themselves can act as a surface for surface-catalysed nucleation processes to occur [181]. Overall, the process of amyloid assembly is determined by numerous factors which deem the process challenging to understand. The development of mathematical models and fits of *in vitro* ThT kinetics of fibril growth by the Knowles lab in the freely available software AmyloFit, has aided the understanding of microscopic processes from macroscopic experimental measurements, enabling the determination of which processes dominate amyloid assembly under defined conditions [182].

Studying fibril assembly is extremely challenging due to the number of internal and external factors which can influence the kinetics. The initial transition from stable monomers to a nucleated species is highly dependent on the protein sequence and the conformation adopted by the protein. In turn, the conformation and interaction behaviour of the protein

are affected by post translational modifications (PTMs), sequence variants and interaction partners. Additionally, the buffer conditions or indeed, the cellular environment including ionic strength, pH and ionic components can influence the rate of amyloid assembly. For instance, divalent metal ions increase the rate of amyloid assembly for the amyloid precursor protein α S [183, 184] but slow the rate of fibril assembly or reduces the resulting amount of amyloid formed for islet amyloid polypeptide (IAPP) depending on the metal ion investigated [185–187]. When considering the crowded cellular environment with various proteins, ions and surfaces in different compartments, the understanding of amyloid assembly *in vivo* is complicated even further. Binding to chaperones and phospholipid membranes can speed up or slow down amyloid assembly and alter the oligomer conformations achieved [188–190, 174, 185, 191]. Altogether, the precise early molecular mechanisms of amyloid aggregation are still unclear, and a more in-depth understanding of the earliest stages of initiation of the process require unravelling.

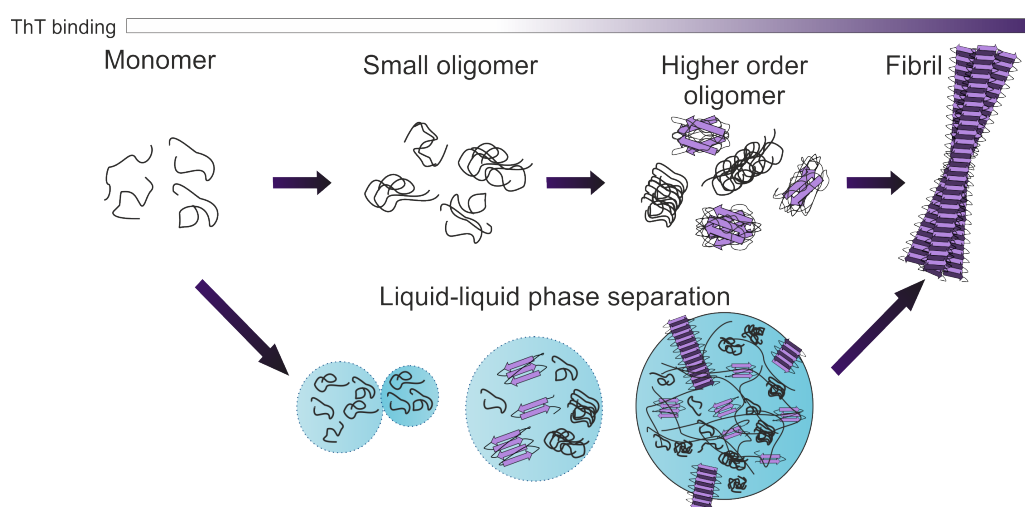


Figure. 1.22 Amyloid assembly pathways. Monomer amyloid precursor proteins nucleate into oligomers which lack of cross- β structure and hence ThT fluorescence does not capture this stage (shown in the top bar). Oligomers grow to eventually form protofibrils, where the increase in cross- β structure facilitates ThT binding and fluorescence. Alternatively, liquid-liquid phase separation can accelerate amyloid assembly.

An additional alternative pathway for amyloid assembly involves liquid-liquid phase separation (LLPS), where the spatial concentration of a relevant amyloid prone protein is increased and results in rapid fibril assembly via the formation of liquid condensate structures [192–195]. Condensates initially form as membrane-less organelles which are spherical and have liquid like properties [196–198]. Fluorescence recovery after photobleaching (FRAP) experiments involve focusing high intensity lasers on pinpoint regions within condensates in order to photo-bleach fluorophores on labeled proteins [199–201]. With time, fluorescence of this region is recovered due to the diffusion of unbleached fluorophore carrying proteins back into the liquid condensate. This property has been shown for islet amyloid polypeptide (IAPP), TAR DNA-binding protein 43 (TDP-43) and α S among many other amyloid proteins, some of which require the binding of RNA or DNA in order to achieve their LLPS potential [202–204]. Eventually condensates can fuse together and fibrils can protrude out of their surface to interact with other condensates until a gel-like network is formed and this becomes insoluble (Figure 1.22). As condensates fuse together, non-proteinaceous material such as mitochondria, ions and lipids may get trapped and this could in turn be a contributing factor to intracellular insoluble deposits such as Lewy bodies [205].

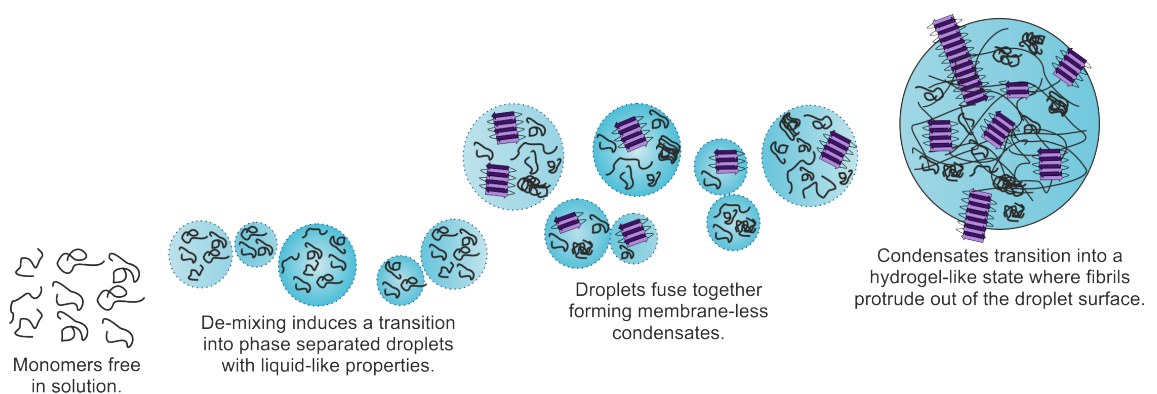


Figure. 1.23 Liquid-liquid phase separation. Monomers de-mix into liquid-like condensates which fuse together into a gel-like state.

1.10.3 The amyloid fold and fibril architectures

Our understanding of amyloid architectures has been greatly advanced through technological advances such as electron microscopy (EM), X-ray diffraction, nuclear magnetic resonance (NMR) and atomic force microscopy (AFM). Due to their highly ordered nature and helical pitch, fibril structures can be analysed by the former mentioned techniques [206–212]. α S, for example has been identified as one of the most polymorphic amyloid proteins in terms of fibril assemblies with > 70 fibril structures solved to this date according to the amyloid atlas [213].

Early X-ray diffraction models identified the characteristic cross- β architecture of amyloid in which β -strands are arranged at a 90° angle to the fibril axis (Figure 1.24 [214, 215]). This pattern was observed by the pioneering biophysicist William Astbury in 1935 through the interrogation of poached egg whites in the X-ray beam, where elongated protein strands were stacked along the fibre axis resulting in parallel sheets, later defined as β -sheets established by hydrogen bonding by Pauling and Corey [145]. However, some exceptions to the canonical cross- β structure exist, bacterial amyloids such as PSM α 3 with functional properties such as virulence activities exhibit a cross- α structure, critical for their cytotoxic function [216]. Generally, amyloid fibrils are around 10 nanometres in width and non-branching, but can form structures up to micrometres in length with curved or bundle like assemblies, and are made up of one to four protofilaments [217, 218]. The precursor material to amyloid fibrils is known as protofibrils which are distinct from protofilaments [219]. Protofilaments are packed together via van der Waals forces and hydrogen bonding to create a steric zipper motif at the interface (Figure 1.24). Nonetheless, despite the similar core architecture found across all amyloid fibrils, their regions of deposition and interaction partners vary and high resolution structures identify differences in monomer conformations, helical rise, cross-over length and protofilament arrangements. Information that is now available in atomic resolution using modern methods of cryo-EM [220–228].

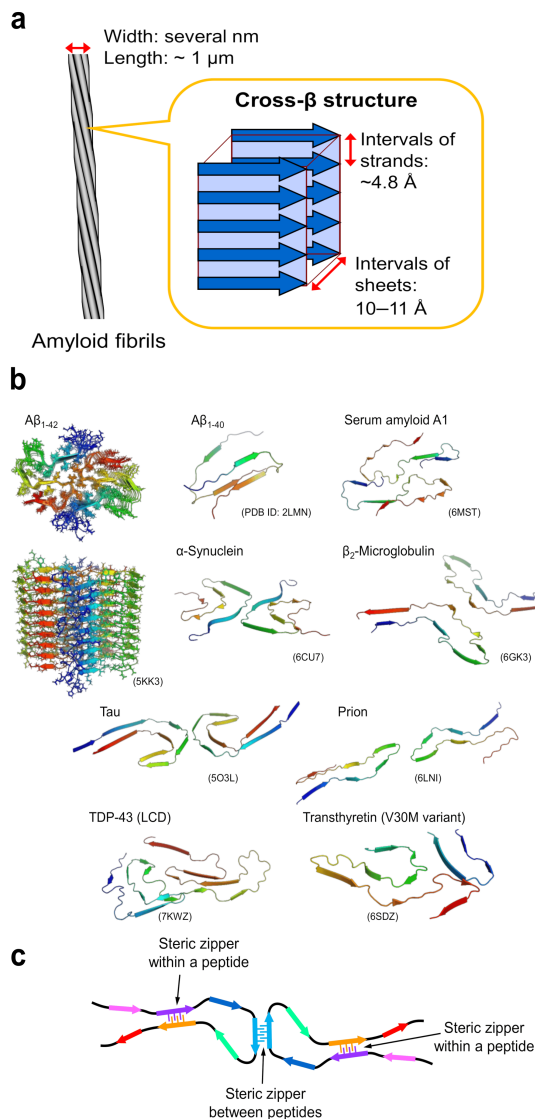


Figure. 1.24 The amyloid cross- β structure. (a) A schematic of the structure of amyloid fibrils. With an unbranched morphology, several protofilaments are assembled a few nano-meters in width and can be up to micrometers in length. In the cross- β structure, β -strands are stacked perpendicular to the long axis of the fibril. (b) A number of solved amyloid fibril structures, for amyloid β , the top and side views are shown. For all other proteins, the three-dimensional polypeptide chains which make up a single layer of the fibril axis are shown. (c) A schematic showing the fundamental architecture exhibited by amyloid fibrils consisting of the steric-zipper motif. Taken from [229].

1.10.4 Seeding potential and mechanisms of disease progression

Amyloid fibrils can be classified as prion-like or non prion-like which defines them as transmissible or non-transmissible, respectively. In prion diseases, misfolded human prion protein (PrP) can self perpetuate infection by converting normal host PrP into misfolded, pathological forms, This is characteristic of Creutzfeldt-Jakob disease and other prionopathies [230, 231]. This process occurs through direct cell-cell transmission of neurotoxic material which can occur via transport through the axons of neurones and through the synaptic cleft in the case of mammals [232, 233]. In the case of yeast prions, such as Sup35 and Ure2 found in *Saccharomyces cerevisiae* aggregates can spread from cell to cell, transmitting a new phenotype [234]. Indeed, in some prion-related diseases, peripheral tissues such as the spleen and lymph nodes can accumulate misfolded prions which then ultimately act as a source of the infectious material [235, 236].

Non-prion proteins such as amyloid β , tau and α -synuclein can seed aggregation and trans-cellular propagation in cell cultures and mouse models, which has been shown for neuron to neuron transmission [237–240]. For instance, adding preformed amyloid fibrils (PFFs) such as α -synuclein fibrils to the surface of cell cultures results in detection of α -synuclein within cells, conversion of cytosolic monomers into fibrils, and pathological symptoms such as apoptosis, calcein release and high levels of reactive oxygen species (ROS) [188, 241, 172]. In the context of Parkinson's disease (PD), the gut-brain hypothesis suggests that pathological α -synuclein aggregates might originate in the gastro-intestinal (GI) tract [242, 243]. This hypothesis originated through the observation of α -synuclein aggregates in the enteric nervous system [244] and GI tract of PD patients [245] which raised the question, how did they get there? Indeed, it seems that perhaps, they originated there. And the question that we should instead ask is, how did they make it to the brain? Research has shown that α -synuclein can in fact travel to the brain via the vagus nerve which connects the GI tract to the brain and this has been directly evidenced in mouse models by introducing α -synuclein into the gut of mice, which spread to the brain leading

to PD-like symptoms [246, 247]. Whilst this hypothesis is compelling, it is important to remember that PD, among other synucleopathies and amyloid-related diseases are complex and vary considerably from patient to patient [248, 249].

1.11 Introduction to α -Synuclein

α -Synuclein (α S) is an amyloidogenic protein characterised as an IDP whose amyloid assembly pathway is associated with the pathology of synucleopathies such as PD, the second most common progressive neurodegenerative disease [250]. In 1817, James Parkinson described the symptoms and characteristics of PD, the neuropathology of which is defined by α S rich insoluble cellular inclusions called Lewy bodies [251, 252]. The deposition of Lewy bodies correlates with the death and loss of dopaminergic neurons in the substantia nigra of the brain which is responsible for motor function [253]. Increased copy number and single nucleotide polymorphisms found in early, aggressive and dominant familial forms of PD have directly linked the SNCA gene which encodes α S to PD, evidencing its core role in the disease [254–256].

1.11.1 Structural properties of α S

Wild-type (WT) α S is composed of 140 amino acid residues with an average molecular weight of 14460.16 kDa. Overall, α S carries a net negative charge of -9 at neutral pH and has an isoelectric point of 4.67 [257]. The primary sequence of α S is composed of three segments: (i) an N-terminal domain, (ii) a non-amyloid β component (NAC) core and, (iii) a C-terminal domain shown in Figure 1.25.

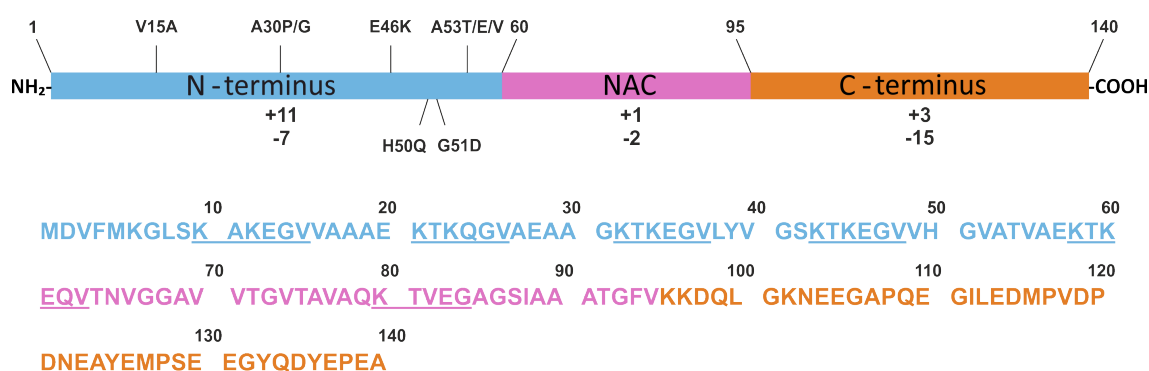


Figure. 1.25 Monomeric α S sequence. The protein sequence of α S is characterised by three distinct regions, the N-terminal region (blue), the NAC region (pink) and the C-terminal region (orange). Imperfect KTKEGV repeats are underlined and the location of familial point mutations are shown in the N-terminal region. The number of positive and negative charges along the sequence segments are also shown.

(i) The N-terminal domain (residues 1-60), is overall positively charged and contains imperfect amino acid repeats (KTKEGV; Figure 1.25) that have a lipid binding function [258]. Interactions with lipid membrane surfaces induce α -helical structure of α S involving the first 100 residues [259, 260]. Membrane-bound structures have been determined by NMR for α S including a broken helix formed of two α -helices V3-V37 and K35-T92 arranged antiparallel to each other when bound to phospholipid vesicles, and an unbroken α -helix between V3-T92 when bound to phospholipid bicelles [261, 262]. Membrane disruption has also been evidenced for α S binding to lipid nanodiscs showing the removal of lipids, resulting in destabilisation of the lipid bilayer [263]. *In vivo*, α S is found to be post-translationally modified (PTM) at various sites along the protein sequence [264–266]. Predominantly, α S is acetylated at the N-terminus which has been shown to influence membrane binding affinity through increased helicity [267, 268, 190, 269–271]. The N-terminal region also contains several missense point mutations correlated with autosomal dominant forms of PD including V15A, A30P/G, E46K, A53E/T/V, H50Q and G51D (Figure 1.25) [272]. A30P and A53T have been shown to alter α S membrane binding

properties by reducing overall membrane binding [273]. A53T, E46K and H50Q have been shown to accelerate the rate of amyloid fibril assembly [274, 254, 275] whereas G51D and A30P have been found to slow the rate of amyloid assembly [276]. (ii) The NAC core (residues 61-95), is a hydrophobic, amyloidogenic region, shown to be crucial for β -sheet formation, promoting amyloid fibril assembly [277–281].

Finally (iii), the C-terminal region (residues 96-140), a highly negatively charged sequence, is responsible for binding metal ions (such as Cu^{2+} , Cu^+ , Mn^{2+} , Co^{2+} , Zn^{2+}), calcium (Ca^{2+}), and dopamine all of which are positively charged and are found to accumulate in Lewy body (LB) formations [282, 283]. The C-terminal sequence includes PTM phosphorylation sites at residues Y125, S129, Y133 or Y135 which have been shown to regulate α S amyloid assembly [284–290]. High levels of phosphorylated α S, mostly at S129, have been detected in LB deposits in patients' brains with PD [291–293]. LB assemblies have been shown to have a complex composition, containing non-proteinaceous material such as lipids, membranous organelles including mitochondria and metal ions [294, 295]. Taking a closer look at LB assemblies has revealed the presence of truncated α S as well as full length α S [296–298]. Using mass spectrometry, Anderson *et al.*, detected five C-terminal truncations from LB samples terminating at: D115, D119, N122, Y133 and D135 [292]. Truncations appeared to occur under natural physiological conditions, suggesting a functional role for these variants. However, findings have also shown that for these C-terminal truncations, assembly into amyloid occurs more readily and may act as effective seeds [292, 297, 298]. N-terminal truncation of α S is also observed in LBs, at residues 5, 10, 18, 19 and 68, possibly due to protease cleavage or incomplete digestion by the proteasome [299, 300].

1.11.2 Physiological properties of α S

α S is found *in vivo* to partition between the cytoplasm and bound to phospholipid membranes that enclose cells, and it is also present in organelles such as mitochondria and

exosomes [301]. Since the discovery of α S, its exact functional roles are still unknown [302–306]. Localisation to presynaptic nerve termini suggests a role in vesicle remodelling, the release of neurotransmitters and vesicle recycling (Figure 1.26). α S has recently been identified as a curvature-sensing and stabilising protein which remodels membranes by inducing curvature, resulting in the loss of membrane integrity, potentially elucidating one of the mechanisms of membrane disruption in PD [307]. The strong binding is driven by the electrostatic interaction between negatively charged lipid bilayers and the positively charged N-terminal region of α S (Figure 1.25), and the affinity of binding is increased for highly curved surfaces, modulated by specific lipid content, achieved using fluorescence correlation spectroscopy [308]. These reports place α S into the class of proteins called amphipathic helix-containing proteins which are unstructured in solution, but begin folding their amphipathic helix in the presence of curved lipid membranes [309–311].

The role of α S in vesicle docking and fusion to the presynaptic plasma membrane for exocytosis has been indicated by studies identifying the involvement of α S in the assembly of the SNARE complex, a process essential for exocytosis of synaptic vesicles [312, 189]. The SNARE complex is made up of syntaxin, synaptosome-associated protein 25 (SNAP-25) and vesicle-associated protein 2 (VAMP2) which assemble together as four helices to zip synaptic vesicles to the plasma membrane [313, 314]. Recent findings reveal that α S has an integral role in endocytosis of synaptic vesicles [189]. α S knockout mice models using fluorescent sensors reporting on recycling of synaptic vesicles showed slowing of vesicle endocytosis, but no observable change in the rate of vesicle exocytosis [315]. α S shares sequence homology with two other members of the synuclein family; β S (134 residues) and γ S (127 residues) [316]. β S features proline residues which make it more rigid and resistant to amyloid assembly, whilst γ S has a truncated C-terminus compared to WT α S, featuring fewer acidic residues and is less amyloid prone but has been associated with Amyotrophic lateral sclerosis [316]. Intriguingly, if β S and γ S isoforms are also knocked-out, but each isoform is returned individually, restoration of the rate of

synaptic vesicle endocytosis occurred, highlighting the complementary function of the synuclein isoform family [315].

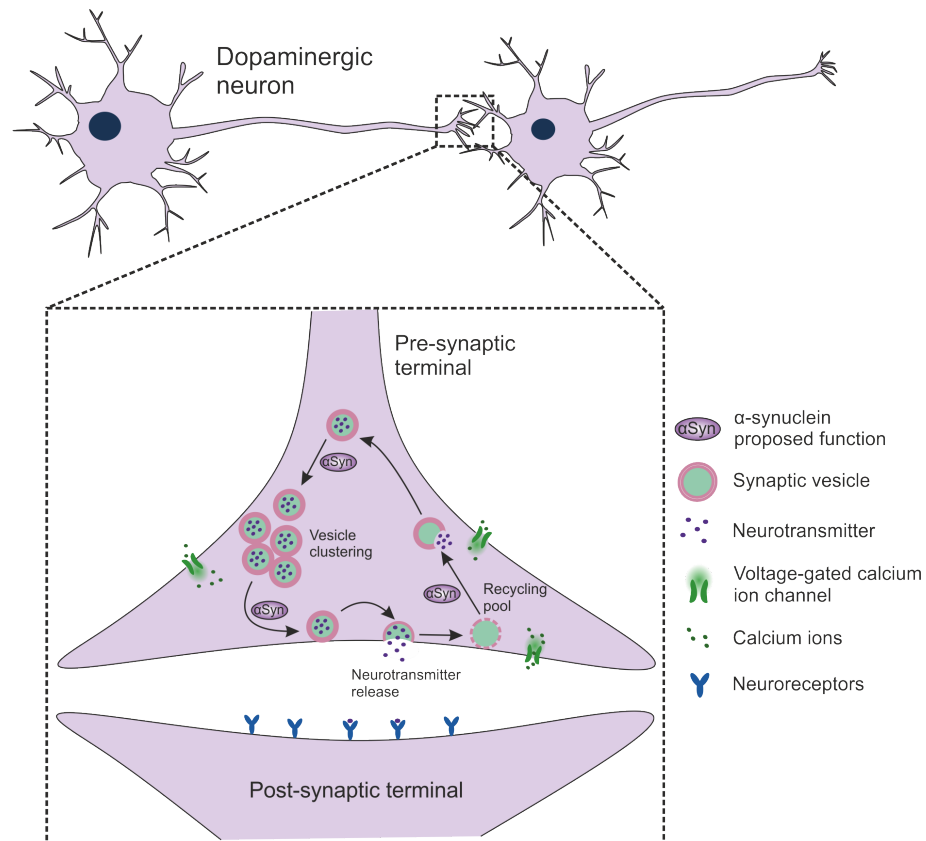


Figure. 1.26 The role of α S in synaptic vesicle exocytosis and recycling. α S mediates vesicle clustering and fusion with the plasma membrane. Redrawn from [189].

Two major models of endocytosis are debated to include α S; kiss-and-run of small synaptic vesicles occurring in <1 s time-frame, and clathrin-mediated endocytosis (CME) occurring on a time-frame of 10-20s [317, 318]. The high affinity of α S to highly curved membranes supports the theory that α S is implicated in the kiss-and-run mechanism of smaller, more curved vesicles. CME involves the assembly of clathrin-coated vesicles that bud from the plasma membrane for internalisation of synaptic vesicles, α S may interact directly with clathrin or interact indirectly with other proteins crucial to the CME process [319]. Using NMR, the first N-terminal 25 residues of α S monomers have been proposed to anchor to small unilamellar vesicles [320]. This binding is enhanced by

N-terminal acetylation and calcium binding to the C-terminal region which neutralises negative residues, increasing interactions of the NAC-region with lipids [269, 321]. Finally, oligomerisation of α S may play a role in its physiological function. A specific type of oligomer; type B* which is kinetically trapped during amyloid assembly [322], induces cellular toxicity by generating ROS and reducing mitochondrial activity within neuronal cells [322]. Type B* oligomers induce the release of calcein from synthetic lipid vesicles and cause the disruption of cell membranes by insertion into the hydrophobic interior of the lipid bilayer [172].

1.11.3 Current treatments/therapeutics towards Parkinson's disease

Our understanding of PD is constantly evolving, and there is still a journey to go in order to understand the initiation and onset of PD to develop effective treatments. Eradication of the disease is not yet possible, but extensive efforts towards therapeutics are constantly being improved upon [323]. Levodopa (L-dopa) is the most common and most effective medicine for managing the motor symptoms associated with PD, such as tremor and bradykinesia by exhibiting neuroprotective action [324, 325]. L-dopa is converted into dopamine in the brain to replenish dopamine levels which are reduced due to the loss of dopaminergic neurons. Long-term use of L-dopa however, can cause increased involuntary movements and reduced drug potency [326]. Drugs with similar modes of action to L-dopa include dopamine agonists which mimic the action of the neurotransmitter dopamine in the brain such as Ropinirole [327]. Additionally drugs which act by inhibiting the enzymes that break down dopamine also aim to maintain dopamine levels within the brain, an example is Selegiline [328]. Other mechanisms for treating PD are more general and include diet and lifestyle changes such as implementing a more balanced diet, stress management, adequate sleep and exercising regularly [329]. It is clear that understanding how PD progresses and develops at the molecular level is key to developing effective treatments. Any efforts in

drug design require that we understand and characterise a specific target linked with the disease, which could be a specific conformation of the protein α S.

1.12 Mass spectrometry analysis of amyloid

Studying the conformations of α S at different stages of amyloid assembly presents experimental challenges. Monomeric α S is a relatively small and disordered protein making it invisible to techniques with high molecular weight cut-off's, such as cryo-EM and challenging for techniques which are ensemble averaging, such as NMR. Oligomers are highly heterogeneous and individual conformations can be present at less than 1 % of the entire ensemble, making it easy to miss specific yet essential, oligomeric states. Fibrils on the other hand, are high mass and stable structures, making their structural elucidation by solid-state NMR and cryo-EM ideal [220–228, 330–332]. In this section, some examples of how MS has been used to overcome these difficulties are discussed and their effort to advance our understanding of α S as well as other amyloid proteins are emphasised.

1.12.1 Monomers

Amyloidogenic monomers generally possess intrinsically disordered regions, making them difficult to study structurally. HDX-MS is a well established tool for studying protein conformational dynamics, but this usually occurs on the 10s of seconds time scale which can fail to capture more rapid dynamics on the micro-milli second timescale [120]. Seetaloo., *et al* recently published research applying their custom millisecond HDX-MS set up to study the conformational dynamics of α S in different physiological matching solution conditions [116] such as the extracellular, cytosolic, lysosomal environments or control of Tris buffer which each differ in pH and ionic composition/strength. Firstly, using ThT fluorescence, α S was shown to aggregate into amyloid the fastest in lysosomal conditions, followed by cytosolic then extracellular conditions, then Tris only. As well as

varied amyloid assembly rates, distinct fibrillar architectures were observed to assemble by atomic force microscopy. Fibrils grown under lysosomal and extracellular mimicking conditions had a similar twist (polymorph p3a with fibril heights of 7-9 nm). When correlated with unique millisecond HDX-MS data, part of the C-terminal region (residues 115-135) was significantly deprotected in the lysosomal and cytosolic state, whilst the N-terminal region and NAC core of residues 2-4, 10-17, 34-38 and 53-94 were protected. The exposure of the C-terminal residues 115-135 is key for nucleation as these residues become deprotected in conditions which induce faster amyloid assembly. The N-terminal region and NAC region impact fibril elongation by becoming protected under conditions in which fibril growth is most rapid. These findings correlate specific structural dynamics of α S monomers with amyloid assembly behaviour and demonstrate the importance of replicating diverse physiological conditions when studying amyloid assembly [116].

Another novel application of MS to study α S monomers utilised charge detection MS to investigate the interaction of α S with lipid nanodiscs which are lipid nanoparticles with a bilayer arrangement [263]. α S was shown to interact strongly with anionic lipids. Non-covalent interactions were observed in which α S-nanodisc complexes were measurable, and predominantly 1-2 α S molecules were detected to be bound. Mass defect analysis where the difference between the measured mass of a complex and the mass of the individual components was calculated (Figure 1.27). This analysis revealed the disruption of the lipid nanodiscs by α S, where lipids are displaced from the nanodisc. This was evidenced as the masses of intact nanodisc complexes were not significantly altered by the addition of α S, which suggests that α S instead displaces the lipids and inserts into the membrane rather than binding peripherally. These findings are key to revealing the toxic properties exhibited by α S in a cellular context. The addition of (-)epigallocatechin gallate (EGCG), which inhibits α S fibril assembly [333, 334], prevented membrane disruption but did not alter α S association with the lipid nanodisc [263].

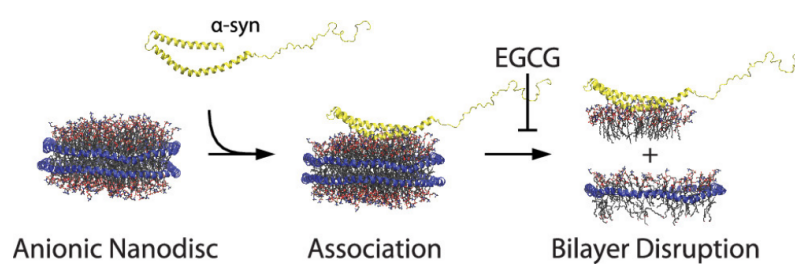


Figure. 1.27 α -Synuclein interacts with lipid nanodiscs. Mass defect analysis identifies the ability of α S to remove lipids from nanodiscs. EGCG prevents lipid removal but maintains the interaction between α S and lipid nanodiscs. Taken from [263].

1.12.2 Oligomers

Oligomeric assemblies are particularly difficult to characterise due to their heterogeneous and potentially unstable nature [169–171, 174, 172, 175, 14, 173]. It has been shown that soluble oligomers of α S can be isolated and were shown to be annular by electron microscopy [335]. Isolated soluble oligomers show an increased proportion of β -sheet content which potentially primes the oligomers for an oligomer-fibril transition. Using HDX-MS to probe the backbone amide solvent exposure in isolated oligomers, more information about the stability and structure of oligomers was revealed [7]. Strong protection against deuterium uptake was observed in residues 5-17 in the N-terminal region of α S oligomers, which infers that these residues in the N-terminus are involved in oligomer assembly, whilst the C-terminal region remained solvent exposed and showed no protection when compared with α S monomers. Additionally, peptides containing residues 39-54 and 70-89 were protected regions (Figure 1.28). The three protected regions were separated by two regions which showed a lower level of protection such as a potentially highly dynamic region of residues 55-76. This protection pattern matches the behaviour of β -strands [7]. HDX-MS proved to be a powerful technique for probing dynamic structural changes in these oligomeric species.

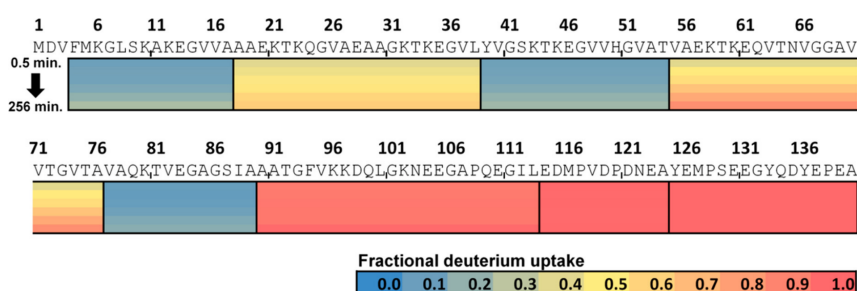


Figure. 1.28 A heat map of deuterium uptake in peptides from α S oligomers. The colour gradient from top to bottom represents deuterium uptake for time-points; 0.5, 2, 8, 32, 128 and 256 min. Taken from [7].

Research from Michael Gross' lab at Washington University, St. Louis demonstrated a new platform for tracking the maturation of amyloid β , associated with Alzheimer's disease from monomer into fibrils [336]. Their workflow utilised covalent labelling of proteins called fast photochemical oxidation of proteins (FPOP) coupled to MS. This workflow relies upon the formation of hydroxyl radicals using an excimer laser operating at 248 nm to photolyse H_2O_2 . Hydroxyl radicals covalently label solvent exposed side chain residues within microseconds and reveal a footprint of the solvent accessible regions of a protein (Figure 1.29). Ki., *et al* used FPOP to follow the amyloid assembly of amyloid β and revealed a highly complicated, multistep process [337]. LysN digestion of covalently labelled amyloid β identified key regions in amyloid β responsible for the assembly of higher order structures. Protection occurred in a step wise manner for the middle segment of the protein corresponding residues 16-27 whilst the N-terminal region remained disordered in monomers and fibrils. The C-terminal segment (residues 28-42) also showed protection from labelling but slightly less so than residues 16-27 which must play a key role in self-association and stabilisation of higher order species. Due to the residue level labelling quantification, residues F19/F20 could be identified to have the highest difference in modification, not only because phenylalanine is highly reactive to hydroxyl radicals compared to the other residues in close proximity, but the high

hydrophobicity of phenylalanine potentially drives the oligomerisation and self association process [338]. Their research is a pivotal example of how MS conjugated techniques reveal hidden details in the assembly of higher order species and is a beautiful example of foot-printing MS transferable to other amyloids. However, no reports have yet appeared of FPOP analysis of α S.

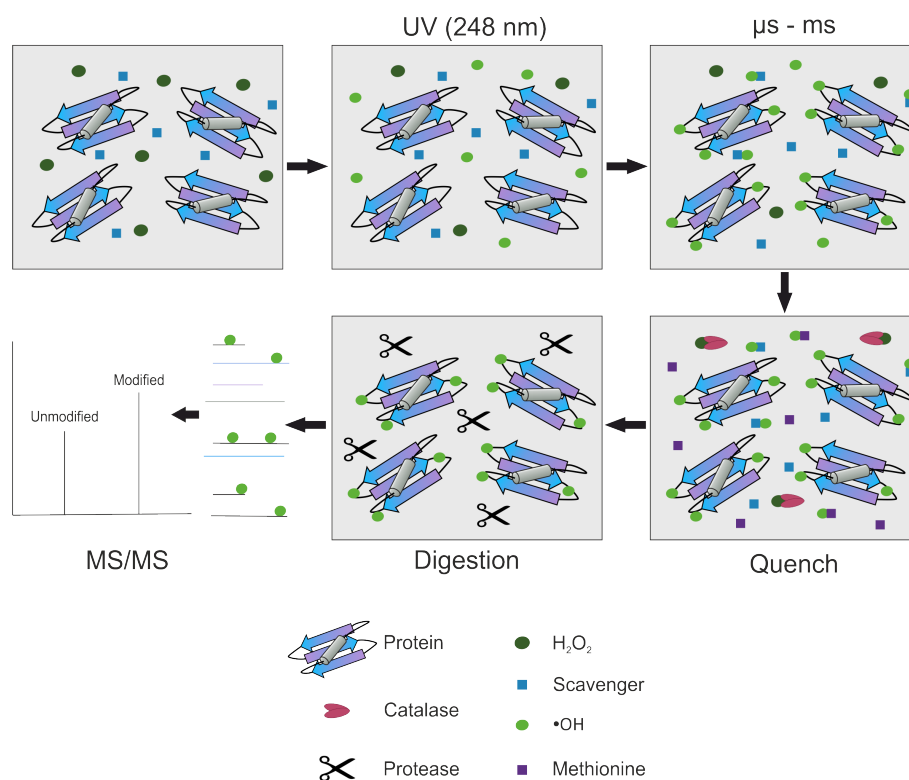


Figure. 1.29 FPOP reaction. H_2O_2 molecules are photolysed into hydroxyl radicals which readily label solvent accessible residues on the surface of proteins and are detected in MS/MS.

1.12.3 Fibrils

Fibril structures are too large for direct MS analysis and are generally de-polymerised before analysis. One example of structural MS of α S fibrils involves limited proteolysis which is a method of using proteolytic enzymes with no specific cleavage sites such as proteinase K, for a short amount of time to cleave peptide bonds of solvent exposed residues

[339]. Following limited proteolysis, MS identifies easily cleaved peptides which can be manually sequenced. They show that the C-terminal domain of α S (residues 94-140) are highly accessible to the solvent in the case of three fibril polymorphs, whilst the N-terminal domain showed different levels of solvent exposure depending on the polymorph [339]. The confirmation of an accessible site raises the potential to design antibodies or drugs to target this region. Additionally, the structural differences between fibril polymorphs may have implications for their interactome within neuronal cells and thus their contribution to PD [339].

1.13 Aims of this thesis

The amyloid assembly process of α S is extremely complex and elaborate. In order to understand how the process begins, the earliest stages of the process must be better understood. In this thesis, the monomer and oligomers are the target of interrogation. The MS tool-kit is utilised to capture the dynamic, transient, heterogeneous, small disordered protein that is α S. By chapter, the specific aims are outlined.

Chapter 3: In this chapter, the aim is to explore how different conditions affect α S conformation and in turn, its amyloid propensity, including N-terminal acetylation and the addition of Ca^{2+} , Mn^{2+} and Zn^{2+} . Variants of α S are explored to understand the importance of the pre-NAC sequence in the N-terminal region for determining amyloid propensity. Results show a distinct correlation between amyloid propensity and the occurrence of compact conformations. With the addition of Zn^{2+} , the 8+ or 7+ charge state of N-terminally acetylated (NTA) α S and its variants shifts its ensemble towards populating compact conformations, and by ThT fluorescence, it is observed that amyloid propensity is increased with the non-amyloid prone N-terminal deletion variant $\Delta\Delta$ α SNTA (through removal of a seven residue sequence $^{36}\text{GVLYVGS}^{42}$ named P1 and a thirteen residue

sequence ⁴⁵KEGVVHGVATVAE⁵⁷ named P2 both found in the N-terminal region) re-establishing its ability to assemble into amyloid fibrils.

Chapter 4: In this chapter, the aim is to identify where Zn^{2+} binds to α SNTA and where exactly the protein chain undergoes compaction. This is probed by NMR, single molecule Förster resonance energy transfer (smFRET), XL-MS and top-down fragmentation in order to identify intramolecular interactions. XL-MS aids in elucidating the conformational dynamics of α SNTA to uncover new insights into the structural transitions and intermolecular interactions of α SNTA. The results demonstrate that Zn^{2+} interacts mostly with H50 and D121, and that when Zn^{2+} is present, long-range intramolecular interactions between the N- and C-terminal regions are increased as shown by XL-MS. By evaluating peak areas using UniDec a K_d of around 50 μ M is established for Zn^{2+} binding to α SNTA.

Chapter 5: To understand the assembly of toxic type B* oligomers of WT α S and familial mutations G51D and A30P oligomers through HDX-MS and mass photometry. The results show that the N-terminal region, in particular the P1 and P2 regions are essential for assembling the oligomeric architecture, whilst P2 remains accessible still to enable binding of the small molecule phenol-soluble-modulin α 3 which stabilises the oligomer structure. HDX-MS reveals that the familial mutant G51D assembles oligomers with a deprotected segment in the N-terminal region (peptide 17-38) compared to WT oligomers, whilst the familial mutant A30P shows protected oligomers in the P2 region. Overall, G51D oligomers appear to assemble as a unique architecture which may hint towards their involvement in early onset PD.

Chapter 6: In this chapter, the results presented in this thesis are discussed in relation to the aims outlined here.

Chapter 2

Materials and Methods

2.1 Materials

Table 2.1 Materials

A	Supplier	Catalogue Number
Acetic acid, glacial	Fisher Scientific, Loughborough, UK	A/0400/PB17
Acetonitrile	Fisher Scientific, Loughborough,	A/0626/15
Acrylamide 30% (w/v) : <i>bis</i> -acrylamide 0.8% (w/v)	Severn Biotech, Kidderminster, UK	20-2100-10
Agar	Melford Laboratories, Suffolk, UK	A20250-500.0
Ammonium acetate 7.5 M stock	Sigma Life Sciences, MO, USA	A2706
Ammonium bicarbonate	Sigma Life Sciences, MO, USA	A6141
Ammonium hydroxide solution	Sigma Life Sciences, MO, USA	221228
Ammonium chloride (¹⁵ N, 99%)	Cambridge Isotope Laboratories Inc, Cambridge, UK	NLM-467-10
Ammonium persulphate (APS)	Sigma Life Sciences, MO, USA	A7460
Ammonium Sulphate	Sigma Life Sciences, MO, USA	A4418
B		
Benzamidine dihydrochloride	Sigma Life Sciences, MO, USA	B6506
Bromophenol blue	Sigma Life Sciences, MO, USA	B0126
C		

Calcium acetate	Sigma Life Sciences, MO, USA	PHR1362
Calcium chloride	Sigma Life Sciences, MO, USA	C5670
Carbenicillin disodium	Fromedium, Norfolk, UK	CAR0025
Chloramphenicol	Sigma Life Sciences, MO, USA	C0378
Cytochrome C from equine heart	Sigma Life Sciences, MO, USA	C2506
D		
n-dodecyl β -D-maltoside (DDM)	Anatrace, OH, USA	D310
Deuterium oxide	Cambridge Isotope Laboratories, Cambridge, UK	DLM-4-PK
D-Glucose C ¹³	Cambridge Isotope Laboratories, Cambridge, UK	CLM-4673-0.25
DMTMM	Sigma Life Sciences, MO, USA	74104
1,4-Dithiothreitol (DTT)	Formedium, Norfolk, UK	DTT025
DNase	Sigma Life Sciences, MO, USA	10104159001
E		
Ethanol	Sigma Life Sciences, MO, USA	E-8751
F		
Formic acid (FA)	Sigma Life Sciences, MO, USA	F0507
G		
GluC sequencing grade	Promega	V1651
Glycerol	Fisher Scientific, Loughborough, UK	G/0650/17
Guanidine hydrochloride	Sigma Life Sciences, MO, USA	50950
H		
HEPES	Sigma Life Sciences, MO, USA	H3375
Hydrochloric acid	Fisher Scientific, Loughborough, UK	10053023
HPLC grade H ₂ O	Fisher Scientific, Loughborough, UK	10221712
I		
Instant Blue Coomassie Blue Stain	Expedeon, CA, USA	ISB1LUK
Isopropyl β -D-1-thiogalactopyranoside (IPTG)	Formedium, Norfolk, UK	IPTG100
L		
LB Miller	Fisher Scientific, Loughborough, UK	1289-1650
M		
Manganese acetate	Sigma Life Sciences, MO, USA	330825-25G
Myoglobin	Sigma Life Sciences, MO, USA	M1882
P		
Phenylmethanesulfonyl fluoride (PMSF)	Sigma Life Sciences, MO, USA	P7762
Phosphate buffered saline (PBS) tablets	Fisher Scientific, Loughborough, UK	BR0014G

Phosphoric acid	Sigma Life Sciences, MO, USA	695017
Precision Plus Protein Dual Xtra Pre-stained Protein Standard	Bio-Rad, CA, USA	1610377
R		
Rubidium chloride	Sigma Life Sciences, MO, USA	83979
S		
SnakeSkin dialysis tubing 3.5K MWCO	Fisher Scientific, Loughborough, UK	68035
Sodium chloride (NaCl)	Fisher Scientific, Loughborough, UK	S/3/160/60
Sodium dodecyl sulphate (SDS)	Fisher Scientific, Loughborough, UK	S/P530/53
T		
Tetramethylethylenediamine (TEMED)	Sigma Life Sciences, MO, USA	T9281
1M Triethylammonium bicarbonate (TEAB)	ThermoFisher Scientific, Loughborough, UK	90114
Thioflavin T	Sigma Life Sciences, MO, USA	T3516
Trifluoroacetic acid (TFA)	Fisher Scientific, Loughborough, UK	85183
Tris	Fisher Scientific, Loughborough, UK	BP152-1
Trypsin protease Pierce™	ThermoFisher Scientific, Loughborough, UK	90057
U		
Ubiquitin	Sigma Life Sciences, MO, USA	U6253
Z		
ZebaSpin desalting column 7K MWCO (0.5 mL)	Fisher Scientific, Loughborough, UK	89883
Zinc acetate	Sigma Life Sciences, MO, USA	1724703

2.2 Molecular biology, protein expression and purification

2.2.1 NatB competent cells preparation

Home-made competent BL21 DE3 cells (originally from Agilent, prepared as competent cells by Dr Roberto Maya-Martinez, University of Leeds) expressing NatB acetylase for post-translational modification of the N-terminus of α S were prepared as follows. BL21 DE3 cells were transformed with the pNatB plasmid (Addgene 53613) and a single

colony was used to inoculate a starter culture of LB media overnight with 25 µg/mL chloramphenicol, at 37°C, 200 rpm. The overnight culture was used to inoculate a 500 mL grow until an OD of 0.4 at 600 nm was reached. Cells were pelleted at 4,500 x g for 5 min. Cells were resuspended in 30 mM potassium acetate, 10 mM CaCl₂, 50 mM MnCl₂, 100 mM RbCl, 15% (v/v) glycerol, pH 5.8. Cells were incubated on ice for 5 min before pelleting and further resuspension in 10 mM MOPS, 75 mM CaCl₂, 10 mM RbCl, 15% glycerol, pH 6.5.

2.2.2 Protein expression and purification

Competent NatB-BL21 DE3 cells (Initially from Agilent, made competent as described above) were transformed with a pET23a plasmid encoding WT human αS (expresses under the control of a T7 promoter, carbenicillin resistance, kindly donated by Prof Jean Baum, Department of Chemistry and Biology, Rutgers University, NJ, USA), ΔP1, ΔP2 or ΔΔ(all generated by Dr Sabine Ulamec, University of Leeds). The C-terminal truncation variant 119 was purchased from TWIST bioscience in a pET-(21+) vector. One colony following transformation was selected for pre-overnight culture in LB media containing 100 µg/mL carbenicillin and 25 µg/mL chloramphenicol and was grown overnight at 37 °C and shaking at 200 rpm. 15 mL of the overnight culture was used to inoculate 1 L of LB media containing 100 µg/mL carbenicillin and 25 µg/mL chloramphenicol and was grown at 37 °C, 200 rpm, until an OD₆₀₀ of 0.6 was reached. Protein expression was induced using 1 mM isopropyl β-D-1-thiogalactopyranoside (IPTG). The induced cell cultures were grown for 4 hours before cells were harvested. For expression of N¹⁵ labelled protein, 0.5 mL of minimal media was used containing (7.5 g Na₂HPO₄, 10 g K₂HPO₄, 9 g K₂SO₄, 10 g KH₂PO₄, 1 g ¹⁵NH₄Cl) supplemented with 1 mM MgCl₂, 100 µM CaCl₂ and 0.8 % (w/v) glucose.

Cells were harvested by centrifuging at 3000 rpm for 15 minutes (rotor JA 8.1) at 4 °C. The cell pellet was resuspended for cell lysis in 25 mM tris-HCl, pH 8.0, 100 µg/mL

lysozyme, 50 µg/mL phenylmethanesulfonyl fluoride (PMSF) and 20 µg/mL DNase and homogenised using an IKA ultra turrant T18 homogeniser (IKA, Staufen, Germany). The lysate was heated to 80°C for 10 min and then centrifuged at 35,000 x *g* for 30 min, 4°C, followed by ammonium sulphate precipitation by adding 29.1 g per 100 mL H₂O. The pellet containing αS was purified by anion exchange using a home-made 300 mL Q-Sepharose fast flow anion-exchange column on an ÄKTA Prime (GE Healthcare., UK). Bound αS was eluted in a gradient of 0-500 mM NaCl, in 20 mM Tris-HCl, pH 8.0 over a volume of 500 mL. Fractions containing αS were dialysed against 5 x 5 L of 50 mM ammonium bicarbonate (SnakeSkin dialysis tubing 3.5K MWCO, FisherScientific) at 4°C. Dialysed protein was filtered (0.22 µm) and loaded onto a HiLoad 26/600 Superdex-75 column at a flow rate of 2.6 mL/min for size exclusion chromatography. Protein was eluted in 50 mM ammonium bicarbonate, lyophilised and stored as lyophilised powder and -20°C.

2.3 Biochemistry

2.3.1 Sodium dodecyl sulphate - polyacrylamide gel electrophoresis (SDS-PAGE)

Tris-tricine buffered SDS-PAGE gels were cast into 8 x 10 cm casts according to the protocol in Table 2.2 shown below to make two gels. Samples were prepared according to the relevant subsections and were diluted 1:1 with 2x loading buffer (100 mM Tris-HCl pH 6.8, 200 mM DTT, 4% (w/v) SDS, 0.2% (w/v) bromophenol blue, 20% (w/v) glycerol) and boiled for ten minutes. Boiled samples were spun down in a bench-top centrifuge for one minute and 15 µL of sample was loaded into each lane. 5µL of Precision plus protein dual colour protein ladder (BioRad, CA, USA) was loaded in the first gel lane as a standard for molecular weight determination. Gels were placed into a tank and the inner reservoir was filled with 1x cathode buffer (100 mM Tris-HCl, 100 mM tricine, 0.1% (w/v) SDS, pH 8.25). The outer reservoir was filled with 1x anode buffer (200 mM Tris-HCl, pH

8.9). Gels were run at a constant current of 30 mA until the dye front migrated through the stacking gel and the current was then increased to 60 mA until the dye front reached the bottom of the resolving gel. Gels were removed from casting plates and were stained in InstantBlue Coomassie protein Stain overnight and imaged on an Alliance Q9 imager (Uvitec).

Table 2.2 Protocol for preparing 2x Tris-tricine buffered SDS-PAGE gels used in this thesis.

Solution component	Resolving gel	Stacking gel
	Volume added (mL)	Volume added (mL)
30 % w/v acrylamide:0.8 % w/v <i>bis</i> -acrylamide	7.5	0.83
3 M Tris-Cl, 0.3 % (w/v) SDS pH 8.45	5	1.55
H ₂ O	0.48	3.72
Glycerol	2	-
10 % (w/v) ammonium persulfate	0.2	0.2
TEMED	0.01	0.010

2.3.2 ThT assays

Kinetics of α S amyloid formation were monitored in a 96-well, non-binding, flat-bottom, half-area microplate (Corning, USA; 10438082) containing one Teflon polyball (1/8" diameter; Polysciences Europe, Eppelheim, Germany) per each well of sample. Samples of 100 μ L containing 100 μ M α S with 20 μ M Thioflavin T (ThT) in 20 mM ammonium acetate, pH 7.5 were incubated at 37 °C shaking at 600 rpm in a FLUOstar omega plate reader (BMG Labtech, Ortenburg, Germany). Fluorescence intensity was measured by exciting at 440 ± 10 nm and collecting emission at 482 ± 12 nm using a bandpass filter. For experiments involving the addition of metal ions, zinc acetate, manganese acetate or calcium acetate (Sigma Life Sciences, Germany) were added at a concentration of 2.5 mM (i.e., 25 fold excess over 100 μ M protein) per well. Results were blank corrected using wells containing 20 μ M ThT in 20 mM ammonium acetate, pH 7.5 and normalised to the maximum fluorescence value of each curve. ThT titrations with Zn²⁺ were performed

under the same conditions, adding 0 μM , 100 μM , 300 μM , 500 μM , 750 μM , 1.5 mM, 2.5 mM or 4 mM of Zn^{2+} .

2.3.3 Transmission electron microscopy (TEM)

A sample of 5 μL was taken from the ThT plate at the end-point of each reaction, loaded onto a glow discharged (30 s; Pelco Easi-glow, Ted Pella, INC, CA, USA), 400 mesh continuous carbon grid and incubated for 2 mins. The sample was blotted with filter paper and washed twice with H_2O before being blotted and stained twice with 2 % (w/v) uranyl acetate. Grids were imaged on a Tecnai F20 transmission electron microscope (FEI) with a Ceta CCD detector (FEI) in the Astbury EM facility (University of Leeds), using a nominal magnification of 9,600x corresponding to a pixel size of 1.05 nm/pixel.

2.3.4 Fibril yields

Fibril yields were determined by pelleting 50 μL of the end point of the ThT reaction at 100,000 $\times g$ (Optima TLX ultracentrifuge, Beckman Coulter, TLA 100 rotor) at 4°C for 30 min. The amount of protein in the remaining soluble material of the sample, as well as an unclarified sample from the reaction end point, was quantified by densitometry of sodium dodecyl sulphate – polyacrylamide gel electrophoresis (SDS PAGE) gels. Tris-tricine buffered 30 % (w/v) acrylamide:0.8 % (w/v) bisacrylamide gels were stained with InstantBlue Coomassie/protein stain and imaged on an Alliance Q9 imager (Uvitec, Cambridge, UK). Band intensities were quantified using ImageJ 1.52a. The ratio between band intensities for the supernatant and the unclarified sample was used to determine the amount of remaining soluble monomer at the end point of the amyloid assembly assay.

2.3.5 Circular dichroism

CD samples were prepared by incubating 100 μM WT, ΔP1 or $\Delta\Delta$ αSNTA , with or without a twenty-five fold excess of zinc acetate in 20 mM ammonium acetate, pH 7.5.

Far-UV CD spectra were acquired in 0.1-mm path length quartz cuvettes (Hellma) using a ChirascanTM plus CD Spectrometer (Applied Photophysics). CD spectra were acquired using a 1-nm bandwidth and 1-s time step, and data were collected at 1-nm increments at 25 °C. An average of three scans (190-250 nm) were acquired per sample.

2.4 Biophysics

2.4.1 NMR

¹⁵N labelled protein was expressed and purified as stated in Section 2.2.2. 2D (¹H, ¹⁵N) HSQC spectra of 100 μM αSNTS, with 1, 2.5, 5, 10, 15 and 25 molar equivalents of zinc acetate, were recorded at 25°C using a Bruker AVANCE III 750 MHz spectrometer equipped with a triple resonance TCI-cryoprobe. Spectra were recorded with 2048 and 512 complex points in the F2 and F1 dimensions respectively. Spectral widths were set to 14.1 ppm centred on 4.7 ppm and 30.0 ppm centred on 119 ppm for F2 and F1 dimensions respectively. Spectra were processed using TopSpin 4.0.6 and analysed using CCPN analysis software [340]. Chemical shifts were calculated using relative domain contributions of 1 and 0.15 for ¹H for ¹⁵N respectively. For K_d determination, chemical shift values were plotted against ligand concentration and fit to the equation described in for single site binding in Williamson (2013) [341]. ¹H-¹⁵N HSQC NMR experiments and data analysis were kindly performed by Dr Ben Rowlinson.

2.5 smFRET

2.5.1 Site directed mutagenesis

Substitution of G7 to a cys residues was created into an αS plasmid generated by Dr Sabine Ulamec, University of Leeds, which already contained the A140C mutation (pET23a encoding A140C αS). G7C was substituted using the NEB Q5 site-directed mutagenesis

kit. Primers are listed in Table 2.3 and were designed by Conor McKay, University of Leeds.

Primer Name	Sequence
α S A140C_G7C_Forward	CTTCATGAAAtgcCTGTCGAAAGCG
α S A140C_G7C_Reverse	ACATCCATATGTATATCTCC

Table 2.3 Primer Sequences for the generation of G7C_A140C α S.

The Q5 mutagenesis was performed by polymerase chain reaction (PCR) using Q5 hot start high fidelity DNA polymerase with template DNA and mutagenic primers using the reaction in Table 2.4,

Component	Volume (μ l) in a 25 μ l Reaction
Q5 High-Fidelity 2X Master Mix Cat No. M0492S	12.5
10 μ M Forward Primer	1.25
10 μ M Reverse Primer	1.25
Template DNA (25 ng/ μ l)	1
Nuclease-Free Water	9

Table 2.4 Components and volumes for a 25 μ l Q5 PCR reaction.

The reaction mixture was placed in a thermocycler and the PCR cycle conditions are outlined in Table 2.5.

Step	Temperature	Time
Initial Denaturation	98°C	30 seconds
25–35 Cycles	98°C	10 seconds
	60°C	30 seconds
	72°C	3 minutes
Final Extension	72°C	2 minutes
Hold	4°C	

Table 2.5 Thermocycling conditions.

Following the PCR reaction, the amplified substituted product was treated with kinase, ligase, Dnpi (KLD) treatment. These enzymes enable phosphorylation, intramolecular

ligation of the plasmid DNA ends and removes the template DNA, respectively. The KLD reaction is outlined in Table 2.6 and was incubated at room temperature for 5 min.

Components	Volume (μ l)
PCR Product	1
KLD Reaction Buffer (2X)	5
KLD Enzyme Mix (10X)	1
Nuclease-free Water	3
Total Volume	10

Table 2.6 Components and volumes for KLD reaction.

5 μ L of the KLD reaction was added to 50 μ L of competent DH5 α *E. coli* cells (Invitrogen) for transformation. The KLD reaction and DH5 α cells were incubated for 30 min on ice before heat shocking at 42°C for 45 s before being placed back on ice for 5 min. An outgrowth step was performed by adding 950 μ L of super optimal broth with catabolite repression (SOC) to the cells and incubating at 37°C for 1 hr, 200 rpm. The SOC and cell mixture was pelleted at 3,000 x *g* for 5 minutes and the pellet was resuspended in 50 μ L of SOC media. Resuspended cells were then plated onto 100 μ g/mL carbenicillin containing LB agar plates and grown overnight at 37 °C. Two colonies were selected, and each was grown in 10 mL LB broth containing 100 μ g/mL carbenicillin overnight at 37 °C, 200 rpm. The culture was centrifuged at 4,000 x *g* and the DNA was purified using a Miniprep kit (Qiagen Miniprep Kit, Qiagen, Cat No, ID:27106). DNA concentration was measured using a NanoDropTM-2000 spectrophotometer (Thermo Fisher Scientific) and 10 μ L of 100 ng/ μ L sample was sent to Source Bioscience Genomics for T7 forward primer Sanger sequencing. The Q5 mutagenesis, KLD reaction, transformation and sequencing were kindly performed by Sophie Cawood and Conor McKay, University of Leeds. α SNTA_{G7C-A140C} was expressed as in Section 2.2.2 with the addition of 1 mM DTT to all buffers.

2.5.2 Labelling of FRET construct

The variant α SNTA_{G7C-A140C} was created with two Cys residues for double fluorophore labelling. 50 μ M α SNTA_{G7C-A140C} was incubated with 75 μ M Atto-565 and 75 μ M Alexa-488 for two hours in the dark at room temperature in 20 mM Tris, pH 7.4. Free dye was removed at the end of the reaction using two rounds of ZebaSpin desalting column 7K MWCO (0.5 mL; Fisher Scientific). The reaction was then separated on a Superdex 75 10/300 GL column on an ÄKTA Prime (GE Healthcare, UK) to remove dimers or higher order aggregates, isolating only monomer. Labelled α SNTA_{G7C-A140C} was snap frozen and stored at -80°C.

2.6 Intact mass analysis

N-terminal acetylation of α S was confirmed by intact denatured liquid chromatography (LC) electrospray ionisation MS using a rapid desalting reverse-phase LC pre-column. 5 μ L of protein at 1 μ M concentration in 0.1% (v/v) trifluoroacetic acid was loaded onto an M-class ACQUITY UPLC BEH C4 desalting column (300 Å, 1.7 μ m, 2.1 mm x 100 mm, Waters Corporation, Wilmslow, UK). LC separation was performed using solvent A (0.1% (v/v) formic acid in H₂O) and solvent B (0.1% (v/v) formic acid in acetonitrile) with a gradient of 20-95% B at a flow rate of 50 μ L/min. The column was washed with 95% B. The eluate was infused into a Xevo G2-XS Q-Tof MS (Waters, UK) via a Z-spray electrospray source in positive TOF mode with 3 kV capillary voltage, 60 V sampling cone, 80 V source offset, 100°C source temperature, 250°C desolvation temperature, 6 V collision energy and a mass range of 350-3000 Da. The instrument was calibrated by a separate injection of 200 pg/ μ L leucine enkephalin.

2.7 Native nESI-IM-MS

2.7.1 Nanospray tip pulling and coating

Borosilicate thin wall glass capillaries (0.78 mm) with filament (Harvard Apparatus, UK) were pulled using a P-97 Flaming/Brown micropipette puller (Sutter Instrument, CA, USA) to make two nanospray tips. The optimal procedure for the needle puller which cycles three times was as follows in Table 2.7. Capillaries were placed into a glass petri dish

Table 2.7 Parameters of heat, pull, velocity and time used for capillary pulling.

Parameter	Unit
Heat °C	560
Pull	250
Velocity	10
Time (s)	50

and coated with gold/palladium in a SC7620 mini sputter coater (Quorum Technologies., Sussex, UK) pressurised with argon at 2×10^{-2} mbar. When a current of 25-30 mA was applied the plasma enabled gold and palladium atoms to deposit on the glass surface. The coating time lasted 75 s after which the petri dish was rotated by 90° followed by a second coating.

2.7.2 Native nESI-IM-MS

Native IM-MS experiments were performed on a Synapt G1 HD mass spectrometer (Waters Corporation, Wilmslow, UK) with travelling (T-wave) ion mobility and a nano-ESI source using in-house generated gold and palladium coated capillaries. Protein was desalted using a ZebaSpin desalting column 7K MWCO (0.5 mL; Fisher Scientific). α S variants were analysed at a concentration of 20 μ M and spectra were collected with and without the addition of 500 μ M zinc acetate, manganese acetate or calcium acetate (Sigma Life Sciences, Germany) at a ratio of 1:25 α S:metal ion unless stated otherwise. The unbound

peak profiles for all three variants were taken from an external control without metal, as the spectra acquired with 25-fold excess of metal resulted in a loss of unbound α SNTA signal. Instrument parameters are outlined below.

2.7.3 Calculation of CCS

MassLynx V4.1 (Waters Corporation, Wilmslow, UK) was used for data processing. Instrument parameters were set at: capillary voltage 1.4 kV, source temperature 30 °C, sampling cone 18 V, extraction cone 1.0 V, trap collision energy 5.0 V, transfer collision energy 2.0 V, trap DC bias 30 V, IM wave velocity 300 m/s, IM wave height 7.0 V. Gas pressures in the instrument were: trap cell 0.0256 mbar, IM cell 0.36 mbar. The IM spectra were calibrated according to the Bush database [53] using denatured cytochrome c (charge states 13+ to 19+), myoglobin (charge states 15+ to 24+) and ubiquitin (charge states 7+ to 13+) at 10 μ M in 50 % (v/v) acetonitrile, 0.1 % (v/v) formic acid. ^{TW}CCS_{N₂} identifies CCS values calculated using traveling wave ion mobility in N₂ buffer gas using calibrants acquired in N₂ buffer gas.

2.7.4 Zn²⁺ titration by IM-MS

Zn²⁺ titrations were acquired using 20 μ M α SNTA, $\Delta\Delta$ α SNTA or 1-119 α SNTA in 20 mM ammonium acetate pH 7.5, with 0 μ M, 2 μ M, 10 μ M, 20 μ M, 40 μ M, 60 μ M, 100 μ M, 150 μ M, 200 μ M, 300 μ M, 400 μ M, 500 μ M or 800 μ M zinc acetate each in triplicate. Protein was desalted using a ZebaSpin desalting column 7K MWCO (0.5 mL; Fisher Scientific). Instrument parameters were set at: capillary voltage 1.4 kV, source temperature 30 °C, sampling cone 18 V, extraction cone 1.0 V, trap collision energy 5.0 V, transfer collision energy 2.0 V, trap DC bias 30 V, IM wave velocity 300 m/s, IM wave height 7.0 V. Gas pressures in the instrument were: trap cell 0.0256 mbar, IM cell 0.36 mbar. Using MassLynx V4.1 (Waters Corporation, Wilmslow, UK), % binding was calculated by extracting peak areas of bound spectral peaks versus the peak area of the unbound spectral

peak, % compaction was calculated by extracting the peak area integration of compact conformations versus extended conformations via arrival time distributions.

2.7.5 Collision induced unfolding

For collision induced unfolding plots, the instrument was calibrated for m/z values with sodium iodide and parameters were identical to Section 2.7.3 except for the trap collision energy. The collision energy was systematically increased in the trap cell positioned prior to the TWIMS cell and an IM-MS spectrum acquired at each voltage. For the Synapt G1 instrument, the voltage was increased from 5 V to 50 V in 5 V increments. IM data was recorded for all detectable charge states. One charge state, typically the 8+ or 7+ charge state was selected to generate CIU plots. Drift time profiles were extracted at each collision voltage from the spectral peak using the full width of the peak at half maximum (FWHM) intensity. Peak intensities were normalised against the maximum and the arrival time distribution profile was plotted using Origin Pro (OriginLab Corp, USA) to visualise each conformation present in an ensemble.

2.7.6 Dimer abundance analysis

Native MS spectra were acquired using a Synapt G1 HD mass spectrometer (Waters Corporation, Wilmslow, UK). Spectra were de-convolved using UniDec v6.0.3 in the Deconvolve MS node, using the following parameters: m/z range: 400-4000 Th, subtract curved: 5, Gaussian smoothing: 10, bin every 10 Th, charge range: 1-50, mass range: 5000-500000 Da, sample mass: every 10 Da, peak FWHM: 0.85 Th, peak detection range: 500 Da, peak detection threshold: 0.01-0.2. Relative dimer abundance was calculated using the following equation: $\text{Dimer abundance}/(\text{monomer abundance} + \text{dimer abundance})$. Relative % dimer was plotted against t_{50} or molar excess of Zn^{2+} using Origin Pro (OriginLab Corp, USA) and plots were fitted to a linear curve or an exponential curve.

2.8 Cross-linking-MS

2.8.1 Cross-linking-MS experimental

WT α SNTA at a concentration of 50 μ M was subjected to chemical cross-linking by incubation with 4 mM 4-(4,6-Dimethoxy-1,3,5-triazin-2-yl)-4-methylmorpholinium chloride (DMTMM) in 20 mM HEPES pH 7.4 for 20 min at RT. The reactions were quenched by adding 20 mM Tris-HCl pH 7.0. A sample of each reaction along with an un-cross-linked control was analysed on an SDS-PAGE gel to check for a band shift and to confirm the absence of dimers. Cross-linked samples were digested using the S-Trap method, an on column digestion approach for high peptide recovery in Section 2.8.2.

2.8.2 Cross linking-MS S-Trap digestion

Cross-linked proteins were first fully solubilised by the addition of 20 μ L of 10 % (w/v) SDS solution to 20 μ L of protein at a protein concentration of 20 μ M. Proteins were fully denatured by the 1:10 (v/v) addition of phosphoric acid to a final concentration of 1.2 % (v/v). Samples were then diluted with S-Trap binding buffer 7:1 (100 mM triethylammonium bicarbonate (TEAB) pH 7.1 in methanol). Enzymes trypsin protease PierceTM (ThermoFisher Scientific) and GluC sequencing grade (Promega) were added from stocks of 0.02 μ g/ μ L to a ratio of 1:20 (protein:enzyme). The protein solution containing the appropriate enzyme was quickly loaded onto the S-Trap column and centrifuged at 4000 x g for 30 s, to enable protein capture within the submicron pores of the S-Trap. The column was washed by adding 150 μ L of binding buffer before being centrifuged at 4000 x g for 30 s. 30 μ L of trypsin or GluC at 0.02 μ g/ μ L was added to the top of the trap to be confined in the submicron pores of the trap with the protein to enable rapid digestion. S-Traps were loosely capped, placed in a 1.5 mL microcentrifuge tube and heated at 37 °C for 1 h. 40 μ L of 50 mM triethylammonium bicarbonate (TEAB) was added and the column was centrifuged at 4000 x g for 1 min. Digested peptides were eluted by adding of

0.2 % (v/v) formic acid (FA), centrifuging the S-Trap at 4000 x *g* for 30 s then adding 50 % (v/v) acetonitrile (ACN) followed by a final centrifugation step at 4000 x *g* for 30 s. The eluates from these steps were combined and dried using a Genevac EZ-2 Plus Evaporating System (Marshall Scientific, NH, USA). The peptides were resuspended in 20 μ L 0.1 % (v/v) TFA for peptide mapping.

2.8.3 Cross linking-MS peptide mapping

For MS acquisitions, samples were resuspended in 0.1 % (v/v) TFA to a protein concentration of 1 μ M. Samples were analysed by a 65 min 0-60% acetonitrile gradient using an EASY-spray reversed phase LC system with column specifications as following. Particle size: 2 μ M, diameter: 75 μ M, length: 500 mM, packing material: spherical, fully porous, ultrapure silica and an EASY-IC ion source (ThermoFisher Scientific) coupled online to an Orbitrap Eclipse Tribrid mass spectrometer (ThermoFisher Scientific). Parameters of the run were as follows for 12 scans. MS scan properties were: Orbitrap detection, 60000 Orbitrap resolution, 450-1800 *m/z* scan range, RF lens (%) 80, normalised AGC target (%) 100, 200 ms maximum injection time, positive polarity mode, microscans 1. Data-dependent MS² properties were: activation type HCD, stepped collision energy mode, HDC collision energies (%) 25, 30, 35, Orbitrap detector type, Orbitrap resolution of 15000, normalised AGC target (%) 200, 250 ms maximum injection time. Dynamic exclusion properties were: exclude after 2 times, if occurs within 7s, exclusion duration 45s with high and low mass tolerance of 10 ppm. Samples were measured with included charge states 2-8 with an intensity threshold of 5.0e4.

2.8.4 Cross linking-MS data processing

Spectra were analysed using ProteomeDiscoverer software v4.2 (ThermoFisher Scientific) with incorporated XlinkX nodes. Analysis parameters were set as follows. Spectra were matched against the α S sequence (UniProt ID P37840). The enzyme was set to GluC and

the number of missed cleavages, 2 and minimum sequence length, 6. Acetyl (N-term) was set as a fixed modification, deamidation (N), EDC (E, K, D) and oxidation (M) were set as variable modifications. Cross-link FDR threshold was 0.01 and the cross-link spectral match (CSM) FDR was 0.01. Precursor mass tolerance was set to 10 ppm and fragment ion mass tolerance was set to 20 ppm.

2.9 ETD fragmentation

Experiments were conducted on an Orbitrap Eclipse Tribrid mass spectrometer (ThermoFisher Scientific, San Jose, CA, USA). The ion transfer tube temperature was 275°C, proteins were ionised using in-house pulled gold/palladium coated nano-spray borosilicate capillaries held at around 1.4 kV. The instrument was operated under high pressure mode (20 mtorr in the ion routing multipole) and under intact protein analysis mode. The 8+ charge state (m/z : 1813) or the 12+ charge state (m/z : 1209) were selected for fragmentation under the following parameters. Scan type: MS² scan. Isolation mode: Quadrupole. Isolation width: 3. Activation type: ETD. ETD reaction time (ms): 5. ETD reagent target: 7.0e5. Maximum ETD reagent injection time (ms): 200. Detector type: Orbitrap. Orbitrap resolution: 120000. Mass range: normal. Scan range: 200-2000. RF lens (%): 60. Normalised automatic gain control (AGC) target (%): 150. Maximum injection time (ms): 100. Microscans: 1. Data were processed using ProSight Native, Proteinaceous by importing raw data and searching against P37840 SYUA_HUMAN, UniProtKB. Fragment ions were visualised using the TDV node with the following settings. Fragment ions: max PPM tolerance 10 ppm, sub tolerance 3.0 ppm, cluster tolerance 0.3, charge range 1-10, minimum score terminal ions 0.6 and internal ions 0.7, S/N cut-off 3.00. General: distribution generator Mercury7. AIM: Thrash S/N cut-off 3.00, max mass 60 kDa, max charge state 40, Xtract S/N cut-off 3.00. [342]

2.10 UVPD fragmentation

Experiments were conducted on an Orbitrap Eclipse Tribrid mass spectrometer (ThermoFisher Scientific) similarly to ETD experiments and processed as outlined in Section 2.9 [342]. For UVPD the activation type was set to: UVPD and the UVPD activation time (ms): 80.

2.11 Cyclic IM-MS

Data was collected on a SELECT SERIES Cyclic IMS at Waters Corp, Wilmslow, UK with Dr. Dale Cooper-Shepherd. The instrument was fitted with an electron capture dissociation cell (e-MSion, Corvallis, OR, USA) fitted post IMS. α S samples were prepared to 20 μ M in 10 mM ammonium acetate, pH 7.5 and loaded into in-house pulled gold/palladium coated borosilicate nano-spray capillaries for direct infusion. For acquisitions the mass range was set to 50-4000 with a 1 s scanning rate. Samples were sprayed in positive mode and the ToF analyser was set to V-mode. Instrument parameters were set as follows, capillary voltage: 1 kV, sampling cone 40 V, source offset 10 V, source temperature 80 °C, trap collision energy 6 eV, transfer collision energy 4 eV. Ions enter the cyclic ions mobility (cIM) separator with a path length of 98 cm and single pass IM resolution of 65. The cIM chamber is filled with N₂ gas to a pressure of 5 mbar. The T-wave height was 0.4 V. Using the quadrupole, the 8+ charge state (m/z 1813) was isolated and injected into the cIM for a single pass of IM separation. For slicing acquisitions, slices of α S were extracted by ATDs and these were 45-70 ms, 70-80 ms, 80-90 ms, 90-100ms . Each slice was individually ejected back into the pre-store rather than toward the detector to be reinjected into the cIM separator. For ECD experiments, the ExD WS-25x cell (eMSion) was post IMS. Data were analysed using MassLynx v4.2 (Waters, UK) and Driftscope v3.0 (Waters, UK). For Gaussian fitting Origin 2019b (OriginLab Corp) was used and Gaussian distributions were fitted manually.

2.12 K_d determination

Zn^{2+} titrations were acquired using 20 μM α SNTA in 20 mM ammonium acetate pH 7.5, with 0 μM , 2 μM , 10 μM , 20 μM , 40 μM , 60 μM , 100 μM , 150 μM , 200 μM , 300 μM , 400 μM , 500 μM or 800 μM of zinc acetate. Raw data were acquired with MassLynx 4.1 (Waters, UK) for Synapt G1 data and FreeStyle (ThermoFisher) for Orbitrap Eclipse Tribrid data and deconvolved using UniDec 6.0.3 using the following parameters: m/z range: 400-4000 Th, subtract curved: 5, Gaussian smoothing: 10, bin every 10 Th, charge range: 1-50, mass range: 5000-500000 Da, sample mass: every 10 Da, peak FWHM: 0.85 Th, peak detection range: 500 Da, peak detection threshold: 0.01-0.2. K_d values were obtained by fitting titration curves in the data collector utility from UniDec with the following parameters: "what to extract: Raw data", "How to extract: Local max", "Window: 2 Th", "Number of proteins: 1", "Number of ligands: 5", "Protein and Ligand Models: All KD 's free" enabling normalization of data and extraction. The equation for K_d fitting was as follows, where R is the ratio of the intensity of protein bound to ligand over the intensity of the unbound protein:

$$\left(\frac{1}{K_d}\right) = \frac{R}{[L]_0 - \left(\frac{R}{1+R}\right)[P]_0} \quad (2.1)$$

2.13 HDX-MS

2.13.1 HDX-MS experimental

HDX-MS experiments were performed using an automated HDX liquid handling robot (LEAP Technologies, Ft Lauderdale, FL, USA) coupled to an Acquity M-Class LC and HDX manager (Waters, UK). Samples contained 50 μM of α S monomer or oligomer in PBS buffer, pH 7.4. The automated robot was used to transfer 95 μL of deuterated buffer (PBS, pD 7.4, 0.01 % w/v DDM) to 5 μL of protein-containing solution to achieve 95% (v/v) D_2O for labelling (20-fold dilution) and the mixture was incubated at 4 $^{\circ}C$ for 0, 0.5,

or 1 or, 5 min. Three replicate measurements were performed for each time point and for each protein condition. 75 μL of quench buffer (PBS buffer, 4 M guanidine HCl, 0.05 % w/v DDM, pH 2.1) was added to 75 μL of the labelling reaction to quench deuterium labelling. 50 μL of the quenched sample was injected onto an Enzymate immobilised pepsin column (Waters, UK) column (20 °C). A VanGuard Pre-column [Acquity UPLC BEH C18 (1.7 μm , 2.1 mm x 5 mm, Waters, UK)] was used to trap the peptides produced for 3 min. A C18 column (75 μm , 2.1 mm x mm, Waters, UK) separated peptides using a gradient of 0-40 % (v/v) acetonitrile (0.1 % v/v formic acid) in H_2O (0.3 % v/v formic acid) over 7 min at 40 $\mu\text{L min}^{-1}$. Separated peptides from the LC column were infused into a Synapt G2Si mass spectrometer (Waters, UK) operated in HDMSE mode. Peptides were separated by ion mobility prior to CID fragmentation in the transfer cell for peptide identification. Deuterium uptake was quantified at the peptide level.

2.13.2 HDX-MS data processing

Data analysis was performed using PLGS (v3.0.2) and DynamX (v3.0.0) (Waters, UK). Search parameters in PLGS were: peptide and fragment tolerances: automatic, minimum fragment ion matches: 1, digest reagent: non-specific, false discovery rate: 4. Restrictions for peptides in DynamX were: minimum intensity: 1000, minimum products per amino acid: 0.3, maximum sequence length: 25, maximum error = 5 ppm, file threshold: 3. Peptides with significant increase/decrease in deuterium uptake were identified using a cut off of 0.5 Da analysed in triplicate. Woods plots were generated using Deuterios [343].

2.14 Mass photometry

Mass photometry measurements were acquired using Refeyn One^{MP} instrument (Refeyn Ltd, Oxford, UK). Cover glass slips were prepared by cleaning with Milli-Q water and isopropanol and dried with N_2 gas. Precut 2x2 culture well gasket (Grace Bio-Labs,

Oregon, USA) was placed onto the coverslip. Mass photometry measurements were performed at room temperature, 16 μL of PBS buffer was loaded onto a well of the gasket for focal adjustment. 4 μL of oligomer sample was added to the same well for a final concentration of 3 μM or 500 nM and mixed by pipetting. Sixty seconds of movie data was recorded using AcquireMP software (Refeyn Ltd). Recordings were analysed using DiscoverMP (Refeyn Ltd). Data were calibrated using bovine serum albumin (BSA), thyroglobulin and aldolase measured in PBS. Data were analysed as mass distributions and Gaussian fitting was performed over the mass histogram. The mass range was set as 0-4000 kDa.

Chapter 3

Probing the Conformational Dynamics of Monomeric α -Synuclein and How it Relates to Amyloid Assembly

3.1 Introduction

Many human diseases arise from the misfolding, unfolding or aggregation of proteins from their native, functional state [141]. Alpha-Synuclein (α S) visits a large conformational space, defined as an intrinsically disordered protein (IDP) [250]. Despite the structural flexibility of α S, ordered structures containing elements of secondary structure are known to form in different conditions, such as an α -helix in the N-terminal region when α S becomes membrane-bound [344]. Two membrane-bound structures have been determined for α S

- i.) a broken helix formed of two α -helices V3-V37 and K35-T92 arranged antiparallel to each other when bound to phospholipid vesicles and
- ii.) an unbroken α -helix between V3-T92 when bound to phospholipid bicelles [261, 262].

The conformational freedom exhibited by α S may play a role in its aggregation pathway. Recently Brodie., et al (2020)

showed that α S is indeed present in solution as a broad conformational ensemble through cross-linking MS and single molecule Förster resonance energy transfer (smFRET) guided molecular dynamics simulations. Their findings identified the importance of inter-residue contacts between the N- and C-terminal regions for stabilising conformations present in the ensemble [89]. Furthering on from this data, Chen., et al (2021) used the existing smFRET data as an experimental restraint to guide discrete molecular dynamics (DMD) simulations in order to generate a snapshot of the α S conformational ensemble [345].

Alternatively, toxic oligomers and fibril structures of α S are composed primarily of β -sheets [346–348]. The adoption of specific conformations under defined conditions alludes to the impression that the roles of α S, be that functional or pathological, might be related to the different conformational state of α S monomers. Therefore, it is crucial to determine how the conformational ensemble of monomeric α S relates to its aggregation profile. Despite the importance of understanding how the monomeric ensemble relates to amyloid formation, characterising transient and heterogeneous species in solution is experimentally challenging by traditional structural biology techniques such as nuclear magnetic resonance (NMR), cryo-electron microscopy (cryo-EM), circular dichroism (CD) and X-ray crystallography which mostly rely on static states (in crystals) or are subjected to population averaging [349]. Although these techniques are powerful biophysical tools, the data outputs fail to capture unique structural fingerprints present in a transient mixture. In this chapter, a combinatorial approach using native nano electrospray ionisation -ion mobility – mass spectrometry (nESI-IM-MS) and thioflavin T (ThT) fluorescence kinetics has been applied to capture the α S conformational ensemble under various conditions, and relate this fingerprint to aggregation kinetics. nESI-IM-MS enables separation of ionic species in the gas phase orthogonal to mass/charge (m/z). Ions are separated based on their mobility through a drift cell filled with neutral buffer gas molecules determined through rotationally averaged collision cross section (CCS) as described in Section 1.5.2.

In this chapter, variants of α S are explored in order to identify regions within the 140 amino acid protein chain that might be important in controlling the conformational space of α S. The variants used here were first detailed by Doherty, *et al* (2020) where *in silico* analysis was used to identify two regions in the N-terminal region of α S that exhibit predicted low solubility and high aggregation propensity including a seven residue sequence 36 GVLYVGS 42 (named P1) and a thirteen residue sequence 45 KEGVVHGVATVAE 57 (named P2; Figure 3.1) [350].

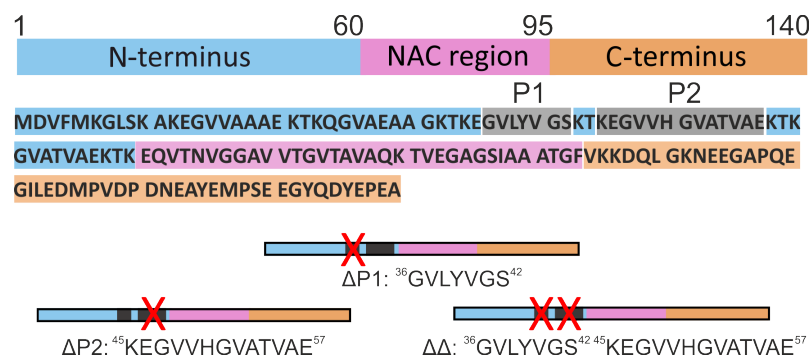


Figure 3.1 The P1 and P2 regions in α S.

Deleting P1 to create the α S variant Δ P1 inhibited aggregation at physiological pH (pH 7.5) but not at acidic, lysosomal pH (pH 4.5). Deleting P2 alone (Δ P2) had no effect on amyloid assembly. However, deleting P1 and P2 in tandem ($\Delta\Delta\alpha$ S) abolished amyloid propensity at both physiological and lysosomal pH within 100 hours all shown by ThT fluorescence assays (Figure 3.2) [350]. Deleting these seemingly critical N-terminal sequences may disrupt intramolecular interactions within the protein chain which affects the ability of α S to achieve an amyloid-competent conformation in which the NAC region is sufficiently exposed. nESI-IM-MS offers the potential to provide an insight into how the conformational heterogeneity of Δ P1, Δ P2 and $\Delta\Delta\alpha$ S correlate with amyloid propensity.

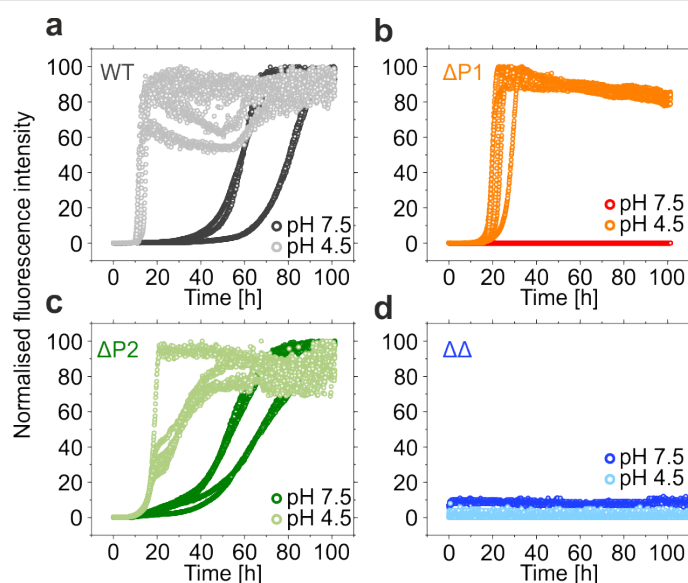


Figure. 3.2 The role of the P1 and the P2 region in amyloid assembly. Amyloid assembly kinetics of (a) WT (b) $\Delta P1$ (c) $\Delta P2$ and (d) $\Delta\Delta$ αS measured by ThT fluorescence. Adapted from [350].

Here, nESI-IM-MS and ThT fluorescence kinetics are used to understand whether N-terminal acetylation of αS has an effect on its conformational dynamics and amyloid assembly kinetics. *In vivo*, αS is found to be predominantly acetylated at the N-terminus [351]. More specifically, the composition of Lewy Body deposits has been shown to contain a high degree of N-terminally acetylated αS ($\alpha SNTA$) [292, 352]. NTA has been shown to increase αS membrane binding affinity through increased helicity of the N-terminal region, as well as to facilitate Hsp90 β , Hdc70, SecB and Skp chaperone binding [269, 267]. Undeniably, using $\alpha SNTA$ mimics physiological αS more closely. αS *in vivo* is local to presynaptic nerve terminals in the brain. The human brain contains around 10^{11} neurons which communicate through synapses where electrical action potentials are converted into chemical signals for neurotransmitter release. Each neuron is proposed to contain approximately 7000 synapses [353]. Calcium ions (Ca^{2+}) are essential for the transduction of electrical signals into chemical signals, but other metal ions have been shown to alter synaptic transmission [354]. Further to this, heavy metal ions have been

linked to neurotoxicity and are markedly elevated in Lewy bodies deposited in the brain [355]. In its native, *in vivo* environment α S will thus experience different physiological environments and conditions to which the protein chain needs to adapt. Due to the high abundance of negatively charged residues in the C-terminal region of α S (Figure 3.3), binding of positively charged ions has been observed in this region [183]. The binding sites of multiple metal ions is shown in Figure 3.3. Binding of metal ions to residues in the C-terminus will affect the charge distribution of α S through neutralisation of Glu and Asp residues [183, 356]. This could influence structural changes and reshaping of α S monomers that may affect amyloid propensity [345, 357, 358, 13]. In this chapter, the binding of divalent ions Ca^{2+} , Mn^{2+} and Zn^{2+} to α SNTA has been observed through native MS and the resultant effects to the conformational ensemble and propensity to form amyloid are investigated through nESI-IM-MS and ThT fluorescence, respectively.

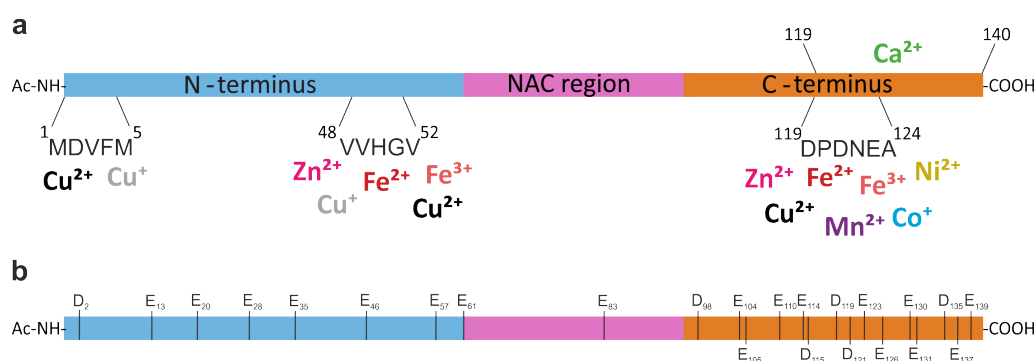


Figure. 3.3 α S is predicted to bind metal ions primarily in the negatively charged C-terminal region. (a) A range of monovalent, divalent and trivalent metal ions are known to bind to negatively charged Asp and Glu residues in the C-terminal region of α S, with the binding sites mapped by NMR [183]. Some transition metals also interact with His50 and methionine residues in the N-terminal region [359]. (b) The full length sequence of WT α SNTA, acetylated at the N-terminus (Ac-NH) with each Glu and Asp residue labelled across the sequence.

3.2 Objectives

This chapter aims to correlate the conformational dynamics of α S monomers with amyloid propensity through a systematic study of sequence variants, N-terminal acetylation and the presence or absence of divalent metal ions. Proteins were expressed and purified with and without N-terminal acetylation, structurally characterised by nESI-IM-MS and the rate of amyloid assembly measured using ThT fluorescence. As discussed, it is evident that the structural heterogeneity of α S influences its amyloidogenic capacity and that the limited detail of these processes offers scope for investigating the relationship between conformational dynamics and amyloid assembly. In this chapter evidence is provided that perturbing the charge distribution of α S, restricting conformational freedom and enhancing compaction of the protein all have marked effects on amyloid assembly and may elucidate the earliest stages of amyloid assembly at the monomer level.

3.3 N-terminal acetylation of α -synuclein

3.3.1 Protein production of acetylated α -synuclein

All α S WT and variant proteins were purified using the same protocol. Plasmids were kindly provided by Dr. Sabine Ulamec, The University of Leeds. The purification of WT α SNTA and Δ P1 α SNTA are shown as examples of the purification process in Figure 3.4 a-e which. Briefly, pET23a plasmids containing the relevant α S gene per variant were transformed into competent BL21 DE3 cells for overexpression of protein as described in Methods Section 2.2.2. For N-terminal acetylation of proteins, a competent BL21 DE3 cell line was created which stably expresses NatB acetylase. Protein purification included a five step protocol outlined in Figure 3.4 a. Cells were lysed, and the lysate was heated to 80°C. Due to the high stability of α S at high temperatures owing to its disordered structure, α S remains in the supernatant at this stage and can be separated from cell debris and thermally denatured proteins through ultracentrifugation. Soluble α S was salted out of solution using

58% (w/v) ammonium sulphate precipitation and pelleted by ultracentrifugation (Section 2.2.2). Both anion exchange chromatography (AEX) and size exclusion chromatography (SEC) were performed to exploit the physicochemical properties of α S for its purification. Firstly, the salted out pellet of α S was re-solubilised by homogenisation in 300 mL of 20 mM Tris HCL pH 8.0 to dilute any remaining ammonium sulphate, and loaded onto a Q-Sepharose AEX column. α S bound to the resin and was eluted using a gradient of 0-50% of 20 mM Tris HCL, 1 M NaCl, pH 8.0. The chromatograms for WT α SNTA and Δ P1 α SNTA are shown in in Figure 3.4 b-c. The main peak eluted from AEX was further purified by SEC. At each stage of purification a sample was analysed by SDS-PAGE (Figure 3.4e).

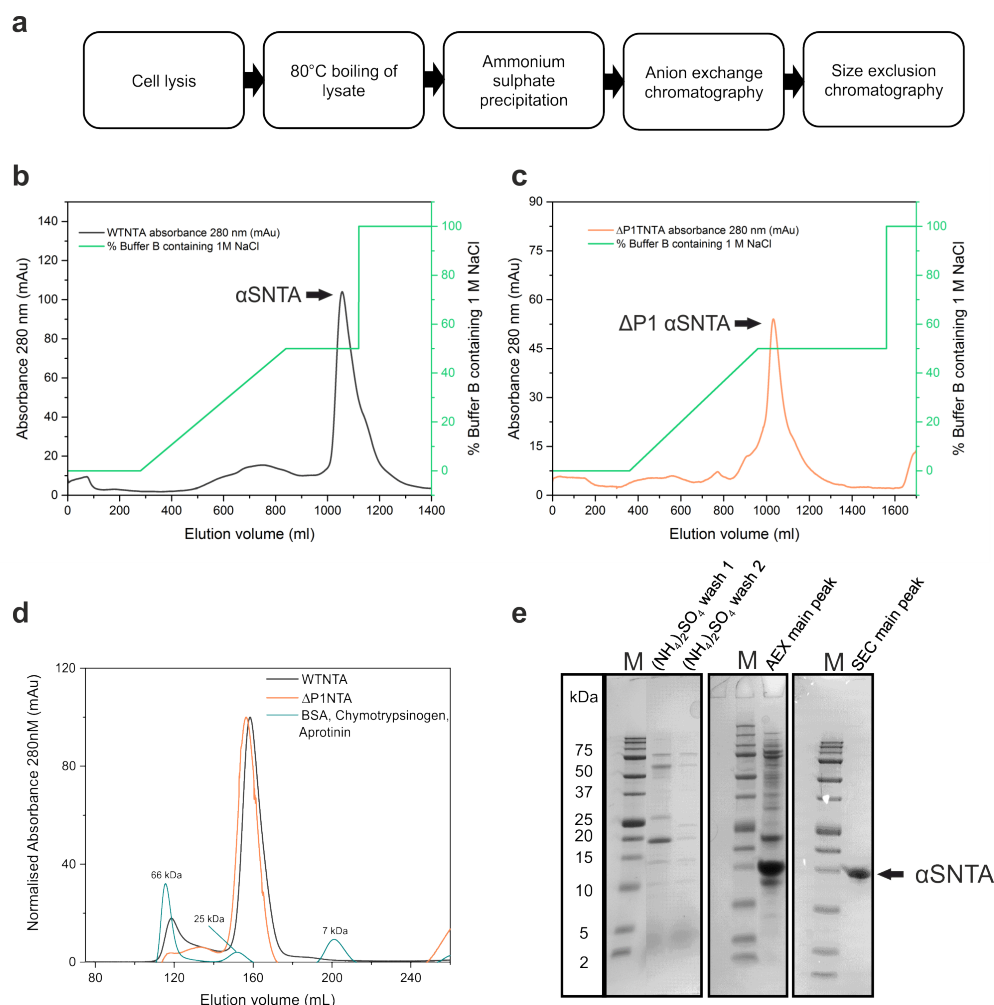


Figure. 3.4 Purification of α S. (a) A schematic of the protocol used in this thesis for purification of α S. (b) AEX chromatogram of WT α SNTA. (c) AEX chromatogram of Δ P1 α SNTA. (d) SEC chromatogram of WT- and Δ P1- α SNTA with calibrants: BSA (66 kDa), chymotrypsinogen (25 kDa) and aprotinin (7 kDa). (e) SDS-PAGE showing stages of purification of WT α SNTA, a band for α S is not observed for the two ammonium sulphate washes, as α S was salted out of solution and pelleted through ultracentrifugation. The band for α S becomes enriched throughout the protocol. M indicates molecular weight markers.

Denaturing LC-MS was used to check the molecular weight of the purified α SNTA protein as well as the efficiency of N-terminal acetylation (Figure 3.5 a-b). The intact mass spectra identified one primary species with a mass of $14501.64 \text{ Da} \pm 0.13$ which is

consistent with the expected mass of N-terminally acetylated WT α S (14502.16 Da). From the deconvolved mass spectrum in Figure 3.5 b some non-acetylated protein is present in the sample (14459.63 Da \pm 0.13), however the efficiency of labelling is around 92% as judged by peak area integration. The technique applied here using competent BL21 DE3 stably expressing NatB is a robust, efficient protocol for expressing N-terminally acetylated proteins.

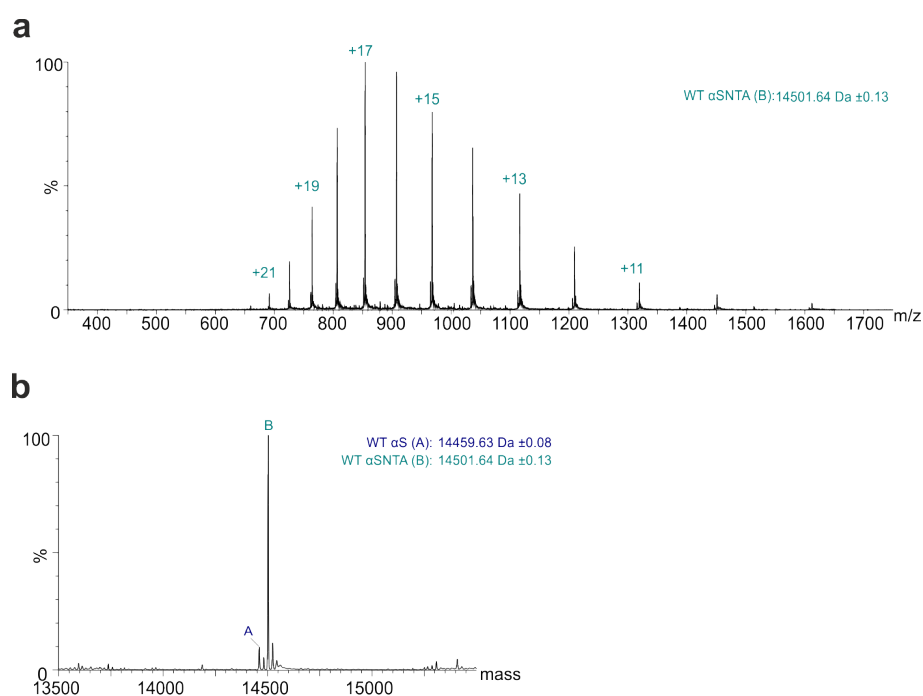


Figure. 3.5 Denatured LC-MS of purified WT α SNTA.(a) Mass spectrum of denatured α SNTA which is deconvolved in (b) where A = WT α S and B = WT α SNTA. Protein was measured at a concentration of 1 μ M in 0.1% (v/v) trifluoroacetic acid on a Xevo G2-XS QToF instrument (Waters Corporation, Wilmslow, UK).

N-terminal acetylation proved robust for Δ P1 (NTA expected mass 13826.37 Da and NTA observed mass 13826.04 Da), Δ P2 (NTA expected mass 13224.71 Da and NTA observed mass 13225.29 Da) and $\Delta\Delta$ (NTA expected mass 12548.93 Da and NTA observed mass 12548.57 Da) as shown in the deconvolved mass spectra in Figure 3.6.

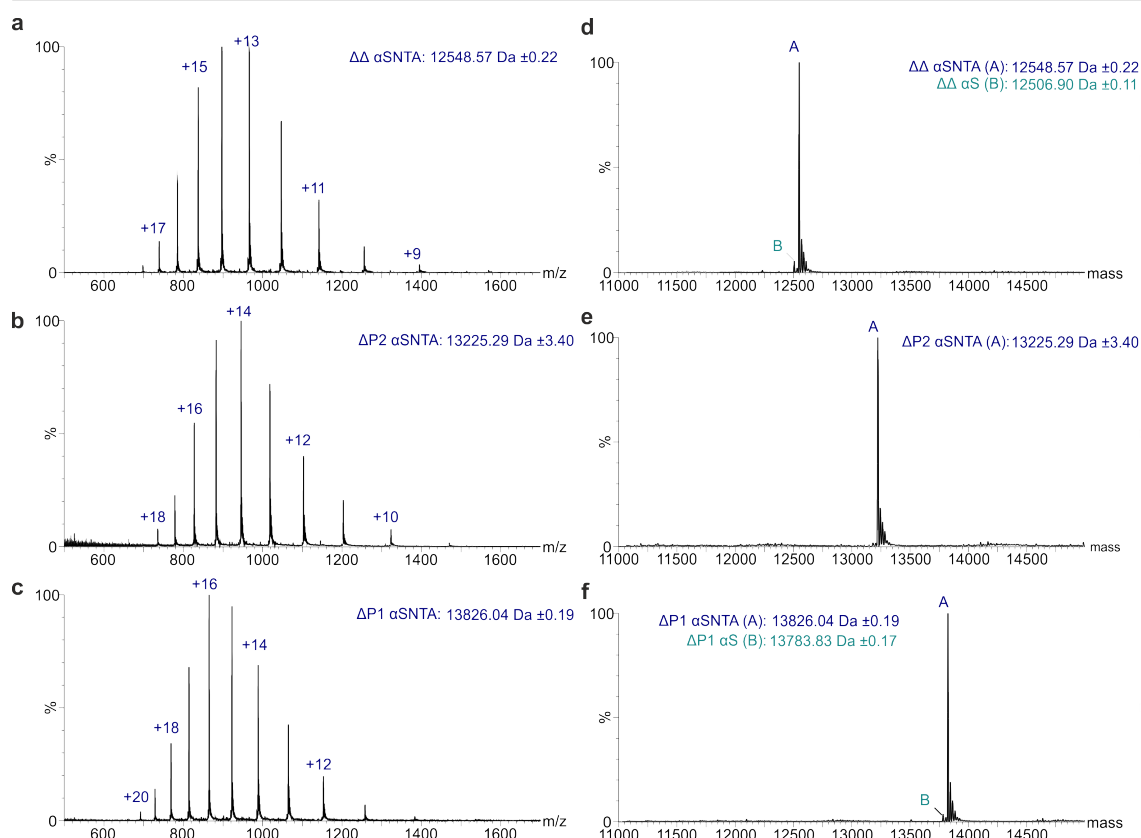


Figure. 3.6 Denatured LC-MS of purified α S variants. Mass spectrum of denatured (a) $\Delta\Delta$ α SNTA, (b) Δ P2 α SNTA, (c) Δ P1 α SNTA. Deconvoluted mass spectrum of (d) $\Delta\Delta$ α SNTA, (e) Δ P2 α SNTA, (f) Δ P1 α SNTA where A = NTA variant and B = non-NTA. Proteins were measured at a concentration of 1 μ M in 0.1% (v/v) trifluoroacetic acid on a Xevo G2-XS QToF instrument (Waters, UK).

3.3.2 Effect of N-Terminal acetylation on α S amyloid assembly

Fibril growth assays were carried out in order to characterise whether acetylation of α S had an effect on its amyloid assembly kinetics. The fluorescent dye Thioflavin T (ThT; Figure 1.21) was used to track the onset of β -sheet assembly in a time dependent manner. As β -sheet rich fibrils assemble, ThT molecules can readily intercalate into the hydrogen bond network of stacked β -sheets [360]. Rotational freedom of the central C-C bond connecting the benzothiazole and aniline rings becomes sterically hindered resulting in a

characteristic red shift in the fluorescence emission where excitation occurs at 440 nm and emission occurs at 480 nm with an increase in intensity [361]. The amyloid assembly of α S (WT, Δ P1, Δ P2 and $\Delta\Delta$) when acetylated vs. non-acetylated are shown in Figure 3.7. Acetylation of the N-terminus of α S slows the amyloid assembly rate for all variants.

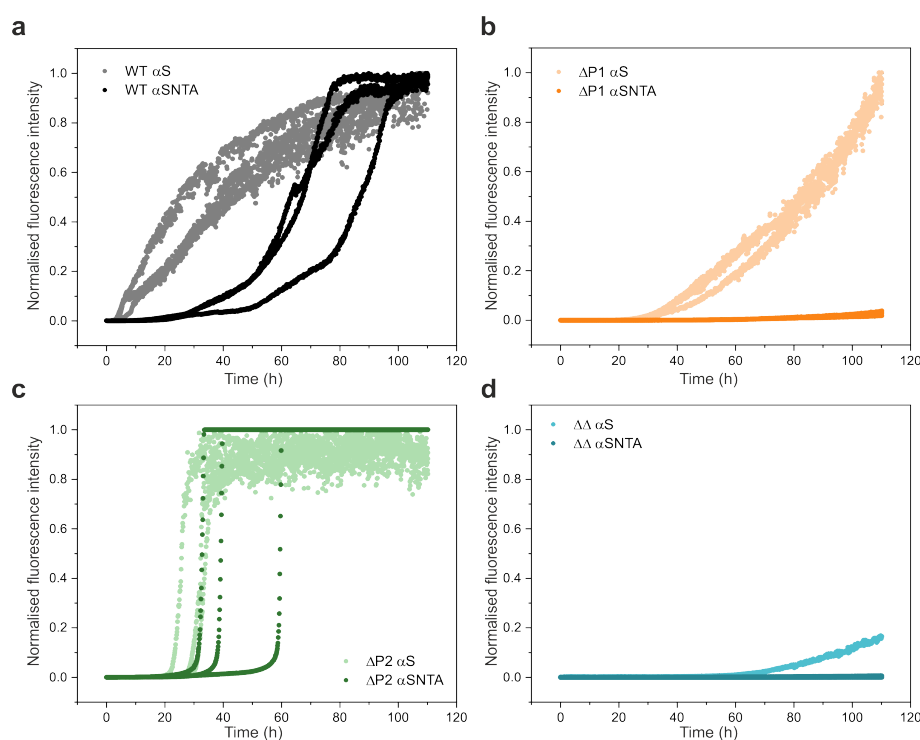


Figure. 3.7 Amyloid assembly ThT fluorescence kinetics of α S with and without N-terminal acetylation. ThT fibril growth assays of 100 μ M α S in 20 mM ammonium acetate pH 7.5 for (a) WT α S and WT α SNTA, (b) Δ P1 α S and Δ P1 α SNTA, (c) Δ P2 α S and Δ P2 α SNTA and (d) $\Delta\Delta$ α S and $\Delta\Delta$ α SNTA. Amyloid assembly was measured at 37 $^{\circ}$ C, shaking at 600 rpm containing one Teflon polyball (1/8" diameter; Polysciences Europe, Eppelheim, Germany) per each well of sample.

3.3.3 Native MS of α SNTA identifies similarities

Native nESI-IM-MS experiments were performed on the acetylated and non-acetylated isoforms of WT, Δ P1, Δ P1 and $\Delta\Delta$ - α S. Initially native nESI-MS was used to compare whether there was an effect on the charge state distribution when each protein is acetylated.

The charge state distribution of a protein can reflect how extended or compact a protein is based on the availability of protonation sites or the solvent accessible surface area (SASA) [20].

Native nESI-MS for the acetylated WT α S (WT α SNTA) in Figure 3.8 a-b showed a slight shift to populate higher charge states (+17 to +8) for WT α SNTA which may reflect more extended protein conformations shown in Figure 3.8. However, this shift is minimal and the same charge series (+5 to +17) can be observed for acetylated vs non-acetylated WT α S. Similarly, in the case of $\Delta\Delta\alpha$ SNTA (Figure 3.8 c-d) a slight population shift towards the more extended, higher charged species is also observed. This shift is minimal as there is no loss or gain of major charge states, meaning that the overall population of compact and extended states is comparable.

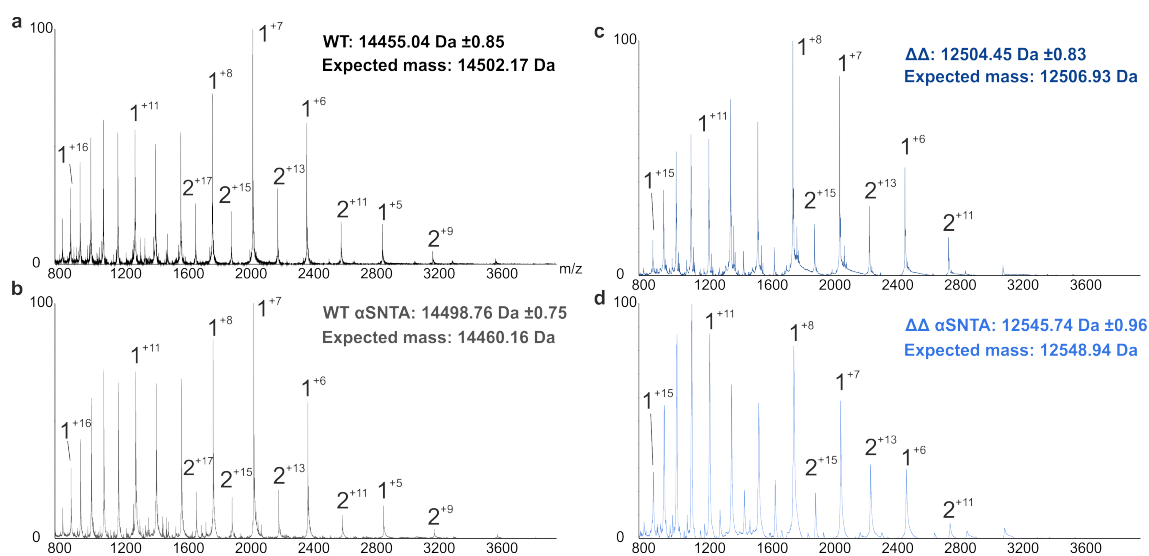


Figure. 3.8 Native nESI-MS comparing N-terminal acetylation of WT and $\Delta\Delta$ α S. (a) WT α S, (b) WT α SNTA, (c) $\Delta\Delta$ α S and (d) $\Delta\Delta$ α SNTA. 1 = monomer, 2 = dimer with the charge state in superscript. Proteins were analysed at 20 μ M, in 20 mM ammonium acetate pH 7.5.

Dimer peaks are detected in both spectra with the same charge states present for both conditions. The charge state distributions in the spectra in Figure 3.8 are largely

indistinguishable. The native mass spectrum comparing Δ P1- and Δ P2- α S with and without acetylation also show no distinct differences, where +7 is the dominant charge state in all spectra, consistent with WT α S (Figure 3.9).

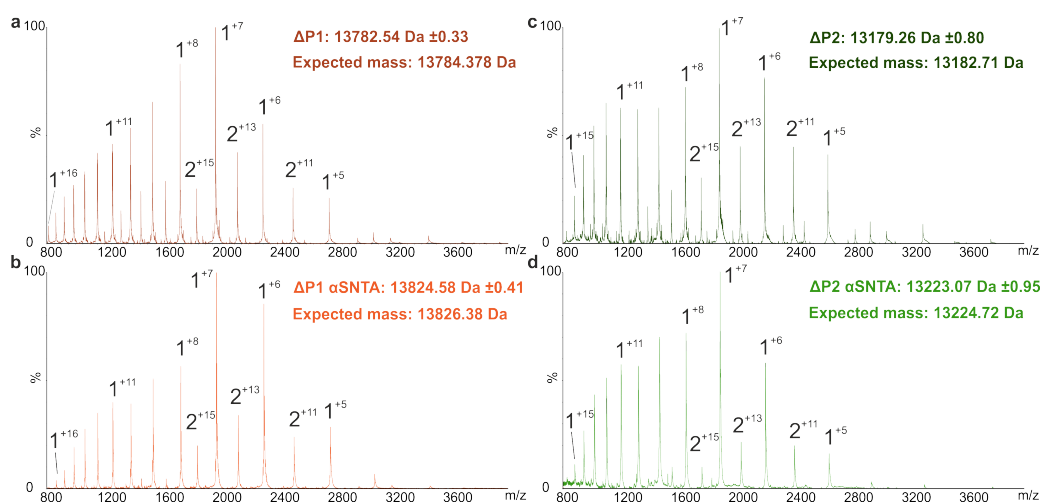


Figure 3.9 Native nESI-MS comparing N-terminal acetylation of Δ P1 and Δ P2 α S. (a) Δ P1 α S, (b) Δ P1 α SNTA, (c) Δ P2 α S and (d) Δ P2 α SNTA. 1 = monomer, 2 = dimer with the charge state in superscript. Proteins were analysed at 20 μ M, in 20 mM ammonium acetate pH 7.5.

The native mass spectrum for monomeric α S shows a multimodal distribution across high (+17 to +11) and low (+9 to +5) charge states, reflecting the presence of an ensemble of conformations that vary in SASA present in equilibrium. Additionally to this, lower charge state ions +5 to +7 were present in the spectra at a higher intensity than one would expect for an IDP [362, 363]. Hence, under the experimental conditions used to acquire the spectra in Figure 3.8 and Figure 3.9 α S variants populate at least three conformational states consisting of an extended conformation with charge states +17 to +12, and intermediate conformation with charge states +11 to +8 and a more compact conformation with charge states +7 to +5. This insight towards the heterogeneity of monomeric α S complements observations in the literature identifying a heterogeneous α S monomer ensemble [89, 345, 364].

3.3.4 Native nESI-IM-MS of α SNTA identifies the same conformational families

The conformational heterogeneity of α S is thought to be governed by the formation of various long-range intramolecular interactions [350, 358, 364, 257, 365–367]. This heterogeneity was identified in the native mass spectra in Figure 3.8 where it can be deduced that α S populates both compact and extended states in equilibrium. Using denatured protein calibrants: myoglobin, ubiquitin and cytochrome c, a logarithmic fit calibration curve was created per each nESI-IM-MS experiment (Figure 3.10 and Table 3.1).

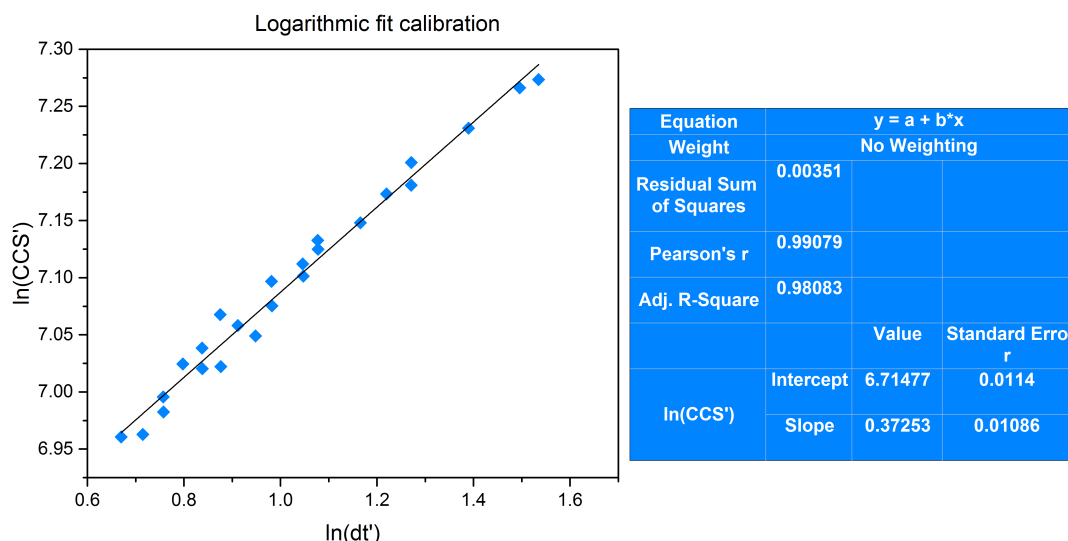


Figure. 3.10 Log-log calibration plot for nESI-IM-MS $^{TW}CCS_{N2}$ calculation. 10 μ M of ubiquitin (charge states +7 to +13), cytochrome c (charge states +13 to +20) and myoglobin (charge states +15 to +26) in 50% (v/v) acetonitrile, 0.1 % (v/v) formic acid were used for calibration. The R^2 value is shown in the table.

From this calibration, the $^{TW}CCS_{N2}$ for each charge state for WT α S was calculated and plotted in order to further understand the heterogeneity observed from the native charge state distribution, and to unpick whether the intrinsically disordered structure of α SNTA samples fewer specific conformations or a broad array of conformations.

Calibrant	MW (Da)	m/z	z	CCS in N ₂ (Å ²)
Ubiquitin	8560	1223	7	1910
Ubiquitin	8560	1070	8	1990
Ubiquitin	8560	951	9	2090
Ubiquitin	8560	856	10	2200
Ubiquitin	8560	778	11	2340
Ubiquitin	8560	713	12	2480
Ubiquitin	8560	659	13	2600
Cytochrome c	12359	951	13	3080
Cytochrome c	12359	883	14	3200
Cytochrome c	12359	824	15	3330
Cytochrome c	12359	773	16	3450
Cytochrome c	12359	727	17	3600
Cytochrome c	12359	687	18	3670
Cytochrome c	12359	651	19	3790
Myoglobin	16960	1131	15	4060
Myoglobin	16960	1060	16	4180
Myoglobin	16960	998	17	4310
Myoglobin	16960	942	18	4440
Myoglobin	16960	893	19	4570
Myoglobin	16960	848	20	4700
Myoglobin	16960	808	21	4820
Myoglobin	16960	771	22	4920
Myoglobin	16960	737	23	5010
Myoglobin	16960	707	24	5090

Table 3.1 Denatured calibrants in 50% (v/v) acetonitrile, 0.1 % (v/v) formic acid used for nESI-IM-MS CCS calculation. Calibrant ^{DT}CCS^{N2} values are found in the literature taken from the Bush database [53].

Native ion mobility mass spectra of WT α SNTA in Figure 3.11 were acquired at a protein concentration of 20 μ M in 20 mM ammonium acetate pH 7.5 and plotted as a ^{TW}CCS_{N2} “fingerprint” heat map. The X-axis represents the number of charges (z) plotted against ^{TW}CCS_{N2} values in Å² on the Y-axis with the relative peak intensity in the Z-axis

(heat map). WT α SNTA populates an extended species (charge states +8 to +17), and intermediate species (charge states +8 to +11) and a compact species (charge states +5 to +8).

The larger $^{TW}CCS_{N2}$ for the higher charge state series from around +12 to +18 may arise as a consequence of the nESI charging process whereby coulombic repulsion from the spatial concentration of protons on the molecule results in chain extension [368]. By contrast, isolating lower charge states reflects a more native-like representation of the protein structure [369]. With particular focus on the +8 ion, three to four conformations are visible represented in the dashed line in Figure 3.11.

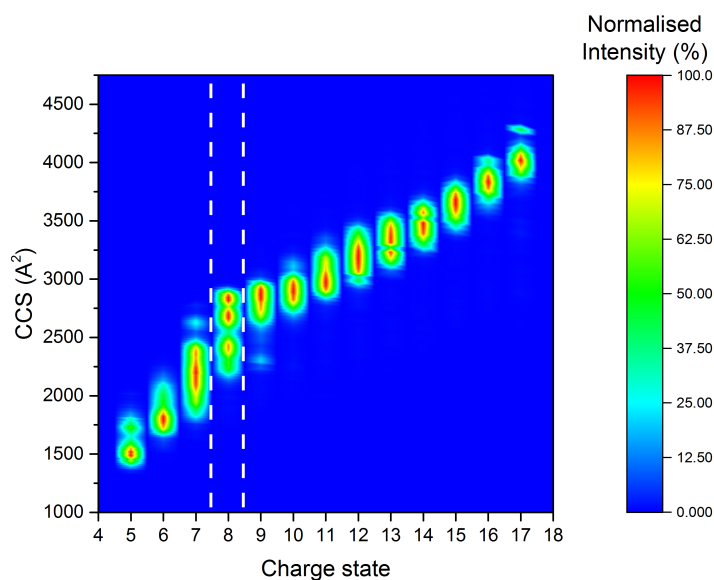


Figure. 3.11 Three dimensional nESI-IM-MS plot of WT α SNTA. Each charge state detected from the native spectra (+5 to +17) is plotted as $^{TW}CCS_{N2}$ calculated from the arrival time distribution (ATD) under individual charge state peaks. Dashed lines show the 8+ charge state. ATDs were extracted using MassLynx 4.1 (Waters, UK).

The degree of separation between $^{TW}CCS_{N2}$ intensities was achieved through rigorous optimisation of parameters on the Waters Synapt G1 instrument for optimal tuning conditions whilst preventing the activation of ions. For this optimisation, the +8 charge

state of WT α SNTA in 20 mM ammonium acetate pH 7.5 was taken as a model for tuning. The trap bias voltage, sampling cone voltage, trap pressure and IM cell pressure were systematically manipulated and the results are displayed in Figure 3.12 a-d. The trap bias voltage is responsible for accelerating ions from an area of relatively low pressure in the trap cell to a region of high pressure in the TWIMS cell by energising (pushing against the gas flow) ions upon injection into the TWIMS cell. If this transfer is too energetic then structural rearrangement and isomerisation may occur in the analyte [370]. The calculated $^{TW}CCS_{N_2}$ for WT α SNTA does indeed shift when modifying the trap bias voltage, at lower trap voltages (20 V) WT α SNTA is significantly compacted whereas high voltages (40 V) induce extension (Figure 3.12 a). Thus, a trap bias of 30 V was selected for nESI-IM-MS experiments in this thesis.

Once protein samples are ionised at atmospheric pressure in the ionisation source, the ion beam passes through the sampling cone into the vacuum system for ion extraction from the bulk plume. When the sample cone voltage is too high (~ 50 V), extension of the +8 charge state of WT α SNTA occurs. The sample cone was kept at 30 V for IM-MS acquisitions in this thesis to ensure more native-like conditions are achieved. The trap pressure which controls the gas flow into the trap cell and thus the collisions that occur with neutral buffer gas within the trap cell was maintained at 3.5 mbar (Figure 3.12 c). The IMS pressure which controls the gas flow into the IM cell showed that a high IMS pressure results in too frequent collisions with neutral buffer gas molecules resulting in longer drift times and analyte unfolding [371]. In this thesis, data acquired on a Synapt G1 used an IMS pressure of 3.0 mBar (Figure 3.12 d).

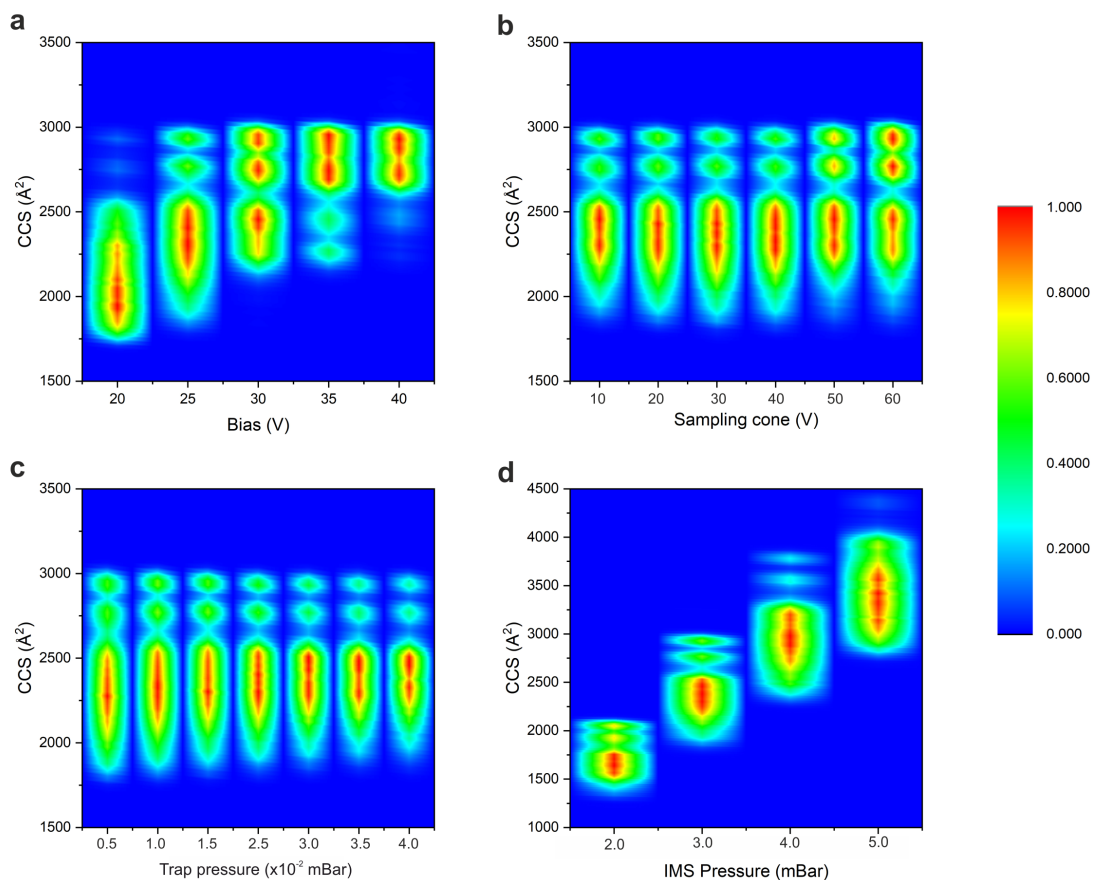


Figure. 3.12 Optimisation of Waters Synapt G1 tuning parameters on the 8+ charge state of α S. 20 μ M WT α SNTA was acquired in 20 mM ammonium acetate pH 7.5. (a) Trap bias, (b) sampling cone, (c) trap pressure and (d) IMS pressure were optimised. All $^{TW}CCS_{N2}$ values were extracted using the 8+ charge state. Optimal conditions chosen from these experiments were: trap bias 30 V, come voltage 18 V, trap pressure 3.5 mbar and IMS pressure 3.0 mBar.

nESI-IM-MS experiments were performed to determine whether NTA affected the monomeric conformational ensemble of WT, Δ P1, Δ P2 or $\Delta\Delta$ α SNTA versus non-acetylated variants (Figure 3.13 a-d). The results show that for all four variants, the distribution of conformations – peaks in the $^{TW}CCS_{N2}$ distribution – remain similar when each protein is acetylated. For WT α S, there is a slight shift towards populating the more

extended conformations which may be due to the addition of the slightly polar acetyl group with removal of the charged amino group. This small change in polarity may be significant enough for a small, IDP such as α S to disrupt long-range intramolecular interactions. However this difference is minimal, and the conformations that are present remain distinct.

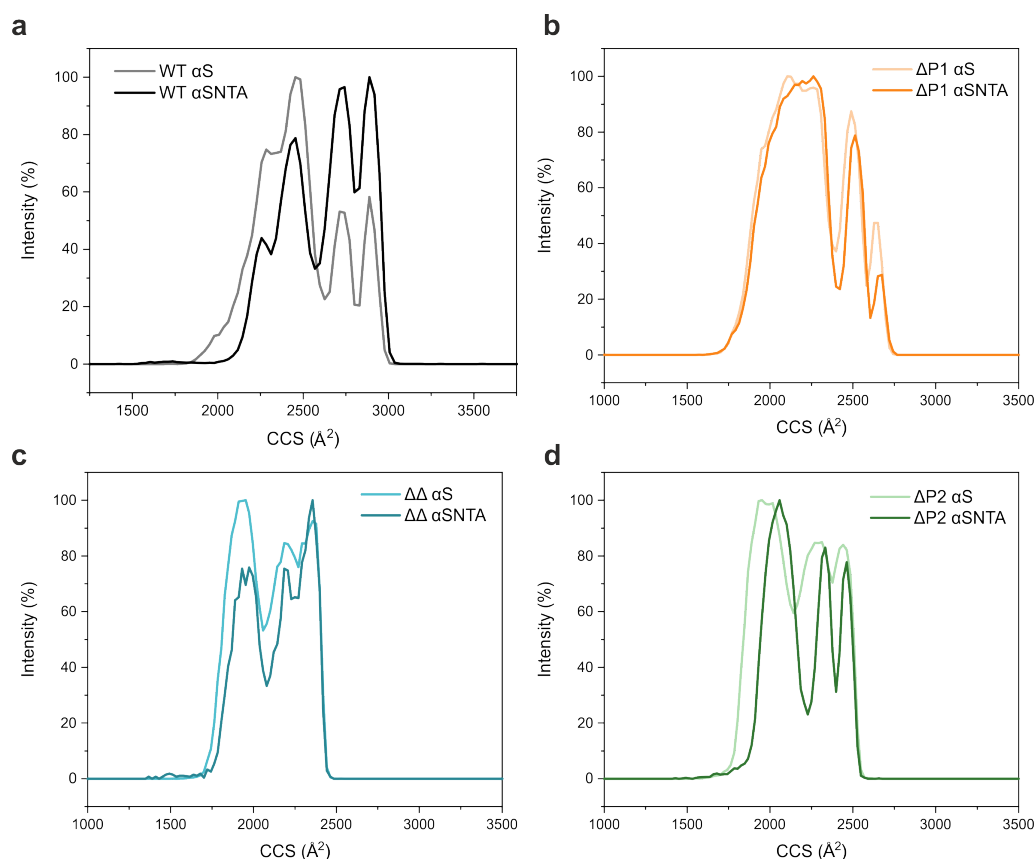


Figure 3.13 Native nESI-IM-MS spectra of acetylated α S. (a) WT α S and WT α SNTA 8+ charge state, (b) Δ P1 α S and Δ P1 α SNTA 7+ charge state, (c) Δ P2 α S and Δ P2 α SNTA 7+ charge state and (d) $\Delta\Delta$ α S and $\Delta\Delta$ α SNTA 7+ charge state. Spectra were acquired using a protein concentration of 20 μ M in 20 mM ammonium acetate, pH 7.5 on a Waters Synapt G1. $^{TW}CCS_{N2}$ values were calculated using ATDs extracted from MassLynx 4.1 (Waters, UK).

Globally, the protein structural space is not perturbed when acetylated at the N-terminus. The same distribution of conformations can be observed with slight variations in intensities

within experimental error of IM-MS experiments [372]. N-terminal acetylation has been shown to increase the helicity of residues 1-9 of α SNTA by NMR but this is not significant to change $^{\text{TW}}\text{CCS}_{\text{N2}}$ [373]. Moving forward in this thesis, all α S proteins including any deletion or truncation variants used are acetylated at the N-terminus unless stated.

3.4 The addition of metal ions affects amyloid kinetics and conformational dynamics

3.4.1 Metal ions on α SNTA increase the rate of amyloid assembly

Fibril growth assays were performed in order to characterise whether the addition of metal ions Ca^{2+} , Mn^{2+} or Zn^{2+} had an effect on the amyloid assembly kinetics of WT-, Δ P1-, Δ P2-, and $\Delta\Delta$ - α SNTA. The addition of Ca^{2+} , Mn^{2+} or Zn^{2+} at a molar excess of 1:25 (protein:ion) increased the rate of WT α SNTA amyloid assembly (Figure 3.14) consistent with previous literature [183, 358].

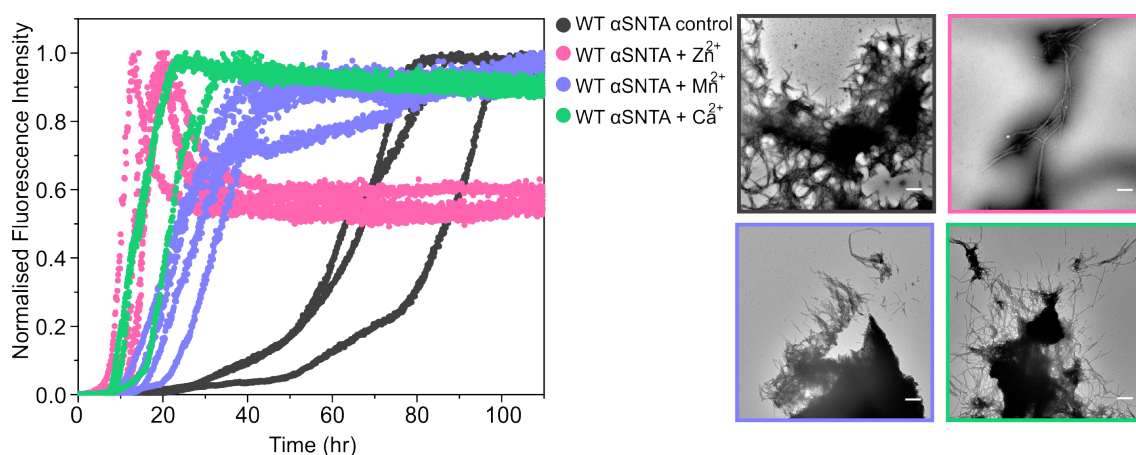


Figure. 3.14 WT α SNTA amyloid assembly is faster in the presence of metal ions. ThT fluorescence intensity of WT α SNTA (grey) unbound and in the presence of 1:25 Ca^{2+} (green), Mn^{2+} (purple) or Zn^{2+} (pink). ThT fluorescence was detected using 100 μM protein in 20 mM ammonium acetate pH 7.5, at 37°C, shaking at 600 rpm with one Teflon polyball (1/8" diameter; Polysciences Europe) per each well of sample. Three replicates for each sample are shown for ThT fluorescence kinetics, with negative stain EM images shown alongside with borders representing the sample colour. The scale bar corresponds to 300 nm in all images.

For WT α SNTA, a decrease in lag time is observed through t_{50} values which represent the time taken for each signal to reach half of the plateau value (Figure 3.16). Zn^{2+} showed the greatest effect on t_{50} . This observation could offer key understandings to the behaviour of α SNTA in its native environment within pre-synaptic nerve terminals in which all of the three tested divalent ions can be found at varied concentrations (nM to mM) during the transmission of neuronal impulses [372, 374].

Under identical conditions to WT α SNTA, in the absence of metal ions, ΔP1 α SNTA slowly begins to show signs of assembled fibrils with a ThT positive signal within 100 hours (Grey trace in Figure 3.15 a). Upon the addition of Ca^{2+} at a molar excess of 1:25, ΔP1 α SNTA strikingly enters an amyloid-competent state. Mn^{2+} and Zn^{2+} addition

accelerates fibril formation more rapidly than the same concentration of Ca^{2+} , similar to that of the WT α SNTA. All three ions also speed up the rate of amyloid assembly of Δ P2 α SNTA (Figure 3.15 b). In the case of $\Delta\Delta$ α SNTA, which does not assemble into ThT positive amyloid in the absence of metal ions, the addition of the tested metal ions here exert an effect similar to Δ P1 α SNTA with the greatest effect observed with $\text{Zn}^{2+} > \text{Mn}^{2+} > \text{Ca}^{2+}$ (Figure 3.15 c). The resistance exhibited by $\Delta\Delta$ α SNTA to assemble into amyloid fibrils is remarkable. The deletion of both P1 and P2 may exert a synergistic effect whereby intramolecular interactions that would ideally form within residues of these peptide sequences in WT α S are removed. The disruption of these suggested intramolecular interactions might impair the ability of $\Delta\Delta$ α SNTA to adopt a specific partially compact structure which is on pathway for amyloid formation, but this conformation could be induced in the presence of metal ions. Hence, whether this conformational effect occurs can be visualised by native nESI-IM-MS was next explained.

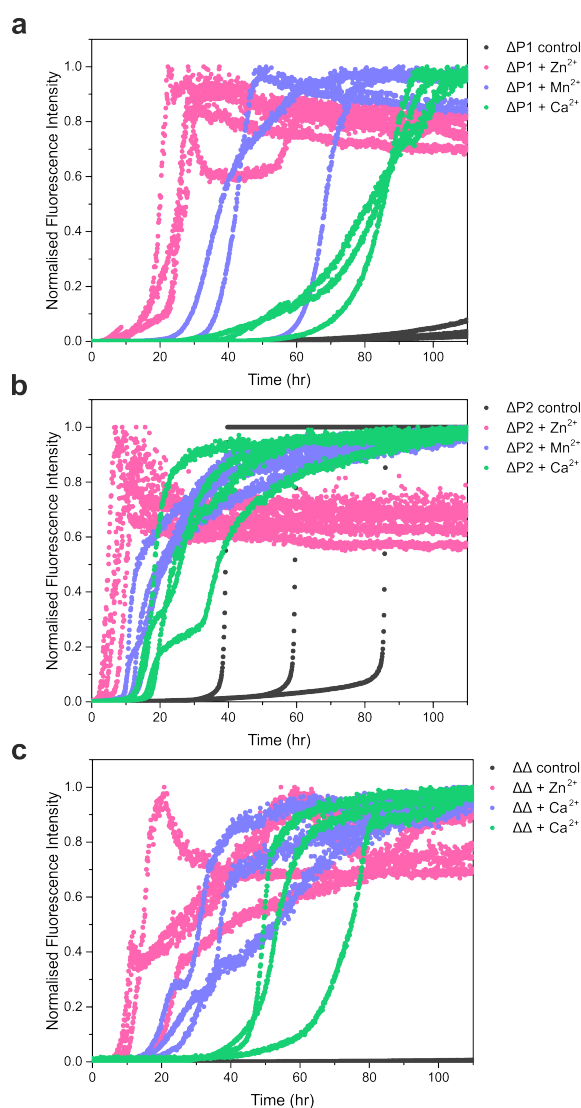


Figure. 3.15 Deletion variants of α SNTA form amyloid faster in the presence of metal ions. (a) ThT fluorescence intensity of Δ P1 α SNTA (grey) unbound and in the presence of 1:25 Ca²⁺ (green), Mn²⁺ (purple) or Zn²⁺ (pink). (b) as in (a) but for Δ P2 α SNTA, and (c) as in (a) but for $\Delta\Delta$ α SNTA. ThT fluorescence was detected using 100 μ M protein in 20 mM ammonium acetate pH 7.5, at 37°C, shaking at 600 rpm with one Teflon polyball (1/8" diameter; Polysciences Europe) per each well of sample. Three replicates for each sample are shown.

t_{50} values for all three variants of α S identify Zn^{2+} as the most effective ion at speeding up amyloid assembly in Figure 3.16. Each ion may exert specific effects through different binding capacities or resulting conformational changes.

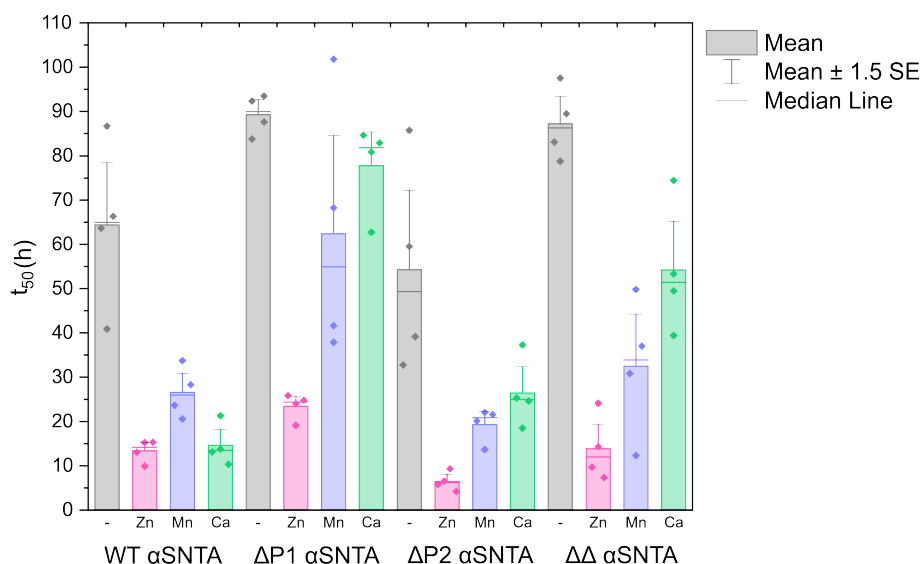


Figure. 3.16 Metal ions decrease the t_{50} values for all variants. t_{50} values identify the time taken for each ThT fluorescence signal to reach half of the plateau final value. t_{50} values were determined using AmyloFit 2.0 [182].

To confirm that the ThT signals represent the formation of fibrillar material, a pelleting assay was performed followed by densitometry (Figure 3.17). The percentage of aggregates at the end point of the ThT reaction for WT α SNTA and Δ P2 α SNTA show minimal variation in the presence or absence of metal ions, suggesting that due to monomer availability becoming the limiting factor, it is mostly the lag time which is impacted. A weak ThT signal is observed for Δ P1 α SNTA control in the absence of metal ions in the later stage of the ThT reaction (between 90-100 h), pelleting reveals that fibril material is unlikely responsible for this, and that perhaps oligomers with β -sheet content are present. However the percentage of pelleted material increases to almost near comparable values to WTNTA in the presence of metal ions for both Δ P1- and $\Delta\Delta$ - α SNTA in Figure 3.17. SDS-PAGE gel images used for densitometry are shown in appendix Figure A.1.

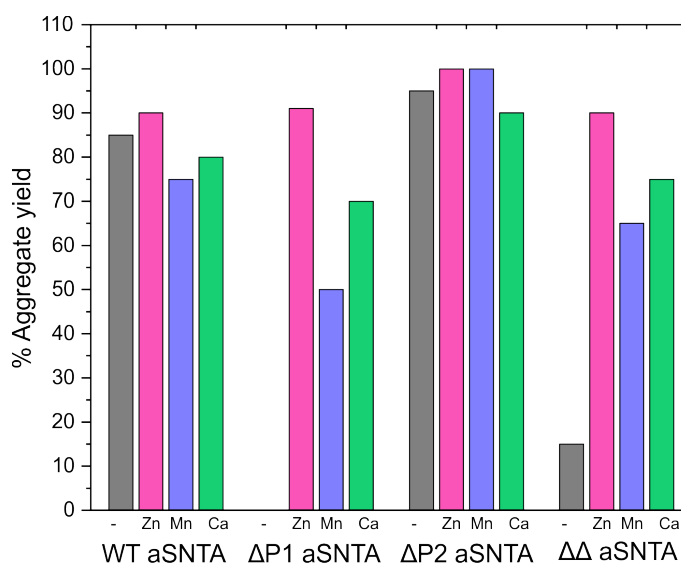


Figure 3.17 Aggregate yields determined through pelleting and densitometry. A sample was taken at the end point of the ThT containing a mixture of monomers and fibrils if present. A separate sample was taken for pelleting at 100,000 x g. Samples were boiled to depolymerise fibrils and analysed by SDS-PAGE. The percent aggregate yield was determined by densitometry of the resulting bands as described in Section 2.3.4

3.4.2 Multiple metal ion binding events revealed by nESI-MS

The ThT fluorescence traces in Figure 3.14 and Figure 3.16 provide evidence that Ca^{2+} , Mn^{2+} and Zn^{2+} all enhance the rate of amyloid assembly of WT-, ΔP1 - and ΔP2 - αSNTA . The literature shows that metal ions predominantly bind to negatively charged Glu and Asp residues in the C-terminal region of αS (Figure 3.3) [183, 358, 321]. Since the C-terminal region remains untouched in the deletion variants used in this thesis thus far, binding to that region of the protein theoretically should still occur.

Native nESI-MS is a powerful tool for determining binding stoichiometry at low concentrations and ratios of protein:ligand. Firstly, binding of Ca^{2+} , Mn^{2+} and Zn^{2+} was characterised for WT αSNTA in Figure 3.18. For WT αSNTA all three metal ions bind

with a range of stoichiometries between six and seven ions binding per α SNTA monomer for all detected charge states. Metal ions are also observed to bind to dimers (Figure A.2). Upon the addition of Zn^{2+} , there is almost a complete loss of the unbound peak as shown in the insets for charge states 1^{2+} and $8+$ (Figure 3.18). This effect is less prevalent when Mn^{2+} is added and even less so in the presence of Ca^{2+} where one less ligand (six) binds to WT α SNTA. Zn^{2+} appears to be the strongest binder and also exerts the greatest reduction in t_{50} (Figure 3.16).

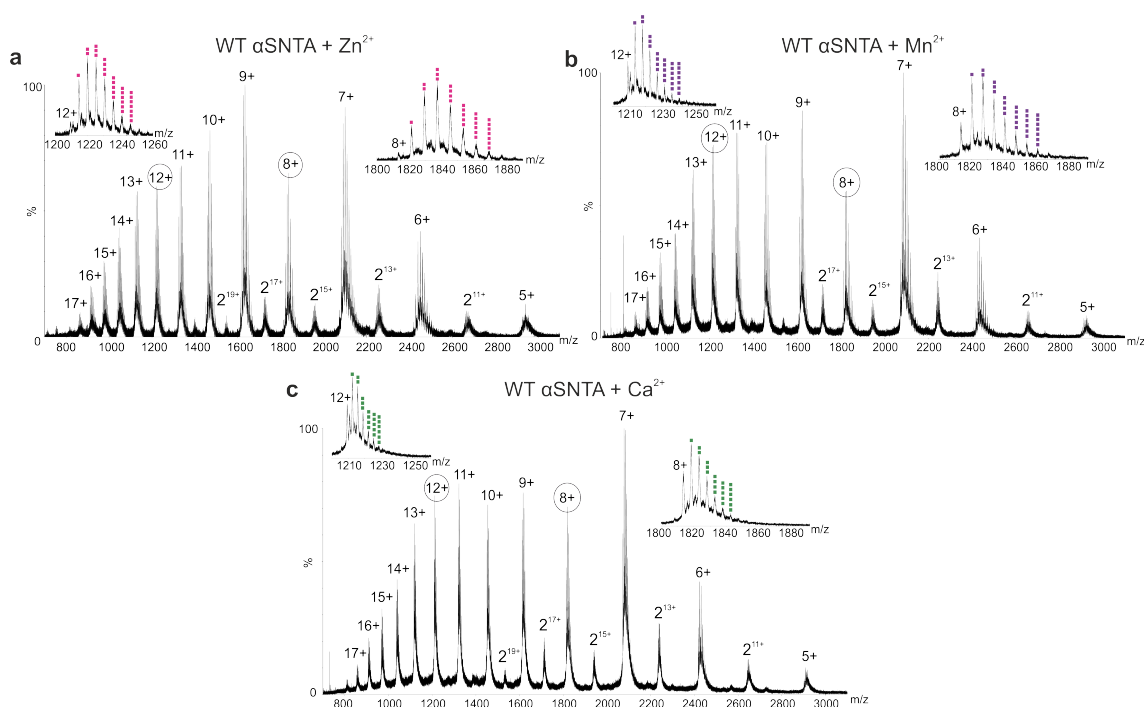


Figure 3.18 Native nESI-MS identifies binding of metal ions to WT α SNTA. The whole spectrum and insets for the +8 and +12 charge states of WT α SNTA (a) Zn^{2+} bound (pink squares), (b) Mn^{2+} bound (purple squares) and (c) Ca^{2+} bound (green squares). The protein concentration was 20 μ M in 20 mM ammonium acetate pH 7.5 and the concentration of metal ion added was 500 μ M to give a molar ratio of 1:25. Spectra were acquired using a Synapt G1 instrument (Waters, UK).

Binding of metal ions to Δ P1 α SNTA also occurs to all charge states with a range of five – seven ions bound per α S monomer. Similarly to WT α SNTA, Zn^{2+} binding results in

the greatest intensity reduction of the unbound ions for charge states 12+ and 7+ (Figure 3.19).

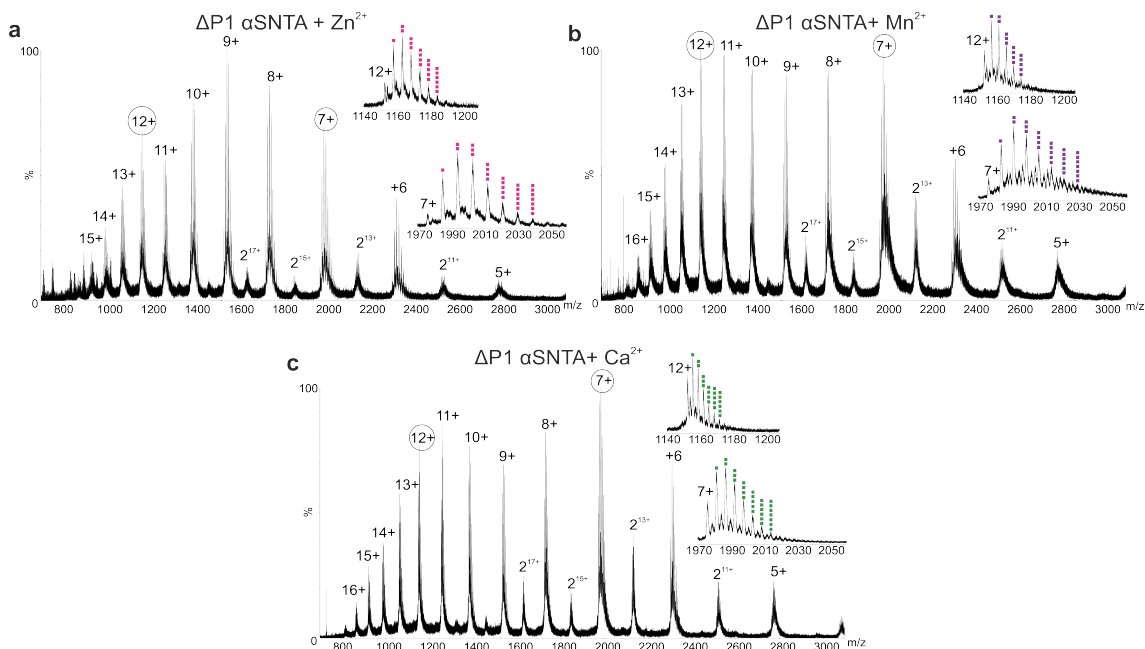


Figure 3.19 Native nESI-MS identifies binding of metal ions to $\Delta P1$ $\alpha SNTA$. The whole spectrum and insets for the +7 and +12 charge states of $\Delta P1$ $\alpha SNTA$ (a) Zn^{2+} bound (pink squares), (b) Mn^{2+} bound (purple squares) and (c) Ca^{2+} bound (green squares). The protein concentration was 20 μM in 20 mM ammonium acetate pH 7.5 and the concentration of metal ion added was 500 μM to give a molar ratio of 1:25. Spectra were acquired using a Synapt G1 instrument (Waters, UK).

Native nESI-MS was repeated for $\Delta P2$ $\alpha SNTA$ and $\Delta\Delta$ $\alpha SNTA$ αS and showed identical binding patterns of binding to WT $\alpha SNTA$ and $\Delta P2$ $\alpha SNTA$ at the 25-fold molar excess of ions used here. $\Delta P2$ $\alpha SNTA$ binds up to five ligands (Figure 3.20). $\Delta\Delta$ $\alpha SNTA$ binds six – seven ions (Figure 3.21).

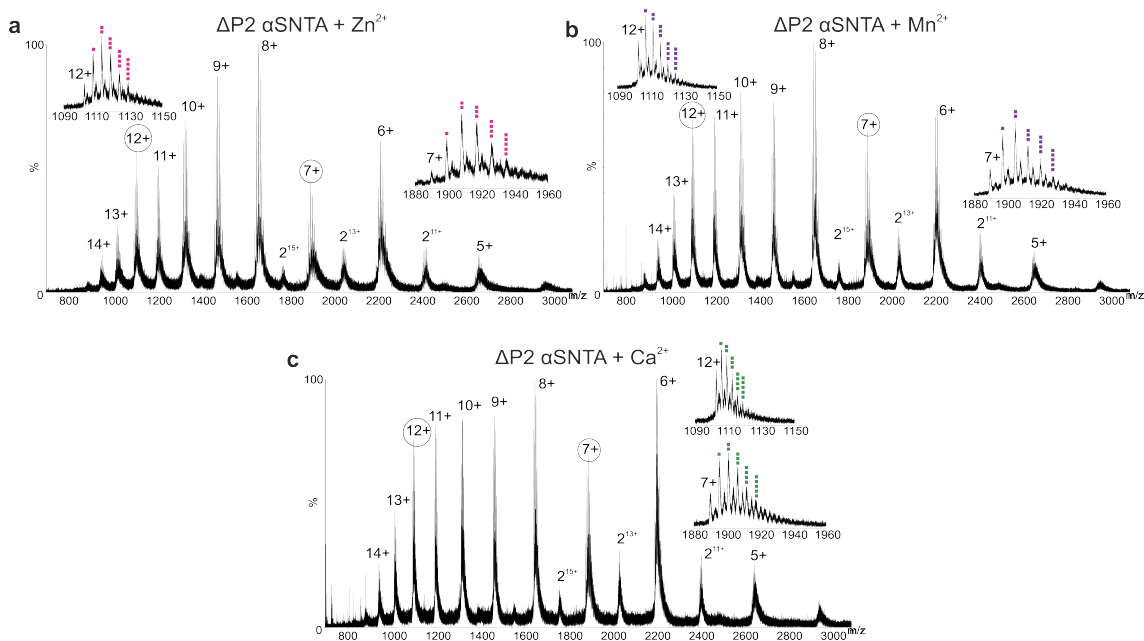


Figure. 3.20 Native nESI-MS identifies binding of metal ions to Δ P2 α SNTA. The whole spectrum and insets for the +7 and +12 charge states of Δ P2 α SNTA (a) Zn^{2+} bound (pink squares), (b) Mn^{2+} bound (purple squares) and (c) Ca^{2+} bound (green squares). The protein concentration was 20 μ M in 20 mM ammonium acetate pH 7.5 and the concentration of metal ion added was 500 μ M to give a molar ratio of 1:25. Spectra were acquired using a Synapt G1 instrument (Waters, UK).

All variants of α SNTA show a similar affinity for all three metal ions as defined by the number of metal ions bound, inferring that the molar excess of ions here saturates binding in all cases. This narrows down the effect of t_{50} of amyloid formation to the resultant conformational effects for binding of the different metal ions to each variant of α SNTA. Next nESI-IM-MS was used to identify any perturbations in $^{TW}CCS_{N_2}$ caused by metal ion binding to the different variants.

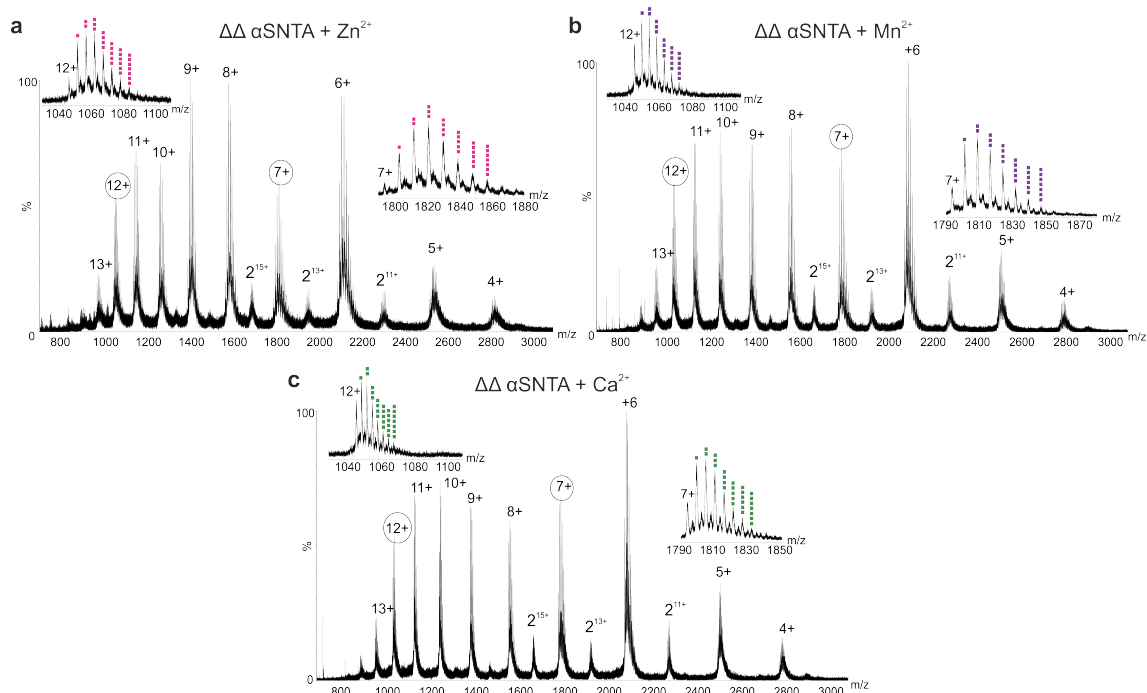


Figure 3.21 Native nESI-MS identifies binding of metal ions to $\Delta\Delta$ α SNTA. The whole spectrum and insets for the +7 and +12 charge states of $\Delta\Delta$ α SNTA (a) Zn^{2+} bound (pink squares), (b) Mn^{2+} bound (purple squares) and (c) Ca^{2+} bound (green squares). In all cases, the protein concentration was 20 μM in 20 mM ammonium acetate pH 7.5 and the concentration of metal ion added was 500 μM to give a molar ratio of 1:25. Spectra were acquired using a Synapt G1 instrument (Waters, UK).

3.4.3 Metal ion binding causes compaction of α SNTA by Native nESI-IM-MS

Ion mobility MS can detect subtle changes in compaction or extension which may not already be visible from the nESI charge state distribution as discussed in Section 1.5.1. Here, the effect on $^{\text{TW}}\text{CCS}_{\text{N}_2}$ when different metal ions; Ca^{2+} , Mn^{2+} or Zn^{2+} bound to the 8+ charge state of WT α SNTA or the +7 charge state of $\Delta\text{P1-}$, $\Delta\text{P2-}$ and $\Delta\Delta$ α SNTA (as this is the most populated charge state for each variant). Each metal ion bound peak, the unbound peak from an external control that can be detected in the native MS spectra

contains a drift time profile used for $^{TW}CCS_{N2}$ determination. In Figure 3.22, the calculated $^{TW}CCS_{N2}$ values for each variant bound to either four Ca^{2+} , Mn^{2+} or Zn^{2+} ions are shown. Ions were added at a molar ratio of 1:25. The peak for monomer bound to four ions was selected as all proteins bound four ions for each ion condition presenting spectral peaks with clear mass resolution from the baseline.

In Figure 3.22 a, when compared to the control unbound protein, Ca^{2+} , Mn^{2+} and Zn^{2+} binding all shift the population intensity towards more compact conformations for WT α SNTA with the greatest conformational shift observed in the presence of Zn^{2+} . Divalent ions are known to bind to negatively charged residues in the C-terminal region of α S (Figure 3.3), therefore the compaction effect observed could be a result of neutralisation of negative residues and the resultant collapse of the C-terminal region of the protein [183, 13]. Alternatively, compaction could be a result of metal ion coordination of multiple amino acid residues along the protein chain to one ligand. Such conformational rearrangements might expose the hydrophobic NAC region resulting in accelerated amyloid kinetics.

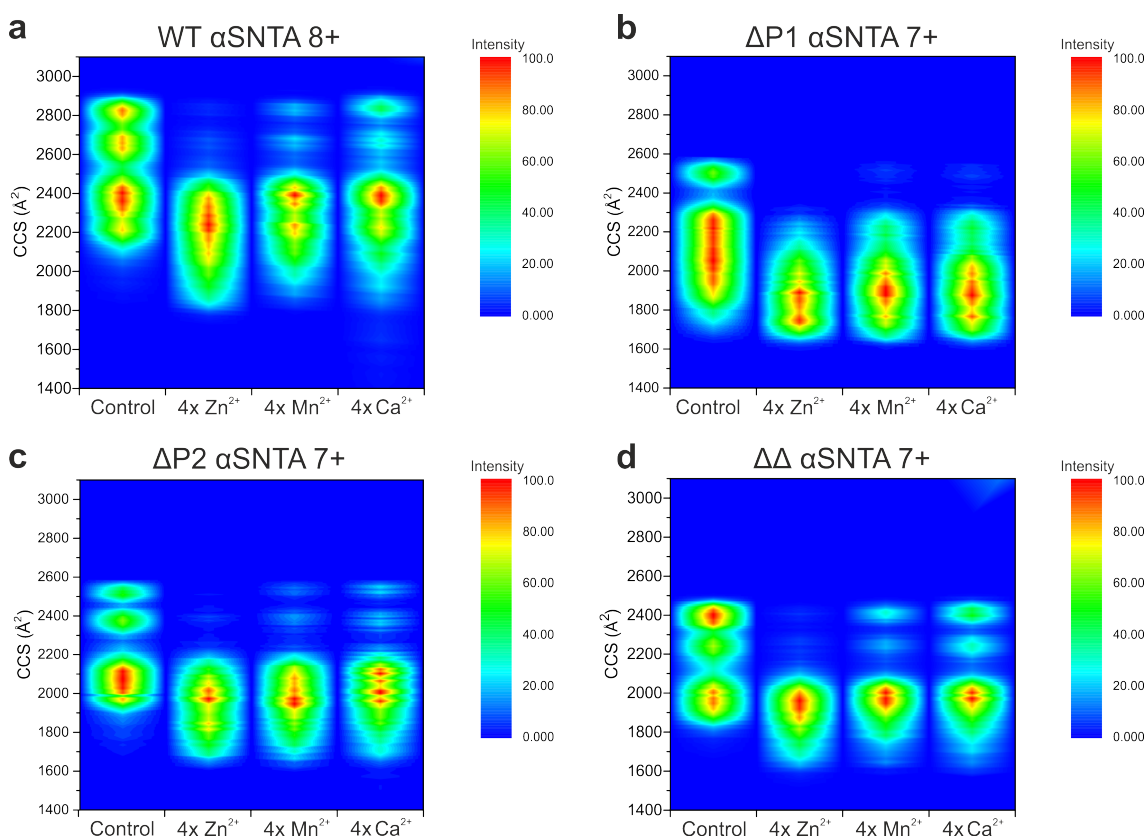


Figure 3.22 Native nESI-IM-MS spectra. $^{TW}CCS_{N2}$ plots of (a) WT α SNTA, (b) Δ P1 α SNTA, (c) Δ P2 α SNTA, and (d) $\Delta\Delta$ α SNTA each unbound and bound to four Ca^{2+} , Mn^{2+} or Zn^{2+} ions. Spectra were acquired using a protein concentration of 20 μ M in 20 mM ammonium acetate, pH 7.5. Spectra with ions present were acquired with the addition of 500 μ M ion acetate conjugate. All spectra were acquired on a Waters Synapt G1. $^{TW}CCS_{N2}$ values were calculated using ATDs extracted from MassLynx 4.1 (Waters, UK).

The effect of metal ion binding for both Δ P1 α SNTA and Δ P2 α SNTA are highly comparable, whereby all three of the tested metal ions result in compaction, with the greatest effect occurring in the presence of Zn^{2+} . All three metal ions also result in compaction of $\Delta\Delta$ α SNTA. In this case, the compaction effect due to Ca^{2+} and Mn^{2+} binding is less pronounced than that observed for the other two variants and WT α S, but the most compact ion occurred with Zn^{2+} , as observed for all variants showed here. The

122

compaction effect in the presence of Zn^{2+} is shown in Figure 3.23 for WT and $\Delta\Delta$ α SNTA bound to one to seven Zn^{2+} ions. Compaction occurred at one binding event highlighting how effective with Zn^{2+} is at structurally remodelling α S. For WT α SNTA, two stages of $^{TW}CCS_{N2}$ shifts are observed, one shift at 1-3 Zn^{2+} and a second shift around 5-7 Zn^{2+} ions bound. A similar effect is observed for $\Delta\Delta$ α SNTA.

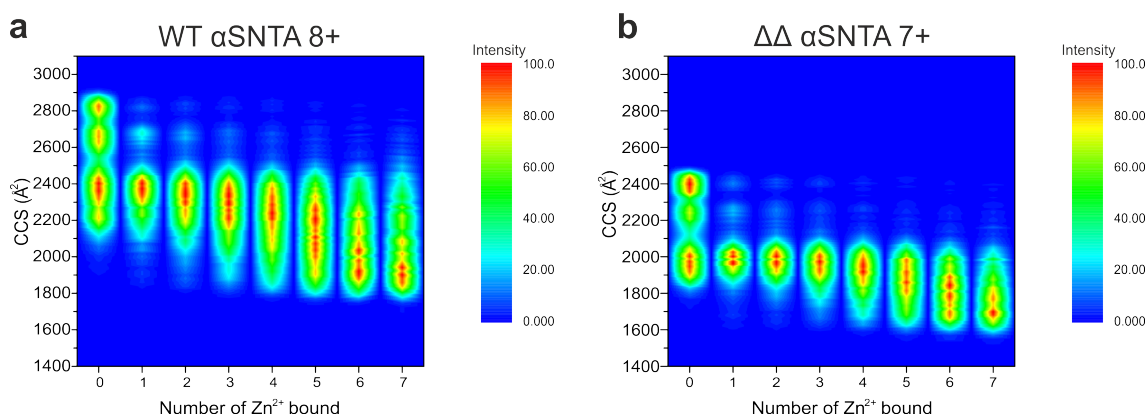


Figure. 3.23 Native nESI-IM mass spectra showing compaction of WT and $\Delta\Delta$ α SNTA when Zn^{2+} ions bind. (a) $^{TW}CCS_{N2}$ fingerprints of the 8+ charge state of WT α SNTA unbound and bound to one to seven Zn^{2+} . (b) $^{TW}CCS_{N2}$ fingerprints of the $\Delta\Delta$ α SNTA 7+ charge unbound and bound to one to seven Zn^{2+} . Spectra were acquired using a protein concentration of 20 μ M in 20 mM ammonium acetate, pH 7.5. A 25-fold molar excess of zinc acetate was added. $^{TW}CCS_{N2}$ values were calculated using ATDs extracted from MassLynx 4.1 (Waters, UK).

When studying conformational changes by IM-MS, it is important to consider all charge states from the broad, multi-modal distribution, as this reflects the entirety of the conformational ensemble [362, 357]. The native nESI mass spectra of WT and $\Delta\Delta$ α SNTA show Zn^{2+} binding to all charge states to a similar extent at the 25-fold molar excess used. Since Zn^{2+} exhibited the greatest accelerator effect on amyloid formation and greatest effect on the extent of compaction for both variants, Zn^{2+} was selected for analysis of $^{TW}CCS_{N2}$ effects. The $^{TW}CCS_{N2}$ fingerprint for each charge state is plotted in Figure

3.4 The addition of metal ions affects amyloid kinetics and conformational dynamics **123**

3.24 a-c for WT α SNTA and Figure 3.24 d-f for $\Delta\Delta$ α SNTA, each unbound, bound to one Zn^{2+} and bound to four Zn^{2+} . Structural remodelling of α S primarily occurs at low charge states (6+ to 9+ for WT α SNTA and 6+ to 8+ for $\Delta\Delta$ α SNTA) which represent compact conformations with smaller SASA. These compact conformations become more compact upon Zn^{2+} binding, whereas ions with higher charge states reflecting a larger SASA (more extended conformations) exhibit no such change in $^{\text{TW}}\text{CCS}_{\text{N2}}$ in response to binding of one or four Zn^{2+} ions. Zn^{2+} exhibits specific conformational effects on particular α S conformations, likely due to facilitated coordination of binding due to the close proximity of negatively charged residues in the C-terminal region, together with the presence of some negatively charged residues, and transition metal coordinating Met and His50 residues in the N-terminal region (Figure 3.3).

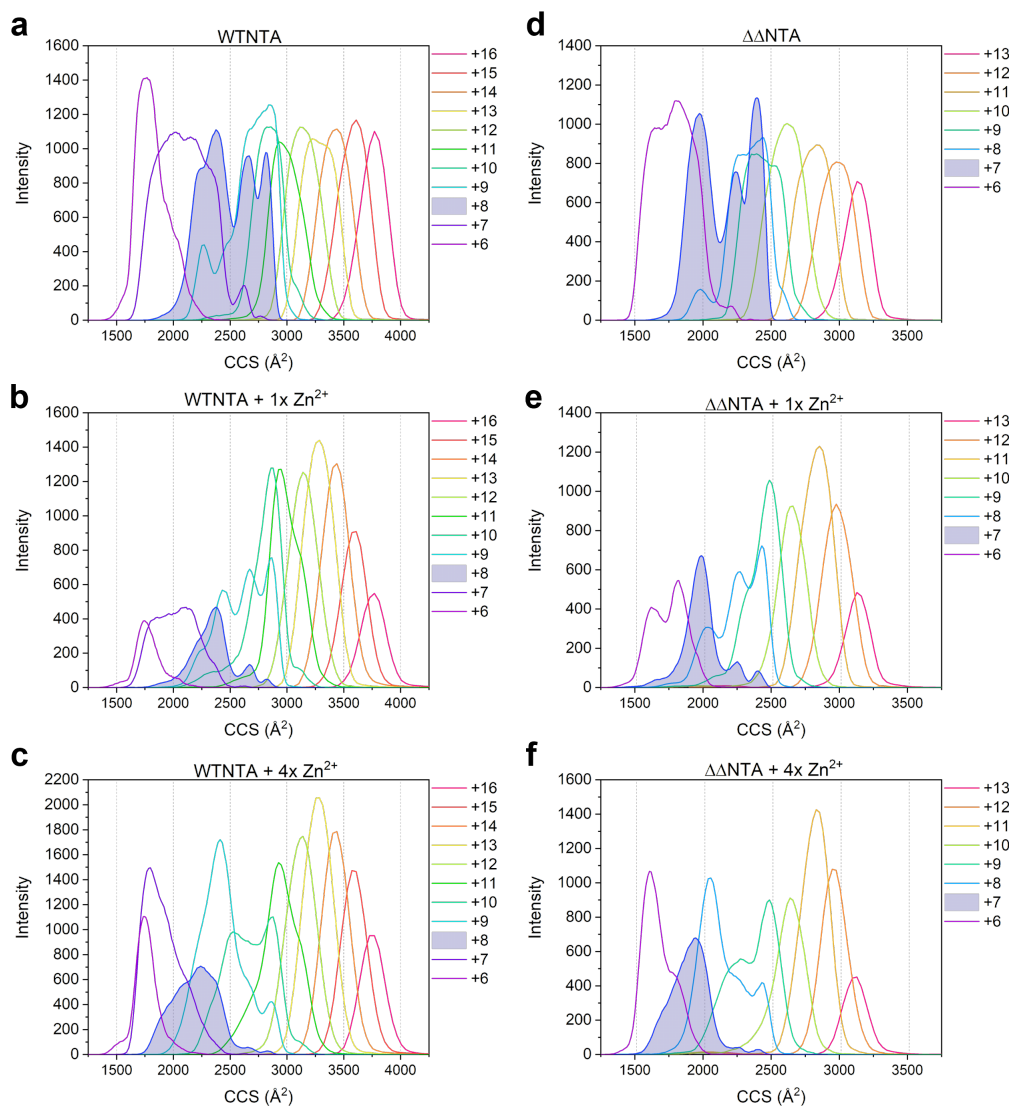


Figure 3.24 Zn^{2+} ions selectively modulate compaction of low charge states of α S. $^{TW}CCS_{N2}$ fingerprints of the entire charge state distribution (6+ to 16+) of (a) WTNTA α S alone, (b) bound to one Zn^{2+} and (c) bound to four Zn^{2+} ions. The 8+ charge state is highlighted by shading in each plot. Lower charge states of WTNTA α S become more compact when Zn^{2+} binds, with higher charge states being relatively unaffected by Zn^{2+} binding. $^{TW}CCS_{N2}$ fingerprints of the entire charge state distribution (6+ to 13+) of (d) $\Delta\Delta$ NTA α S alone, (e) bound to one Zn^{2+} and (f) bound to four Zn^{2+} ions. The 7+ charge state is highlighted in d-f where a similar effect can be observed to WTNTA α S. ATDs were extracted using and calibrated MassLynx 4.1 (Waters, UK).

3.4.4 Collision Induced Unfolding of α S probes the stability of the compact conformational family

To assess the relative gas phase stability of the conformations observed in nESI-IM-MS, collision induced unfolding (CIU) can be used [375]. CIU involves sequentially increasing the voltage supplied to the trap cell which precedes the IM cell. Protein ions collide more energetically with the neutral buffer gas molecules present in the trap cell, increasing the internal energy in the protein ions leading to unfolding [376–378, 375]. CIU data were acquired for WT α SNTA in the presence of Ca^{2+} , Mn^{2+} and Zn^{2+} and the CIU fingerprints for WT α SNTA unbound, and bound to one Ca^{2+} , one Mn^{2+} or one Zn^{2+} are shown in Figure 3.25 a-d. For each CIU plot, the +8 charge state was selected as this charge state represented the most conformational diversity of α S as discussed previously.

The WT α SNTA control, unbound CIU fingerprint is broad with poorly defined unfolding as the trap collision energy is increased. However, when one ion of Ca^{2+} , Mn^{2+} or Zn^{2+} bind, the conformations observed become much more resolved, and the transition to the most extended species becomes clearer. This effect is more pronounced for Mn^{2+} and Zn^{2+} , which is particularly interesting as the effect of speeding up amyloid assembly of WT α SNTA is much greater for Mn^{2+} and Zn^{2+} . There are clear transitions from compact conformations to populate only the most extended conformation at the highest voltage applied. Zn^{2+} requires the highest activation energy to achieve the most extended conformation, becoming more extended than in the control. The increase in resolution when WT α SNTA is bound to divalent ions could be due to increased rigidity of the protein chain from charge neutralisation of the C-terminal region. This could reduce the flexibility of the disordered C-terminal region. The stability of compact conformations is slightly increased in the presence of metal ions indicated by the higher trap collision energy (20 V) needed to disrupt the conformations of lower $^{\text{TW}}\text{CCS}_{\text{N}_2}$. A reduction, or 'dip' in $^{\text{TW}}\text{CCS}_{\text{N}_2}$ for

the most compact conformational family is observed which could represent initial further collapse due to collisional activation.

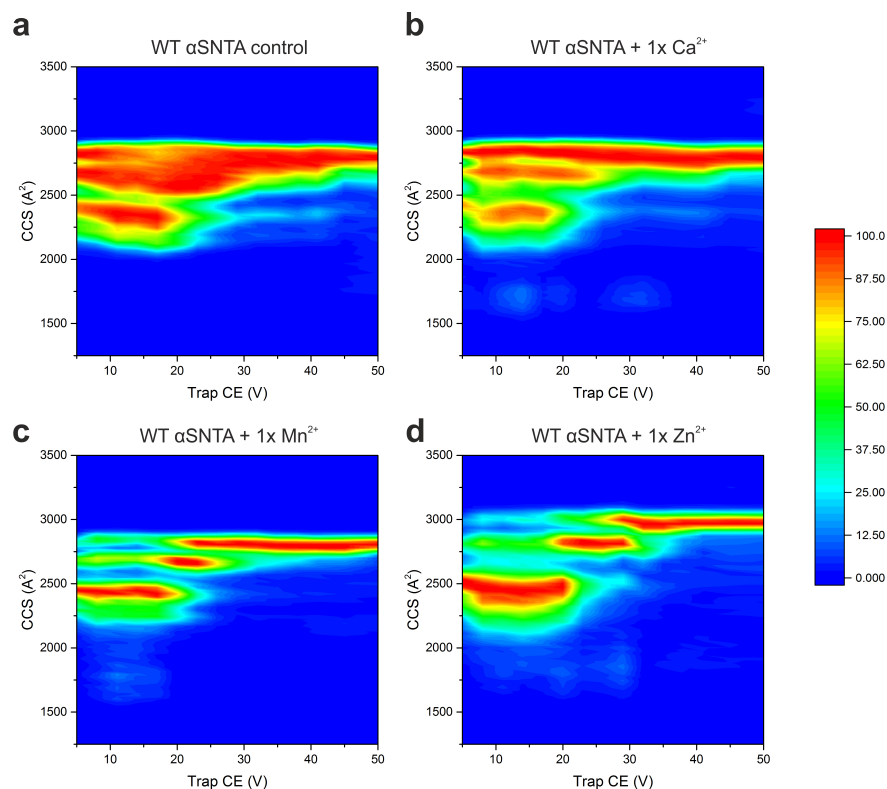


Figure. 3.25 Collision induced unfolding with metal ions. WT α SNTA (a) unbound (b) bound to one Ca^{2+} (c) bound to one Mn^{2+} (d) bound to one Zn^{2+} . The 8+ charge state is plotted for all conditions. ATDs were extracted using MassLynx 4.1 (Waters, UK).

Next, using CIU, the stability of compact conformations were assessed with 1-4 Zn^{2+} bound to WT α SNTA (Figure 3.26 a-d). The $^{\text{TW}}\text{CCS}_{\text{N}_2}$ of the most compact conformation is smaller as more Zn^{2+} bind to WT α SNTA. This conformation also exhibits increased stability, as when one Zn^{2+} is bound it is converted to populate only the most extended conformation at 22 V, whereas when four Zn^{2+} ligands are bound the energy needed increases to around 30 V.

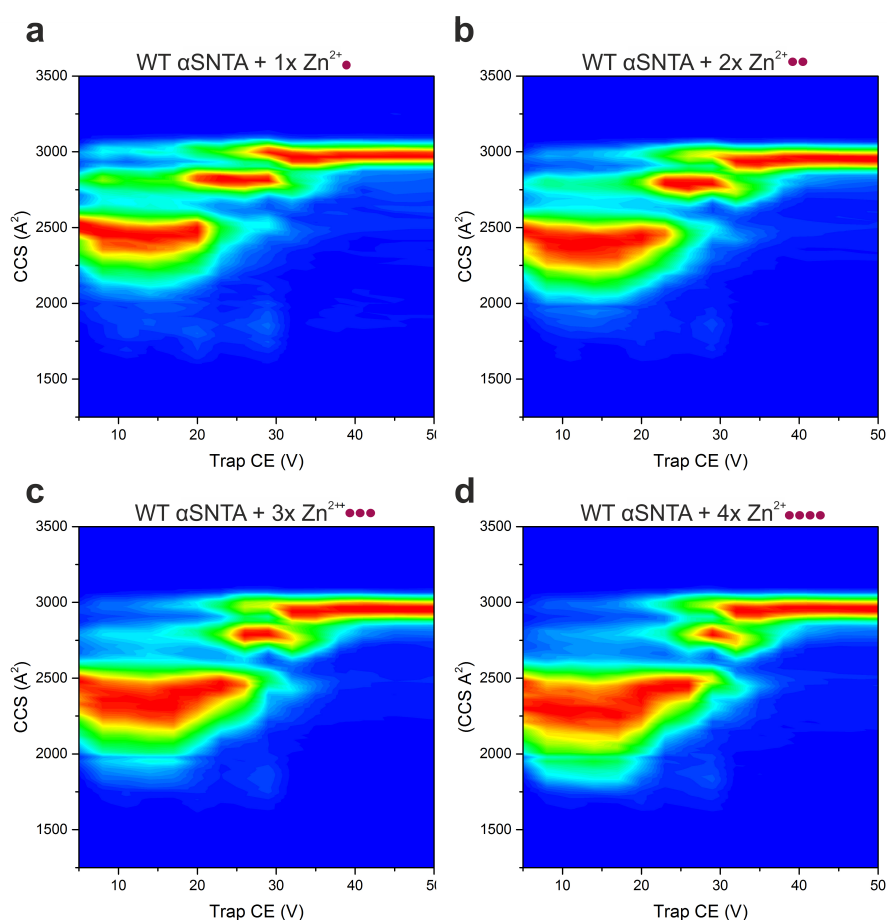


Figure. 3.26 Collision induced unfolding of WT α SNTA bound to Zn^{2+} . WT α SNTA (a) bound to one Zn^{2+} (b) bound to two Zn^{2+} (c) bound to three Zn^{2+} and (d) bound to four Zn^{2+} . The 8+ charge state is plotted for all conditions. ATDs were extracted using MassLynx 4.1 (Waters, UK).

The observed increased stability of the compact conformations may occur through ion coordination with bound Zn^{2+} ligands in which multiple Asp and Glu residues are involved in assembly of a ligand sphere coordinated by Zn^{2+} . This may require more energy to disrupt. An interesting observation is the life-time of the central $^{\text{TW}}\text{CCS}_{\text{N}2}$ conformation (2800 \AA^2). With one Zn^{2+} bound, this conformation is populated from the initial collision voltage. With four Zn^{2+} bound, this conformation is only marginally populated before conversion into the most extended conformation. This reinforces the increased stability of

the most compact conformation as more Zn^{2+} ions bind to the protein chain and that the transition through the intermediate conformation is reduced. Again, a dip in $^{\text{TW}}\text{CCS}_{\text{N}2}$ is observed for the most compact conformational family, which becomes more prevalent with more Zn^{2+} bound can be observed. This $^{\text{TW}}\text{CCS}_{\text{N}2}$ dip could reflect collisional activation which induces structural collapse.

3.4.5 Secondary structure of α SNTA by circular dichroism is not induced by metal ion binding

Conformational changes in $^{\text{TW}}\text{CCS}_{\text{N}2}$ have been established for N-terminally acetylated α S and the P1 and P1P2 deletion variants in the presence of metal ions, particularly Zn^{2+} , and it is clear that these changes occur when ions are bound evidenced by native nESI-MS and IM-MS. However it is unclear whether the observed compaction involves conformational rearrangements that involve changes in secondary structure. WT α SNTA monomer is an intrinsically disordered protein with no stable (long-lived), secondary structure, except for when bound to lipids and membranes, α -helical structure can be detected in the N-terminal region [320, 379]. Here, far-UV circular dichroism (CD) was performed on WT-, Δ P1- and $\Delta\Delta$ - α SNTA in the presence of Zn^{2+} at a ratio of 1:25 (Figure 3.27). The results show that there are no prominent differences in secondary structure in the case of all variants. Indeed, all spectra remain as random coil, suggesting that the compaction observed by native MS is not due to secondary structure formation.

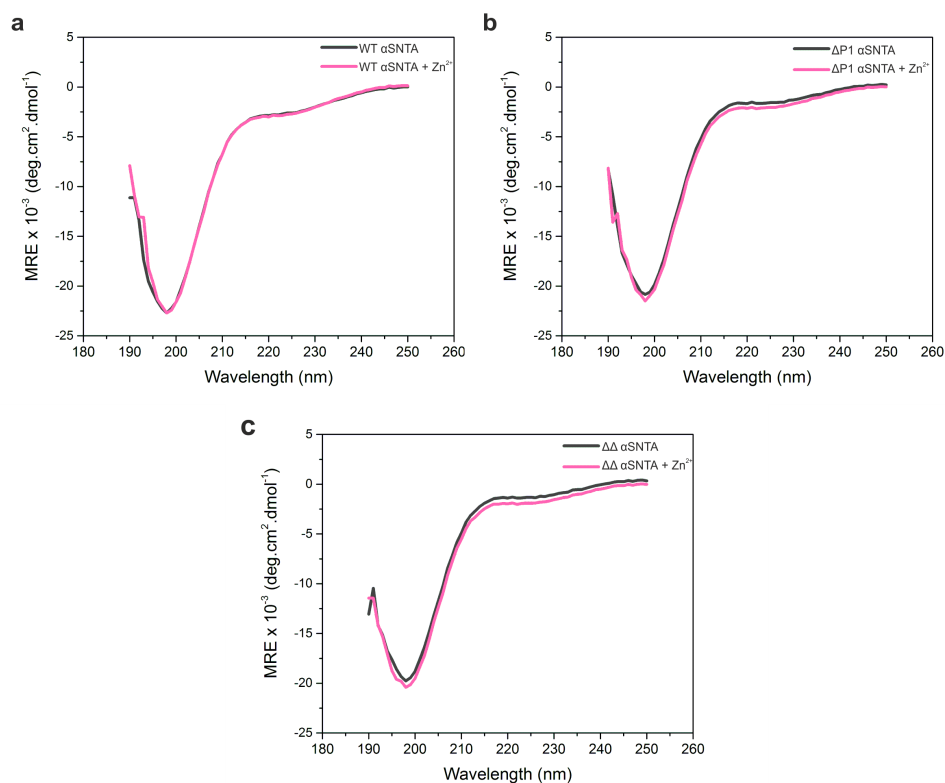


Figure 3.27 Zn^{2+} binding does not induce secondary structure by far UV circular dichroism. CD spectra for (a) WT α SNTA unbound (grey) and in the presence of Zn^{2+} (pink), (b) Δ P1 α SNTA unbound (grey) and in the presence of Zn^{2+} (pink), (c) $\Delta\Delta\Delta\Delta$ α SNTA unbound (grey) and in the presence of Zn^{2+} (pink). Zn^{2+} was added at a 25-fold molar excess. Proteins were analysed at 100 μM concentration in 20 mM ammonium acetate, pH 7.5.

3.5 P1 Peptide binding to α S

The role of the P1 region in amyloid formation was investigated using a synthetic peptide with the sequence of P1 including a four residue extension on both the N- and C-terminal ends which maintained the sequence of human α S from the SNCA gene and enhanced solubility (Ac-KTKE-GVLYVGS-KTKE-NH₂) [380]. The P1 peptide was added in trans to WT, Δ P1 and $\Delta\Delta$ α S to identify if adding this sequence affected amyloid kinetics, and

the results were kindly provided by Dr. Sabine Ulamec (University of Leeds) and published in [380]. When added at a 10-fold molar excess to WT α S, the P1 peptide increased the rate of amyloid assembly. At equimolar concentration, the P1 peptide resulted in ThT positive fibril assembly of Δ P1 α S at pH 7.5, which does not occur in the absence of peptide, and these fibril assembly kinetics were enhanced further at a 10-fold molar excess of peptide (Figure 3.28). The P1 peptide also resulted in ThT positive fibril assembly for $\Delta\Delta$ α S only at a 10-fold molar excess. Along with control ThT kinetics and negative stain transmission electron microscopy (TEM) images for the peptide alone which showed no self-assembly into fibrils, these results highlighted the role of the P1 sequence in enhancing ThT positive amyloid assembly when added in trans [380]. However at this stage, it was unknown how many peptide moieties could bind to α S, and how addition of the peptide stimulates amyloid formation. Hence native MS was used to study how the peptide binds interacts with the different α S variants (non-acetylated).

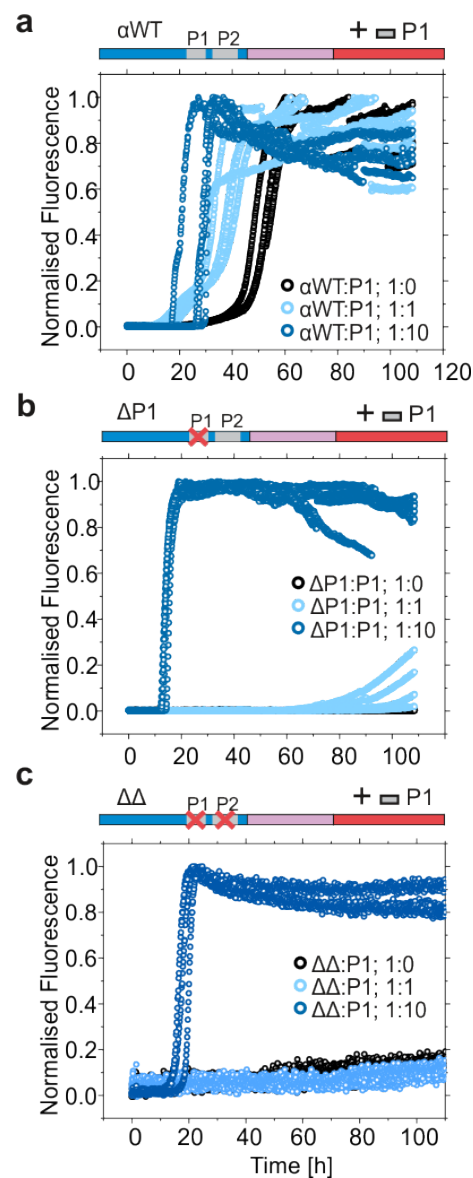


Figure. 3.28 Amyloid formation kinetics of WT, Δ P1 and $\Delta\Delta$ α S in the presence of the P1 peptide. Amyloid assembly kinetics of (a) WT (b) Δ P1 (c) $\Delta\Delta$ in presence of the P1 peptide added in trans. All experiments were carried out using 100 μ M α Syn and peptide concentrations of 0 μ M, 100 μ M or 1 mM, at pH 7.5, 200 mM NaCl, 37°C, 600 rpm. Teflon beads were not used for these experiments, and low-binding 96-well plates were used (Corning, USA). Note that under conditions of no or low amyloid formation, data points for different conditions overlay. Figure adapted from [380].

3.5.1 Native nESI-MS of the P1 peptide bound to α S and collision induced dissociation to map binding stability

Native nESI-MS was used in order to determine the stoichiometry of the P1 peptide binding to α S where the P1 peptide was added to protein at a molar ratio of 10:1 (peptide: α S). This technique has been widely applied to the study of amyloid precursors interacting with ligands [358, 381]. The nESI native mass spectra of WT α S unbound or in the presence of the P1 peptide (expected MW of the α S-P1 complex 16,151.08 Da) are shown in Figure 3.29a (iii, iv) and b (i-iv). In the presence of the P1 peptide, binding is observed to the protein monomer at a ratio of 1:1. Binding was not observed to dimers. Collision induced dissociation (CID) experiments showed that dissociation of the P1 peptide from WT α S occurred at a CID₅₀ value of 40 V (Figure 3.29 d).

The nESI native mass spectra of Δ P1 α S unbound or in the presence of the P1 peptide (expected MW of the Δ P1-P1 complex 15,475.29) are shown in Figure 3.29 a (i, ii) and b (i-iv). Binding at a ratio of 1:1 peptide to protein monomer was observed similarly to that of WT α S. However, the CID₅₀ increased to 44V. The binding of the P1 peptide was therefore stronger in the case of Δ P1, and this binding results in the acceleration of fibril assembly for Δ P1 to a greater extent. Binding of the P1 peptide could compete with long range intra- and/or inter-molecular interactions along the protein sequence between the N- and C-terminal regions of α S which might be involved in protection from nucleation and therefore amyloid assembly. Further work would be required to identify the specific binding region of the P1 peptide and whether different molecular mechanisms occurs when the peptide binds to WT versus Δ P1 α S.

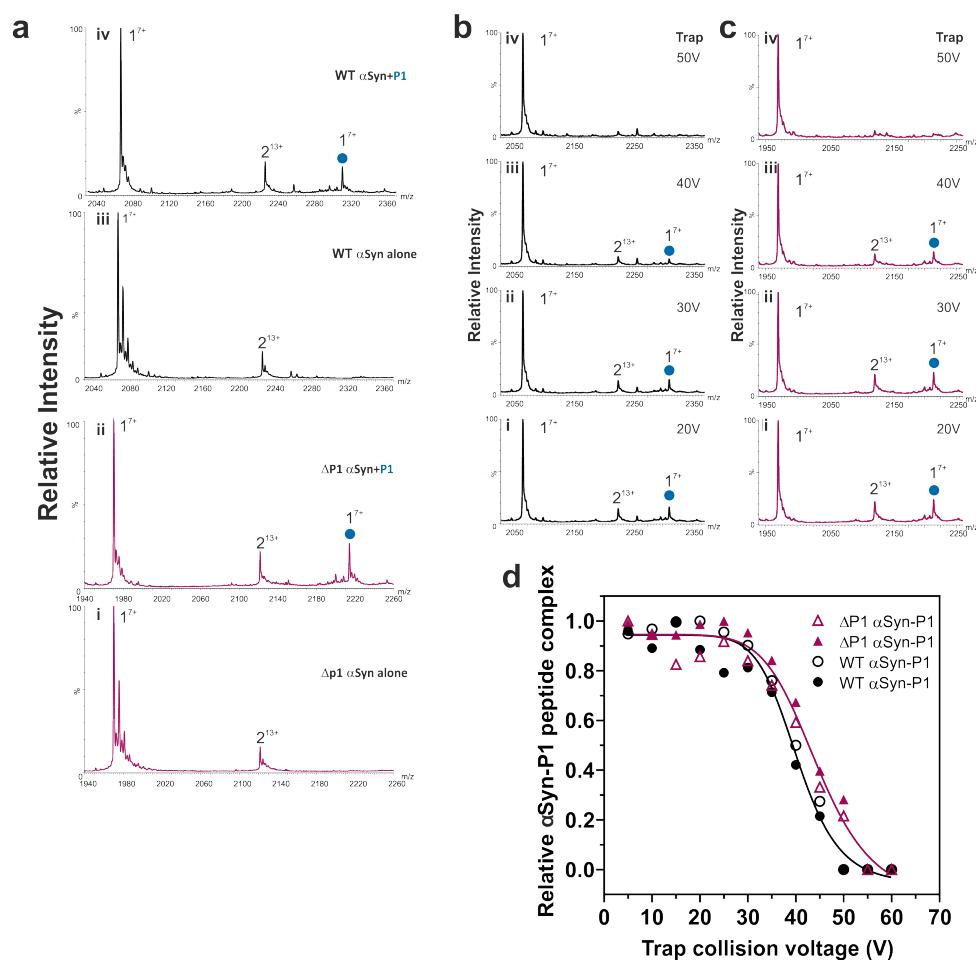


Figure. 3.29 The interaction between WT α S, Δ P1 and the P1 peptide characterised by native nESI-MS. (a) Positive-ion nESI mass spectra of (i) Δ P1 α S alone, theoretical mass 13784 Da; (ii) Δ P1 α S with added P1 peptide (theoretical mass 1708 Da) at a molar ratio of Δ P1 α S:P1 peptide of 1:10; (iii) WT α S alone, theoretical mass 14460 Da; (iv) WT α S with added P1 peptide at a molar ratio of Δ P1 α S:P1 peptide of 1:10. 1:1 peptide:protein binding is denoted with a blue circle. (b) nESI mass spectra obtained of the WT α S-peptide P1 complex at different trap cell voltages; (i) 20 V; (ii) 30 V; (iii) 40 V; (iv) 50 V performed through collision induced dissociation (CID). (c) as (b), but for the Δ P1 α S-peptide P1 complex. (d) CID of WT α S-peptide P1 complex and Δ P1 α S-peptide P1 complex with the intensity of the complex relative to the sum of the bound and unbound intensities plotted versus the trap cell voltage. The experiment was performed in duplicate (indicated in the inset legend) and the data fitted to a sigmoid function (solid line).

3.6 C-terminal truncation of α S: residues 1-119

Within Lewy bodies, around 15% of total α S is estimated to be truncated within the C-terminal region, resulting in various naturally occurring different length variants of α S which can act as seeds for aggregation of full-length α S [382, 279, 298, 297, 382, 383]. C-terminally truncated variants include truncations at residues 103, 110, 113, 114, 115, 119, 122, 124, 125, 133, and 135 [382, 384, 383, 385]. From *in vivo* studies of Lewy bodies, truncations at residues 119 and 122 are most prevalent [300] and when truncated at residue 119, amyloid assembly occurs around nine times faster than for full-length α S. The exact molecular mechanisms governing α S amyloid assembly *in vivo* are unknown, but it is clear that C-terminal truncation could have a pivotal pathological role, indicating that impaired degradation of α S through proteasomal or lysosomal control might contribute to this [386–389]. It has also been indicated that the metabolism of α S by the proteolytic enzyme calpain is also involved in α S cellular turnover by cleavage, demonstrated both *in vitro* and *in situ* generating C-terminal truncations at residues 114 and 122 [385, 390, 391].

Truncation at residue 119 (119 α S) removes half of the C-terminal segment of α S, this could have a significant effect on the binding of metal ions presumed to bind primarily to negatively charged residues concentrated in the C-terminal region (Figure 3.3). Primary metal ion binding has been localised to residues Asp121, Asn122 and Glu123 through NMR resonances, with Asp121 as a key anchoring residue [183]. The significance of this region drove the final section of this chapter to narrow down the localisation of metal ion binding and investigate the role of the C-terminal truncated variant 119 of α S in metal ion binding and amyloid formation. 119 α SNTA was expressed in *E. coli* with an N-terminal acetyl group as discussed in Methods Section 2.2.2. The mass spectrum under denaturing conditions is shown in Figure 3.30.

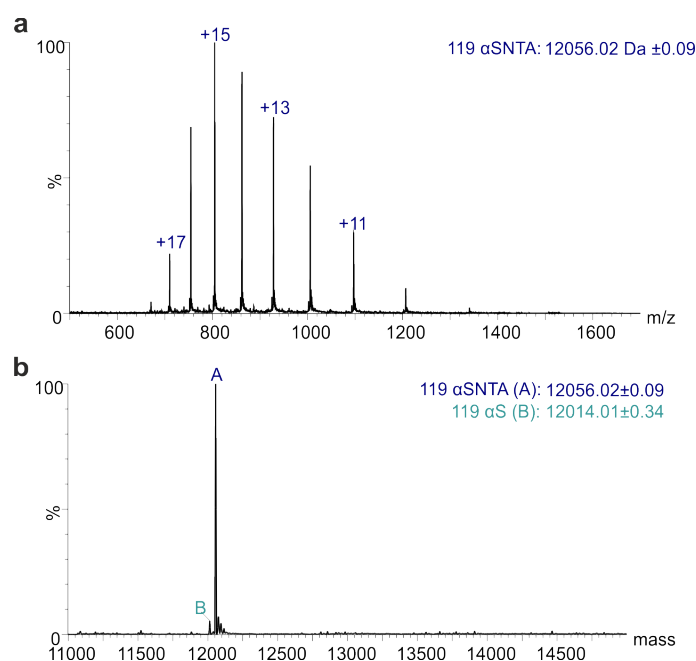


Figure 3.30 LC-MS of purified 119 α SNTA. (a) Mass spectrum of denatured 119 α SNTA which is deconvolved in (b). The expected mass of acetylated 119 α S is 12,014.69 Da and 12,056.69 Da for non-acetylated. A = 119 α SNTA and B = 119 α S. Protein was measured at a concentration of 1 μ M in 0.1% (v/v) trifluoroacetic acid on a Xevo G2-XS QToF instrument (Waters, UK).

3.6.1 1-119 α SNTA rate of amyloid assembly increases with metal ions

The C-terminal region of full length α S has been suggested to exert a protective effect against aggregation due to the large number of negative charges which could form long-range interactions with the N-terminal region that shield the hydrophobic NAC region from nucleation events [392, 279, 298, 297, 382, 383]. Truncation of the C-terminal sequence has been shown in several studies to increase the rate of α S amyloid assembly, which was recapitulated here (Figure 3.31) [297, 393, 298]. Whether divalent metal ions could exert a similar effect on 119 α SNTA on amyloid formation, despite eight divalent metal ion binding sites being truncated, was explored (Figure 3.31).

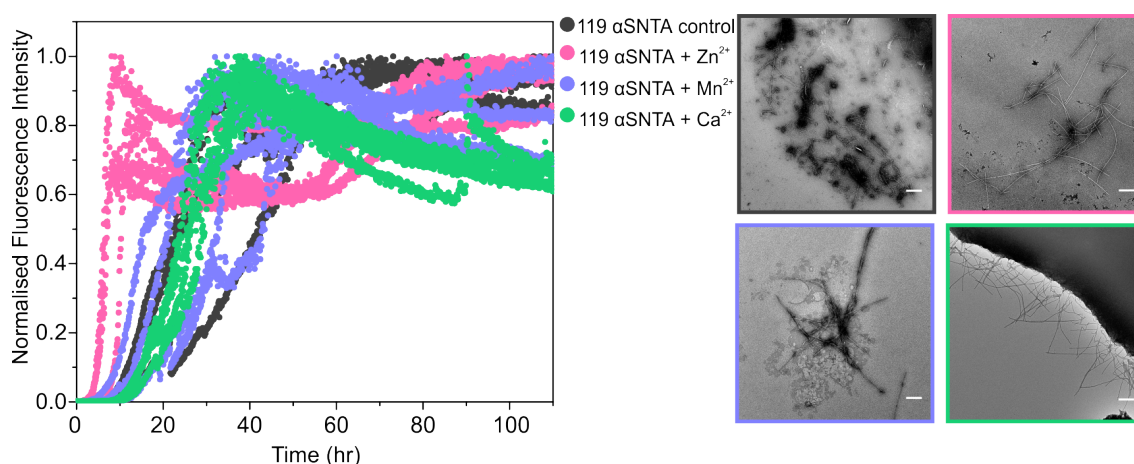


Figure. 3.31 Metal ion binding modulates the rate of 119 α SNTA amyloid assembly. Amyloid assembly of 119 α SNTA (black) alone or in the presence of Zn^{2+} (pink), Mn^{2+} (purple) or Ca^{2+} (green). ThT fluorescence was detected using 100 μM protein in 20 mM ammonium acetate pH 7.5, at 37°C, shaking at 600 rpm with one Teflon polyball (1/8" diameter; Polysciences Europe) per each well of sample. Three replicates for each sample are shown for ThT fluorescence kinetics, with negative stain EM images shown alongside with borders representing the sample colour. The scale bar corresponds to 300 nm in all images.

The effect of adding Zn^{2+} , Mn^{2+} or Ca^{2+} to 119 α SNTA on amyloid formation is shown in Figure 3.31 and 3.32. While Ca^{2+} results in comparable kinetics to the rate of amyloid assembly in the absence of metal ions, both Mn^{2+} and Zn^{2+} induce faster kinetics, despite the fact that the truncated variant forms amyloid already five-fold more rapidly than WT α SNTA and lacks two aspartic acid and six glutamic acid residues of the WT sequence.

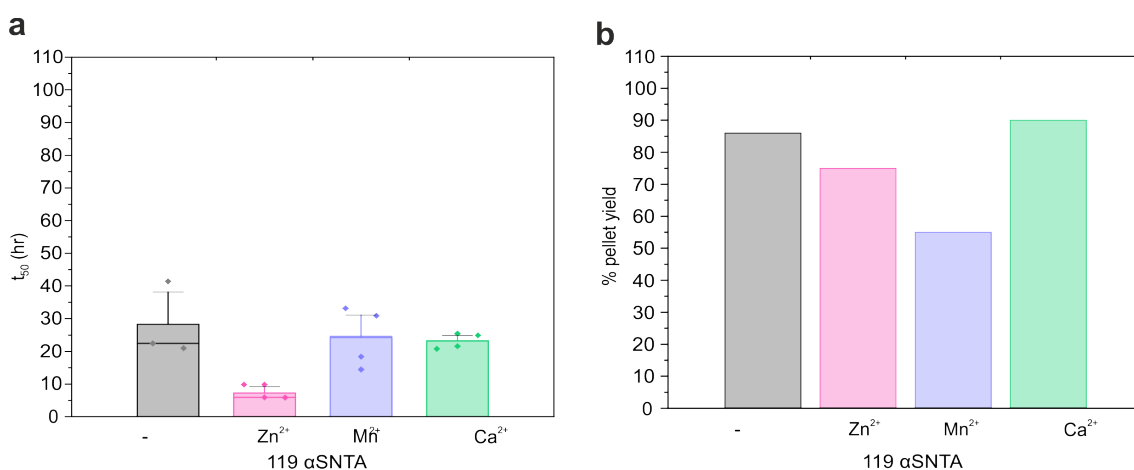


Figure. 3.32 t_{50} values and fibril yields for 119 α SNTA amyloid assembly. ThT fluorescence kinetics is shown in the absence of and presence of 25-fold molar excess of each metal ion (Zn^{2+} , Mn^{2+} or Ca^{2+}). (a) t_{50} values for the rate of amyloid assembly for 119 α SNTA, determined from ThT plate assays. Each condition shows three to four replicates. Error bars show the standard deviation of the mean of the replicates. (b) Yields of pelletable material from the end-points of amyloid assembly for 119 α SNTA. Values are rounded to the nearest 5%.

3.6.2 Native nESI-MS and IM-MS of 119 α SNTA confirms compaction upon metal ion binding

Native MS of 119 α SNTA displayed a multimodal charge state distribution similar to that of WT α SNTA (Figure 3.33).

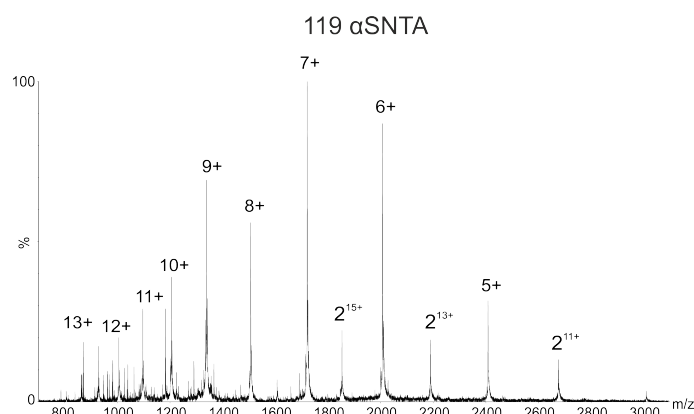


Figure. 3.33 Native nESI mass spectrum of 119 α SNTA. The protein concentration was 20 μ M in 20 mM ammonium acetate pH 7.5. Dimers are indicated by '2'.

The native mass spectra in Figure 3.34 show that although eight D/E residues have been removed from the sequence, all three types of metal ions still bind to the protein sequence with similar numbers of metal ions bound as observed for WT α SNTA (Figure 3.18).

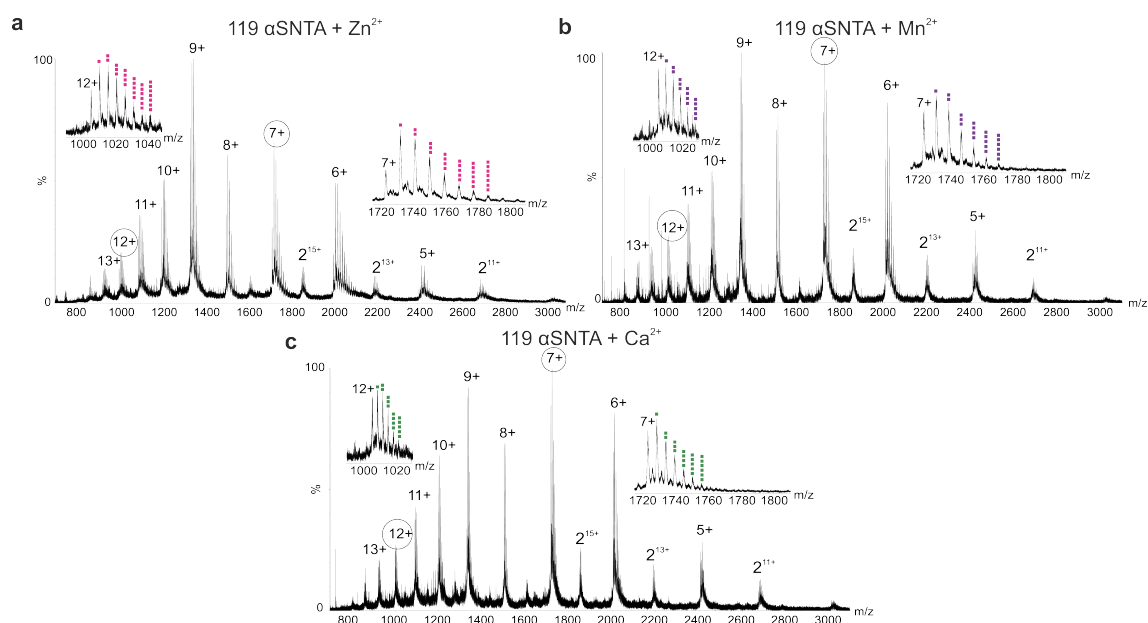


Figure 3.34 Native nESI-MS identifies binding of metal ions to 119 α SNTA. The whole spectrum and insets for the +8 and +12 charge states of 119 α SNTA (a) Zn^{2+} bound (pink squares), (b) Mn^{2+} bound (purple squares) and (c) Ca^{2+} bound (green squares). The protein concentration was 20 μ M in 20 mM ammonium acetate pH 7.5 and the concentration of metal ion added was 500 μ M to give a molar ratio of 1:25. Spectra were acquired using a Synapt G1 instrument (Waters, UK).

IM-MS shows that all three metal ions shift the ensemble to populate compact conformations with the greatest conformational shift again observed in the presence of Zn^{2+} (Figure 3.35). The N-terminal region is unaffected in 119 α SNTA, with seven Asp residues and one Glu residue in this region. These negative charges also offer additional binding sites for metal ions, which may have been overlooked in previous studies using very low concentrations (100 μ M) of ions such as Mn^{2+} , Fe^{2+} , Co^{2+} , Cu^{2+} and Ni^{2+} [183]. Additionally to these residues, the N-terminal region contains Met residues (M1, M5, M116 and M127 [394]) which can act as interaction sites for transition metals [358]. Furthermore, His50, which is removed in the $\Delta\Delta$ variant of α SNTA may act as a compensatory metal ion binding site for 119 α SNTA (Figure 3.3). 119 α SNTA populates fewer conformational

states than $\Delta\Delta$ α SNTA, where the intensity is split between one extended conformation and one compact conformation with some additional compact $^{TW}CCS_{N2}$ values represented as weaker intensity below the intense compact $^{TW}CCS_{N2}$.

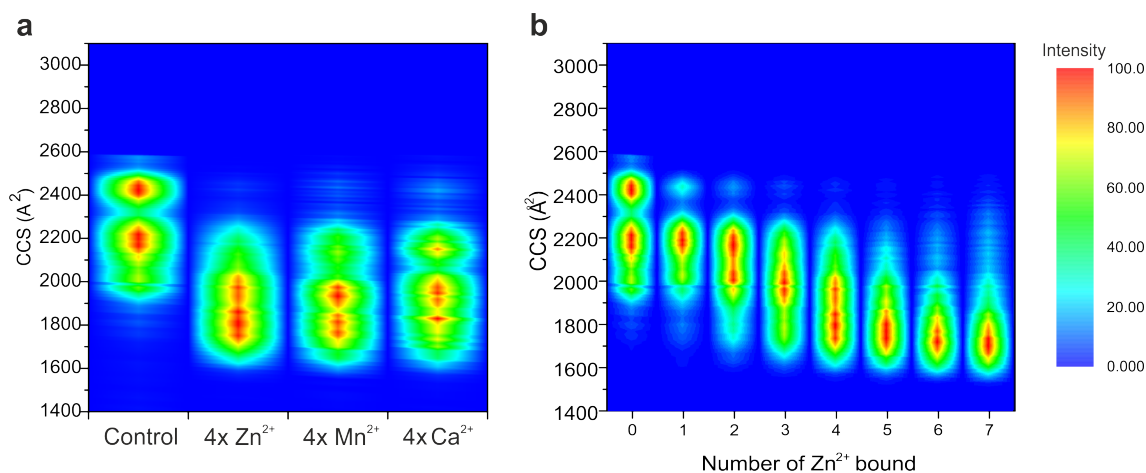


Figure. 3.35 Native nESI-IM-MS spectra show compaction of 119 α SNTA when metal ions bind. (a) $^{TW}CCS_{N2}$ fingerprints of 119 α SNTA 7+ charge state alone or bound to four ions of either Zn^{2+} , Mn^{2+} or Ca^{2+} . (b) $^{TW}CCS_{N2}$ fingerprints of the 7+ charge state of 119NTA α S unbound and bound to one to seven Zn^{2+} . Spectra were acquired using a protein concentration of 20 μ M in 20 mM ammonium acetate, pH 7.5. A 25-fold molar excess of zinc acetate was added. $^{TW}CCS_{N2}$ values were calculated using ATDs extracted from MassLynx 4.1 (Waters, UK).

3.7 Dimer abundance correlates with amyloid propensity

The amyloid assembly process of α S can be described as a nucleated polymerisation model where soluble species undergo self-assembly into oligomeric intermediate conformations which grow through monomer addition [395]. α S amyloid kinetics feature a lag phase which could be a result of a build-up of kinetically trapped intermediate oligomers which sterically occlude the hydrophobic NAC region from being exposed to the solvent [90]. The earliest stage of α S self association would be the assembly of a dimeric conformation.

The existence of a naturally occurring dimer has been identified previously using IM-MS, ECD, smFRET and NMR [68, 90]. Dimers have also been proposed as inhibitors of fibril elongation by binding to fibril ends with a higher affinity than monomers, where dimers possess a structural constraint preventing further monomer addition [396]. Dimers could act as a kinetic trap potentially responsible for the lag phase in amyloid assembly making it essential to characterise their structure, abundance and correlation to the rate of amyloid assembly. Here, native MS was used along with UniDec to deconvolve native mass spectra to quantify relative dimer abundances. Firstly, relative dimer abundance was compared for different variants and conditions which affect t_{50} of amyloid assembly (Figure 3.36). The raw mass spectra for the plotted dimer abundances are shown in Figure A.4 and Figure A.5.

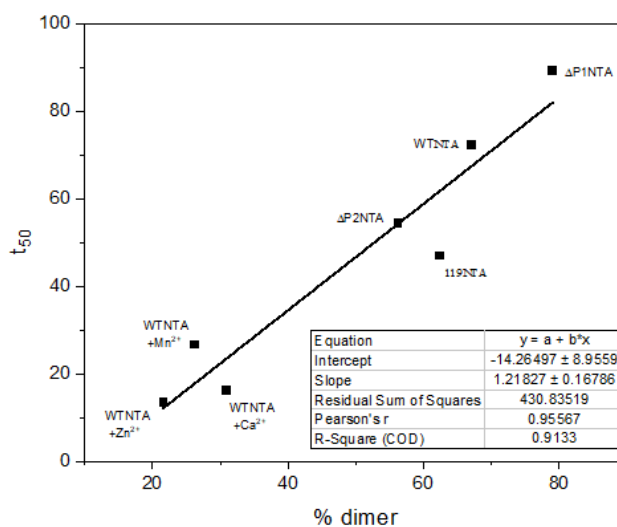


Figure. 3.36 Dimer abundance versus t_{50} . The relative dimer abundance was determined using UniDec and the relative population quantified against monomer abundance. With a Pearson's r value = 0.961 higher dimer abundance correlated with longer lag times. Note that no lag time can be determined for $\Delta\Delta \alpha$ SNTA which is plotted at the maximum value of 110 hours.

A clear correlation is observed where the higher relative dimer abundance correlates with higher t_{50} and even the inability to assemble amyloid fibrils under the timescale of the experiment (110 hours). In order to validate these findings further, a separate experiment was conducted to determine relative dimer abundance for a titration where the molar excess of Zn^{2+} was gradually increased which, continually decreased the t_{50} of amyloid assembly (Figure 3.37).

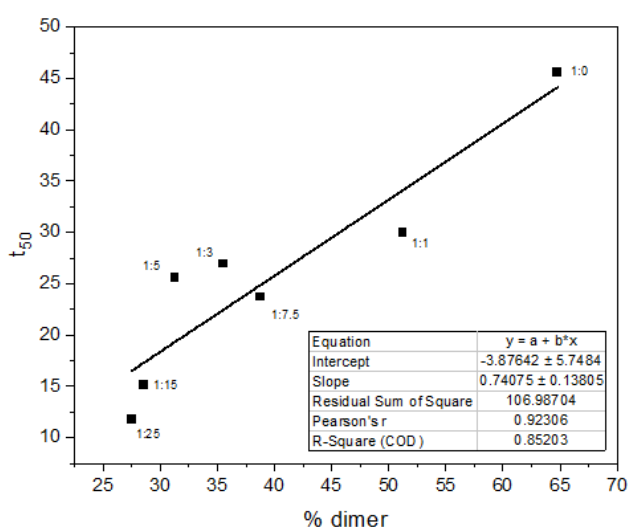


Figure 3.37 Dimer abundance versus t_{50} with the addition of Zn^{2+} to WT α SNTA. The relative dimer abundance was determined using UniDec and relatively quantified against monomer abundance. With a Pearson's r value = 0.922 higher dimer abundance correlated with longer lag times. The molar ratio (α S : Zn^{2+}) is annotated in the plot.

Dimer abundance clearly falls as t_{50} decreases, also evidenced as an exponential decrease in Figure 3.38. Hence, dimers could be off pathway or, present a high energy conversion barrier on pathway to amyloid assembly. With more characterisation, stabilising the dimer could offer a potential therapeutic target to prevent the assembly of toxic conformations during α S amyloid assembly.

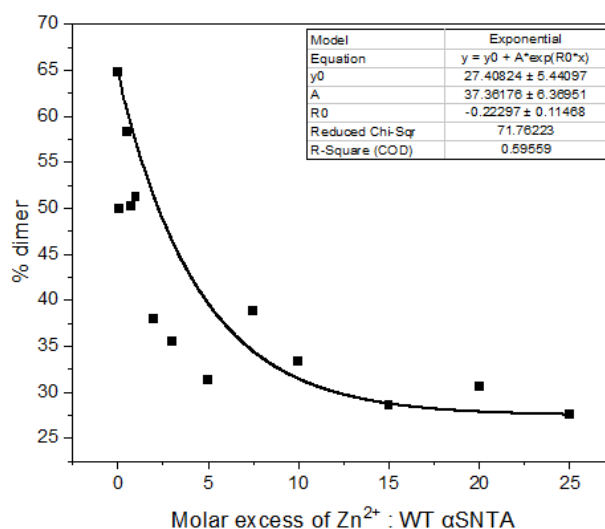


Figure 3.38 Dimer abundance versus the molar excess of Zn^{2+} when added to WT αSNTA . The relative dimer abundance was determined using UniDec and relatively quantified against monomer abundance. Dimer abundance decreases as the molar excess of Zn^{2+} increases.

3.8 Discussion

αS is an IDP and its conformational behaviour is known to be affected by divalent metal ion binding [183, 358, 13, 184, 397]. Native IM-MS has shown that WT αSNTA populates four major conformational families at the 8+ charge state, consistent with previous data [13, 114]. Here, $^{\text{TW}}\text{CCS}_{\text{N}_2}$ measurements demonstrate that there is a clear and consistent link between the compaction of monomeric WT αSNTA at the 8+ charge state, and the 7+ charge state for $\Delta\Delta$ αSNTA with an increased rate of amyloid formation, possibly indicating that key species in the ensemble are compacted such that they are more competent to form amyloid. How the properties of species observed in the gas phase relate to those in solution (e.g. their hydrodynamic radius, or the formation of intra- or inter-molecular contacts) will require further analyses using solution-based assays. For example it is well known that

the hydrophobic contacts are diminished in the absence of water, while hydrogen bonding and electrostatic interactions are enhanced [398]. Such effects are especially important to consider for weak complexes, such as the early oligomers in amyloid formation, and dynamically disordered monomeric proteins, such as IDPs.

Importantly, however, previous analyses comparing gas phase and solution properties of IDPs have shown that the ESI process does not have a substantial effect on structure, and that IM-MS $^{TW}CCS_{N_2}$ can report accurately on their solution phase properties [399]. Backed up with solution phase assays, therefore, MS-based methods provide a unique power for understanding the structure, populations and stabilities of proteins in complex mixtures, as exemplified here for the effects of different metal ions in the self-assembly of α S. $^{TW}CCS_{N_2}$ values obtained also enable us to compare different deletion variants of α SNTA in the absence of metal ions to determine the effect the protein sequence and distribution of charged residues on the conformational behaviour of the apo state. WT α SNTA visits more conformational states than $\Delta\Delta$ α SNTA overall (Figure 3.22) some of which presumably are competent to form amyloid. Shifting the conformational ensemble to populate species with smaller $^{TW}CCS_{N_2}$ combined with charge neutralisation from divalent metal ion binding appear to have a key regulatory effect in increasing the rate of ThT positive amyloid assembly. Carija et al. used a disulfide link strategically placed between residues Val71 and Thr92 to lock the monomeric structure of WT α S into the Greek-key motif of α S amyloid fibrils. This compacted monomer resulted in reduced rate of amyloid formation, highlighting the importance of conformational flexibility and dynamic conformational exchange in the early stages of assembly to generate the amyloid fold [357].

There is a hierarchal reduction in the t_{50} of amyloid formation for WT α SNTA, whereby Zn^{2+} is the most effective, followed by Mn^{2+} and Ca^{2+} . A study using laser ablation-inductively coupled plasma-MS (LA-ICP-MS) of homogenized human olfactory bulb samples from PD patients identified that Zn^{2+} was present at 10-200 μ g/g concentrations,

co-localised with aggregates of phosphorylated α S, whilst Mn^{2+} was found at trace levels (less than 1 μ g/g on average). Zinc in particular was thought to contribute to Lewy body pathology in PD through oxidative stress, having a mostly pathological role [372]. Physiological Ca^{2+} concentrations can vary from tens of nM to several hundreds of μ M, depending on whether neuronal cells are in a resting state or undergoing depolarisation during an action potential [374]. With a K_D of 21 μ M for α S with Ca^{2+} , it is clear that α S will interact with Ca^{2+} in the physiological, cellular context [321]. Lautenschläger et al. showed a relationship between C-terminal Ca^{2+} binding and α S synaptic vesicle interactions [321]. Moreover, the presence of Ca^{2+} ions increased the affinity of α S to synaptic vesicle membranes, which resulted in increased clustering of vesicles [321]. The presence of metal ions influences the behaviour of α S within cells and may elude to mechanisms hidden in synucleopathies. This study provides further molecular detail into the resulting effects on α S when metal ions bind.

In vivo, binding of other small molecules or proteins such as chaperones may offer a protective effect against pathological structural remodelling of α S. Molecules such as dopamine are known to also bind to the C-terminal region of α S, and binding results in extension of the protein chain which offers a protective effect, switching off amyloid assembly [283]. Additionally, chaperones such as Hsp70 are known to interact with the N-terminal region of α S, protecting it from amyloid assembly [400, 401]. *In vivo*, chaperone binding could offer a protective effect which counteracts the effects of metal ion binding.

Introducing the $\Delta\Delta$ variant to the α S sequence through removal of P1 and P2 sequences switches off the potential for α S to assemble into amyloid by altering the long-range interactions necessary to induce an amyloid-competent conformation [350]. Even though these sequences remove critical interaction sites, nESI-IM-MS herein showed that $\Delta\Delta$ α SNTA still remains conformationally dynamic (Figure 3.22d). However, this variant populates three distinct conformations at the 7+ charge state wherein the largest $^{TW}CCS_{N2}$ conformation (most extended) is the most intensely populated, whereas WT α SNTA populates four

$^{TW}CCS_{N2}$ conformations (at the 8+ charge state) with the population intensity weighted towards the most compact conformations. When divalent metal ions are present, the $\Delta\Delta$ α SNTA amyloid assembly potential is re-established, and this effect consistently correlates with compaction, reinforcing the correlation between chain compaction and the rate of amyloid formation.

As metal ion binding is believed to be located primarily to negatively charged Asp and Glu residues in the C-terminal region of α S [402, 183], physiologically relevant C-terminally truncated variants of α S may inform on the necessity of charge neutralisation in this process, or whether compaction alone is the primary driver. Additionally, transition metals can also interact with Met and His residues, potentially recruiting the N-terminal region of α S [183, 358, 321]. Native IM-MS and ThT kinetics on a variant of 119 α SNTA (truncated at residue 119; Figure 3.35) showed that 119 α SNTA populates fewer conformational states than $\Delta\Delta$ α SNTA, where the intensity is primarily split between one extended conformation and one compact conformation. Interestingly, despite half of the putative C-terminal metal binding region being removed in 119 α SNTA, an almost comparable number of Zn^{2+} ions still bind to the protein, with 1-2 fewer binding events on average compared to WT α SNTA. These binding events still result in $^{TW}CCS_{N2}$ compaction and faster amyloid assembly kinetics. These results imply that the N-terminal region must also be important for metal ion binding, and that the presence of a compact conformation is compatible with metal ion binding to this region. The seven Asp residues and single Glu residue within the N-terminal region may become preferential sites for divalent metal ion binding when the C-terminal region is truncated. His50 may offer an essential binding mechanism which anchors metal ions by coordination with the C-terminal region creating a seemingly looped structure of α S.

Compact conformations may offer a preferential, higher stability orientation for metal ion binding as the close proximity of negatively charged amino acids creates a binding pocket when the C-terminus folds backwards to interact with the N-terminus or with itself.

Ions can create a coordination network between these negatively charged amino acids which pull the structure into a tighter, more compact conformation which may also result in increasingly rigid conformations, depicted from low charge states in the ${}^{\text{TW}}\text{CCS}_{\text{N}_2}$ evaluation in Figure 3.24 and presented as a schematic in Figure 3.39. ${}^{\text{TW}}\text{CCS}_{\text{N}_2}$ compaction has been observed previously in the case of increased numbers of Ca^{2+} binding to calmodulin, established by IM-MS [403]. The higher charge states, or extended conformations still bind to Zn^{2+} and other metal ions, however, due to the distance between the N- and C-termini, metal ions cannot coordinate distant residues, resulting in no significant observable conformational change.

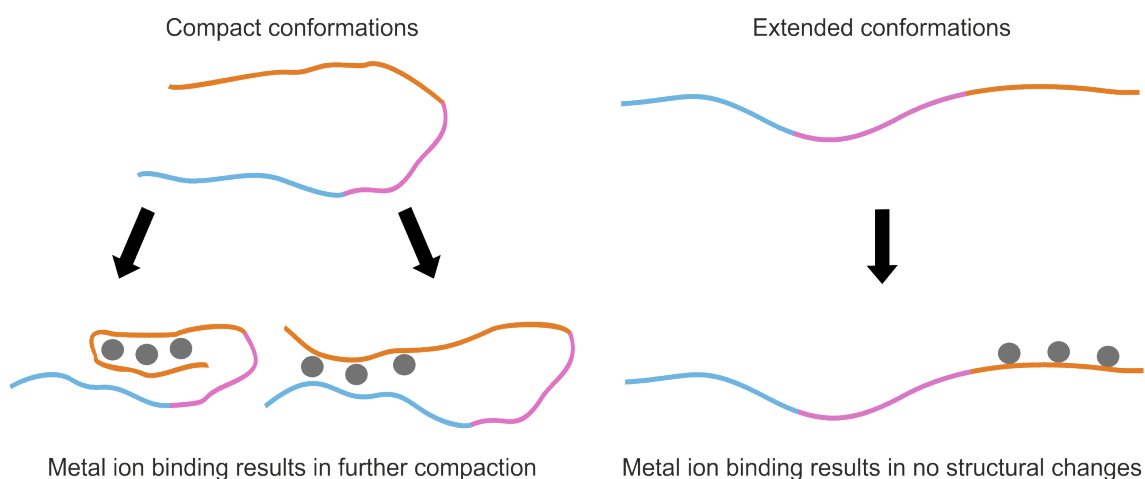


Figure. 3.39 Schematic of the resulting conformational effects when metal ions bind to α SNTA.

3.9 Conclusion

Based on the results presented in this chapter, it appears that the conformational ensemble of the monomeric state predisposes α SNTA amyloid forming behaviour. The charge distribution across the sequence of the protein might be naturally fine-tuned in a way that prevents the rapid onset of amyloid assembly, tipping the toxicity versus function of α S away from toxicity. Binding of metal ions or other ligands such as small molecules, lipids

or membranes could bias α S towards amyloid-prone conformations, resulting in the rapid assembly of toxic oligomers and ultimately amyloid fibrils associated with disease.

Further information regarding the exact binding sites of metal ions to WT-, $\Delta\Delta$ - and 119- α SNTA, will help to elucidate the exact molecular rearrangement that the α S protein chain undergoes when different metal ions bind. Binding sites can be mapped using techniques such as native top-down electron transfer dissociation (ETD) tandem mass spectrometry (MS/MS) which fragments the backbone of intact proteins whilst maintaining non-covalent ligand interactions. In addition, residue- and region-specific details of the conformational changes that α S undergoes in the presence of metal ion binding could be unravelled using techniques such as NMR or cross-linking MS to identify specific intra-protein interactions that stabilise compact conformations, or studies using techniques such as smFRET analysis of population shifts using fluorescent probes placed at relevant sites on the protein sequence [349]. With powerful MS methods adding to a fast-growing structural biology toolbox, our next goal is to target the structural gap in protein amyloid pathways between monomer and fibril, by elucidating structural intermediates and identify potential targets for pharmaceutical intervention. Experiments towards these goals are presented in the next chapter.

Chapter 4

Understanding the molecular mechanisms that govern α S compaction

4.1 Introduction

Monomeric α S is highly conformationally dynamic. As in Chapter 3, small perturbations in CCS result in significant differences in the amyloid propensity of α S, highlighting the significance of specific partially compact conformational families within the overall ensemble. Indeed, long-range intramolecular interactions have been characterised within the ensemble of α S monomers, involving primarily the P1 and P2 regions, as well as N- to C-terminal interactions as visualised by smFRET and NMR paramagnetic relaxation enhancement [380, 350, 89, 345].

In the presence of Ca^{2+} , HDX-MS was performed on α S by Stephens.A., *et al* (2020) who revealed conformational rearrangements of the α S protein backbone. Along with NMR, these experiments showed that upon the addition of Ca^{2+} , the C-terminal region of α S becomes significantly protected from HDX due to intramolecular hydrogen bonding and possibly compaction, whilst the N-terminal region revealed significant de-protection

[114]. This suggests that when Ca^{2+} binds, the C-terminal region collapses due to charge neutralisation and this is reflected as compaction in IM-MS (Figure 3.22). The N-terminal region could remain exposed to the solvent, more so than in the absence of metal ions due to the disruption of long-range intramolecular interactions (between the N- and C-terminus). Thus, the P1 and P2 regions lose the ability to form intramolecular interactions with the C-terminal region, and a new pathway to form amyloid is created, independent of P1 and P2. In this case, amyloid assembly is dependent on the binding of metal ions and subsequent C-terminal collapse. It should also be noted, that the highly negatively charged C-terminal region is thought to protect α S from self-assembly by shielding the hydrophobic NAC region from the solvent [392, 297, 393, 298]. Charge neutralisation of this protective region therefore, could result in aggressive amyloid assembly which could occur in the brain within elevated concentrations of metal ions.

Understanding the lifetime of the compact conformation, how much of the overall ensemble it constitutes, and the intramolecular interactions responsible for stabilising such an amyloid competent conformation(s) could enable the design of novel therapeutics to target only the toxic conformations of monomeric α S, preventing amyloid assembly whilst maintaining its functional properties.

4.2 Objectives

In this chapter, the molecular mechanisms which govern, and stabilise, the most amyloid-prone conformations of α SNTA are explored in more detail. Overall, the objective was to characterise specific intramolecular interactions necessary to stabilise compact conformational families by elucidating where compaction occurs along the α SNTA protein chain.

In order to correlate local structure with amyloid propensity, a number of techniques were applied. cIM-MS was used to identify hidden conformational families by offering

higher resolution IM separation. Specific intramolecular interactions were probed using quantitative XL-MS to identify changes in XL abundance in the presence of Zn^{2+} . Accompanying the MS approach, smFRET was used to detect changes in structure of αSNTA in the presence of Ca^{2+} . Native top-down fragmentation was applied to probe compaction of the αS ensemble under native conditions. Finally, using NMR, specific residues which bind Zn^{2+} or undergo conformational rearrangement were explored. Together, these biophysical techniques were used to elucidate the molecular arrangement of the compact conformational families of αSNTA with implications towards understanding how monomeric conformational dynamics influence amyloid propensity.

4.3 Correlating ion mobility with the rate of amyloid formation

The effect of Zn^{2+} on the amyloid propensity of WT, $\Delta\Delta$ and 119 αSNTA was explained in detail by a titration of Zn^{2+} concentration on amyloid formation kinetics measured by ThT fluorescence. Figure 4.1a-c show that Zn^{2+} reduces the t_{50} of amyloid formation when added at low stoichiometry. At a molar ratio of 1:1, $\Delta\Delta : \text{Zn}^{2+} \alpha\text{SNTA}$, the protein re-establishes its propensity to form amyloid at rates comparable to that of WT αSNTA . In order to directly compare the effects of Zn^{2+} binding on amyloid propensity observed in solution with compaction effects and binding events observed in the gas phase, the titration with Zn^{2+} was performed from molar ratios of 1:1 to 1:40 ($\alpha\text{SNTA} : \text{Zn}^{2+}$) to enable direct comparison of the t_{50} of amyloid formation (using 100 μM αSNTA) with native IM-MS acquired at (20 μM αSNTA).

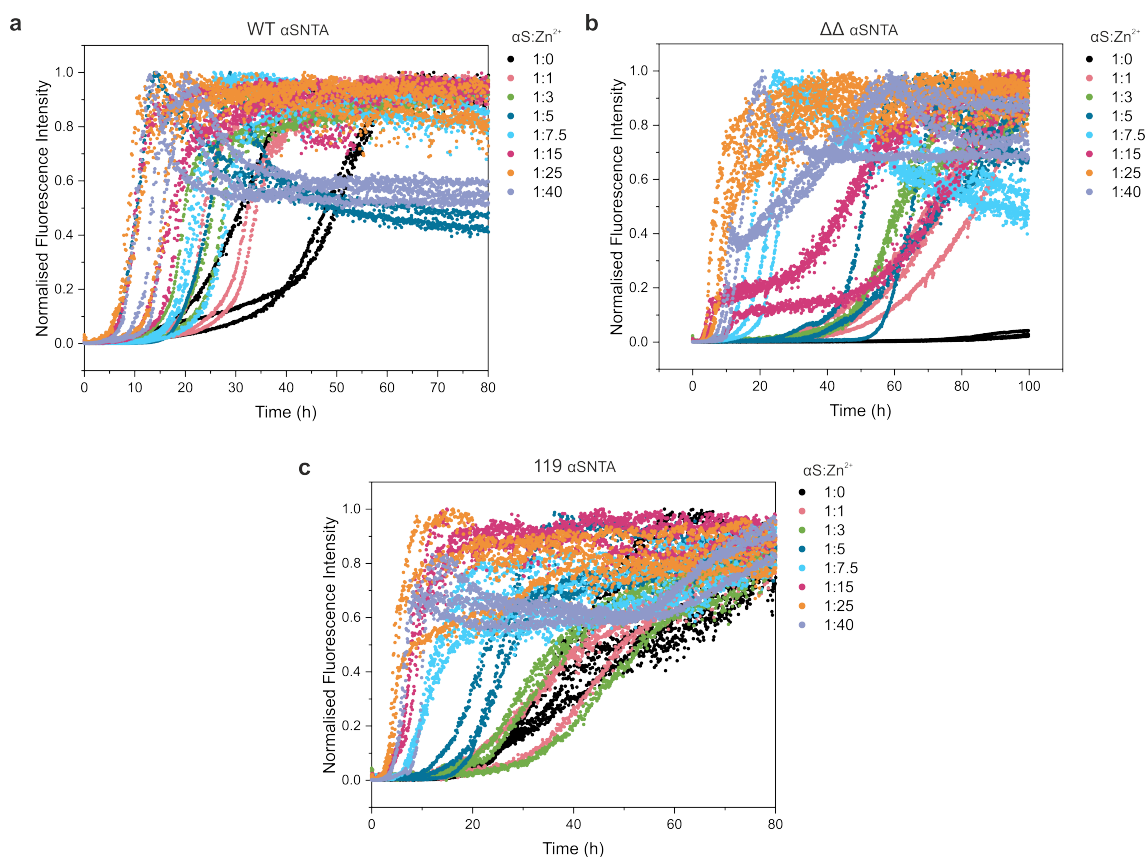


Figure 4.1 ThT fluorescence showing a titration of α SNTA with Zn²⁺. The molar excess of Zn²⁺ is increased stepwise in the presence of (a) WT, (b) $\Delta\Delta$ or (c) 119 α SNTA. ThT fluorescence was detected using 100 μ M protein in 20 mM ammonium acetate pH 7.5, at 37°C, shaking at 600 rpm with one Teflon polyball (1/8" diameter; Polysciences Europe) per each sample.

The percent occupancy of Zn²⁺ binding (all number of bound states versus the unbound state) and the shift in CCS towards compact species at different α S : Zn²⁺ ratios was analysed using native IM-MS and compared to t_{50} of amyloid formation for WT and $\Delta\Delta$ α SNTA and plotted as correlation plots in Figure 4.2. Intracellular Zn²⁺ within the brain, at a concentration of \sim 150 μ M, is predominantly inaccessible due to cytosolic metal binding proteins which sequester Zn²⁺ into organelles [404]. However, when neurones become damaged, such as during oxidative stress, transfer to the cytosol occurs [405].

Indeed, synaptic Zn^{2+} can transfer from presynaptic neurones through Ca^{2+} channels or via vesicles, where αS is localised [404]. Whilst the physiological concentration of αS in neuronal synapses is estimated to be around 50 μM the concentrations used in these analyses reflect the range of physiological concentrations [406].

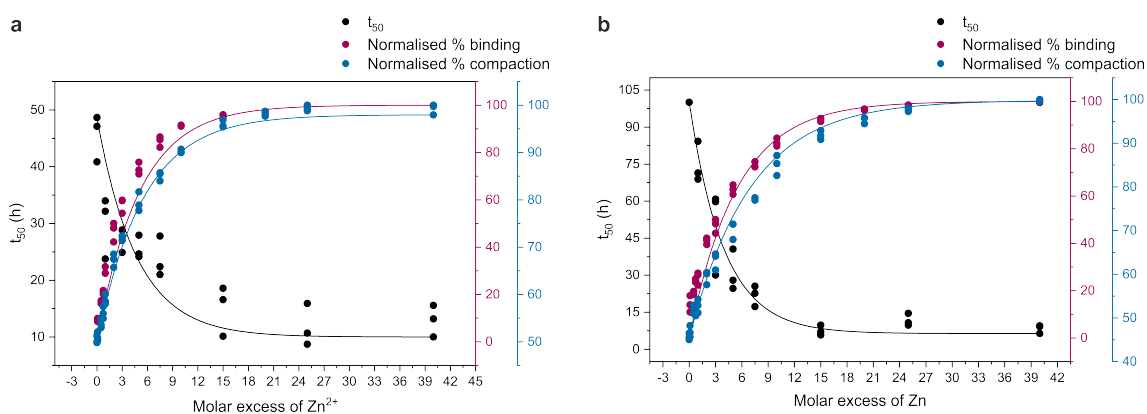


Figure. 4.2 Correlating CCS with t_{50} directly links compaction with amyloid propensity in the presence of Zn^{2+} . For (a) WT and (b) $\Delta\Delta$ $\alpha SNTA$ the effect of Zn^{2+} concentration on amyloid propensity (t_{50}), CCS and percent occupancy by binding saturates at around a 15-fold molar excess of Zn^{2+} . For CCS measurements, spectra were acquired using a protein concentration of 20 μM in 20 mM ammonium acetate, pH 7.5 on a Waters Synapt G1. CCS values were calculated using ATDs extracted from MassLynx 4.1, % compaction and % binding were calculated using peak areas. All measurements were taken in triplicate and all replicates are plotted where the line is the average fit.

It is clear in Figure 4.2a-b that gas phase measurements of Zn^{2+} binding and subsequent CCS compaction correlate with solution phase t_{50} values. Binding follows a hyperbolic trend which does not suggest cooperative but rather stepwise ion binding until saturation. An interesting finding between WT and $\Delta\Delta$ $\alpha SNTA$ is that the effects of Zn^{2+} occur at the same molar excess such as saturation at ~ 15 -fold excess and a midpoint at ~ 3 -fold Zn^{2+} excess suggesting that binding of Zn^{2+} is independent of the P1 and P2 regions. When comparing these features to those of 119 $\alpha SNTA$ (Figure 4.3), although native IM-MS

experiments were not carried out in triplicate, in this case, the midpoint of t_{50} reduction with % occupancy and % compaction appears shifted to around a 5-fold molar excess of Zn^{2+} , which highlights the role of the C-terminal region not only in binding but also in compaction due to collapse where more Zn^{2+} is needed for the same level of effect as for WT α SNTA. These different types of measurements which compare solution and gas phase properties of three α S variants versus Zn^{2+} concentration confirms the validity of using gas phase measurements to accurately reflect the molecular properties of α SNTA in solution which must be retained as the protein is transferred into the gas phase natively by ESI and analysed in a gentle manner by IM-MS.

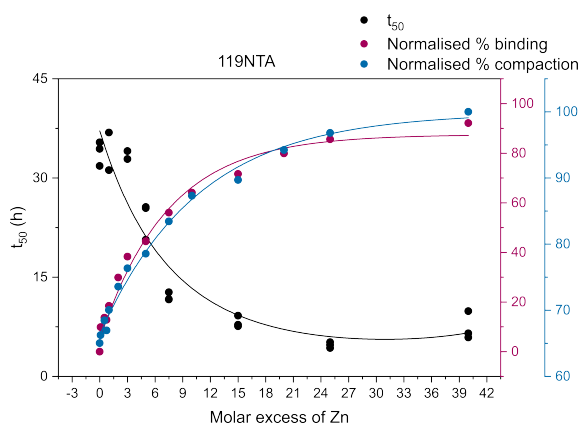


Figure 4.3 Correlating CCS with t_{50} directly links compaction with amyloid propensity of 119 α SNTA in the presence of Zn^{2+} . For 119 α SNTA the effect of Zn^{2+} on amyloid propensity (t_{50}), CCS and percent occupancy by binding saturates at around a 15-fold molar excess of Zn^{2+} . For CCS measurements, all protein spectra were acquired using a protein concentration of 20 μ M in 20 mM ammonium acetate, pH 7.5 on a Waters Synapt G1. CCS values were calculated using ATDs extracted from MassLynx 4.1, % compaction and % binding were calculated using peak areas. t_{50} measurements were obtained in triplicate and all replicates are plotted, CCS and binding measurements were acquired as single acquisitions.

4.3.1 Fitting binding curves to obtain Zn^{2+} binding affinities to αSNTA

Native MS provides the mass of a protein or protein complex and is also gold-standard for reporting the stoichiometry of ligand-binding events. Within these data, native MS can also be used to determine apparent binding affinities [407–409]. Assuming that peak intensities in an ESI mass spectrum reflect binding in solution, where ideally all species present ionise with the same efficiency, the affinity of a ligand can be determined not just globally, but to individual charge states themselves [410]. Thus, binding affinities can be determined for different conformational families present. Binding affinities are calculated by fitting the relative intensities of bound versus unbound peaks as a function of increasing ligand concentration and this therefore requires high resolution data for accurate extraction of peak areas [411]. By first deconvolving the spectra, accurate peak areas can be extracted and subsequent micro- and macroscopic K_d fitting can be performed.

Using UniDec to deconvolve spectra, followed by the data collector node to fit K_d , apparent binding affinities were determined for WT αSNTA with Zn^{2+} [412] using equation 2.1. Data for this analysis were acquired on a Waters Synapt G1 (Figure 4.4). Interestingly, the fitted K_d determined for the 6+, 8+ and 10+ charge state, which reflect compact and extended conformations separately, are similar. For the first binding event, K_d values for the compact 6+ ion, (29.5 μM), the highly heterogeneous 8+ ion (32.2 μM) and the extended 10+ ion (26.7 μM) are similar, suggesting that Zn^{2+} binds to all conformations with the same affinity. This could mean that the C-terminus is easily accessible and the P1 and P2 regions which stabilise long range interactions may not be involved in the first binding event. Each subsequent binding K_d value was similar (29.5 μM , 32.2 μM and 26.7 μM) ruling out cooperative binding, and suggesting instead step-wise, independent binding events. However, the resolution of the extracted data acquired on the Synapt G1 is relatively poor with low signal to noise, evidenced as the unbound peak does not start at a normalised intensity of 1.0 (100%) when Zn^{2+} is absent, which could skew calculated K_d 's to lower values.

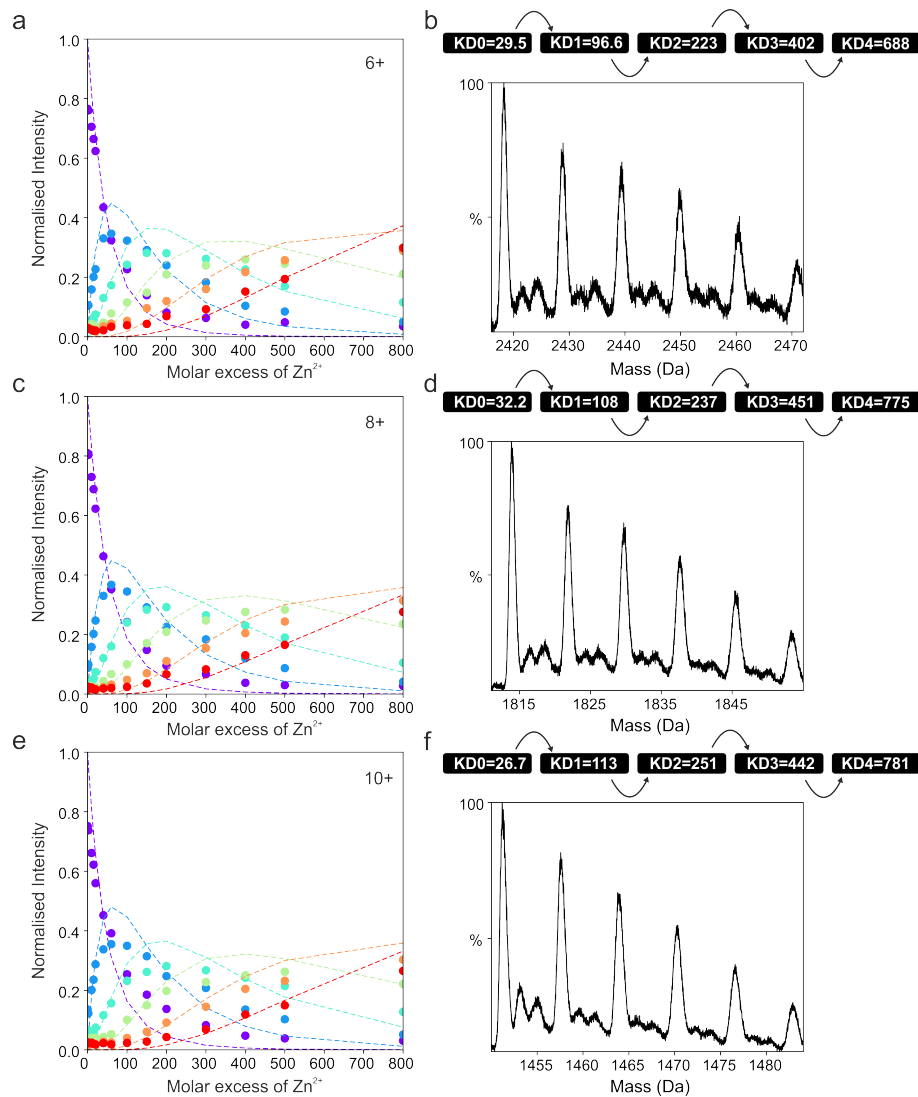


Figure 4.4 Determination of K_d values of Zn^{2+} binding events to WT α SNTA acquired using the Waters Synapt G1 HDMS. (a) K_d fitting for the 6+ charge state where the unbound peak is represented in purple, 1 Zn^{2+} bound in blue, 2 Zn^{2+} bound in cyan, 3 Zn^{2+} bound in green, 4 Zn^{2+} bound in orange and 5 Zn^{2+} bound in red, (b) K_d value determination for the 6+ charge state with extracted data. (c) K_d fitting for the 8+ charge state, (d) K_d value determination for the 8+ charge state with extracted data. (e) K_d fitting for the 10+ charge state, (f) K_d value determination for the 10+ charge state with extracted data. 20 μ M α SNTA was used for experiments in 20 mM ammonium acetate, pH 7.5. Raw data was extracted using Waters MassLynx v4.2 (Waters, UK) and processed using UniDec [412].

In order to achieve more accurate extracted K_d values, a similar Zn^{2+} titration was performed on the ThermoFisher Orbitrap Eclipse Tribrid MS which achieves data with higher resolution (Figure 4.5). The reported apparent K_d for the 8+ charge state using this instrument (Figure 4.5) is 53.7 μ M for the first binding event to WT α SNTA which indicates a low affinity and weak binding. Similar K_d values were observed for different charge states (Figure 4.4 and 4.5). At a molecular level Zn^{2+} is proposed to compete with intramolecular interactions involving the N- and C-terminal regions [413]. The data presented here adds to this model since compact conformations become more compact due to metal ion co-ordination and collapse of the densely negatively charged C-terminal region. By contrast, more extended conformational families remain extended upon binding. This suggests that the most amyloid-prone conformational family is the most compact, and that this constitutes only a small proportion of the overall ensemble of α S, but is enough to act as a highly competent conformation to drive amyloid assembly.

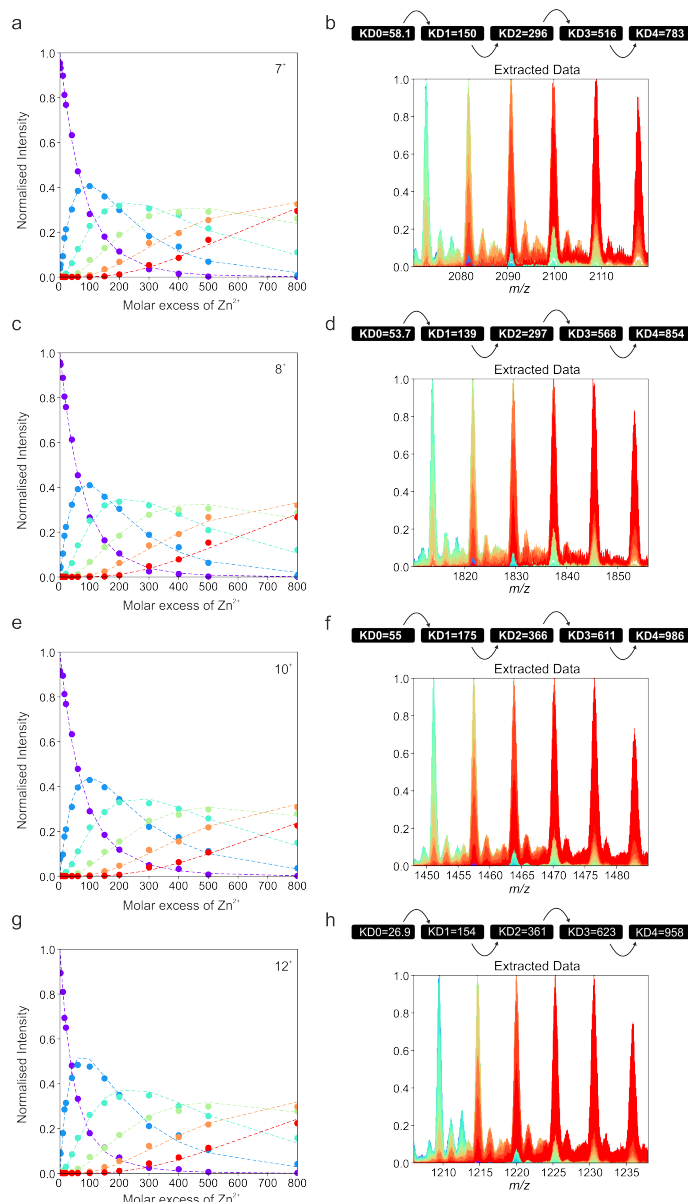


Figure 4.5 Determination of K_d values of Zn^{2+} with WT α SNTA acquired using the ThermoFisher Orbitrap Eclipse Tribrid MS. (a) K_d fitting for the 7+ charge state showing the unbound species (purple), 1 bound (blue), 2 bound (cyan), 3 bound (green), 4 bound (orange) and 5 bound (red), (b) K_d value determination for the 7+ charge state with extracted data. (c) K_d fitting for the 8+ charge state, (d) K_d value determination for the 8+ charge state with extracted data. (e) K_d fitting for the 10+ charge state, (f) K_d value determination for the 10+ charge state with extracted data, (g) K_d fitting for the 12+ charge state, (h) K_d value determination for the 12+ charge state with extracted data. 20 μ M α SNTA was used for experiments in 20 mM ammonium acetate, pH 7.5. Raw data was extracted using ThermoFisher FreeStyle and processed using UniDec [412].

4.4 Cyclic ion mobility mass spectrometry reveals hidden conformational families

The data presented in this thesis and elsewhere [367, 414, 364, 415] highlight that IM-MS is a powerful method for interrogating protein conformational ensembles and dynamics. Recently, the first commercial quadrupole ToF (QToF) instrument analogous to the Waters Synapt G2 model containing a cyclic IM (cIM) cell capable of consecutive cycles of IM (IM^n), has been introduced by Waters Corporation [54, 55, 69, 56]. The difference in this instrument is a lengthened IM separation distance which enables higher resolution of conformationally separated peaks. This separation power can be further improved through multiple passes around the cIM cell in agreement with the expected diffusion limit of resolving power [416]. Sub-populations of conformational families can be individually probed through the use of a multidirectional array by selecting "slices" of ion packets [417].

The methodology of slicing or, taking subpopulations of ATDs and analysing those ion packets by IM^n , was demonstrated in 2021 [417]. Here, in collaboration with Dr Dale Cooper-Shepherd and Waters Corporation, cIMS was used to explore the conformations of WT α SNTA. The 8+ charge state, which has shown to encompass a diversity of conformational families of α SNTA (Figure 3.11) was interrogated by cIM with the aim of revealing hidden conformational families and identify the stability of these populations by sampling their lifetime in the cIM cell. The mass spectrum of WT α S after one pass of the cyclic are shown in Figure The resulting ATD (Figure 4.7) show that more conformational families than the initially predicted value of four are observed after two passes of the cIM.

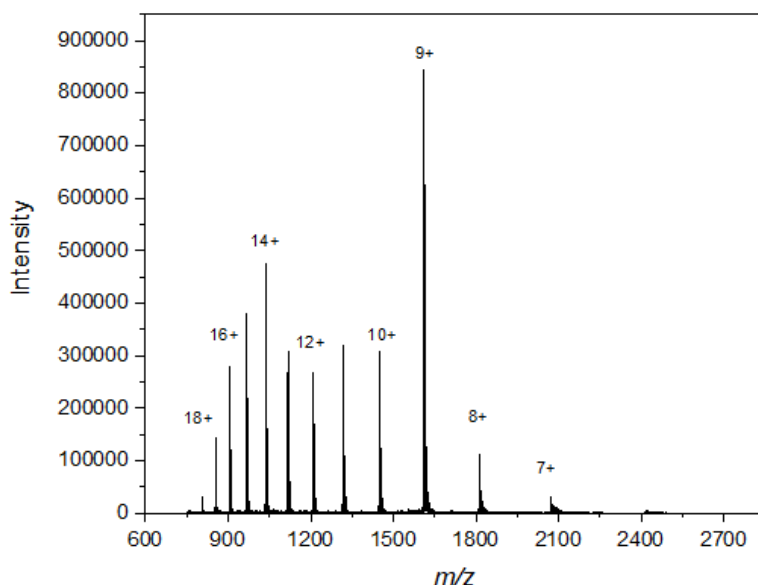


Figure. 4.6 Mass spectrum of WT α S measured on the Waters SELECT series cyclic ion mobility mass spectrometer. The charge state distribution identifies lower charge state species of high abundance (8+ and 7+) inferring that the spectrum is native. Data were acquired with Dr Dale Cooper-Shepherd at Waters Corporation.

The first slice (slice *a*) which is the most compact conformational family broadens and this similarly occurs for slice *b* which, after two passes, is separated into two peaks. Slices *c* and *d* do not broaden upon two passes through the cIM, which confirms that the peak broadening observed for slice *b* does not result from diffusion during the time spent in the instrument, but instead results from the separation of distinct conformational families. The timescale of two passes for the slices in Figure 4.7 reaches up to 300 ms, which infers high stability (low exchange rate) of conformational families which do not re-establish or re-equilibrate back into the initial ATD distribution (Figure 4.7a). It should be noted that proteins are expected to exhibit higher stability in the gas phase than observed in solution or simulation, likely due to the loss of water molecules which catalyse conformational

transitions, however, a conformational family existing for up to 300 ms is particularly striking for an IDP [418].

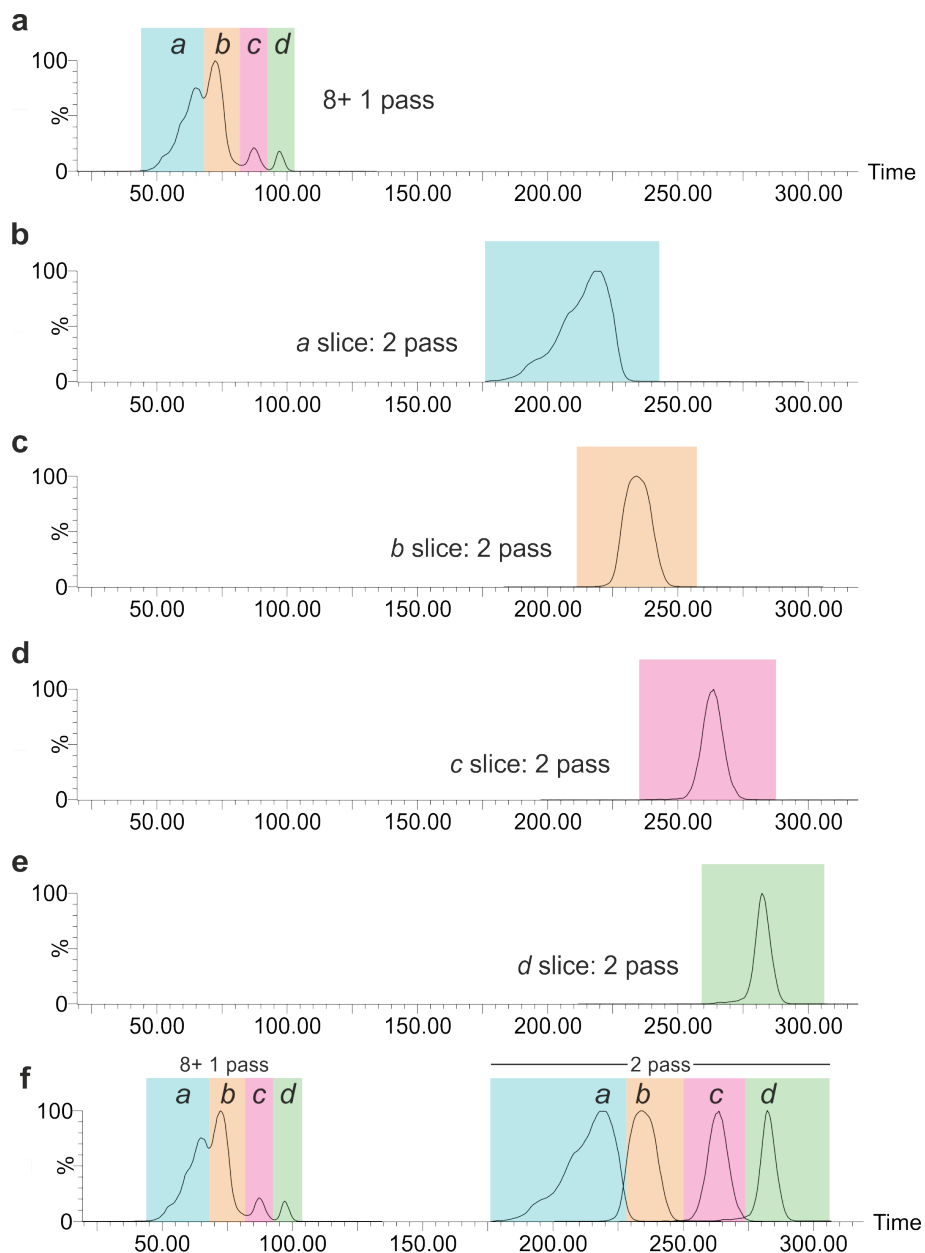


Figure 4.7 Cyclic IM-MS of the 8+ charge state of WT α SNTA. Arrival time distribution for (a) the 8+ charge state of WT α SNTA after one pass of the cIM cell, (b) Slice "a" after two passes, (c) slice "b" after two passes, (d) slice "c" after two passes and (e) slice "d" after two passes. All ATDs are combined in (f). ATDs were extracted using MassLynx 4.1. Data were acquired with Dr Dale Cooper-Shepherd at Waters Corporation.

To further determine whether diffusion played a role in the broadening of ATDs, slices were passed around the cyclic until the wrap-around effect was observed (catching up of low mobility ions). Slice *b* was passed four times, and slices *c* and *d* were passed six times. Slice *d* remained a sharp peak, which infers that the conformational families within the *d* peak do not become more resolved with multiple cIM passes, and that the broadening of slices *a* and *b* is likely due to resolving multiple conformational families.

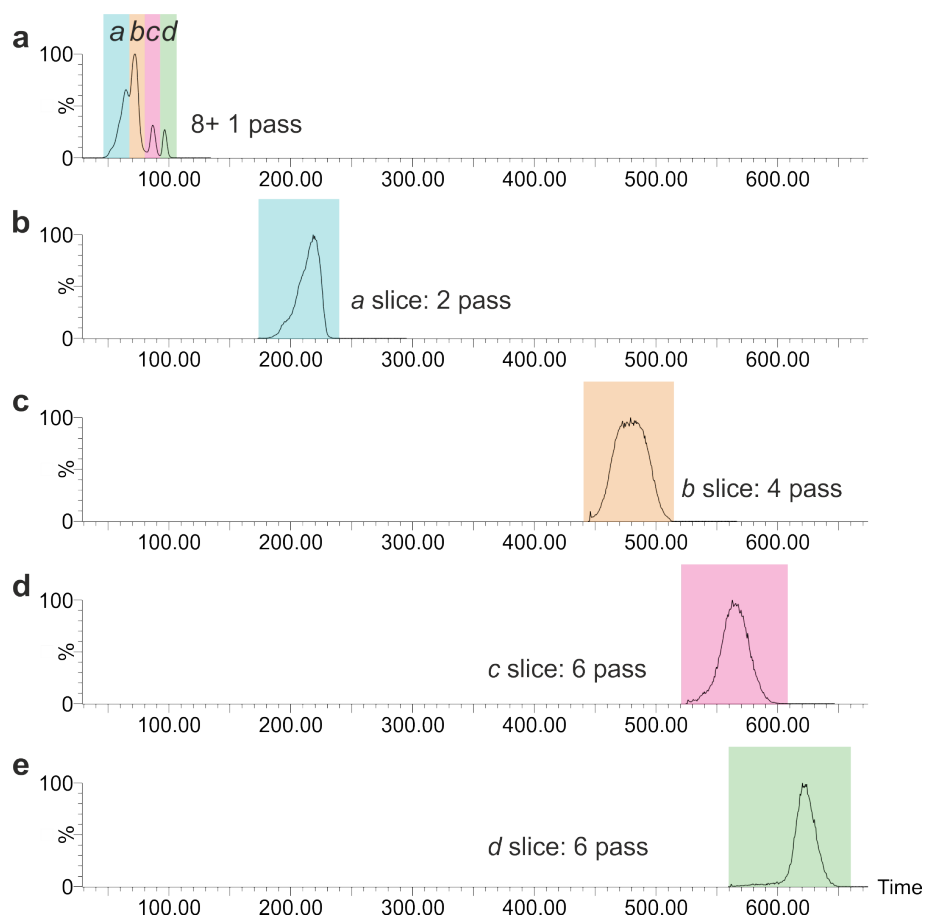


Figure. 4.8 Cyclic IM-MS of the 8+ charge state of WT α SNTA for the maximum number of passes. Arrival time distribution for (a) the 8+ charge state of WT α SNTA after one pass of the cIM cell, (b) Slice "a" after two passes, (c) slice "b" after four passes, (d) slice "c" after six passes and (e) slice "d" after six passes. All ATDs are combined in (f). ATDs were extracted using MassLynx 4.1. Data were acquired with Dr Dale Cooper-Shepherd at Waters Corporation.

In order to characterise the conformational heterogeneity observed further, ATDs were fitted to Gaussian distributions (Figure 4.9). Here, it can clearly be seen that after two passes slice *b* in particular is resolved, and best fit to two conformational families, and slice *a* resolves into at least three distinct families.

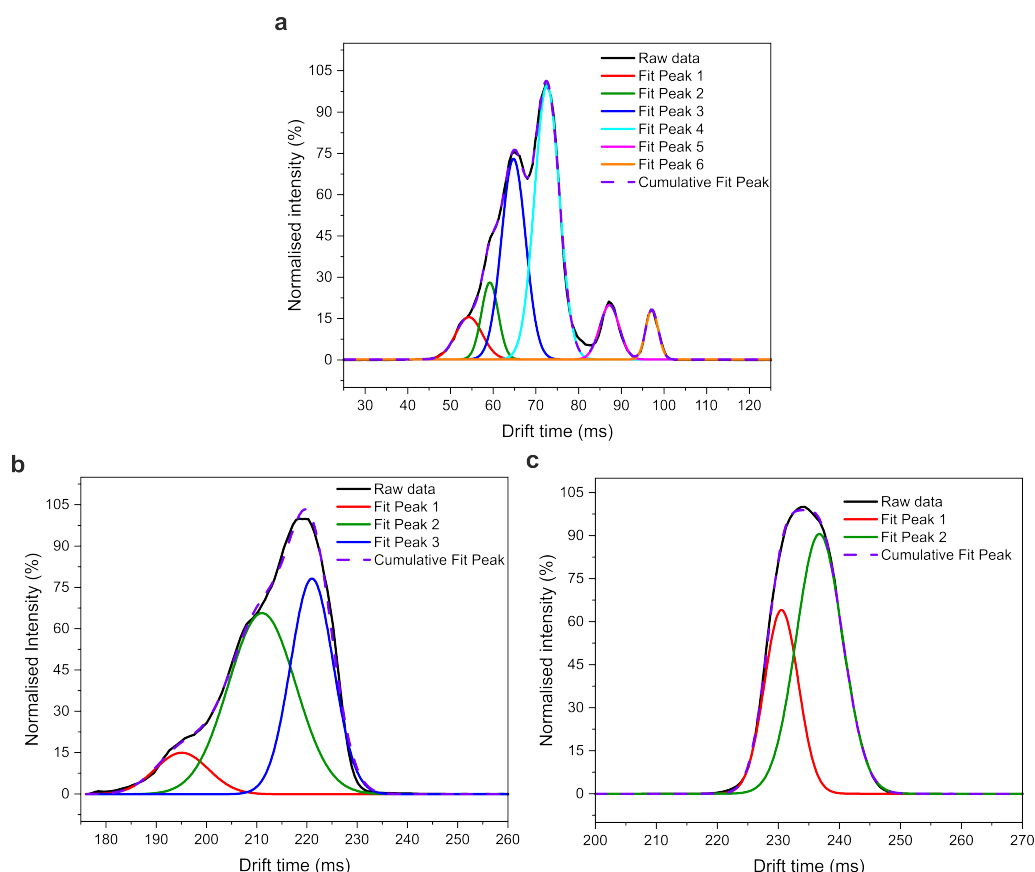


Figure 4.9 Gaussian fitting of cIM-MS for the 8+ charge state of α SNTA. Gaussian fitting for (a) the 8+ charge state after one pass of the cyclic, (b) slice *a* after two passes and (c) slice *b* after two passes. ATDs were extracted using MassLynx 4.1. Data were acquired with Dr Dale Cooper-Shepherd at Waters Corporation.

Next, slice *a* was interrogated further after different numbers of passes through the cyclic. After two passes, each fitted distribution is broader than observed in Figure 4.9a after one pass. Slice *a* was subsequently split further into three slices; *a1*, *a2*, and *a3*, each

of which was passed around the cyclic a further five times resulting in the spectra shown in Figure 4.10.

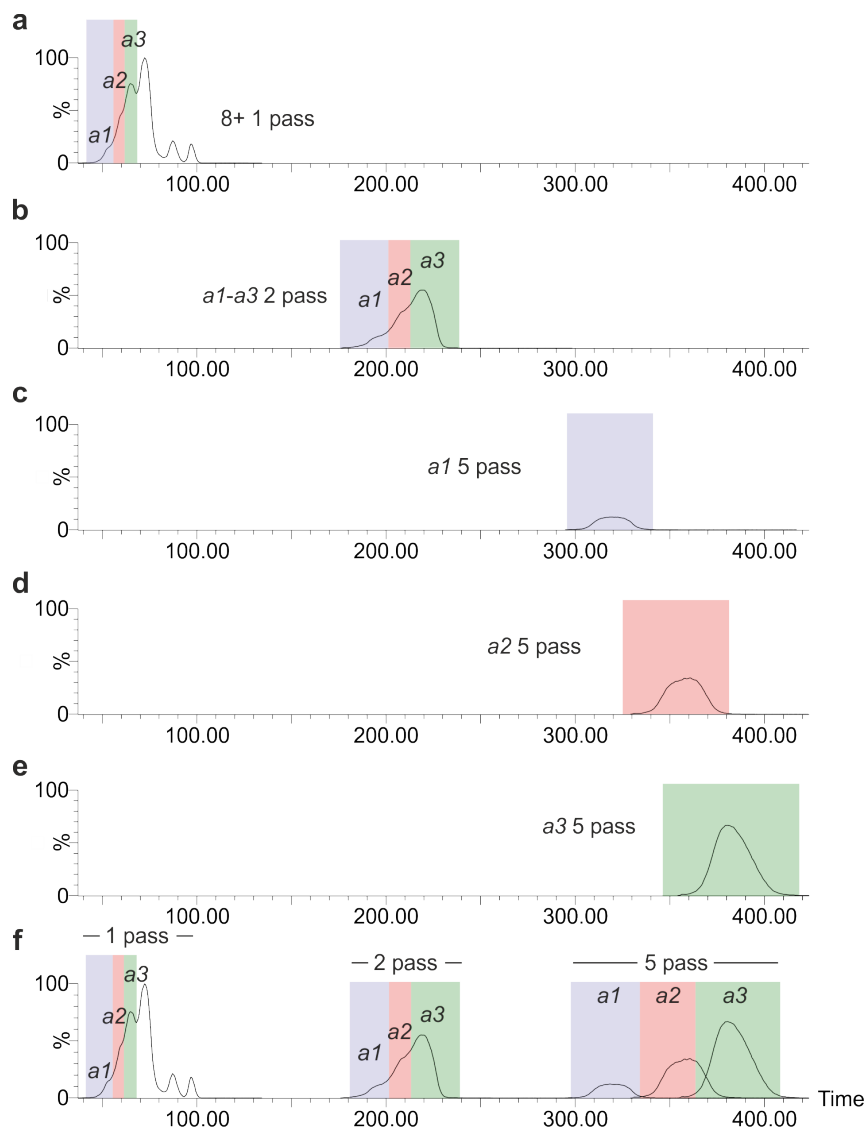


Figure 4.10 Cyclic IM-MS of slice *a* of the 8+ charge state of WT α SNTA. Arrival time distribution for (a) slice *a* from within the 8+ charge state of WT α SNTA after one pass of the cIM cell identifying three components; *a1*, *a2* and *a3*, (b) Slice *a1-3* after two passes, (c) slice *a1* after five passes, (d) slice *a2* after five passes and (e) slice *a3* after five passes. All ATDs are combined in (f) by superposition of the individual spectra. ATDs were extracted using MassLynx 4.1. Data were acquired with Dr Dale Cooper-Shepherd at Waters Corporation.

Each slice from peak *a* in Figure 4.10 was passed around the cyclic five times. The resulting ATDs were fitted to Gaussian distributions (Figure 4.11). Slice *a1*, *a2* and *a3* each separate into two components, all of which are stable on the hundreds of ms timescale.

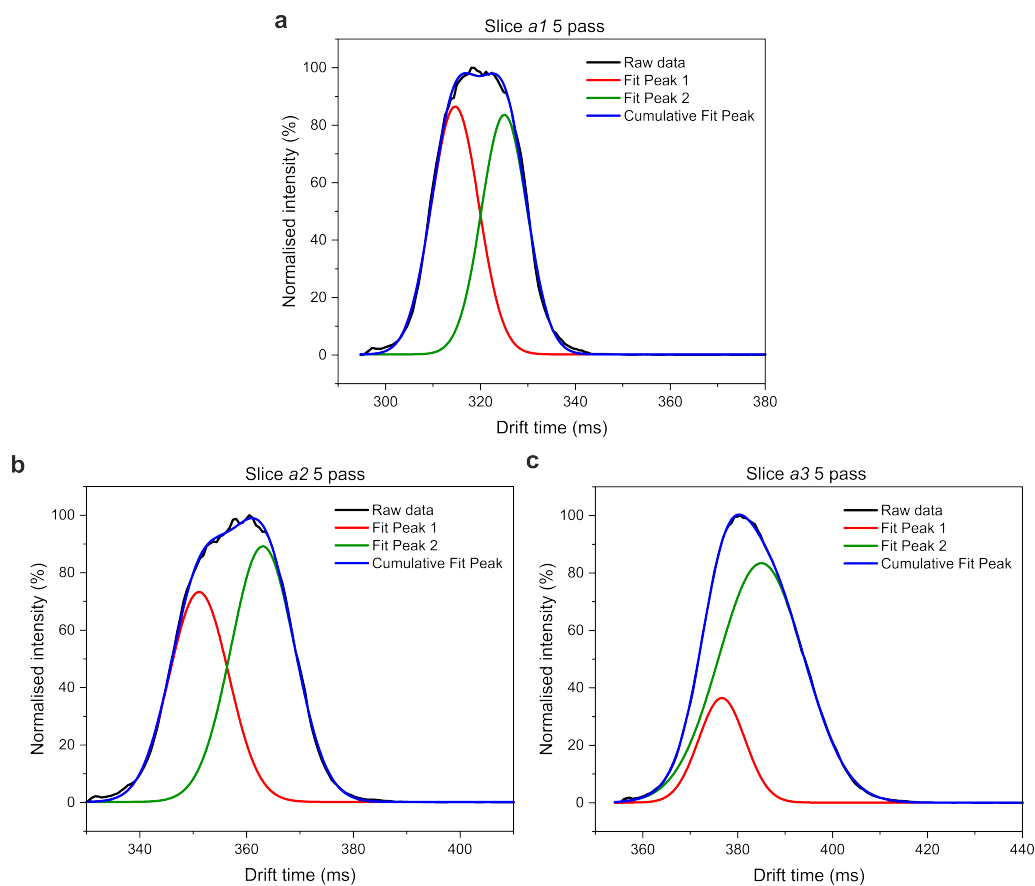


Figure. 4.11 Gaussian fitting of cIM-MS of slice *a* for the 8+ charge state of α SNTA. Gaussian fitting for (a) slice *a1* within the 8+ charge state after five pass of the cyclic, (b) slice *a2* after five passes and (c) slice *a3* after five passes. ATDs were extracted using MassLynx 4.1. Data were acquired with Dr Dale Cooper-Shepherd at Waters Corporation.

cIM showed that α SNTA occupies multiple distinct conformational families which are slowly interconverting species. XL-MS is used to gain a deeper understanding of the conformational ensemble at a residue specific level, shown in the next section of this chapter.

4.5 Long range intramolecular interaction increase in the presence of Zn^{2+}

In order to characterise the interactions which stabilise the compact conformational families induced when Zn^{2+} binds to WT α SNTA, an XL-MS approach was applied. Cross-linking captures the most abundant inter- and intramolecular interactions present in solution at one snapshot in time, all of which can be mapped onto the protein sequence using MS/MS. Nonetheless, capturing the discrete, close intramolecular interactions that occur within an IDP is particularly challenging [419, 93, 420]. Therefore the methodology applied in this section was carefully devised to prevent over-cross-linking and cover the entire sequence of α S.

The N-terminal region of α S contains 11 Lys residues and 7 Glu/Asp residues, whilst the C-terminal region contains 15 negative Asp and Glu residues and 3 Lys residues (Figure 1.25). This different distribution in charged residues could be responsible for long-range intramolecular interactions and XL of these residues was used to define the XL chemistry needed to capture α S conformations. As well as this, due to the length of the α S sequence, a short cross-linker would be needed to capture close interactions. The cross linker DMTMM (Figure 1.16) fulfils these requirements, and the optimisation process is shown in Figure 4.12. DMTMM cross-links Lys primary amines to activated carboxyl groups of Asp and Glu residues, and is also a zero-length cross linker with optimal activity at pH 7.5 [103].

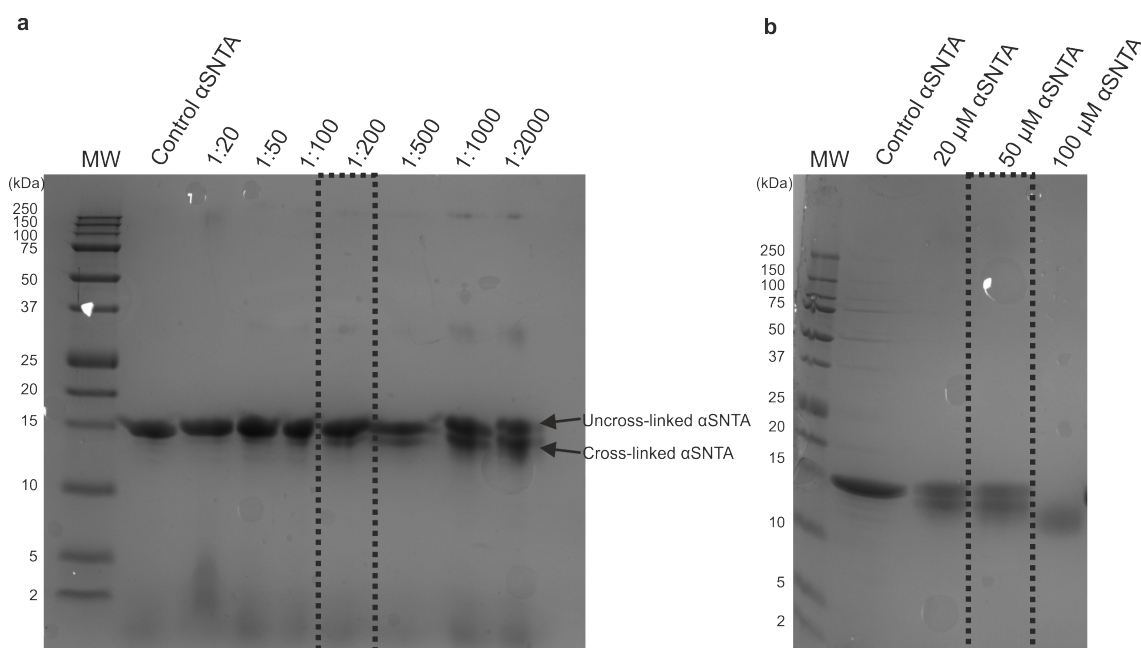


Figure. 4.12 Optimisation of DMTMM cross-linking of WT α SNTA. Cross-linking was performed in 20 mM HEPES, pH 7.4 at room temperature for 20 min. (a) Optimisation of DMTMM concentration with 60 μ M α SNTA, the lane highlighted was selected for MS/MS analysis. (b) Optimisation of protein concentration, 50 μ M protein was chosen for experiments. The band at higher MW reflects the un-cross-linked protein.

In order to ensure capture of monomer only and avoid intermolecular cross-linking, a ratio of 200-fold molar excess of cross-linker with 50 μ M α SNTA was used for cross linking experiments. Carried out in triplicate, the SDS-PAGE gel in Figure 4.13 shows the occurrence of a second band below that of α SNTA in the control lane and no-minimal dimer abundance. This band was assumed to contain cross-linked monomers capturing partially compact conformational families. A high concentration of un-crosslinked protein remains (at least as estimated by a mobility unchanged relative to the α SNTA control lane) which infers that minimal cross linking has occurred to not perturb the conformational families of α SNTA in solution.

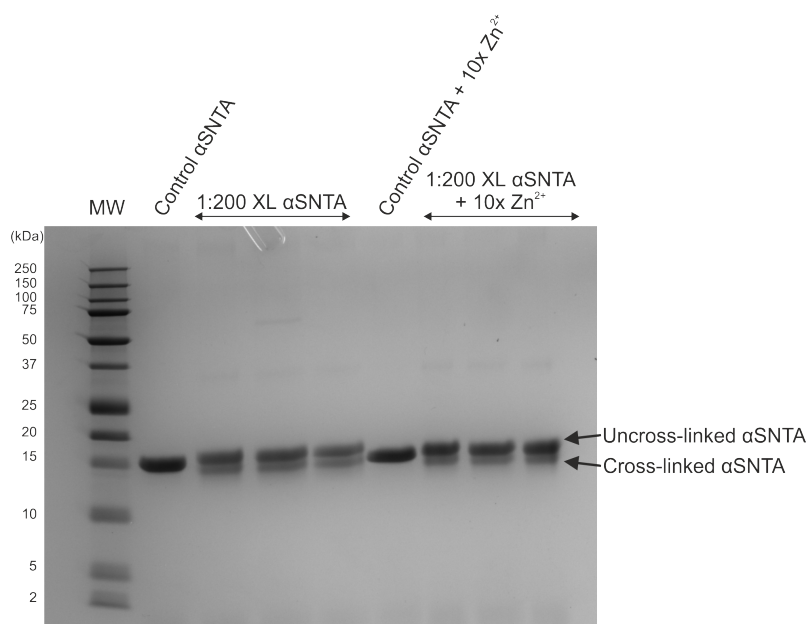


Figure 4.13 DMTMM cross-linking of WT α SNTA with Zn^{2+} . 50 μ M α SNTA was reacted with 500 μ M Zn^{2+} (10x molar excess), 10 mM DMTMM was added as a 200-fold excess. Cross-linking was performed in 20 mM HEPES, pH 7.4 in triplicate with and without Zn^{2+} .

Cross linked α SNTA was digested with 0.02 μ g/ μ L GluC as a ratio of 1:20 (protein:enzyme). Proteolysis was carried out using S-trap digests in Methods Section 2.8.2. GluC offers coverage of the entire α S sequence due to the distribution of Glu residues (coverage shown in Figure A.7). GluC and analysed by LC-MS/MS on the Thermo Fisher Orbitrap Eclipse tribrid. Label-free relative quantification was performed using the XlinkX node in ProteomeDiscoverer (ThermoFisher Scientific) to calculate cross-link abundances from precursor ion peak areas across replicates. In Figure 4.14a, the error bars appear large representing the spread of peak areas across all detected cross-links. Replicates are varied which highlights the complexity of cross-linking the conformational ensemble of an IDP [419, 93, 420]. Since there is no clear increase in cross-links when Zn^{2+} is present, it can be assumed that there are also some cross-links that decrease in abundance with Zn^{2+} . The enzyme GluC cleaves at the C-terminus of Glu residues which is also a potential

Zn^{2+} binding site. Hence, the cross linked peptides observed were particularly long in length (Figure 4.14b) which makes localising the precise position of cross-links difficult and this is reflected in the number of missed cleavages in Figure 4.14c which reduced sequence coverage. Cross link spectral matches (CSMs) with an XlinkX score above 40 are suggested by ThermoFisher to present a "good" fragment ion series and this cut-off was used when filtering the data to observe cross links.

After manual filtering of the chromatograms containing precursor peak areas used for quantification, the final cross links are presented in Figure 4.14e. The green cross links increase in abundance in the presence of Zn^{2+} , which may reflect an increase in long-range interactions responsible for stabilising compact conformations. For these cross-linking experiments, a ratio of 1:10 molar excess of Zn^{2+} was used to optimise compaction of the ensemble of α SNTA whilst minimising the number of Zn^{2+} binding events. Some cross-links decrease or are not detected at all with Zn^{2+} which could be due to loss of intramolecular interactions, or blocking of cross linking sites due to Zn^{2+} binding.

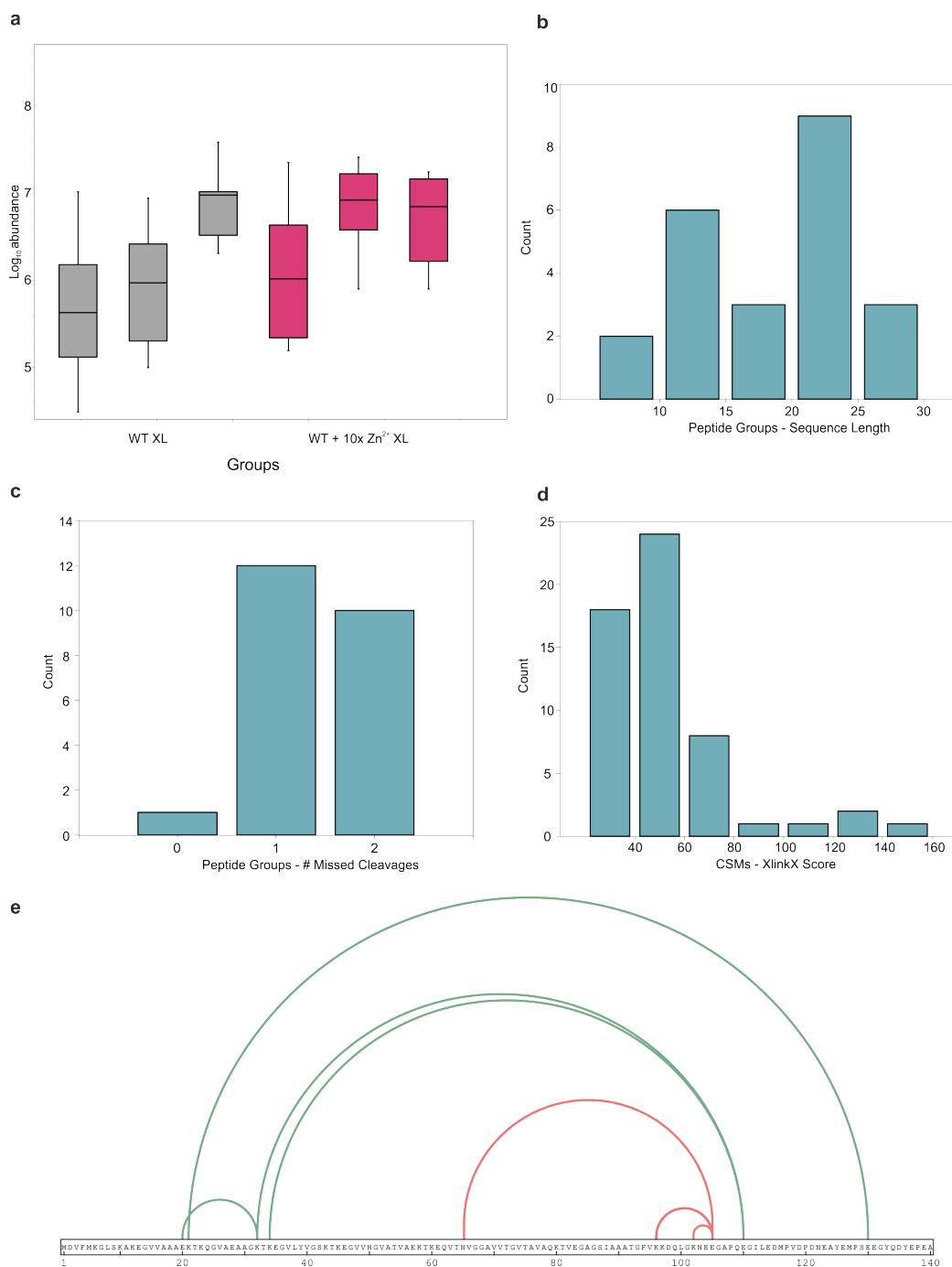


Figure. 4.14 XL-MS of α SNTA in the presence of Zn^{2+} identifies an increase in long range intramolecular interactions. (a) Comparison of the \log_{10} abundance of cross-link spectral matches (CSMs) across replicates. (b) The sequence length of peptides generated by the GluC digest for detected cross-links. (c) The number of missed cleavages for the GluC digest. (d) CSM XlinkX score. (e) A map of the final detected XLs which increase (green) or decrease (red) in the presence of a 10-fold molar excess of Zn^{2+} to $50 \mu\text{M}$ α SNTA). Analysed using the XlinkX node on Proteome Discoverer (ThermoFisher).

Using the XlinkX node in proteome discoverer (ThermoFisher), quantification is determined by the intensity of the precursor ion peak area detected normalised to total peptides and this is shown for the groups defined "WT XL" and "WT Zn²⁺ XL" across replicates (WT representing WT α SNTA). For the cross links that increase with Zn²⁺, the quantification channels are shown in Figure 4.15.

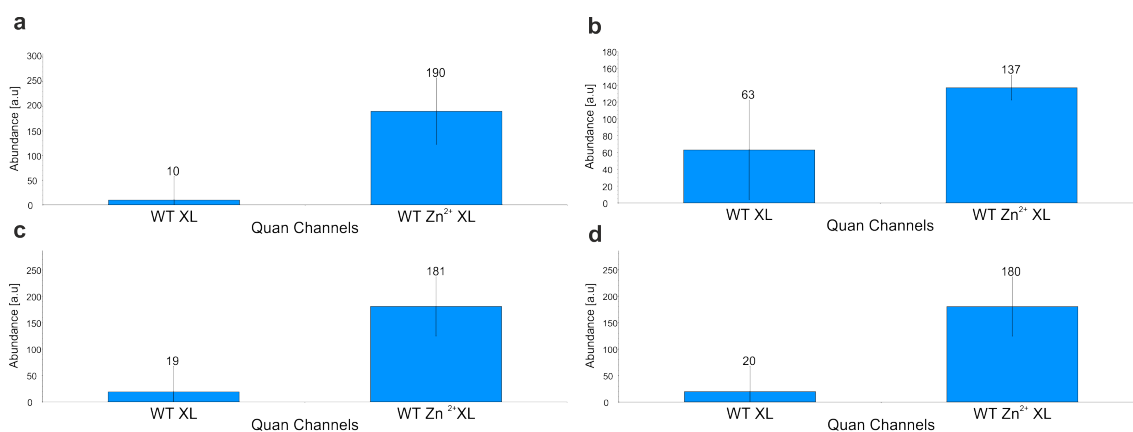


Figure 4.15 Quantification channels for precursor ion quantification of cross-linked peptides which increase in the presence of Zn²⁺. Residues (a) 21-130. (b) 20-32. (c) 32-110. (d) 34-110. Analysed using the XlinkX node on Proteome Discoverer (ThermoFisher).

The quantification channels for cross links that decrease with Zn²⁺ depicted in Figure 4.14e, are shown in Figure 4.16. For all quantification channels show in Figures 4.15 and 4.16, the errors bars are large, highlighting the variability of cross-linking across replicates, particularly in the WT control samples (in the absence of Zn²⁺). This could be due to high heterogeneity in samples, with long lived conformations, but is likely due to the stochastic nature of attempting to cross link an IDP, and especially α S with its unstructured and non-random distribution of Lys and Glu/Asp residues.

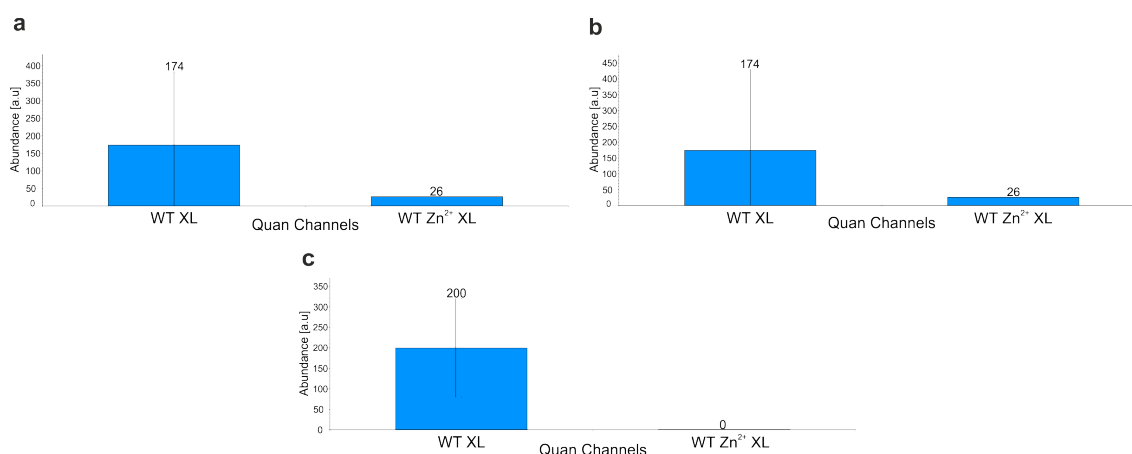


Figure 4.16 Quantification channels for precursor ion quantification of cross-linked peptides which decrease in the presence of Zn^{2+} . Residues (a) 97-105. (b) 102-105. (c) 65-105. Analysed using the XlinkX node on Proteome Discoverer (ThermoFisher).

A powerful approach that enables intra- and inter-protein cross-links to be distinguished was demonstrated in [102] and could present a route to establish how the monomer conformational ensemble adapts throughout amyloid assembly (intramolecular interactions), how oligomers assemble (intermolecular interactions) and how the monomeric conformational ensemble relates to monomer packing within oligomeric and fibril assemblies (intramolecular interactions). The authors introduce COMPASS, a methodology which relies on ^{14}N or ^{15}N protein labelling to characterise intra-molecular from inter-molecular cross-links. Their approach was used to analyse the behaviour of α S during LLPS, showing that the formation of liquid droplets is associated with an increase in inter-molecular interactions between α S monomers. Through analysis of intra-molecular cross-links formed using EDC, the authors showed that elongated conformational families of α S are adopted during LLPS. Such an approach would be ideal in the future to investigate the role of Zn^{2+} in enhancing amyloid assembly via its effect on monomer conformations during amyloid assembly.

4.6 Zn²⁺ titration with α SNTA by NMR

The interaction between α S and divalent and monovalent metal ions has been studied using NMR [402, 183, 421–423, 394, 413, 424, 425, 321]. These studies identified H50 and D121 as key interactors with Cu²⁺ [402] and D121 in the peptide ¹¹⁹DPDNEA¹²⁴ with Cu²⁺, Mn²⁺, Fe²⁺, Co²⁺ and Ni²⁺ [183]. Additional key interaction sites were observed in the N-terminal region at D2 and M1 with Cu²⁺ [426]. Measurements of K_d for α S with Cu⁺ identified the imidazole ring of H50 as a key anchoring residue for binding (K_d of 50 μ M), with key sites also M1 and M5 as co-ordination sites with K_d values of 20 μ M, whilst M116 and M127 in the C-terminal region were measured to have K_d values of 270 μ M [394]. Different metal ions have been shown to interact with different regions of α S, where Cu²⁺ ions have a high propensity to interact with the N-terminal residues and H50, whilst Ca²⁺ preferentially interacts with the C-terminal region [321]. Similarly, Zn²⁺ preferentially binds to H50 and the C-terminal region, particularly ¹¹⁹DPDNEA¹²⁴, preferring carboxyl groups over nitrogen containing groups [413].

The interaction of Cu⁺ with N-terminal acetylated α S has also been investigated. Similarly to non-acetylated α S, key binding sites for Cu⁺ were observed in the N-terminal region (M1 and M5), with the addition of the acetyl group also increasing the occurrence of α -helical structural content occurring near the N-terminus [424].

As a more *in vivo* approach, α S synaptic vesicle interactions in the presence of Ca²⁺ have also been probed by NMR. These studies showed, the binding of Ca²⁺ to the C-terminal region of α S increased the interaction of α S with synaptic vesicles by increasing lipid binding properties [321]. A K_d value of 21 μ M was reported for α S : Ca²⁺ affinity, which lies within the physiological concentration range of Ca²⁺ in pre-synaptic nerve terminals which can reach up to 200-300 μ M in healthy stimulated neurones [321, 427, 428]. Inspired by these studies, the interaction of α SNTA with Zn²⁺ was probed here by

employing ^{15}N - ^1H NMR to identify binding sites and regions of conformational change upon Zn^{2+} addition (Figure 4.17).

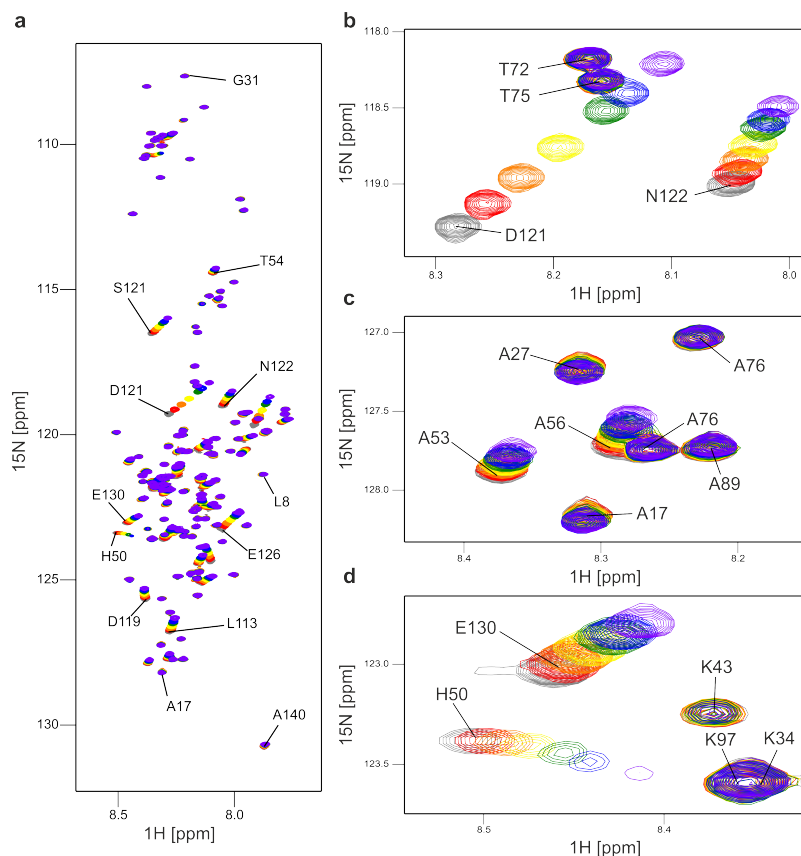


Figure 4.17 ^{15}N - ^1H HSQC NMR spectra showing a Zn^{2+} titration with α SNTA. The concentrations of Zn^{2+} used were 0 μM (grey), 100 μM (red), 250 μM (orange), 500 μM (yellow), 1 mM μM (green), 1.5 mM (blue) and 2.5 mM (purple). (a) ^1H - ^{15}N HSQC spectra of α SNTA in the absence (grey) of Zn^{2+} or in the presence of Zn^{2+} (red-purple). (b) Cross-peaks of residue D121 which shows significant movements in peak positions, cross-peaks of N122 which shows some peak movement. No chemical shifts are observed for T72 or T75. (c) Cross-peaks for Ala residues show no significant peak movements with Zn^{2+} . (d) Cross-peak movement of H50 and E130. Spectra were acquired at 25°C in 20 mM ammonium acetate, pH 7.5, 100 μM α SNTA. Spectra were acquired and analysed by Dr Ben Rowlinson the University of Leeds.

¹⁵N α SNTA expression is outlined in methods Section 2.2.2 and all NMR experiments and data analysis were kindly performed by Dr Ben Rowlinson, the University of Leeds. In agreement with previous studies [183, 413], Figure 4.17 identified H50 and D121 as key residues for Zn²⁺ binding. Clear chemical shifts were observed for D121 throughout the Zn²⁺ titration (Figure 4.17b). Interestingly for H50, whilst the cross-peaks continue to shift with increasing concentrations of Zn²⁺, the intensity of the H50 resonance decreases (Figure 4.17d) which could be due to the population of a new conformation of α SNTA at high concentrations of Zn²⁺ which is also supported by the observation that the shift is not linear. Backbone chemical shift perturbations (CSP) identify changes in environments which include binding events and conformational changes, and from this apparent K_d values can be determined per residue by performing best fit analysis (Figure 4.18).

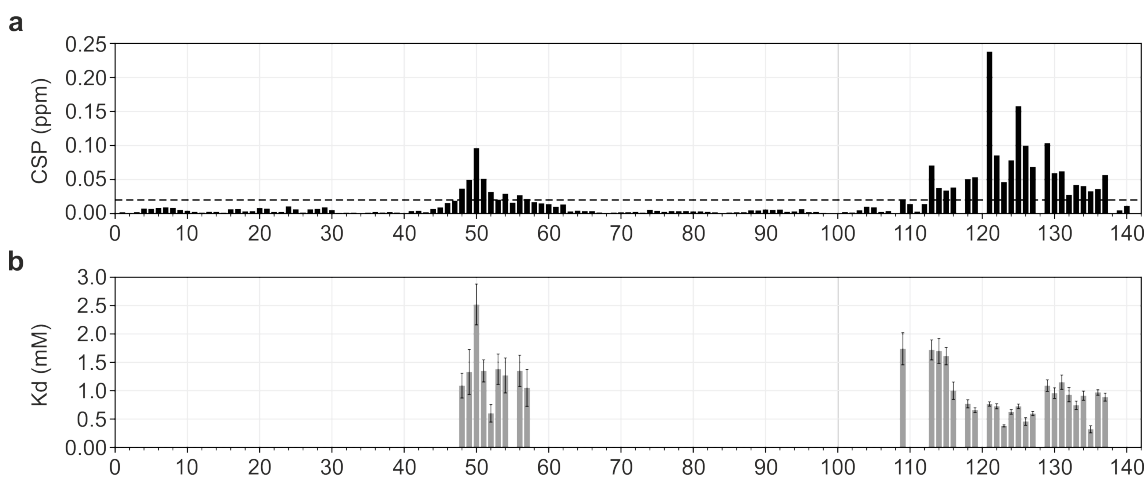


Figure. 4.18 Chemical shift perturbations and fitting of α SNTA Zn²⁺ binding from ¹H-¹⁵N HSQC spectra. (a) CSP of α SNTA after the addition of Zn²⁺ at 25 °C in 20 mM ammonium acetate, pH 7.5. The dashed line represents an arbitrary cut-off value of 0.02 determined by fits for K_d. (b) K_d fitting of α SNTA ¹H-¹⁵N HSQC spectra at increasing Zn²⁺ concentrations. Error bars represent the standard deviation of the K_d fitting. Spectra were acquired and analysed by Dr Ben Rowlinson the University of Leeds.

CSPs are sensitive to changes in the local chemical environment of each of the backbone amide bonds. The magnitude of CSPs is shown in Figure 4.18a and, in agreement with the literature, the greatest CSPs were observed for H50 and D121, as well as Y125 and S129 [402, 183], adjacent residues likely due to conformational change. Because some peaks are in immediate exchange (i.e. peaks are moving and lose intensity through the titration with Zn^{2+}), the K_d values determined in Figure 4.18b are estimated based on the CSP data and may over-estimate the K_d . This is particularly apparent for H50, where a significant loss in peak intensity is observed (Figure 4.17d). Another plausible explanation for the large K_d values determined (10-100 times larger than observed by MS) is the change in conformation adopted by α SNTA which occurs on a slow (hundreds of μs to possible ms) time-scales, as observed by cIM. These slow dynamics of intermediate exchange are observed in the NMR spectra by the occurrence of new, unassigned peaks with low intensity, which also move as Zn^{2+} binds, and change in intensity. Several examples of such peaks are shown in Figure 4.19a-c.

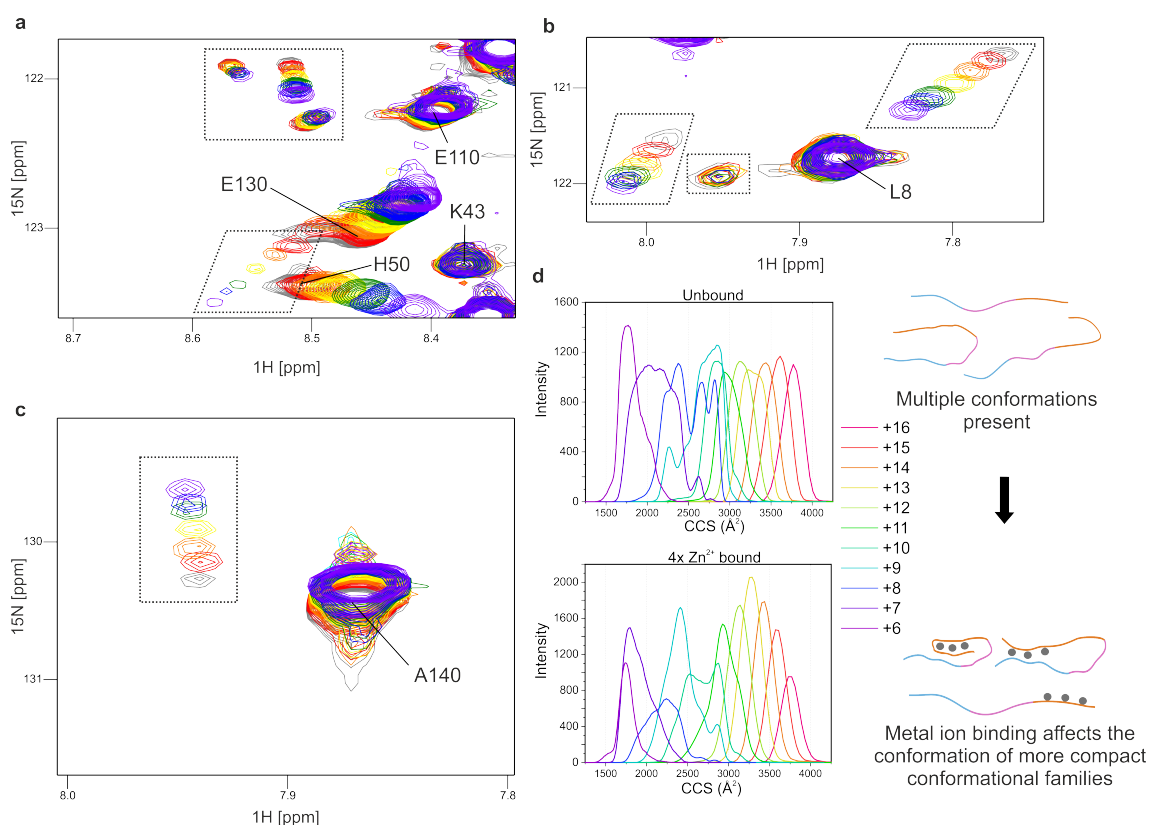


Figure 4.19 Minor peaks observed in ¹⁵N-¹H HSQC NMR spectra. Observation of minor peaks of low intensity which shift with increasing excess of Zn²⁺ are shown in dashed boxes. (d) IM-MS showing the conformational ensemble of α SNTA by ^{TW}CCS_{N2} of all charge states without Zn²⁺ present, and when Zn²⁺ is added the shift of lower charge states to populate decreased ^{TW}CCS_{N2} represented by the schematic on the right. ¹⁵N-¹H HSQC NMR spectra were acquired and analysed by Dr Ben Rowlinson the University of Leeds.

The minor peaks may reflect IM-MS findings presented in Figure 3.24. An ensemble of partially compact and extended conformations of α SNTA exist, and this snapshot was observed in the gas phase by IM-MS. When α SNTA is bound to four Zn²⁺ ions, the lower charge states representing more compact conformations become more compact (lower ^{TW}CCS_{N2}) whereas the higher charge states which reflect more extended conformations in solution do not change [369]. The compact conformation may be responsible for the minor peaks in the NMR spectra, which become more compact as Zn²⁺ binds, resulting

in the movement of cross-peaks, which may become more intense as the population of the compact species increases. This could be a direct correlation between the minor peaks observed in NMR and the $^{TW}CCS_{N2}$ values attained by IM-MS, and additionally reinforcing the slow dynamics of interconversion exhibited by α SNTA also observed by cIM-MS in Figure 4.7.

4.7 Revealing conformational sensitivity with native top-down intact fragmentation

4.7.1 Investigating α SNTA structure using ETD

Native top-down proteomics is emerging as a powerful protein and peptide sequencing and conformational foot-printing tool, for example in the direct identification of membrane proteins liberated from their native membrane environments [429, 430]. Here, ETD is applied to probe the effect of native versus denaturing conditions on the structure of α SNTA through the fragmentation fingerprint detected. The nESI mass spectrum for native α SNTA is shown in (referring to the solution conditions used in the experiments, 20 mM ammonium acetate, pH 7.5) Figure 4.20a and denaturing conditions (50 % (v/v) acetonitrile, 0.1 % (v/v) formic acid.) α SNTA in Figure 4.20b.

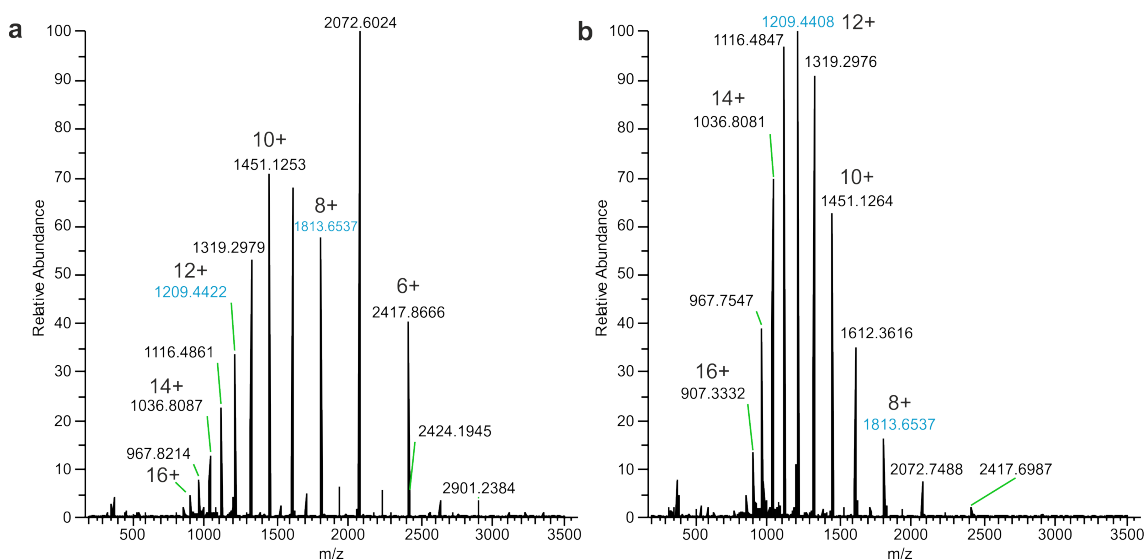


Figure. 4.20 Native and denatured mass spectra of α SNTA recorded on a ThermoFisher Orbitrap Eclipse instrument. (a) Mass spectrum acquired in 20 mM ammonium acetate, pH 7.5. (b) Mass spectrum acquired in 50 % (v/v) acetonitrile, 0.1 % (v/v) formic acid. The 12+ (m/z 1209) and the 8+ (m/z 1813) charge states are shown in blue.

The ETD fragmentation spectrum for α SNTA in denaturing solution conditions is presented in Figure 4.21. The 12+ charge state was selected as higher charge states result in more efficient ETD fragmentation. The high density of positive charges increases interactions with negatively charged electrons[431]. Additionally, the 12+ charge state has been demonstrated by IM-MS to populate an extended conformational family (Figure 3.11) and, is therefore a more fragmentation-competent state.

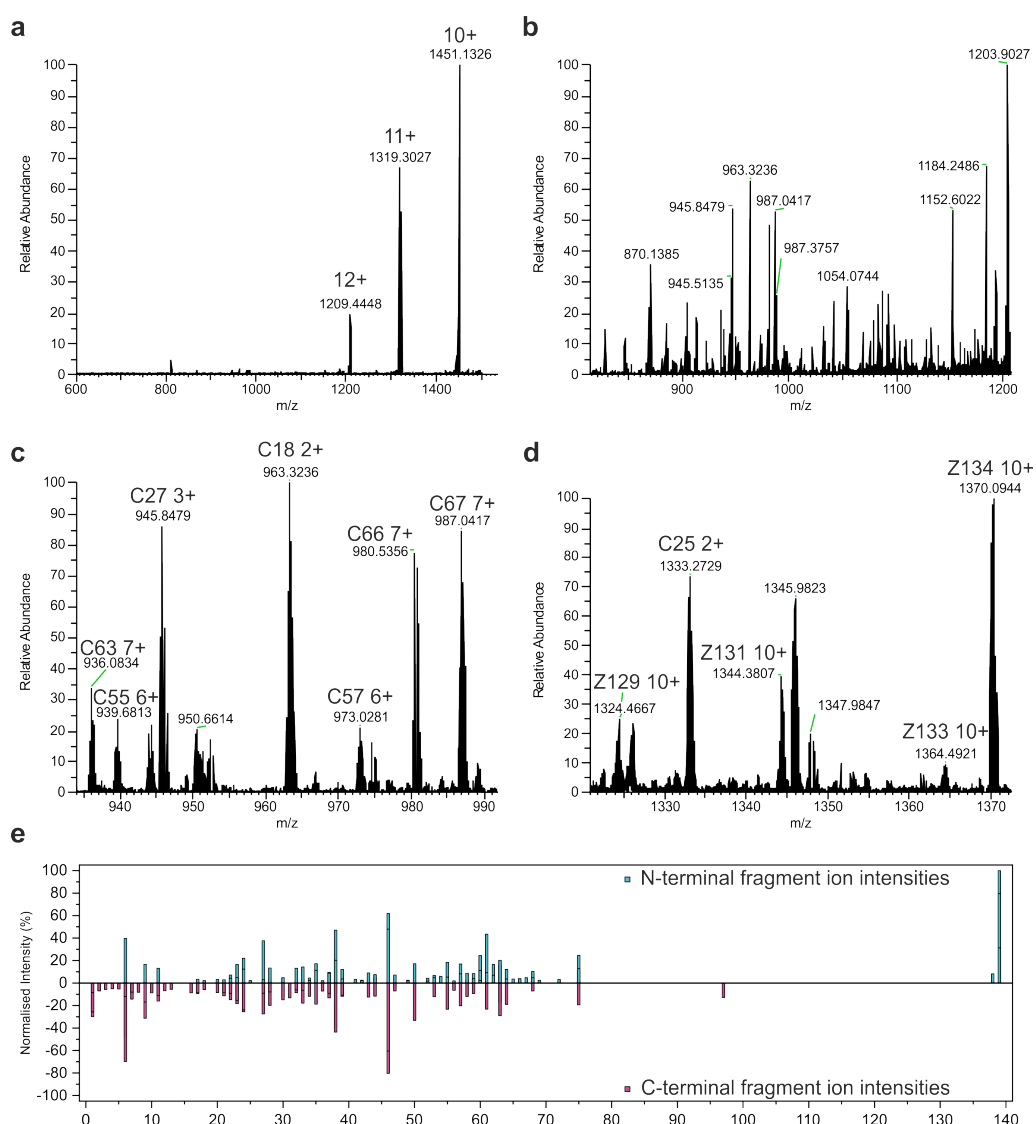


Figure. 4.21 α SNTA ETD fragmentation spectra for denaturing solution conditions. (a) Full MS1 spectrum for the isolated 12+ charge state (m/z 1209) subjected to ETD for a duration of 5 ms. ETnoD states are shown as the 11+ and 10+ charge state. (b) Zoomed area from the full spectrum, showing the low abundant fragment ions. (c) Annotation of some c-type ions. (d) Annotation of some c-type and z-type ions. (e) Normalised intensity plot of all of the c- (N-terminal fragment ions; blue) and z-type (C-terminal fragment ions; pink) ions detected extracted using the TD validator node in ProSight Native by Proteinaceous. The ETD spectrum was acquired on the ThermoFisher Orbitrap Eclipse, 20 μ M α SNTA in 50 % (v/v) acetonitrile, 0.1 % (v/v) formic acid.

Denaturing solution conditions produce many fragment ions visible in the mass spectrum (Figure 4.21b). Coverage of c- and z-type ions is absent across the C-terminal region (residues 90-140), presumably due to the high density of negatively charged residues in this region, which would electrostatically repel negatively charged reagent ions which reduces fragmentation efficiency[432]. ETnoD states may represent the non-covalent intramolecular interactions holding compact protein conformations together [73]. Overall, in terms of c- and z-type terminal ion coverage, more C-terminal fragments are observed (c-type ions). Many mass spectral peaks, however, remain unassigned and can instead be described by multiple cleavage events generating internal fragment ions which can be used to improve sequence coverage. The number and variation of internal products theoretically possible is greater than the number of possible terminal fragments, which means that the probability of matching a spectral peak to an internal fragment becomes larger if both cleavage sites are individually found to be abundant. In turn, the ambiguity of assigning internal fragments must be considered and potentially increases the false discovery rate [433, 434]. Examples of a c-type, z-type and internal ion respectively are shown in Figure 4.22.

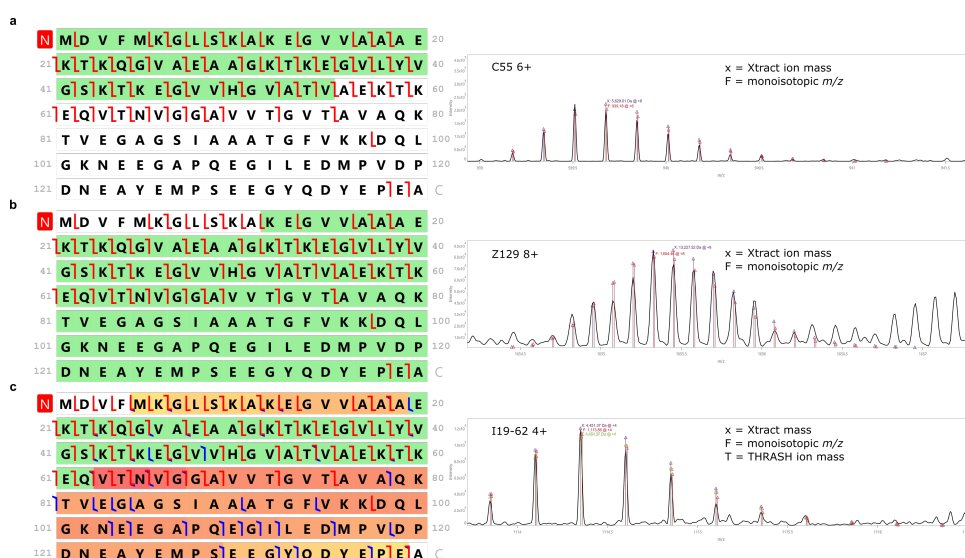


Figure 4.22 Denaturing solution conditions α SNTA ETD example fragment ion spectra. For each panel, the selected fragment ion is shown in green (a) C55 6+ terminal fragment ion. (b) Z129 8+ terminal fragment ion. (c) I19-62 4+ internal fragment ion, internal ions are shown as gradient colours where blue ticks identify internal fragment ion termini. Extracted using the TD validator node in ProSight Native by Proteinaceous

Fragmentation spectra were processed using the Top Down Validator node (TDV) in ProSight Native by Proteinaceous. The assigned isotopic spectral matches for ions C55 6+ (6+ ion with terminal fragmentation at residue 55), Z129 8+ (8+ ion with terminal fragmentation at residue 129) and the internal ions I19-62 4+ (4+ ion with internal fragmentation at residues 19 and 62) are shown in Figure 4.22. All c, z and internal ions detected are presented in Table A.1. A key aspect of native/denaturing top down fragmentation is the conformational sensitivity that could be achieved through varied fragmentation efficiencies offered by different conformational families (extended conformations offer more exposed fragmentation sites) [435]. To compare with denaturing solution conditions, the ETD fragmentation spectrum for the 12+ charge state of α SNTA in native solution conditions is shown in Figure 4.23.

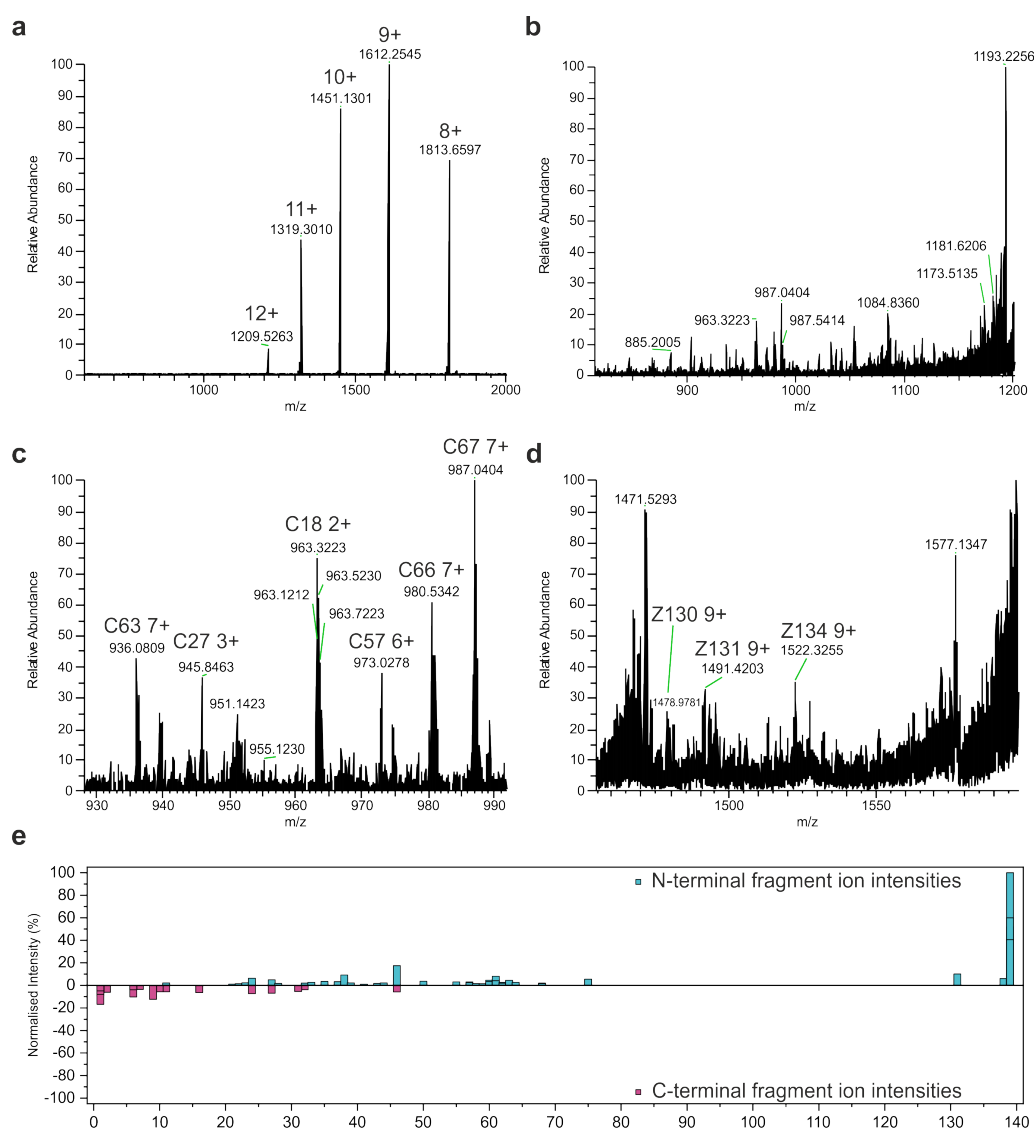


Figure. 4.23 α SNTA ETD fragmentation spectra for native solution conditions. (a) Full MS1 spectrum for the isolated 12+ charge state (m/z 1209) subject to ETD for a duration of 5 ms. ETnoD states are shown as the 11+ to 8+ charge state. (b) Zoomed area from the full spectrum showing the low abundant fragment ions. (c) Annotation of some c-type ions. (d) Annotation of some z-type ions. (e) Normalised intensity plot of all of the c- (N-terminal; blue) and z-type (C-terminal; pink) ions detected the TD validator node in ProSight Native by Proteinaceous. The ETD spectrum was acquired on the ThermoFisher Orbitrap Eclipse, 20 μ M α SNTA in 20 mM ammonium acetate, pH 7.5.

In the ETD fragmentation spectra for α SNTA under native solution conditions, fragment ions appear less intense than previously observed for denaturing solution conditions (Figure 4.23e). All assigned fragment ions are presented in Table A.2. The sequence coverage for denaturing solution conditions compared to native solution conditions are shown in Figure 4.24 for direct comparison.

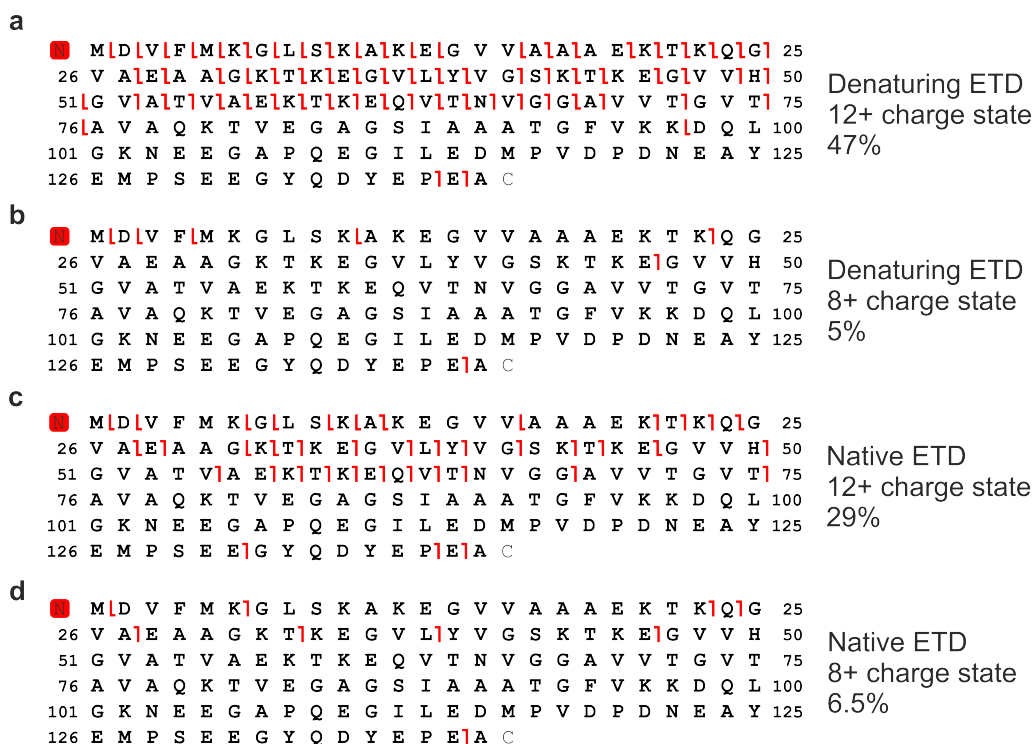


Figure 4.24 ETD sequence coverage of terminal fragment ions α SNTA using the TD validator node in ProSight Native by Proteinaceous. c- and z-type ions are shown as red ticks. Denaturing conditions ETD coverage of the (a) 12+ charge state, (b) 8+ charge state. Native conditions ETD coverage of the (c) 12+ charge state, (d) 8+ charge state.

As mentioned previously, higher charged precursor ions offer better ETD fragmentation efficiency due to faster reactions and their exposed SASA [433]. The 12+ charge state and 8+ charge state were selected for comparison for α SNTA ETD and a clear difference in fragmentation efficiency is observable. The sequence coverage in Figure 4.24 was achieved using ETD reaction times of 5 ms. Therefore for better coverage of the 8+ charge state,

longer reaction time would be required (~ 10 ms). ETD of α SNTA in denaturing solution conditions presented the best sequence coverage here, at 47% coverage, where the loss of coverage occurred in the C-terminal region due to the density of negatively charged residues. As previously stated, inclusion of internal ions can increase sequence coverage [436], and ETD sequence coverage maps including internal ions are shown in Figure 4.25.

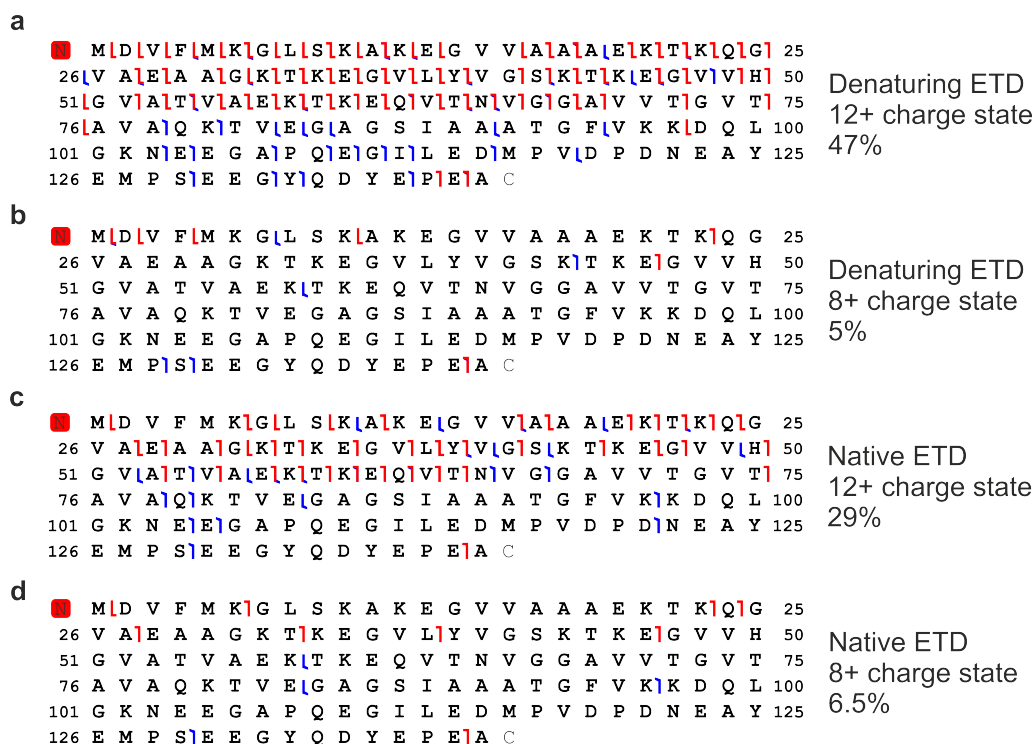


Figure 4.25 ETD sequence coverage of terminal and internal fragment ions α SNTA using the TD validator node in ProSight Native by Proteinaceous. Internal ions are shown as blue ticks and c- and z-type ions are shown as red ticks. Denaturing conditions ETD coverage of the (a) 12+ charge state, (b) 8+ charge state. Native conditions ETD coverage of the (c) 12+ charge state, (d) 8+ charge state.

Including internal ions in the fragmentation spectral matching increases the overall potential coverage of α SNTA and evidences more clearly which conditions offer optimal sequence coverage. Indeed, more internal ions are assigned for acquisitions of the 12+ charge state of α SNTA, highlighting the requirement of a higher charge state. ETD of the

12+ charge state in denaturing solution conditions offers the highest possible sequence coverage under the conditions used in this thesis (47%). Despite the fragmentation efficiency of the 12+ charge state under denaturing conditions, one must consider that the stated charge state is of much higher intensity in the denatured α SNTA acquisition which may influence assignable fragment ions and sequence coverage.

4.7.2 Investigating α SNTA structure using UVPD

UVPD fragmentation relies upon photon induced excitation of the peptide backbone when using a 213 nm wavelength laser [437]. One possible mechanism of UVPD fragmentation is direct and occurs on the femtosecond timescale and in this mechanism no energy redistribution occurs and the electronic states are excited producing ETD-like c- and z-type ions [73]. The second mechanism occurs on the femto- to pico-second timescale and involves the internal conversion of the photon energy into vibrational kinetic energy, known as intramolecular vibrational energy redistribution (IVR) [73]. The result is dissociation within a vibrationally hot molecule, leading to b- and y-type ions but also a- and x-type ions. Direct dissociation relies on little energy (6.4 eV for a 193-nm photon) available for breaking non-covalent bonds, such as the intramolecular non-covalent interactions holding the compact conformations of a protein together [438]. Internal conversion, however, would likely yield mostly b- and y-type ions which are the result of high energy vibrational dissociation due to heating. Both mechanisms together increase the coverage of proteins by UVPD [439, 440, 73]. UVPD fragmentation of α SNTA is presented in Figure 4.26.

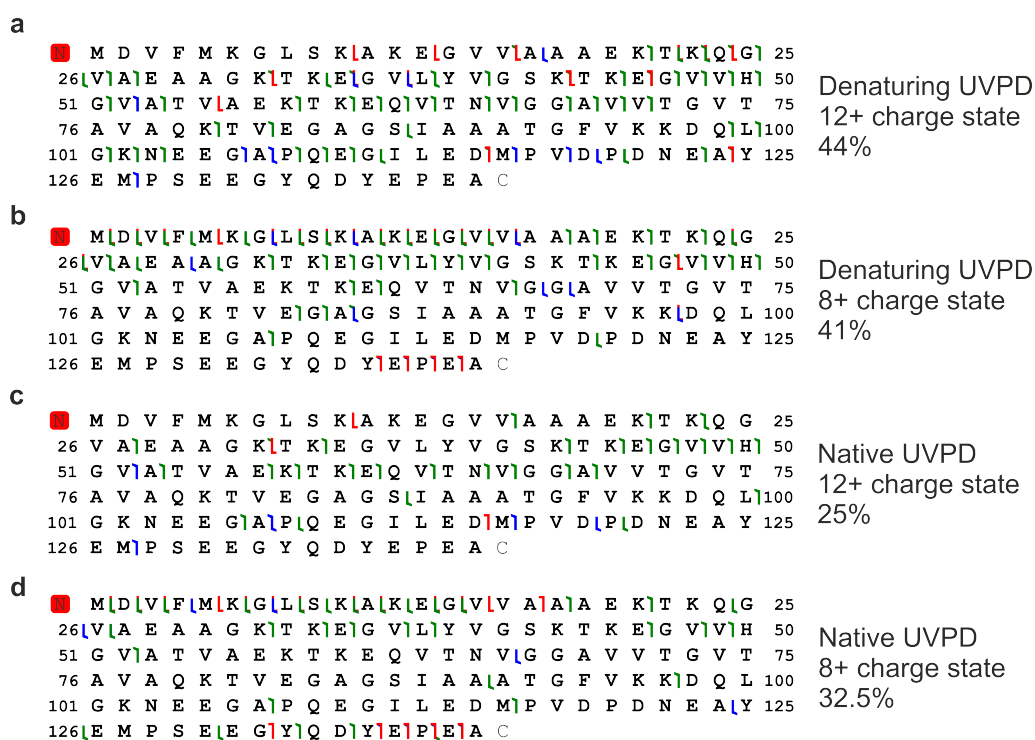


Figure. 4.26 UVPD sequence coverage of terminal fragment ions α SNTA using the TD validator node in ProSight Native by Proteinaceous. c- and z- ions are shown as red ticks, b- and y- ions are shown as blue ticks, a- and x- ions are shown as green ticks. Denaturing conditions UVPD coverage of the (a) 12+ charge state, (b) 8+ charge state. Native conditions UVPD coverage of the (c) 12+ charge state, (d) 8+ charge state.

One favourable aspect of UVPD is that the charge state of the precursor ion does not influence fragmentation efficiency and, therefore, lower charge states can be probed for conformational sensitivity [441]. This is evidenced when comparing the denatured spectra of α SNTA 12+ and 8+ UVPD coverage which are comparable (44% and 41% respectively). Nonetheless, the high abundance of b- and y-type ions could infer that the fragmentation achieved did not occur under gentle experimental conditions. UVPD fragmentation of α SNTA in denaturing solution conditions (44-41%) revealed a higher fragmentation efficiency than α SNTA in native solution conditions (25-32.5%) which could be due to the occurrence of partially compact conformations retained in ammonium

acetate, where coverage is lost in the end of the N-terminal region, the NAC region and the C-terminal region.

4.7.3 Comparing ETD and UVPD for α SNTA structure interrogation

Both ETD and UVPD fragmentation provided information regarding the optimal conditions for fragmentation and the conformational sensitivity of both mechanisms. The sequence coverage for each fragmentation experiment carried out is shown in Figure 4.27.

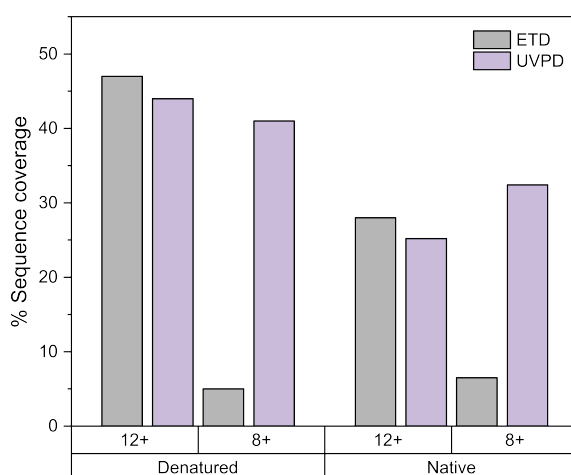


Figure 4.27 Comparing ETD versus UVPD on the fragmentation of α SNTA. A bar chart showing the % sequence coverage per condition comparing: ETD, UVPD, 12+ charge state, 8+ charge state, denaturing and native solution conditions. Sequence coverage was determined via fragment ion assignments using the TD validator node in ProSight Native by Proteinaceous.

UVPD appears to be consistent across both charge states of α SNTA selected for fragmentation, whilst ETD is much more efficient when selecting the 12+ charge state. The sequence coverage achieved here is preliminary and requires much more rigorous optimisation in order to improve back bone fragmentation and fragment assignment. Nonetheless, from the data obtained it could be concluded that top-down fragmentation methods including ETD and UVPD offer conformational sensitivity. The charge state

of a target ion is important for efficient ETD fragmentation (Figure 4.24). Following on from this work, adding Zn^{2+} ions could enable the elucidation of residue specific binding sites due to the non-covalent interaction formed, which would be retained [66]. However, since Zn^{2+} can form co-ordination spheres with proteins, interacting with multiple residues to stabilise binding, the resulting fragmentation spectra could become highly complex, revealing multiple potential binding sites [442].

4.8 smFRET

Förster resonance energy transfer (FRET) is a technique used to measure distances between labelled sites (usually 1-10 nm) in biomolecules by measuring the energy transfer between two fluorescent probes, providing information regarding conformational changes, folding or protein interactions [443, 444]. Single-molecule FRET (smFRET) enables the direct observation of individual molecules and reveals information hidden within an ensemble, providing insight into structure and the rate of interchange between conformational states. Here, pulsed interleaved excitation (PIE) was used to extract information not only about the intensity of the fluorescent probes (i.e., the number of photons emitted), but also their fluorescent lifetime (τ ; the time spent on average in the excited state), as well as the labelling stoichiometry to select bursts which contain both a donor and acceptor dye (due to stochastic labelling, not all molecules contain a donor and an acceptor fluorophore) [445].

The gene encoding α SNTA was mutated to contain Cys residues at positions 7 in the N-terminal region and 140 at the C-terminus (α SNTA_{G7C-A140C}) for double labelling with Alexa Fluor 488 and ATTO 565 maleimide (Figure 4.28) and was expressed and purified as discussed in 2.2.2 (Figure 4.28a). This construct was designed to probe the end-to-end distance of α SNTA to monitor extension or compaction of the protein upon

addition of metal ions. smFRET data were kindly acquired and analysed by Dr Joel Crossley, University of Leeds.

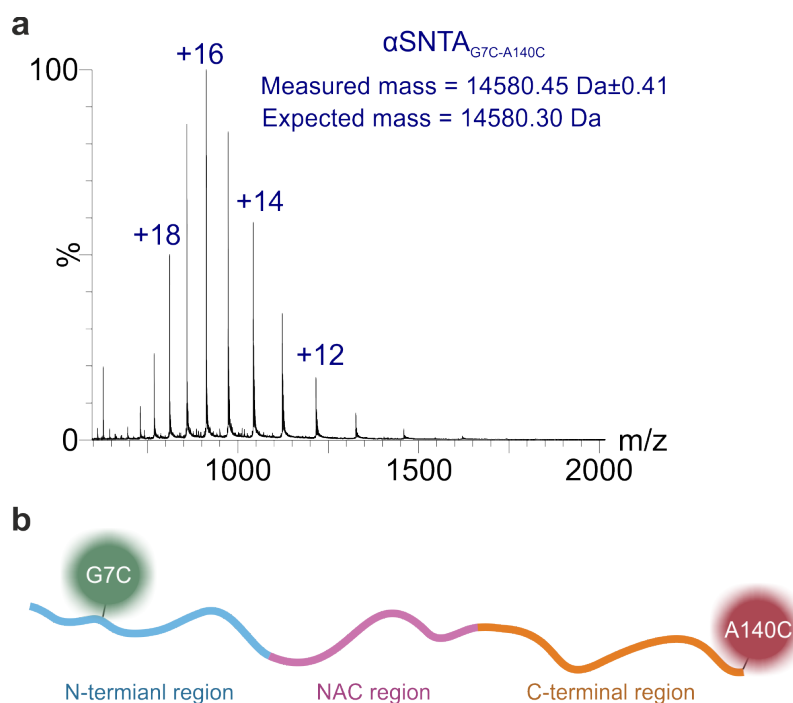


Figure. 4.28 α SNTA_{G7C-A140C} smFRET construct. (a) Denaturing LC-MS of purified α SNTA_{G7C-A140C} measured at a concentration of 1 μ M in 0.1% (v/v) trifluoroacetic acid on a Xevo G2-XS QToF instrument (Waters, UK). (b) the two labelling positions as green and red circles. Under the labelling conditions used, fluorophore labelling is stochastic (i.e., the donor or acceptor dye can label each Cys residue).

An example of the first second of the time trace for the experiment is shown in Figure 4.29, where single proteins that diffuse through the confocal volume are detected as individual bursts of photons. In the case of a protein labelled with both a donor and an acceptor dye (a FRET pair), photons are emitted in both spectral channels [446].

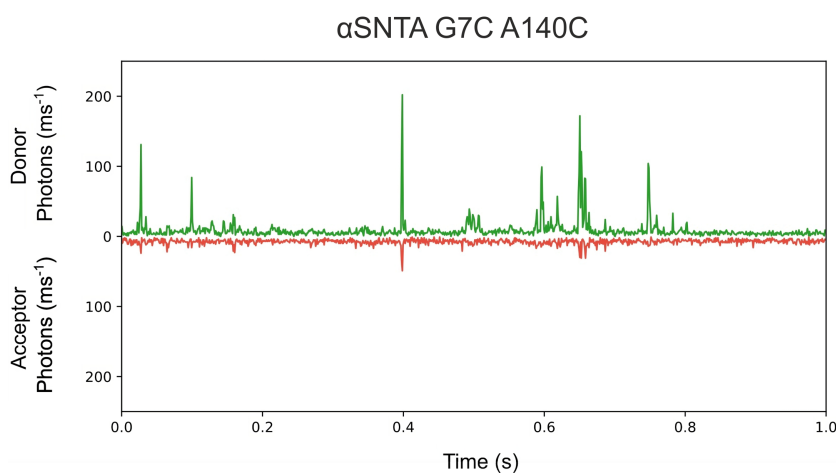


Figure. 4.29 Time trace of $\alpha\text{SNTA}_{\text{G7C-A140C}}$ in 20 mM Tris HCl, pH 7.5 at 50 pM protein concentration. Upon donor excitation, emission in the donor channel (green) and the acceptor channel (red) was recorded in time. Each burst represents one labelled $\alpha\text{SNTA}_{\text{G7C-A140C}}$ protein molecule diffusing through the confocal volume. Data were acquired and analysed by Dr Joel Crossley, University of Leeds.

For each burst where a donor burst coincides with an acceptor burst, FRET efficiency (E) was obtained from the ratio of the emission intensity of the donor and the acceptor fluorophores. For $\alpha\text{SNTA}_{\text{G7C-A140C}}$, the FRET efficiency is shown in Figure 4.30 a. FRET efficiency reflects the average distance between the donor and acceptor whilst the protein traversed the confocal volume. Two major populations are observed in the histogram, with $E \approx 0.35$ and $E \approx 0.05$. To investigate any potential dynamics in the sample, τ_{D} was calculated and plotted against E (Figure 4.30b). In this plot, FRET populations which remain static during their passage of the confocal volume (~ 1 ms) land on the 'static line' (solid black line), while molecules which are dynamic deviate from this line. A model for dynamics following a Gaussian chain model is shown as a dashed black line [447]. For $\alpha\text{SNTA}_{\text{G7C-A140C}}$, the high FRET population ($E \approx 0.35$, $\tau_{\text{D}} \approx 3.5$ ns) lies on the dynamic line, suggesting the FRET population is a dynamic average of fast dynamics (e.g. ns to μs) as expected for chain dynamics in disordered systems [448]. Additionally,

α SNTA_{G7C-A140C} exhibits slower dynamics on the ms time-scale to a lower, more expanded, FRET state ($E \approx 0.05, \tau_D \approx 4.0$ ns).

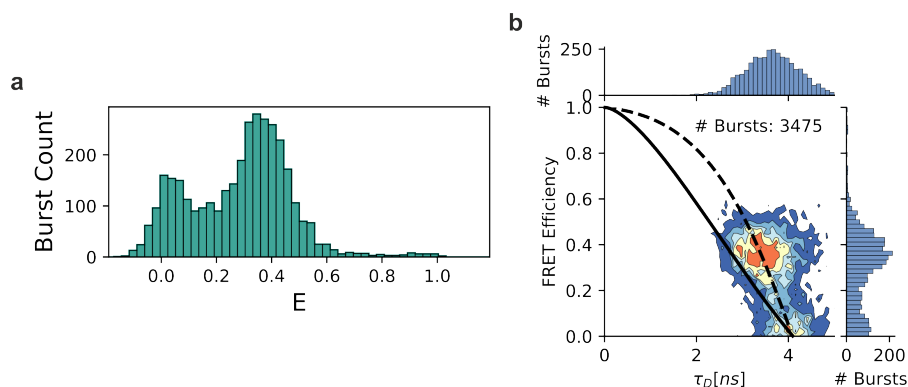


Figure 4.30 Lifetime analysis of α SNTA_{G7C-A140C}. (a) FRET efficiency histogram. (b) Donor fluorescence lifetime (τ_D ; ns) versus FRET efficiency. The colour scale from blue to red represents the density of bursts from low to high density, respectively. 50 pM protein was analysed in 20 mM Tris HCl, pH 7.5. Data were acquired and analysed by Dr Joel Crossley, University of Leeds.

1 mM Ca^{2+} was added to establish whether divalent ion binding results in conformational perturbations visible by smFRET which may correlate with IM-MS findings in the gas phase (Figure 3.22; adding Zn^{2+} resulted in fluorescent quenching which prevented single-molecule detection of the dyes). Upon the addition of Ca^{2+} , bursts fall into one major population with a FRET efficiency (E) of around 0.3. This major population remains dynamic on the ns- μ s time-scale, albeit with a slightly lower burst averaged FRET than in the absence of Ca^{2+} suggesting the dynamic chain is slightly more expanded. The population at $E \approx 0.05$ that was observed in the absence of Ca^{2+} (Figure 4.30), which could represent an extended conformation is absent when Ca^{2+} is added. Overall, there is a shift in FRET efficiency towards higher average FRET when Ca^{2+} is present, suggesting that the ensemble, as a whole, is more compact. These findings, in solution reinforce the compaction effect in $^{\text{TW}}\text{CCS}_{\text{N}_2}$ observed by nESI-IM-MS in Chapter 3 of this thesis. This supports the use of gas phase measurements in structural biology to capture conformational

dynamics that occur in solution prior to transfer into the gas phase. However, with multiple α SNTA constructs with labelling sites at different locations along the sequence, a more detailed understanding of the protein chain dynamics can be achieved, providing localised information on where compaction occurs.

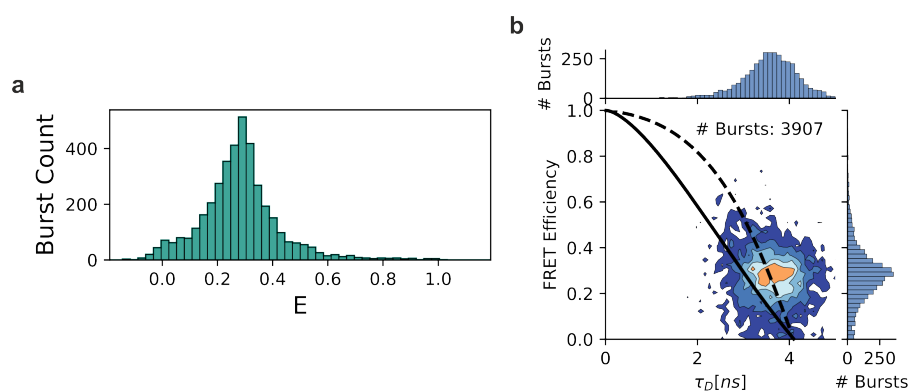


Figure 4.31 Lifetime analysis of α SNTA_{G7C-A140C} with 1 mM Ca²⁺. (a) FRET efficiency histogram. (b) Donor fluorescence lifetime (τ_D ; ns) versus FRET efficiency. The colour scale from blue to red represents the density of bursts from low to high density, respectively. 50 pM protein was analysed in 20 mM Tris HCl, pH 7.5, with the addition of 1 mM calcium chloride. Data were acquired and analysed by Dr Joel Crossley, University of Leeds.

4.9 Discussion

In this chapter, a more detailed investigation of the molecular mechanisms which govern α SNTA compaction with Zn²⁺ was explored. A direct correlation between compaction measured using IM-MS and t_{50} of amyloid formation measured using ThT fluorescence in the context of a Zn²⁺ titration with α SNTA highlighted the comparable conformational sensitivity achieved in the gas phase by IM-MS, to amyloid assembly kinetics observed in solution. The addition of Zn²⁺ leads to a reduction in the t_{50} of α SNTA, which occurs at low stoichiometry (1:5 α S : Zn²⁺; Figure 4.2). With the physiological concentration of Zn²⁺ in the brain being around low nM to high μ M range (100 μ M) [449], the titration

used in this thesis reflects physiological environments. Clearly evidenced is a relationship between the conformation exhibited by α SNTA and its amyloid propensity.

Determination of the K_d of Zn^{2+} binding by nESI-MS to α SNTA shows that, binding is not a cooperative process, but instead, occurs in a stepwise manner. The approach of applying native MS to calculate binding affinities helps to provide information on whether there are conformational preferences for Zn^{2+} binding. With K_d values of around 50 μ M, Zn^{2+} binds weakly to α SNTA and this occurs for charge states 6+, 8+ and 10+ representing the more native-like conformational ensemble that α SNTA adopts (Figure 4.5). These findings reinforce the observations shown in Figure 3.24, in which Zn^{2+} was shown to bind to all charge states with equal affinity but results in conformational effects that occur only on the lower charge states of α SNTA.

XL-MS was next applied to attempt to capture long-range intramolecular interactions which are increased in the presence of Zn^{2+} . Due to the heterogeneity of the cross-linking mechanism, capturing cross-links across replicates proved difficult. With the cross-links detected (Figure 4.14) through label-free quantification, intramolecular interactions between the N- and C-terminal regions were observed to increase upon the addition of Zn^{2+} suggesting that compaction occurs across the entire protein sequence and not just due to collapse of the C-terminal region. Indeed, this could be due to the occurrence of two distinct binding sites to Zn^{2+} within α SNTA; H50 and D121 which showed chemical shifts in NMR in the presence of Zn^{2+} (Figure 4.18). The possibility of Zn^{2+} co-coordinating these residues to each other or to other residues in the opposing termini presents evidence for how the α SNTA chain compacts with Zn^{2+} binding [423].

The conformational sensitivity of ETD and UVPD fragmentation techniques were highlighted. The sequence coverage achieved (47% for denaturing ETD and 44% for denaturing UVPD) could offer the potential to locate residue specific Zn^{2+} binding sites within α SNTA through the formation of non-covalent interactions.

4.10 Conclusion

Throughout this chapter, a comprehensive study on the impact of Zn^{2+} on α SNTA has been explored, particularly regarding its amyloid propensity, conformational changes, binding affinity and long-range interactions. Various analytical techniques including native MS, IM-MS including cIM, NMR and smFRET were employed. Evidence is provided into the location of Zn^{2+} binding to H50 and D121 and provide information towards understanding how Zn^{2+} binding causes compaction that drives amyloid formation. Further investigation into the effects of familial mutations such as the H50Q common missense mutation and other C-terminal truncation on their interaction with Zn^{2+} would be interesting to pursue. Overall, these findings contribute to a clearer understanding of the potential role of Zn^{2+} in neurodegenerative disease and highlight the validity of using gas phase measurements to study protein conformations and to be able to relate those findings to the molecular effects that occur in solution.

Chapter 5

Defining the structural assembly of toxic type B* oligomers of α S

5.1 Introduction

During the assembly of amyloid fibrils, α S forms transient oligomeric conformations which are considered responsible for its gain-of-toxic function [450, 451]. Knowledge of α S oligomer structures is limited, which hinders the opportunity to design therapeutics and drug treatments to inhibit the toxic effects in synucleopathies. The formation of long-lived kinetically trapped oligomers has been extensively studied due to their association with α S toxicity. Examples include type B* oligomers which have a high degree of β -sheet content ($35\% \pm 5$) and elicit a toxic response in SH-SY5Y neuroblastoma cell lines by way of ROS production and calcein release [172, 322]. However, details of their structure and mechanism(s) of oligomer to fibril conversion has not yet been understood.

One mechanism to stabilise type B* oligomers is through finding binding molecules which increase their structural stability. Phenol-soluble modulins (PSMs) are a family of anti-microbial peptides produced and secreted by the bacterium strain *Staphylococcus*

aureus [452–454]. PSMs are secreted to stimulate an inflammatory response in the host, contribute to biofilm formation, and can cause lysis of human immune response cells such as T cells [455]. PSMs have been characterised by their ability to form amyloid which contributes to their function and activity [456, 457]. The amyloid architecture formed by some PSMs such as PSM α 1 and PSM α 4, is characterised by a classic cross- β structure and shown to assemble into fibrils that form stable biofilm to protect bacterial cells against the immune system and antibiotics [458–460]. However, in the case of PSM α 3 (which is the most cytotoxic member of the PSM family), the peptide assembles into a unique fibril architecture characterised by a cross- α structure of amphipathic α -helices arranged perpendicular to the fibril axis held together by a hydrophobic core [461, 462] (Figure 5.1).

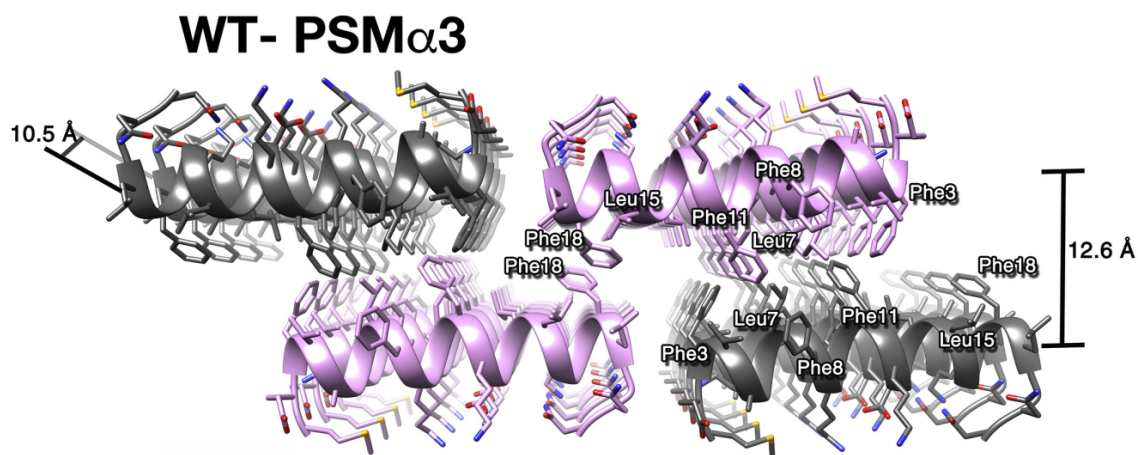


Figure. 5.1 The cross- α amyloid structure of PSM α 3. Protofibrils are held together by a strong hydrophobic core. Taken from [459, 463].

The α S type B* oligomer structure shares similar features to amyloid fibrils such as exposed lipophilic clusters, an exposed negatively charged C-terminal region and hydrophobic surfaces. Hydrophobic surfaces present a binding site for an amphipathic cationic peptides. Such as the α -helical, 22-residue peptide PSM α 3. Indeed, PSM α 3 was shown by dual-colour fluorescence cross-correlation spectroscopy (dcFCCS) (a time resolved single molecule fluorescence technique used to observe co-diffusing fluorescent species) to bind to type B* α S oligomers (K_d 6.67 nM), and more weakly to fibrils (K_d

7.8 nM), while it does not bind to type A* oligomers (oligomers formed in the presence of EGCG shown to be non-toxic and more disordered than type B* oligomers [172]) or monomers of α S (Figure 5.2). Additionally, PSM α 3 binding led to inhibition of fibril assembly for α S, and resulted in the accumulation of oligomer species observed by negative stain EM [464].

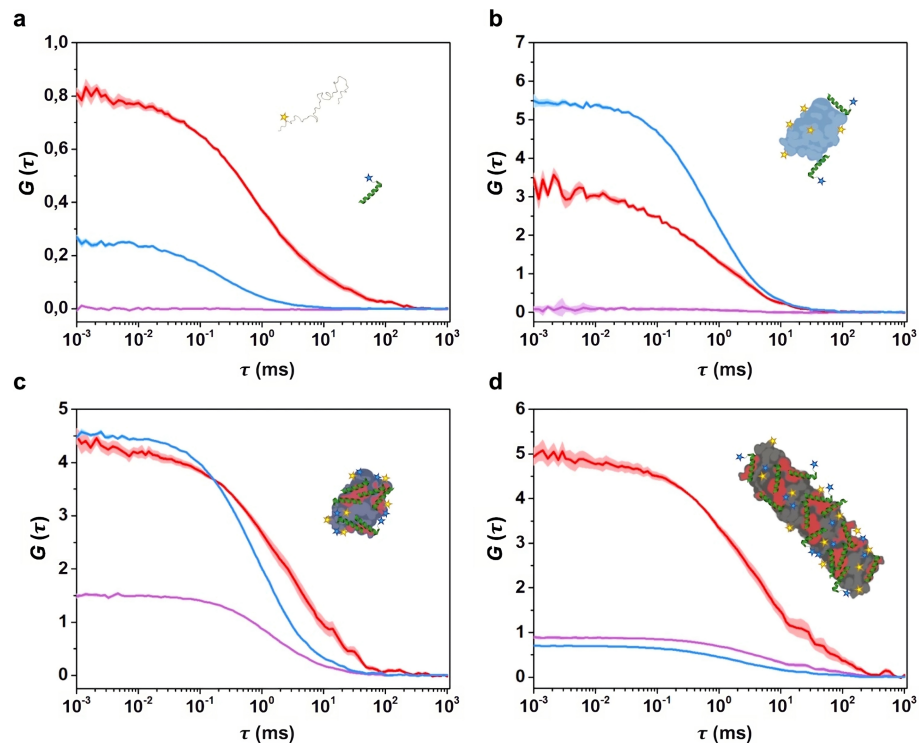


Figure 5.2 PSM α 3 binds to type B* α S oligomers. FCCS for α S (blue), PSM α 3 (red) and cross-correlation curves (purple). The amplitude (G) error is represented as a semi-transparent area around correlation curves. (a) 15 nM α S monomer with 15 nM PSM α 3. (b) 1 nM type A* oligomers with 5 nM PSM α 3. (c) 1 nM type B* oligomers with 5 nM PSM α 3. (d) 5 nM sonicated α S fibrils with 5 nM PSM α 3. Taken from [464].

Using a plethora of techniques the structural organisation of type B* oligomers has been assessed [168]. Using negative stain EM images, an accumulation of annular species were observed, particularly during the amyloid assembly of Δ P1 and Δ P2 α S at the time-point where WT α S reached the plateau phase of amyloid assembly as observed by ThT

fluorescence [168]. WT α S showed these annular structures too, but of lower abundance than Δ P1 and Δ P2. These negative stain species are shown in Figure 5.4d occurring for the familial variant of α S G51D which forms amyloid at a slower rate than WT α S (Figure 5.4b) [168].

Using cryo-EM, the type B* oligomers identified by negative stain were solved to 16 Å (Figure 5.4a) [168]. The resolution of 2D classes was improved upon the addition of PSM α 3 where a six membered ring stacked into five layers was determined to form a thirty-mer oligomer (Figure 5.4b). The finding that resolution is increased by PSM α 3 suggests that binding may stabilise the oligomer architecture. The oligomer features a pore-like centre and is barrel like. Using solid state NMR, a high β -sheet content is observed for these oligomers in the N-terminal and NAC regions, while the C-terminal region remains random coil [172]. Since the accumulation of oligomers was more substantial for variants of α S that either do not form amyloid under defined experimental conditions (Δ P1) or form amyloid more slowly than WT α S (Δ P2 and G51D), it can be concluded that the N-terminal P1 and P2 regions may be required for oligomer-fibril conversion [168].

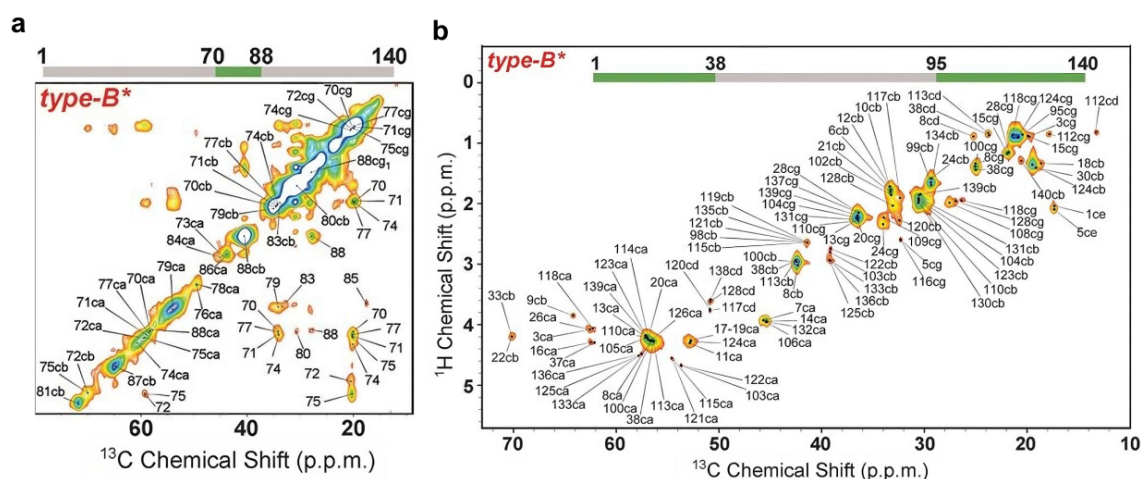


Figure 5.3 solid state NMR of type B* oligomers. (a) ^{13}C - ^{13}C dipolar-assisted rotational resonance (DARR) correlation spectra of aliphatic, rigid regions of type B* αS oligomers identifies static regions between residues 70-88 shown in green. (b) ^1H - ^{13}C insensitive nuclei enhanced by polarisation transfer (INEPT) correlation spectra identifies dynamic regions on the order of ms, shown in green for residues 1-38 and 95-140. The labels ca, cb, cg, cd and ce indicate C^α , C^β , C^σ and C^ϵ , respectively. Detected residues in the spectra are noted by residue number and are highlighted green in the panels above the spectra. Taken from [172].

In this chapter, a HDX-MS approach is used to compare the structure and assembly of the type B* oligomer for WT αS , the addition of PSM α3 and two familial variants of αS G51D and A30P and to identify the structural effects/binding site of PSM α3 to type B* oligomers. Oligomers were kindly prepared and donated by Dr Jaime Santos in the laboratory of Salvador Ventura, University of Barcelona. Briefly, type B* αS oligomers were prepared by incubating 800 μM of 0.22 μm filtered αS in phosphate buffered saline (PBS) buffer, pH 7.4 at 37°C, quiescently for 24 hours. The reaction was centrifuged at 288,00 $\times g$ to remove fibrillar species, and excess monomer was removed through consecutive filtering using 100 kDa cut-off centrifuge filters. The type B* oligomer-PSM α3 complex was prepared by incubating the oligomers with a 3-fold molar excess of

PSM α 3 for 30 minutes (excess PSM α 3 was removed through cycles of centrifugal filtering using 100 kDa cut-off filters). Protection from deuterium uptake indicates less solvent exposure of a particular region or increased hydrogen-bonding. PSM α 3 addition is shown to result in protection from deuterium uptake in the P1, P2 regions, and the NAC region of WT type B* oligomers, suggesting binding to these regions, while substantial difference in deuterium uptake protection/deprotection is observed for the two familial variants studied (G51D and A30P) type B* oligomers. The results are discussed in terms of the role of the P1 and P2 regions in fibril assembly and the role of the familial variants in aggregation and possible disease onset.

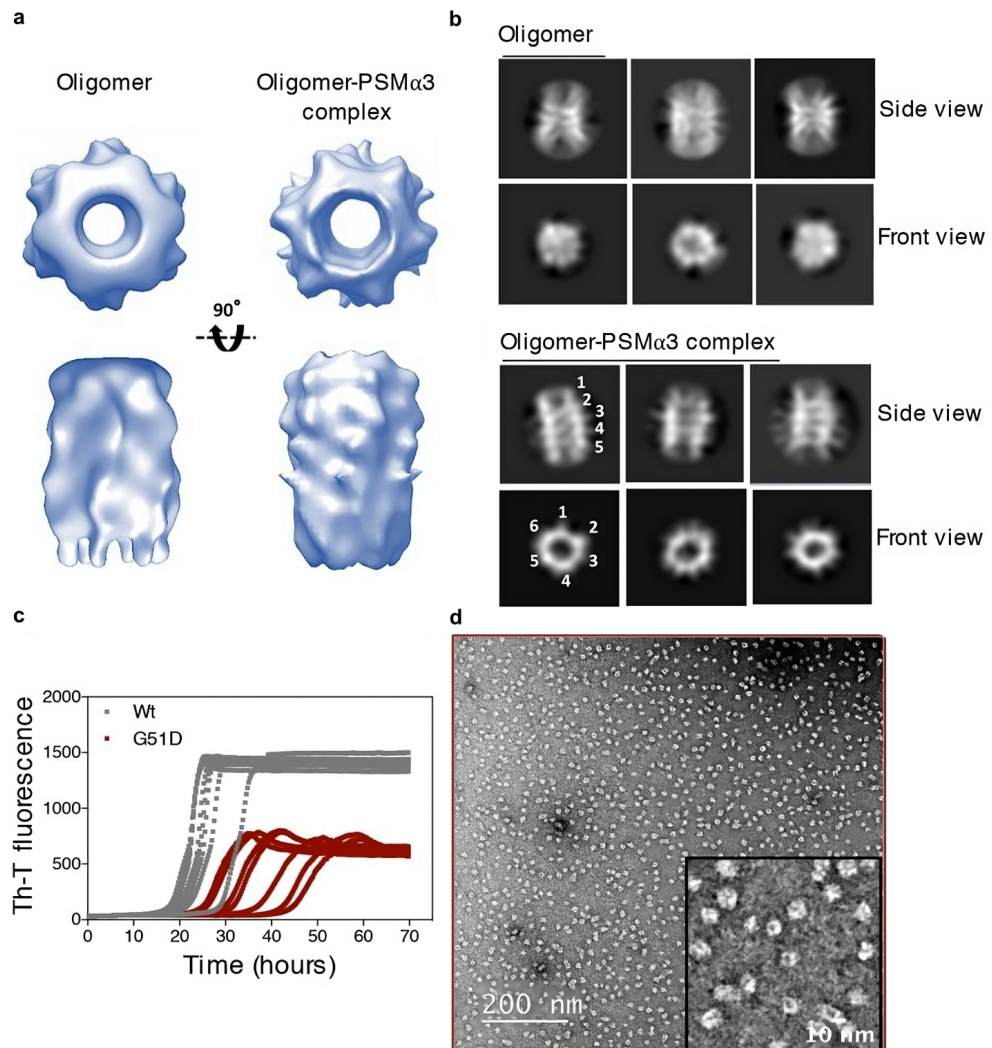


Figure. 5.4 Characterisation of type B* oligomers. (a) 3D reconstruction with six-fold symmetry in the absence of PSM α 3 (left; 16 Å resolution) and in the presence of PSM α 3 (right; 16.7 Å resolution). (b) 2D cryo-EM classes of oligomers in the absence or presence of PSM α 3. The architecture is labelled by numbers identifying a six membered ring oligomer stacked into five layers constituting a thirty-mer structure. (c) Amyloid assembly kinetics measured by ThT fluorescence comparing WT α S and the familial mutant G51D. (d) Negative stain EM image of G51D oligomers after 28 hr of amyloid assembly. Taken from [168].

5.2 The N-terminal and NAC regions are important for α S oligomer assembly

In order to elucidate the structural arrangement of type B* oligomers HDX-MS was used to compare deuterium uptake for oligomers compared to α S monomers. The sequence coverage identifying the peptides that were detected and used to determine differences in deuterium uptake are shown in Figure 5.5. Following incubation with deuterium for time points of 30 s, 1 min or 5 min the reaction was quenched under acidic conditions. To denature the oligomers ready for proteolysis, 4 M guanadine HCL was added to the quench buffer. Quenched reaction samples were injected into a immobilised pepsin column for digestion into peptides, full details of the methods used are shown in Chapter 2, Section 2.13.1. The sequence coverage shown in Figure 5.5 of 75 % covers the N-terminal region, NAC core and C-terminal region.

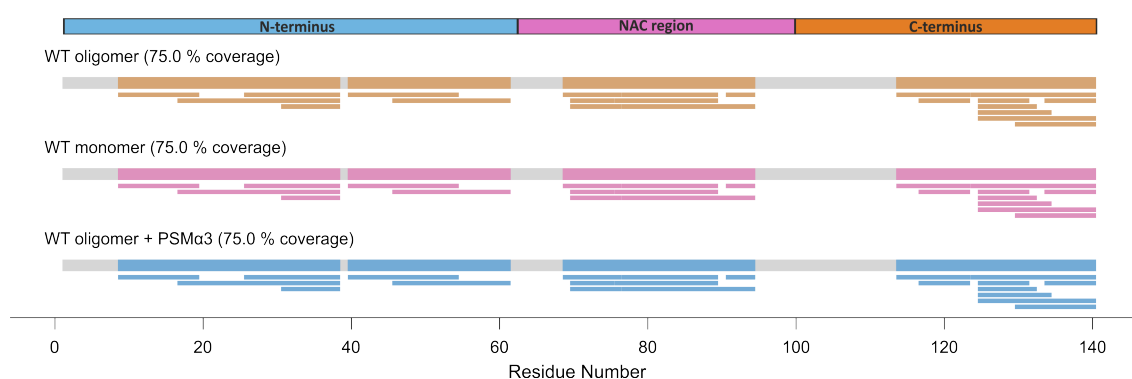


Figure. 5.5 Sequence coverage of α S monomers, oligomers and oligomers with PSM α 3 used to detect deuterium uptake.

Protection from deuterium uptake indicates less exposure to the solvent, or involvement in hydrogen bonding [465, 466]. Oligomer assembly results in increased protection of the N-terminal region of peptides comprising residues 17-38 and 40-54 and also in the NAC region (residues 69-94) using a cut-off of 0.5 Da (Figure 5.6). The C-terminal region shows no significant difference in deuterium uptake. This pattern could be indicative of

the β -sheet content observed by solid state NMR in the N-terminal and NAC regions of type B* oligomers [172].

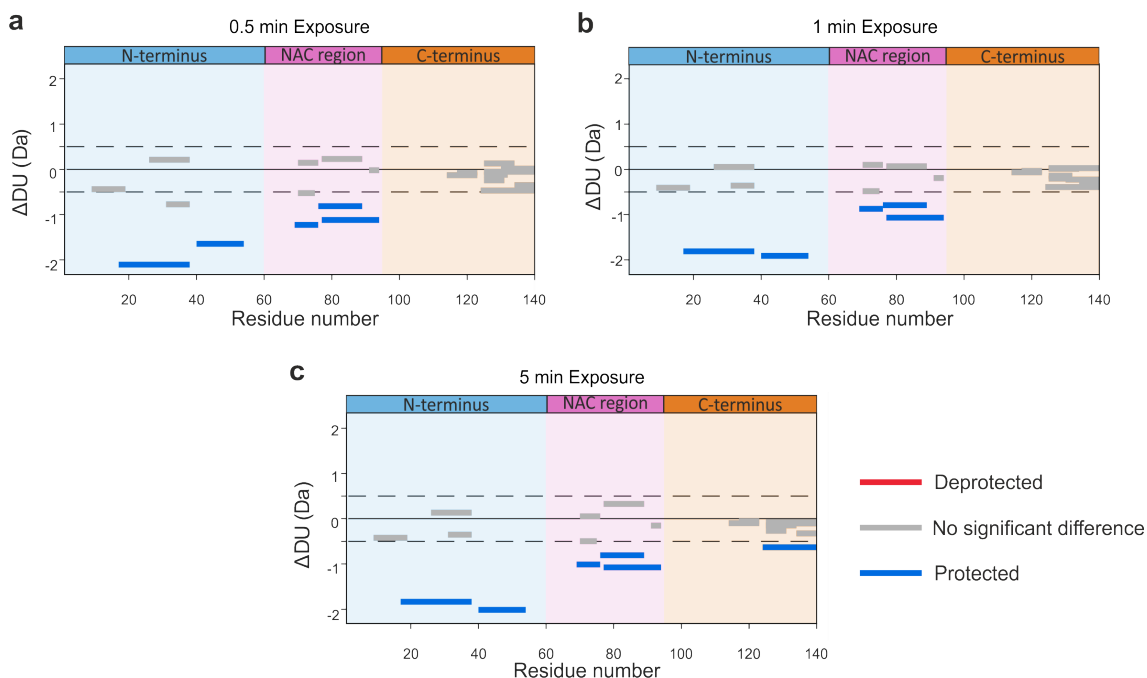


Figure 5.6 HDX-MS of type B* α S oligomers compared to α S monomers. Woods plots showing the difference in deuterium uptake (Δ DU) in Da when comparing α S oligomers to α S monomers for (a) 0.5 min, (b) 1 min or (c) 5 min exposure to deuterium. Oligomers are protected from deuterium uptake in the N-terminal region (residues 17-38 and 40-54) and the NAC region. (residues 69-76, 76-89 and 77-94) Deuterium uptake was calculated using DynamX 3.0 and Woods plots were generated using Deuterios.

The differences in deuterium uptake for the type B* oligomers compared to the monomer suggests that the oligomer is stabilised by shielding the hydrophobic NAC core and by interactions that involve the P2 (45-57) motif in the N-terminal region. Since the peptide 26-38 is not significantly protected, yet the peptide 17-38 is, protection can also be localised to residues 17-26, however this could indicate that back-exchange has occurred and would need validating using fully deuterated controls. The C-terminal region remains exposed to the solvent, at least as analysed here by HDX-MS experiments. These features

(burial/hydrogen bonding in P1, P2 and NAC but not the C-terminal region) are observed for α S fibril structures established by cryo-EM [228, 227, 209, 211, 467]. Next, type B* oligomers in the presence of PSM α 3 were analysed by HDX-MS to detect differences in deuterium uptake which result (directly or indirectly) from PSM α 3 binding or structural rearrangement of the oligomeric architecture. XL-MS revealed PSM α 3 binding sites in four regions; 1-6, 24-32, 35-43 and 46-58 (Figure 5.7).

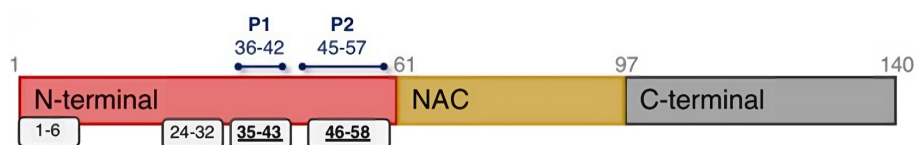


Figure 5.7 A schematic showing PSM α 3 binding sites to α S oligomers revealed by XL-MS. White boxes show PSM α 3 binding sites in the N-terminal domain, bold underlined numbers indicate sites which overlap with HDX-MS findings. The P1 and P2 regions are labelled in blue.

When comparing the PSM α 3 bound type B* α S oligomers to α S monomers, protection from deuterium uptake is again observed in residue 17-38, 40-54, with additional protection observed in residues 9-19 in the N-terminal region, and residues 70-75, 70-76, 76-89, 77-94 in the NAC core (Figure 5.8). This pattern of protection is similar to that observed when oligomers alone were compared to monomer, with one additional peptide showing protection from deuterium uptake which could indicate a more rigid structure achieved by PSM α 3 binding.

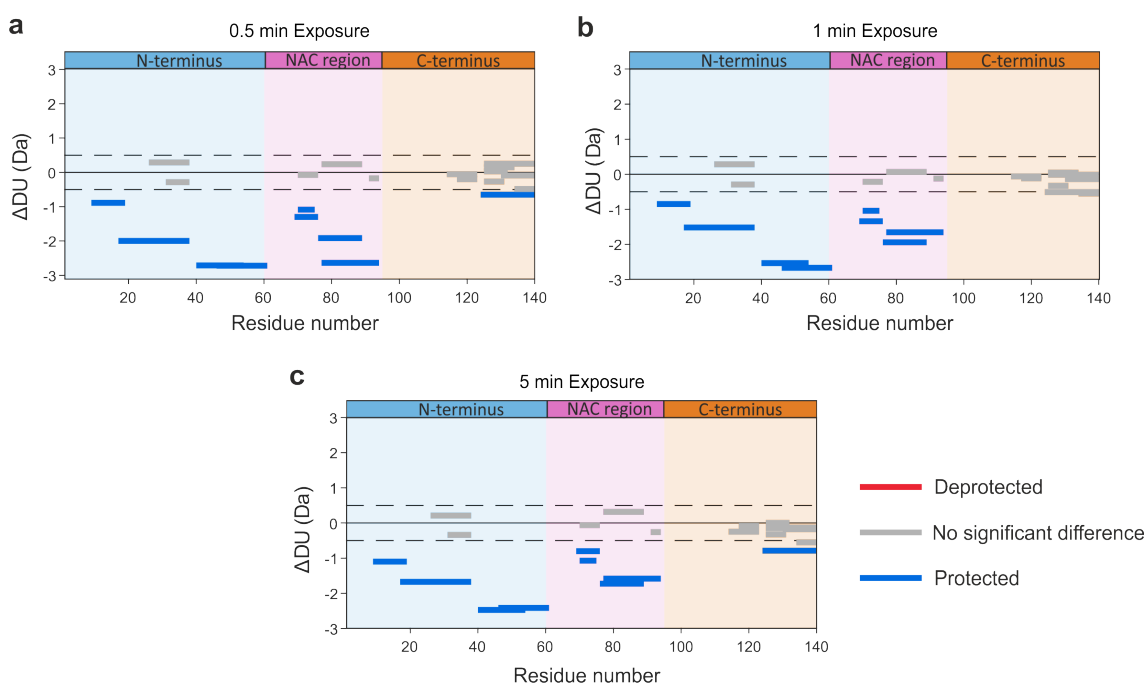


Figure 5.8 HDX-MS of type B* α S oligomers with PSM α 3 compared to α S monomers. Woods plots showing the difference in deuterium uptake (Δ DU) in Da when comparing α S oligomers with PSM α 3 to α S monomers for (a) 0.5 min, (b) 1 min or (c) 5 min exposure to deuterium. Oligomers are protected from deuterium uptake in the N-terminal region and the NAC region. Deuterium uptake was calculated using DynamX 3.0 and Woods plots were generated using Deuterios.

Comparing the oligomer-PSM α 3 complex to oligomers alone revealed additional differences in the patterns of protection from deuterium uptake. Peptides comprising the N-terminal region (residues 40-61) and the NAC core (residues 70-94) take up more deuterons in the presence of PSM α 3 compared with the absence of the ligand and are hence less protected in these regions. This suggests that despite being protected in the HDX oligomer the P2 region (peptide 40-61) is still accessible for interactions such as PSM α 3 binding.

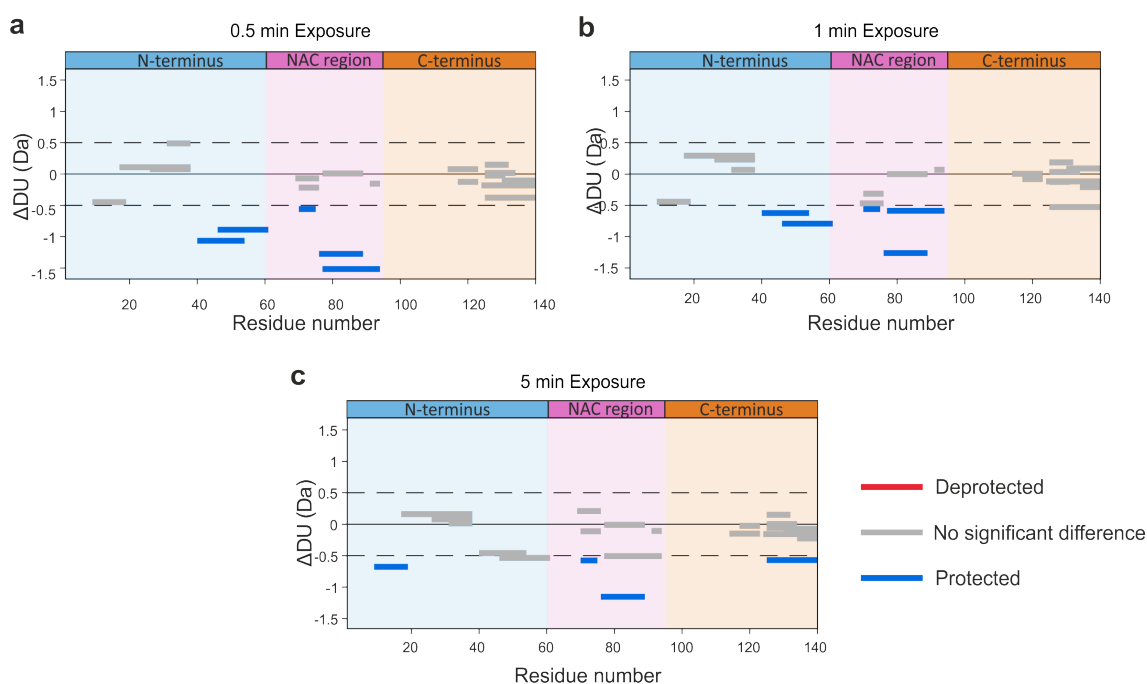


Figure 5.9 HDX-MS of type B* α S oligomers with PSM α 3 compared to apo type B* α S oligomers. Wood's plots showing the difference in deuterium uptake (Δ DU) in Da when comparing α S oligomers + PSM α 3 to apo type B* α S oligomers for (a) 0.5 min, (b) 1 min or (c) 5 min exposure to deuterium. Oligomers are differently protected from deuterium uptake in residues 40-54 and 46-61 in the N-terminal region and residues 70-75, 76-89 and 77-94 in the NAC region. Deuterium uptake was calculated using DynamX 3.0 and Wood's plots were generated using Deuterios.

The P1 and P2 regions (residues 36-42 and 45-57, respectively) are protected from deuterium uptake in the oligomer conformation compared with monomer (Figure 5.10, A.13 and A.14). Yet the accessibility of the P2 region shown by further protection upon the addition of PSM α 3 suggest that this N-terminal motif might be critical for amyloid fibril formation and assembly of the amyloid fold. No deprotection is observed in any regions.

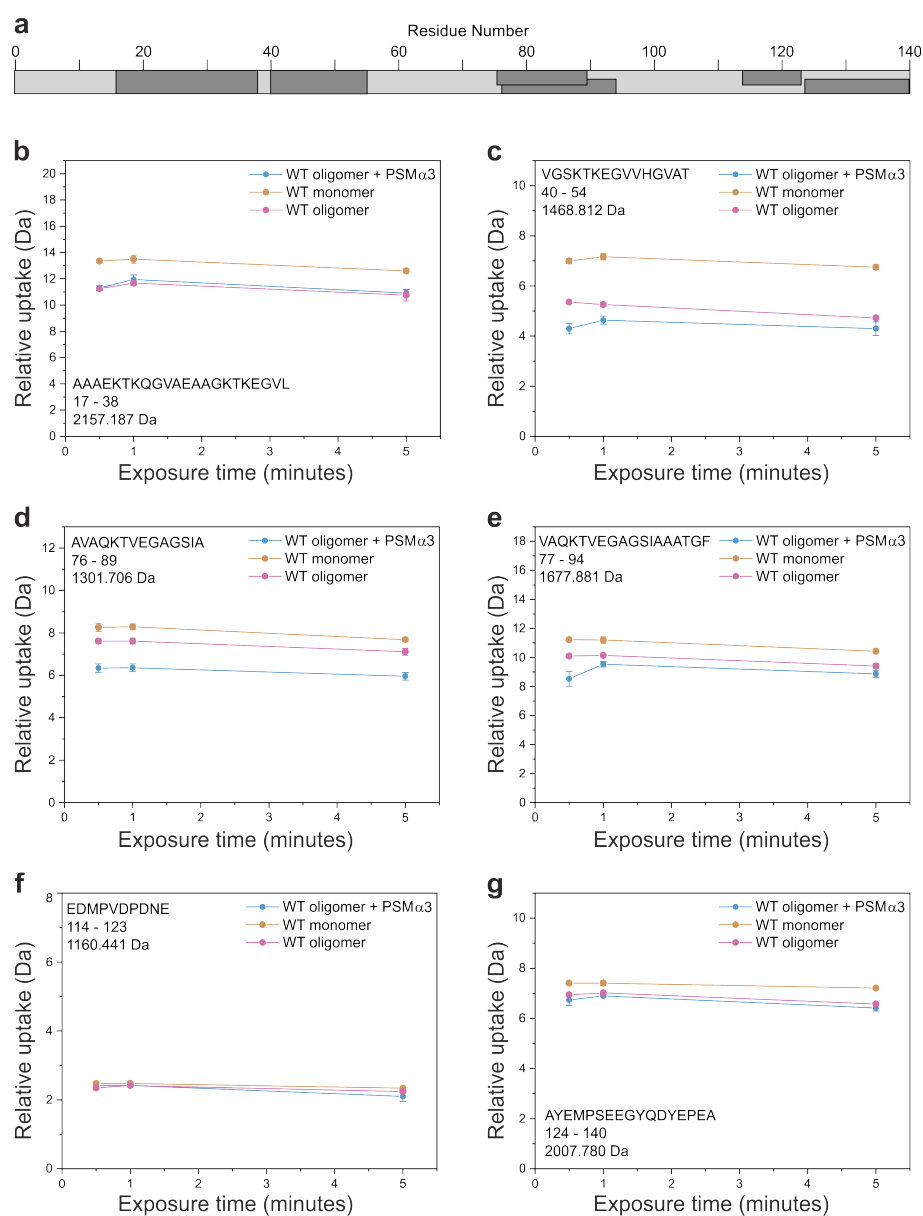


Figure 5.10 Uptake plots identify significant protection from deuterium uptake in the N-terminal and NAC regions for α S oligomers by HDX. (a) An overview of the sequence of α S showing where the peptides in b-g occur. (b) N-terminal peptide residues 17-38. (c) N-terminal peptide residues 40-54. (d) NAC peptide residues 76-89. (e) NAC peptide residues 77-94. (f) C-terminal peptide residues 114-123. (g) C-terminal peptides residues 124-140.

5.3 G51D and A30P alter the α S oligomer architecture

Establishing the potential role of the P1 and P2 regions in oligomer assembly, the clustering of familial mutations shown in Figure 1.25 might rationalise their effects on amyloid assembly kinetics and familial PD [272–274, 254, 275, 276]. This would imply that changes in the P1 or P2 sequence could influence the conformational architecture and physicochemical properties of the oligomer, and ultimately, the ability of oligomers to convert into amyloid fibrils.

The G51D familial mutation has been shown to slow the rate of fibril assembly by ThT fluorescence compared to WT α S [276]. However, G51D oligomers have been isolated and studied using a similar procedure to those used to create WT type B* α S oligomers, displaying a significantly higher toxicity to cells, analysed using MTT reduction, than WT oligomers [468]. Interestingly, G51D oligomers also contain a distinctive α -helical component (15.3–26.8%) by CD [468, 168]. Since α S contains four tyrosine residues, three of which are located in the C-terminal region (Y125, Y133 and Y136) which are unlikely to be involved in structural rearrangements (C-terminal regions remains disordered in Figure 5.12), the fourth tyrosine residue Y39 is likely to be involved in structural changes in oligomers. Indeed, Y39F oligomers lacked tyrosine fluorescence 345nm emission, which was present for WT oligomers, and accentuated in G51D oligomers suggesting that G51D oligomers have a pre-formed helical structure in the N-terminal region around residue Y39 [468]. Using HDX-MS the regions where structural differences might occur can be probed at the peptide level. The sequence coverage achieved for HDX-MS of G51D oligomers compared to WT oligomers used for analysis of differences in deuterium uptake is shown in Figure 5.11.

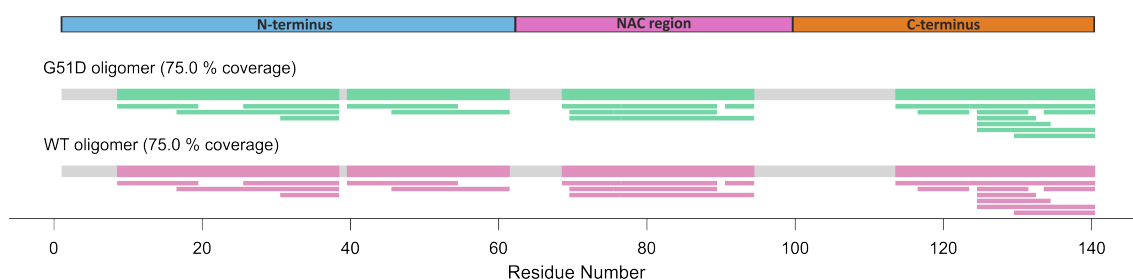


Figure. 5.11 Sequence coverage of G51D α S oligomers and WT α S oligomers used to detect deuterium uptake.

HDX-MS of G51D type B* oligomers compared with WT type B* oligomers reveals significant deprotection from deuterium uptake in the N-terminal region (peptide 17-38) in Figure 5.12 with no other significant changes across the protein sequence. The deprotected peptide observed could be due to the α -helical content of G51D oligomers resulting in increased uptake when compared to WT oligomers which was suggested to occur in the N-terminal region around Y39 [468].

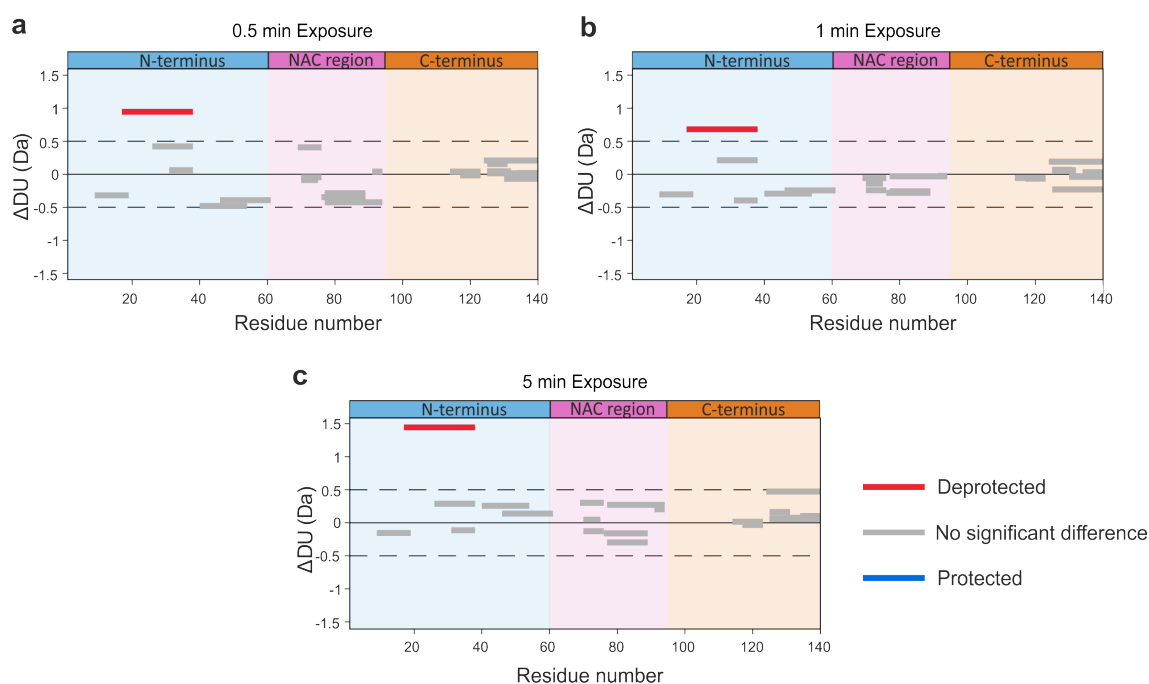


Figure 5.12 HDX-MS of type B* G51D α S oligomers compared to type B* WT α S oligomers. Woods plots showing the difference in deuterium uptake (Δ DU) in Da when comparing α S oligomers to apo type B* α S oligomers for (a) 0.5 min, (b) 1 min or (c) 5 min exposure to deuterium. G51D oligomers are deprotected from deuterium uptake in the N-terminal peptide residues 17-38, since significant deprotection is not observed in the peptide (26-38), deprotection can be localised to residues 17-26 (Figure A.15). Deuterium uptake was calculated using DynamX 3.0 and Woods plots were generated using Deuterios.

Whilst the peptide comprising residues 17-38 showed significant deprotection, the rest of the G51D oligomer sequence showed no significant difference in protection pattern compared to WT type B* oligomers (Figure 5.13, A.15 and A.16). Therefore, the C-terminal region remains disordered and highly exposed to the solvent, whilst the P1, P2 and NAC regions are significantly protected compared to monomeric α S to stabilise the oligomeric architecture with a hydrophobic interface.

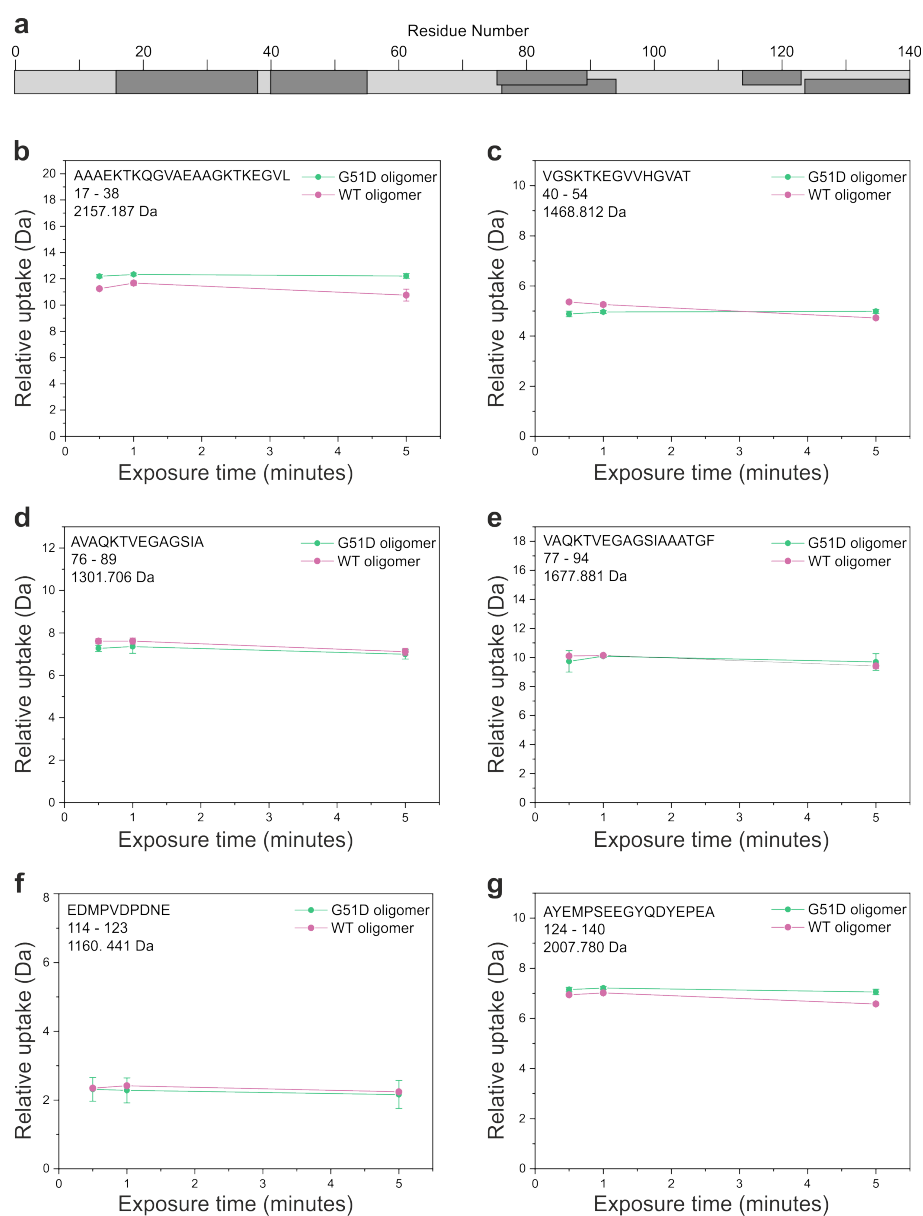


Figure. 5.13 Uptake plots identify significant deprotection from deuterium uptake in the N-terminal region for G51D type B* α S oligomers by HDX. (a) An overview of the sequence of α S showing where the peptides in b-g occur. (b) N-terminal peptide residues 17-38. (c) N-terminal peptide residues 40-54. (d) NAC peptide residues 76-89. (e) NAC peptide residues 77-94. (f) C-terminal peptide residues 114-123. (g) C-terminal peptides residues 124-140.

The A30P α S familial mutation has been shown to slow the rate of fibril assembly compared to WT by ThT fluorescence [276] and also reduces the membrane affinity of the N-terminal region of α S [469] (residues 21-25 were not involved in anchoring A30P α S to membranes [469]). Nonetheless, soluble A30P monomers were depleted more rapidly than soluble WT monomers during fibril growth, resulting in the acceleration of oligomerisation and accumulation of oligomers during fibril assembly [169]. A30P oligomers showed similar solvent-accessible hydrophobicity to WT oligomers using 8-anilinonaphtalene sulphate (ANS) binding [468]. A30P type B* oligomers prepared by Dr Jaime Santos in the laboratory of Salvador Ventura, University of Barcelona, were compared to WT oligomers by HDX-MS to identify whether differences in deuterium uptake occur within the sequence, the sequence coverage used for deuterium uptake calculation are shown in Figure 5.14.

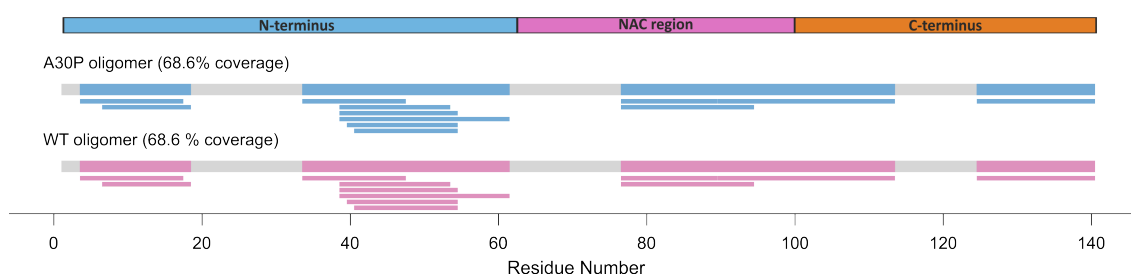


Figure 5.14 Sequence coverage of A30P α S oligomers and WT α S oligomers used to detect deuterium uptake.

A30P type B* oligomers were found to be more protected from deuterium uptake than WT type B* oligomers in the late N-terminal region at residues 39-61, no significant differences were observed elsewhere in the sequence (Figure 5.15). This could be due to a stabilised A30P type B* oligomer which can accumulate more readily as observed by rapid monomer consumption with delayed fibril assembly compared to WT α S type B* oligomers [169].

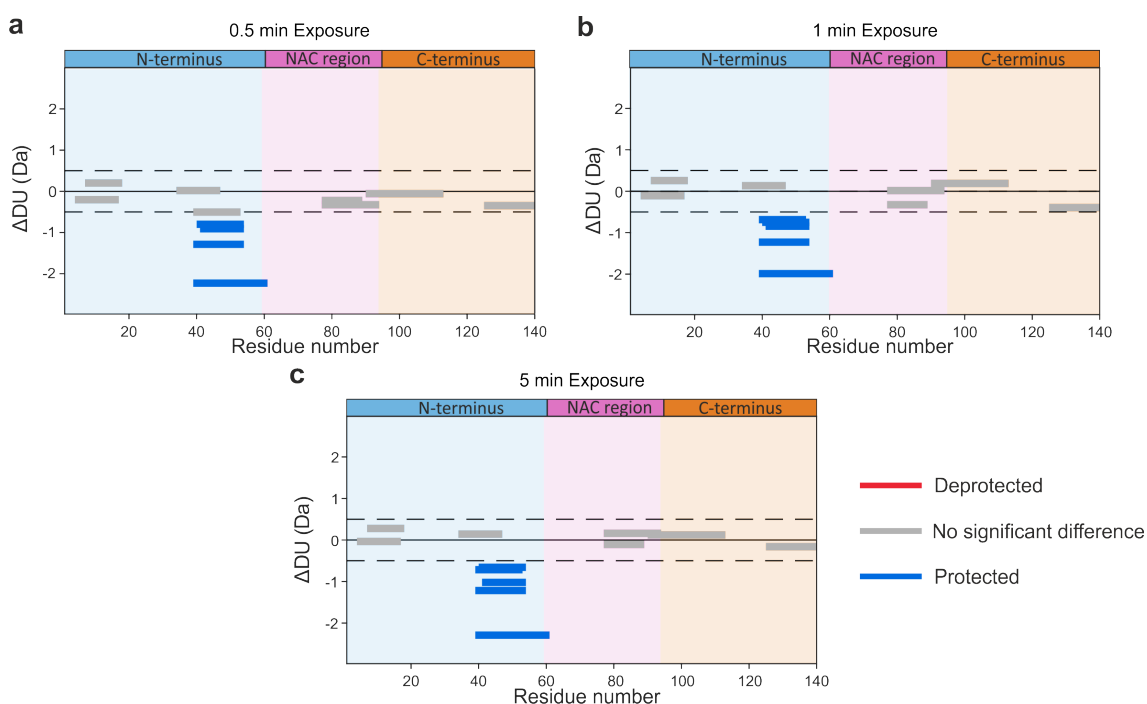


Figure 5.15 HDX-MS of type B* A30P α S oligomers compared to type B* WT α S oligomers. Woods plots showing the difference in deuterium uptake (Δ DU) in Da when comparing A30P α S oligomers to WT type B* α S oligomers for (a) 0.5 min, (b) 1 min or (c) 5 min exposure to deuterium. A30P oligomers are protected from deuterium uptake in residues 39-61, 39-54, 40-54 and 41-54 in the N-terminal region. Deuterium uptake was calculated using DynamX 3.0 and Woods plots were generated using Deuterios.

All other regions of the A30P oligomer sequence showed no significant difference to WT oligomers in Figure 5.16 and A.17. This suggests a similar oligomeric architecture between A30P and WT type B* oligomers, with perhaps a more rigid β -sheet structural content for A30P oligomers in the P2 region. This change in protection may enable the rapid accumulation of A30P oligomers, and the sequestration of P2 could rationalise the delay in the oligomer to fibril conversion.

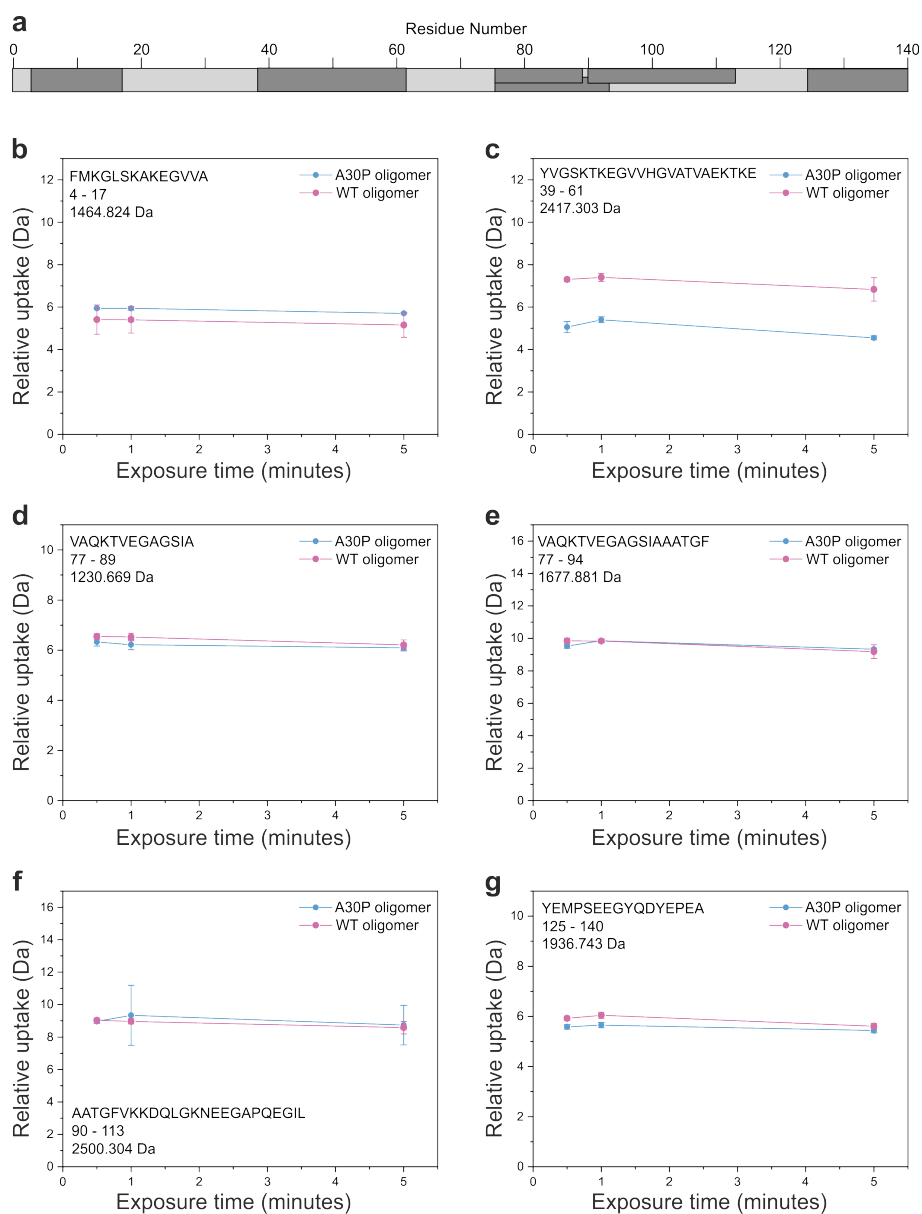


Figure 5.16 Uptake plots identify significant protection from deuterium uptake in the N-terminal region for A30P α S oligomers by HDX. (a) An overview of the sequence of α S showing where the peptides in b-g occur. (b) N-terminal peptide residues 4-17. (c) N-terminal peptide residues 39-61. (d) NAC peptide residues 77-89. (e) NAC peptide residues 77-94. (f) C-terminal peptide residues 90-113. (g) C-terminal peptides residues 125-140.

5.4 Oligomers constitute a thirty-mer arrangement

Mass photometry (MP) is a method that uses interferometric light scattering to determine the mass of an analyte [470]. With an analytical range of 40 kDa to around 5 MDa of unlabelled sample, MP can reveal information about the mass of α S oligomer stoichiometry [471]. MP measures the interference between light that is scattered by an analyte molecule on the surface to the light of which is reflected by the measurement surface itself, at single molecule resolution. The detected signal directly correlates with molecular weight (MW) [472]. Additionally, the single molecule detection gives an intensity reading as "counts" which represent the abundances of each detected MW species relative to one another, revealing heterogeneity and the population of species within a distinguishable ensemble. The technique is label-free and compatible with many buffer systems, advantageous for studies of protein ensembles [473]. MP was used to determine the MW of WT α S oligomers, WT-PSM α 3 α S oligomers, G51D α S oligomers and A30P α S oligomers (Figure 5.17). Oligomers were kindly prepared and donated by Dr Jaime Santos in the laboratory of Salvador Ventura, University of Barcelona.

The detected MW for WT α S type B* oligomers in Figure 5.17a of 433 KDa, 68% of the detected signal corresponds to a thirty-mer oligomer stoichiometry with a theoretical MW of 433.805 kDa. This reinforces the cryo-EM model which constitutes a six membered ring stacked into five rings [168]. An abundant distribution with an average MW of 71 kDa, 21% of the detected signal and a sharp peak indicated by a low σ value (< 100) calculates as a pentamer of α S which may be a result of oligomers disassembling at the low μ M concentrations used for analysis (0.5-5 μ M monomer equivalent concentration).

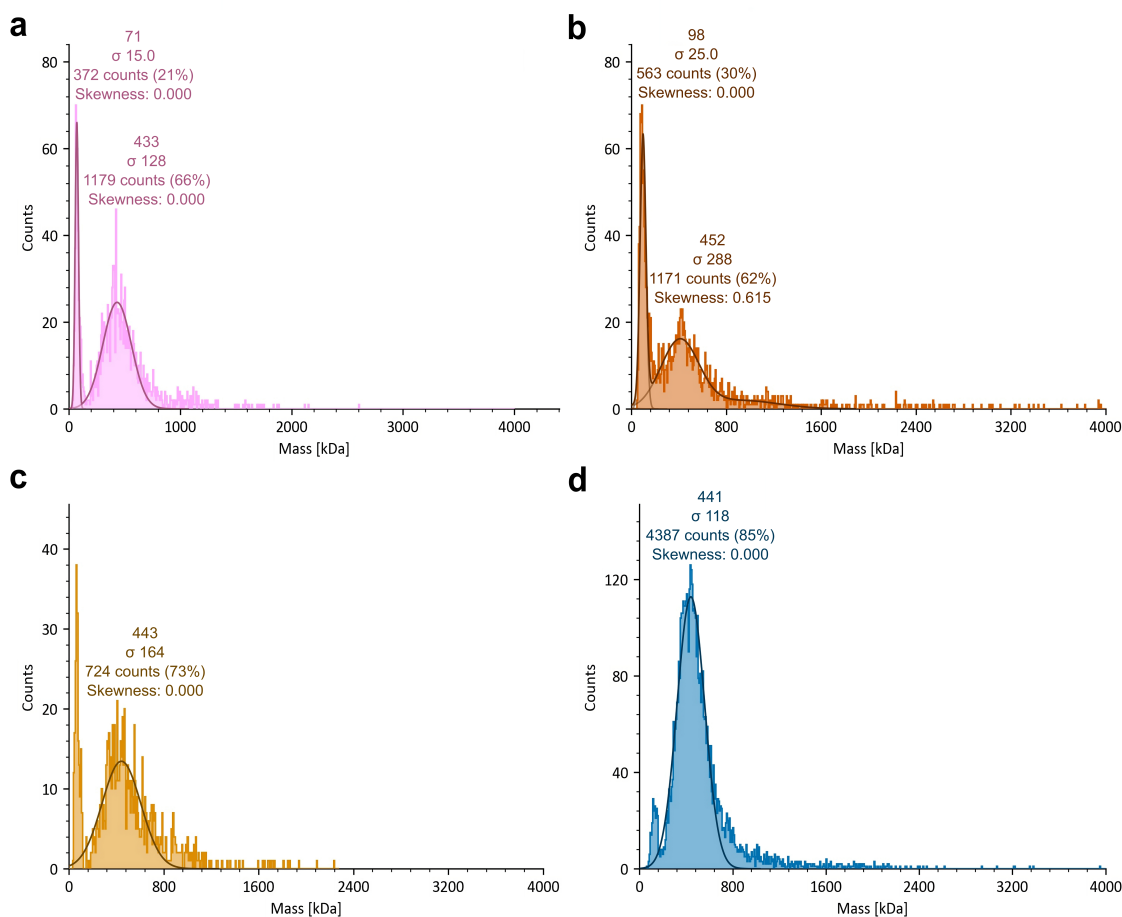


Figure 5.17 Molecular weight histograms obtained from mass photometry measurements of WT, WT-PSM α 3, G51D and A30P oligomers. Measured in PBS buffer, pH 7.4 the calibrated histograms of molecular weight are shown for (a) WT α S type B* oligomers (3 μ M), (b) WT-PSM α 3 α S type B* oligomers (3 μ M), (c) G51D α S type B* oligomers (500 nM) and (d) A30P α S type B* oligomers (500 nM). MW was determined by calibrating the instrument with BSA, thyroglobulin and aldolase using AcquireMP software and figures were generated using DiscoverMP software. Histograms are fitted with a Gaussian function where the peak height of the most abundant peak correlates with the average MW of the molecule(s). The width of peaks or standard deviation is represented by σ and the skewness is the Pearson median where a value of 0, identifies normal distribution, a value < 0 , where the mean is smaller than the median identifies outliers to the left of the peak and a value of > 0 where the mean is greater than the median identifies outliers to the right of the peak.

Analysis of the WT α S oligomer-PSM α 3 complex (Figure 5.17b) identifies a species with an average MW of 452 kDa and which calculates theoretically as a thirty-mer α S oligomer bound to around seven PSM α 3 (PSM α 3 MW 2,607 kDa) molecules (452.054 kDa). However the broadness of the distribution (highlighted by the σ value of 288) could indicate that there are many stoichiometries observed with differing numbers of PSM α 3 bound. For G51D oligomers, where the average MW of the monomer is 14518.19 Da, type B* oligomers would result in a thirty-mer oligomer of 435.546 kDa. Detected by MP in Figure 5.17c, the MW of the oligomer appears as 443 kDa which constitutes 30.5 monomers of G51D and therefore is within about 2% error of the theoretical value. For a broad heterogeneous distribution this error suggests that G51D oligomers likely constitute a thirty-mer arrangement. For A30P oligomers, where the average MW of the monomer is 14486.19 Da, type B* oligomers result in a thirty-mer oligomer of 434,586 kDa. In Figure 5.17d, the MW detected was 441 kDa which is 1.5% within error of the theoretical value of a thirty-mer A30P α S oligomer. Other techniques such as analytical ultracentrifugation and high-mass MS would be needed to further analyse the MW of type B* oligomers, but MP shows that type B* oligomers correspond with stable thirty-mer structures.

Overall, the results presented show that the oligomers assembled for WT and familial mutations of α S type B* oligomers agree with the thirty-mer arrangement postulated to constitute a six-membered ring stacked into five layers observed by cryo-EM for the WT α S type B* oligomers [168]. This stoichiometry is retained for WT, G51D and A30P α S oligomers. The broadness of oligomer MW peaks might be due to the low concentrations used for MP measurements (< 3 μ M) which might result in disassembly of oligomers into monomers which are below the MW detection limit of 40 kDa of MP.

5.5 Discussion

Oligomers of α S are thought to be responsible for the gain-of-toxic function exhibited by α S [169–172]. Indeed, a pore-forming β -barrel oligomer has been established for A β ₄₂ with an internal diameter of 9Å–17Å which could insert into membranes resulting in Ca²⁺ release [176].

Type B* oligomers of α S are well studied as kinetically trapped species observed during α S amyloid assembly generated *de novo* in PBS buffer, quiescently at 37°C for 24 hours [169–172]. In this chapter, the structural assembly of type B* α S oligomers was explored. The N-terminal region containing the P1 and P2 motifs as well as the NAC region appear important for oligomer assembly as shown by protection from deuterium uptake in samples which aggregate most slowly (A30P; Figure 5.6). The C-terminal region remains disordered and not protected from deuterium by HDX-MS for all oligomers shown. These features are reminiscent of cryo-EM structures of α S amyloid fibrils [228, 227, 209, 211, 467]. In the oligomer-PSM α 3 complex, increased protection from deuterium uptake was observed in the P2 region (Figure 5.9). These results suggest that PSM α 3 may bind to the P2 region, which stabilises the oligomer and prevents its conversion into fibrils, whether binding and protection from HDX correlate with fibril assembly warrants more detailed investigation. These findings hint to the essential role of the P1 and P2 regions in amyloid fibril assembly, perhaps in oligomer to fibril conversion.

Indeed, the sequence specificity of the P1 and P2 regions might be important factors in determining oligomer structure, dynamics and cytotoxic effects. Familial point mutations cluster in the P1 and P2 regions (Figure 1.25), and these might be important factors in determining a role of type B* or other oligomers in PD and other synucleopathies. For the familial variant of α S, G51D, which delays the rate of fibril assembly, the peptide spanning residues 17–38 is deprotected to deuterium uptake compared to WT α S type B* oligomers (Figure 5.12). This could be due to α -helical structure in this region which is more exposed

to the solvent and less protected than this peptide in WT α S type B* oligomers or due to conformational changes elsewhere in the structure [468]. The A30P familial mutant also slows the rate of amyloid assembly compared to WT α S and has been shown to rapidly form oligomers, accelerating the rate of oligomer assembly [169]. A30P α S type B* oligomers showed protection from deuterium uptake in peptides comprising residues 39-61 (Figure 5.15) containing half of the P1 region and all of the P2 region, which could infer that the oligomer structure is tighter and more stable which may result in the rapid accumulation of these oligomers for A30P α S. MP showed that the thirty-mer oligomer stoichiometry is conserved for WT, G51D and A30P α S oligomers (Figure 5.17). In combination with HDX-MS, mapping of regional protection or deprotection from exchange with the solvent, this architecture is established by the rigid NAC domain and the flanking regions P1 and P2.

5.6 Conclusion

HDX-MS was used herein to interrogate the stability of type B* α S oligomers through their deuterium uptake patterns at the peptide level in comparison to α S monomers, and changes in HDX protection in familial mutations and the presence of the nM affinity binder, PSM α 3. The P2 region is essential in the assembly of fibrils [211, 209] and shown here to be protected in the oligomer structure. The C-terminal region consistently remains exposed to the solvent carrying a dense negative charge which might capture positively charged ions (Chapters 3 and 4). Further characterisation of the MW of oligomers could utilise charge detection MS which directly measures the charge of single ions in an Orbitrap mass analyser for accurate high mass measurements. The observations established in this chapter highlight the role of the P2 region in oligomer assembly and oligomer to fibril conversion. The P2 region could therefore offer a target site to design novel drug-like molecules which prevent the self-association of α S and assembly of cytotoxic oligomers.

Chapter 6

Concluding remarks

PD is the second most prevalent neurodegenerative disease worldwide and, with an ageing population, the number is expected to rise [474]. Hence, pressing need for therapeutics which treat PD is becoming ever more important. Understanding the molecular mechanisms that govern amyloid assembly and the loss-of-function and/or toxic-gain-of function of α S is of great importance to human health and disease. The work presented in this thesis describes new findings which advance the use of structural MS to study the amyloid-prone protein α S. In this section, the overall findings and results of this thesis are drawn together and discussed with regards to the initial aims presented in Section 1.13.

6.1 Final overall conclusion

A key strength of MS-based techniques is the ability to combine results with complementary structural information. Native nESI-MS and IM-MS, combined with XL-MS, HDX-MS and top down fragmentation, can reveal discrete details regarding the conformation of a protein in relation to how many ligands are bound, their affinity and where they might bind and where within the sequence the protein chain might undergo structural reconfiguration in space, locally and globally [342, 112, 93, 399, 122, 367]. Chapter 3 of this thesis applied

nESI-IM-MS to interrogate the dynamics and structural properties of α SNTA along with the N-terminal deletion variant $\Delta\Delta$ α SNTA (removal of the P1 and P2 regions) [350], and the naturally occurring C-terminal truncated 119 α SNTA [300, 382, 384, 383, 385]. The P1 and P2 motifs in the N-terminal region of α S have been shown to act as "master controllers" of α S amyloid assembly by serving as a hub for intra- and inter-molecular interactions [350, 380]. α S has been shown to populate multiple conformational families by nESI-IM-MS, but it was not clear whether specific conformational families play a role in amyloid assembly [13]. Chapter 3 used divalent ions (Ca^{2+} , Mn^{2+} and Zn^{2+}) which are known to bind to α S [183, 402, 183, 421–423, 394, 413, 424, 425, 321, 356] to assess how the conformational dynamics of α S are perturbed, and whether this, in turn, affects amyloid formation kinetics. Physiologically relevant N-terminally acetylated α S was investigated because of its dominant form in physiological conditions [292, 352].

Chapter 3 showed that the binding of metal ions to the studied variants of α SNTA resulted in a shift towards more compact conformations of the 8+ or 7+ charge state by nESI-IM-MS (Figure 3.22). ThT fluorescence reported that, upon the addition of Ca^{2+} , Mn^{2+} or Zn^{2+} , WT α SNTA, Δ P1 α SNTA, Δ P2 α SNTA and 119 α SNTA all formed amyloid at a much faster rate than in the absence of metal ions. Whilst the variant $\Delta\Delta$ α SNTA regained its ability to form amyloid, which does not occur in the absence of the tested divalent ions. These findings suggest that the abundance of the compact monomeric conformation(s), and in fact the occurrence of an even more compact conformation as more divalent ions bind, as observed through nESI-IM-MS of each Zn^{2+} bound state in Figure 3.23, increases the rate of amyloid assembly for α SNTA. Indeed, this finding was built upon in Chapter 4, and comparison of Zn^{2+} binding with the t_{50} of amyloid formation showed that the rate of amyloid assembly correlated with the percentage of ion binding and the percent shift towards compact species (Figure 4.2). The co-localisation of α SNTA with Zn^{2+} and Ca^{2+} at presynaptic nerve terminals in the brain at physiological concentrations (around 50 μM for α S, low nM to 100 μM for Zn^{2+} and 200–300 μM

for Ca^{2+}) [404, 321, 427, 428] are similar to the concentrations used experimentally in this thesis, divalent metal ions may play a significant role in the amyloid assembly of αSNTA . Indeed, using constraint guided MD, driven by smFRET data, eight clusters of αS conformational families have been structurally modelled, and highlight the conformational heterogeneity of monomeric αS which features specific conformations (Figure 6.1). These findings support the observations in this thesis, in the gas phase for αSNTA .

Chapter 4 outlines the use of a combination of structural MS techniques which were used to map the compact conformation(s) of αSNTA in response to Zn^{2+} binding. By analysing peak areas in native MS of unbound and Zn^{2+} bound spectral peaks, K_d values were determined using the data collector node in UniDec [412]. K_d values were calculated for different charge state species which ultimately represent a snapshot of conformations with differing SASA in solution before being transferred into the gas phase. This is an advantage that MS presents over ensemble averaging techniques such as NMR, which carry their own benefits, such as residue specific assignment. K_d values for the 7+, 8+, 10+ and the 12+ charge states of αSNTA binding Zn^{2+} are comparable, which infers that Zn^{2+} does not bind to one conformation (compact or extended) more so than the others. This finding, coupled with nESI-IM-MS analysis of the effects of Zn^{2+} binding on $^{\text{TW}}\text{CCS}_{\text{N}_2}$, shows that whilst Zn^{2+} binds to all conformations of αSNTA , it is the resulting conformational effects that differ. Extended conformations do not change in $^{\text{TW}}\text{CCS}_{\text{N}_2}$, whereas compact species are drawn into a more compact conformation when Zn^{2+} binds.

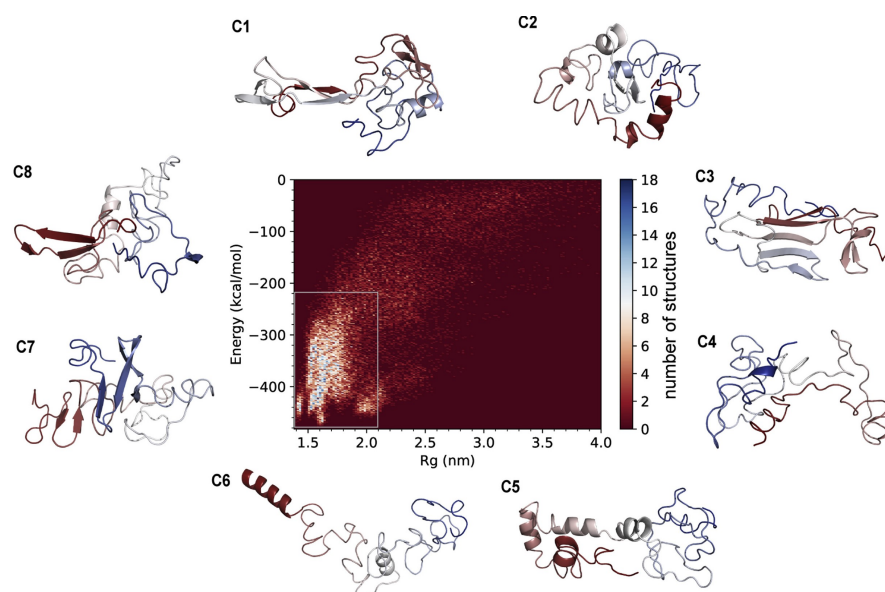


Figure 6.1 Cluster analysis of α S MD guided by smFRET and validated by XL-MS. A plot of energy versus the radius of gyration (R_g) for the structural ensemble of α S and the example centroid structures of the eight clusters (C1-C8) with a gradient colouring from the N-terminal region (red) to the C-terminal region (blue). Taken from [345].

Finally, in Chapter 5, HDX-MS was used to study the toxic type B* α S oligomer assembly [169–172, 168]. HDX-MS revealed that the N-terminal and NAC regions become protected from deuterium uptake in type B* oligomers (Figure 5.6). The C-terminal region remained unprotected, possibly available for interactions, chaperone binding and capture of divalent ions [401]. Further protection of the P2 region in the WT oligomer-PSM α 3 complex hints at PSM α 3 binding to the P2 region or the NAC region, stabilising the oligomer and hindering its conversion into fibrils by rendering P2 inaccessible. The identification of a differing oligomer architecture with α -helical structure for the familial mutant G51D α S suggests that this variant may play a role in disease pathology in familial PD. Mass photometry indicated that the thirty-mer oligomer stoichiometry is conserved across WT, G51D and A30P α S oligomers (Figure 5.17). Overall, the study highlights the

importance of specific regions in α S oligomer assembly, offering insight into the structural dynamics of these species in the context of neurodegenerative disease.

Many factors have been shown to influence α S amyloid assembly, some are shown in Figure 6.2. Here, evidence is provided that divalent ions such as Ca^{2+} , Mn^{2+} and Zn^{2+} result in compaction of a proportion of the overall monomeric α SNTA ensemble. This increase in population of a more compact, collapsed state of α SNTA results in a faster rate of amyloid assembly.

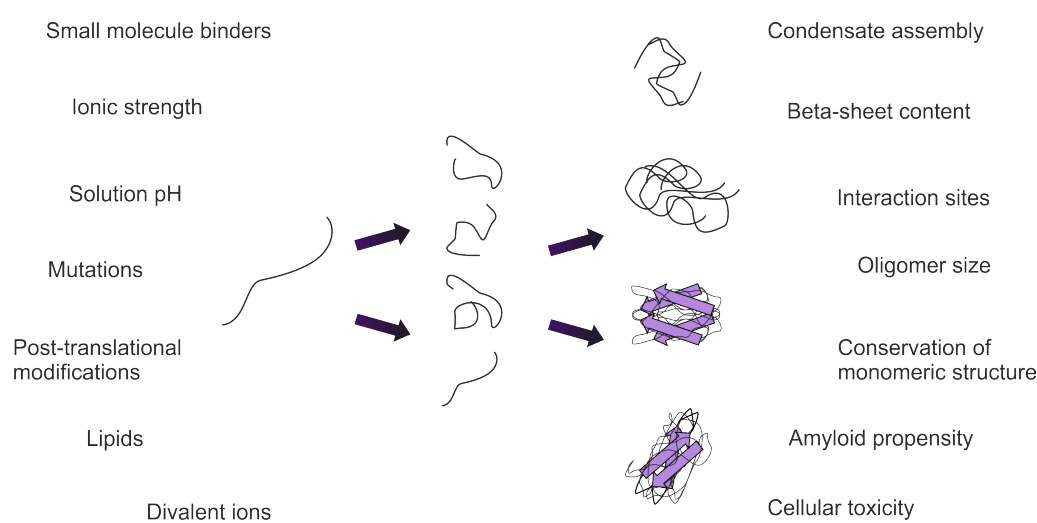


Figure. 6.2 Factors that influence α S self-assembly. Many factors including environmental conditions (pH and ionic strength), protein sequence variations (mutations and PTMs), and the presence/absence of interacting partners (lipid membranes, divalent ions and small molecules) affect the monomeric conformational ensemble of α S. The conformation of the monomer can in turn, affect oligomers that assemble and ultimately fibril formation.

Although much more information and analysis is required to answer the questions regarding how amyloid assembly from α S monomer and oligomers occurs, this thesis has provided evidence that the conformation of the α SNTA monomer is an important factor in governing amyloid assembly. During the four years of this PhD thesis, the idea of α S populating defined conformational ensembles has become a compelling picture of how α S

exists in solution [89, 345]. More molecular detail is required in order to directly target a perhaps toxic conformation of α S for drug discovery and development to treat PD, offering promise for future efforts.

6.2 Future work

6.2.1 The role of dimers and small oligomers

The research in this thesis highlights the potential of applying MS to study the early stages of α S amyloid assembly. In Section 3.7, dimer abundance was shown to inversely correlate with amyloid propensity. In cases where the t_{50} of amyloid assembly was the fastest, such as in the presence of Zn^{2+} , the relative abundance of dimers was the lowest. Whereas when amyloid assembly was the slowest, as in the case of $\Delta\Delta$ α SNTA which does not form amyloid on the time-scale of the experiments performed in this thesis, dimer abundance was the highest. These findings highlight the importance of studying small oligomers, facing the challenge that these species are part of heterogeneous mixtures and of low abundance.

Native MS could be applied to structurally interrogate the abundance of small oligomers. Indeed, for α S amyloid assembly a folded tetramer has been observed, which was purified from mammalian cell lines or red blood cells and exists as an α -helical structure [475–478]. The tetramer was distinguished by SEC and native PAGE identifying a species with a MW of 58–60 kDa which corresponds to four N-acetylated monomers ($4 \times 14,502 \text{ Da} = 58,010 \text{ Da}$) [479], was identified to contain α -helical structure by CD analysis, and was shown to not form amyloid by ThT fluorescence over a time-frame of 10 days, whereas recombinant monomeric α S did [476].

Characterising the abundance of specific species of α S oligomers that correlate with amyloid assembly might introduce novel targets for the design of drug-like molecules

which could induce a degradation response for cellular removal of toxic species. In addition to this, applying a covalent labelling workflow using FPOP, similar to research from Michael Gross' lab at Washington University, St. Louis to track the sequences in α S involved in oligomer and ultimately fibril assembly [338] could further elucidate druggable targets.

6.2.2 Using top-down fragmentation to identify metal ion binding sites

Chapter 4 of this thesis demonstrates the conformational sensitivity of top-down fragmentation such as ETD and UVPD (Figure 4.27). One of the key benefits of ETD and UVPD top-down fragmentation is the preservation of non-covalent interactions [480]. With high sequence coverage (around 70% and above), this enables the potential elucidation of ligand binding sites at the single residue level. Identifying the specific amino acid residues involved in forming electrostatic interactions between either proteins or of proteins-ligand could prove to be vital for understanding amyloid assembly both *in vitro* and *in vivo*. Indeed, one example of this is research from David Clarke's lab at the University of Edinburgh, where the dimer interface of α S was mapped using ECD fragmentation, wherein the dimer was shown to assemble by the C-terminal region of two α S monomers interacting together [68]. This finding is crucial for understanding the role of α S dimers. Identifying primary binding sites for divalent ions such as Zn^{2+} and Ca^{2+} could be an important factor for addressing α S amyloid assembly which occurs within cells. MS methods are developing rapidly, mapping structures of dynamic monomers and oligomers of α S is fundamentally important for understanding how α S forms amyloid.

References

- [1] K. Biemann, "MASS SPECTROMETRY OF PEPTIDES AND PROTEINS," *Annu. Rev. Biochem.*, vol. 61, pp. 977–1010, June 1992.
- [2] T. M. Allison and C. Bechara, "Structural mass spectrometry comes of age: new insight into protein structure, function and interactions," *Biochem. Soc. Trans.*, vol. 47, no. 1, pp. 317–327, 2019.
- [3] H. M. Britt, T. Cragolini, and K. Thalassinos, "Integration of mass spectrometry data for structural biology," *Chem. Rev.*, vol. 122, pp. 7952–7986, Apr. 2022.
- [4] A. N. Calabrese and S. E. Radford, "Mass spectrometry-enabled structural biology of membrane proteins," *Methods*, vol. 147, pp. 187–205, Sept. 2018.
- [5] T. P. Wörner, T. M. Shamorkina, J. Snijder, and A. J. R. Heck, "Mass Spectrometry-Based structural virology," *Anal. Chem.*, vol. 93, pp. 620–640, Jan. 2021.
- [6] S. Medhe, "Mass spectrometry: detectors review," *Chem Biomol Eng*, vol. 3, no. 4, pp. 51–58, 2018.
- [7] S. Mysling, C. Betzer, P. H. Jensen, and T. J. D. Jorgensen, "Characterizing the dynamics of α -synuclein oligomers using hydrogen/deuterium exchange monitored by mass spectrometry," *Biochemistry*, vol. 52, pp. 9097–9103, Dec. 2013.
- [8] O. Cornwell, S. E. Radford, A. E. Ashcroft, and J. R. Ault, "Comparing hydrogen deuterium exchange and fast photochemical oxidation of proteins: a structural characterisation of Wild-Type and Δ N6 β (2)-Microglobulin," *J. Am. Soc. Mass Spectrom.*, vol. 29, pp. 2413–2426, Dec. 2018.
- [9] E. Illes-Toth, G. Meisl, D. L. Rempel, T. P. J. Knowles, and M. L. Gross, "Pulsed Hydrogen-Deuterium exchange reveals altered structures and mechanisms in the aggregation of familial alzheimer's disease mutants," *ACS Chem. Neurosci.*, vol. 12, pp. 1972–1982, June 2021.
- [10] C. H. Ihling, L. Piersimoni, M. Kipping, and A. Sinz, "Cross-Linking/Mass spectrometry combined with ion mobility on a timsTOF pro instrument for structural proteomics," *Anal. Chem.*, vol. 93, pp. 11442–11450, Aug. 2021.
- [11] D. T. Johnson, L. H. Di Stefano, and L. M. Jones, "Fast photochemical oxidation of proteins (FPOP): A powerful mass spectrometry-based structural proteomics tool," *J. Biol. Chem.*, vol. 294, no. 32, pp. 11969–11979, 2019.

- [12] K. S. Li, L. Shi, and M. L. Gross, "Mass Spectrometry-Based fast photochemical oxidation of proteins (FPOP) for higher order structure characterization," *Acc. Chem. Res.*, vol. 51, pp. 736–744, Mar. 2018.
- [13] R. Moons, A. Konijnenberg, C. Mensch, R. Van Elzen, C. Johannessen, S. Maudsley, A.-M. Lambeir, and F. Sobott, "Metal ions shape α -synuclein," *Sci. Rep.*, vol. 10, p. 16293, Oct. 2020.
- [14] N. Österlund, M. Lundqvist, L. L. Ilag, A. Gräslund, and C. Emanuelsson, "Amyloid- β oligomers are captured by the DNAJB6 chaperone: Direct detection of interactions that can prevent primary nucleation," *J. Biol. Chem.*, vol. 295, pp. 8135–8144, June 2020.
- [15] A. C. Leney and A. J. R. Heck, "Native mass spectrometry: What is in the name?," *J. Am. Soc. Mass Spectrom.*, vol. 28, pp. 5–13, Jan. 2017.
- [16] S. Banerjee and S. Mazumdar, "Electrospray ionization mass spectrometry: a technique to access the information beyond the molecular weight of the analyte," *Int. J. Anal. Chem.*, vol. 2012, p. 282574, 2012.
- [17] J. B. Fenn, "Electrospray wings for molecular elephants (nobel lecture)," *Angew. Chem. Int. Ed Engl.*, vol. 42, pp. 3871–3894, Aug. 2003.
- [18] L. Konermann, E. Ahadi, A. D. Rodriguez, and S. Vahidi, "Unraveling the mechanism of electrospray ionization," *Anal. Chem.*, vol. 85, pp. 2–9, Jan. 2013.
- [19] M. L. Abramsson, C. Sahin, J. T. S. Hopper, R. M. M. Branca, J. Danielsson, M. Xu, S. A. Chandler, N. Österlund, L. L. Ilag, A. Leppert, J. Costeira-Paulo, L. Lang, K. Teilum, A. Laganowsky, J. L. P. Benesch, M. Oliveberg, C. V. Robinson, E. G. Marklund, T. M. Allison, J. R. Winther, and M. Landreh, "Charge engineering reveals the roles of ionizable side chains in electrospray ionization mass spectrometry," *JACS Au*, vol. 1, pp. 2385–2393, Dec. 2021.
- [20] I. A. Kaltashov and A. Mohimen, "Estimates of protein surface areas in solution by electrospray ionization mass spectrometry," *Anal. Chem.*, vol. 77, pp. 5370–5379, Aug. 2005.
- [21] M. T. Donor, S. A. Ewing, M. A. Zenaidee, W. A. Donald, and J. S. Prell, "Extended protein ions are formed by the chain ejection model in chemical supercharging electrospray ionization," *Anal. Chem.*, vol. 89, pp. 5107–5114, May 2017.
- [22] D. J. D. Pimlott and L. Konermann, "Using covalent modifications to distinguish protein electrospray mechanisms: Charged residue model (CRM) vs. chain ejection model (CEM)," *Int. J. Mass Spectrom.*, vol. 469, p. 116678, Nov. 2021.
- [23] H. Metwally, Q. Duez, and L. Konermann, "Chain ejection model for electrospray ionization of unfolded proteins: Evidence from atomistic simulations and ion mobility spectrometry," *Anal. Chem.*, vol. 90, pp. 10069–10077, Aug. 2018.
- [24] A. Natalello, F. Benetti, S. M. Doglia, G. Legname, and R. Grandori, "Compact conformations of α -synuclein induced by alcohols and copper," *Proteins: Struct. Funct. Bioinf.*, vol. 79, pp. 611–621, Feb. 2011.

- [25] M. Karas, U. Bahr, and T. Dülcks, "Nano-electrospray ionization mass spectrometry: addressing analytical problems beyond routine," *Fresenius J. Anal. Chem.*, vol. 366, no. 6-7, pp. 669–676, 2000.
- [26] G. L. Glish and R. W. Vachet, "The basics of mass spectrometry in the twenty-first century," *Nat. Rev. Drug Discov.*, vol. 2, pp. 140–150, Feb. 2003.
- [27] J. E. Campana, "Elementary theory of the quadrupole mass filter," *Int. J. Mass Spectrom. Ion Phys.*, vol. 33, pp. 101–117, Mar. 1980.
- [28] P. E. Miller and M. B. Denton, "The quadrupole mass filter: Basic operating concepts," *J. Chem. Educ.*, vol. 63, p. 617, July 1986.
- [29] J. P. Savaryn, T. K. Toby, and N. L. Kelleher, "A researcher's guide to mass spectrometry-based proteomics," *Proteomics*, vol. 16, pp. 2435–2443, Sept. 2016.
- [30] B. A. Collings and D. J. Douglas, "An extended mass range quadrupole for electrospray mass spectrometry," *Int. J. Mass Spectrom. Ion Process.*, vol. 162, pp. 121–127, Mar. 1997.
- [31] C. Weickhardt, F. Moritz, and J. Grotemeyer, "Time-of-flight mass spectrometry: State-of-the-art in chemical analysis and molecular science," *Mass Spectrom. Rev.*, vol. 15, no. 3, pp. 139–162, 1996.
- [32] E. A. Dennis, A. W. Gundlach-Graham, S. J. Ray, C. G. Enke, and G. M. Hieftje, "Distance-of-Flight mass spectrometry: What, why, and how?," *J. Am. Soc. Mass Spectrom.*, vol. 27, pp. 1772–1786, Nov. 2016.
- [33] J. Lee and P. T. A. Reilly, "Limitation of time-of-flight resolution in the ultra high mass range," *Anal. Chem.*, vol. 83, pp. 5831–5833, Aug. 2011.
- [34] B. A. Mamyurin, V. I. Karataev, D. V. Shmikk, and V. A. Zagulin, "The mass-reflectron, a new nonmagnetic time-of-flight mass spectrometer with high resolution," *J. Exp. Theor. Phys.*, 1973.
- [35] G. C. Stafford, P. E. Kelley, J. E. P. Syka, W. E. Reynolds, and J. F. J. Todd, "Recent improvements in and analytical applications of advanced ion trap technology," *Int. J. Mass Spectrom. Ion Process.*, vol. 60, pp. 85–98, Sept. 1984.
- [36] R. A. Zubarev and A. Makarov, "Orbitrap mass spectrometry," *Anal. Chem.*, vol. 85, pp. 5288–5296, June 2013.
- [37] S. Eliuk and A. Makarov, "Evolution of orbitrap mass spectrometry instrumentation," *Annu. Rev. Anal. Chem.*, vol. 8, pp. 61–80, 2015.
- [38] A. G. Marshall and F. R. Verdun, *Fourier Transforms in NMR, Optical, and Mass Spectrometry: A User's Handbook*. Elsevier, Feb. 2016.
- [39] M. Hardman and A. A. Makarov, "Interfacing the orbitrap mass analyzer to an electrospray ion source," *Anal. Chem.*, vol. 75, pp. 1699–1705, Apr. 2003.

- [40] H. Stewart, D. Grinfeld, A. Giannakopoulos, J. Petzoldt, T. Shanley, M. Garland, E. Denisov, A. Peterson, E. Damoc, M. Zeller, T. N. Arrey, A. Pashkova, S. Renuse, A. Hakimi, A. Kühn, M. Biel, A. Kreutzmann, B. Hagedorn, I. Colonius, A. Schütz, A. Stefes, A. Dwivedi, D. Mourad, M. Hoek, B. Reitemeier, P. Cochems, A. Kholomeev, R. Ostermann, G. Quiring, M. Ochmann, S. Möhring, A. Wagner, A. Petker, S. Kanngiesser, M. Wiedemeyer, W. Balschun, D. Hermanson, V. Zabrouskov, A. Makarov, and C. Hock, "Parallelized acquisition of orbitrap and astral analyzers enables High-Throughput quantitative analysis." June 2023.
- [41] L. R. Heil, E. Damoc, T. N. Arrey, A. Pashkova, E. Denisov, J. Petzoldt, A. C. Peterson, C. Hsu, B. C. Searle, N. Shulman, M. Riffle, B. Connolly, B. X. MacLean, P. M. Remes, M. W. Senko, H. I. Stewart, C. Hock, A. A. Makarov, D. Hermanson, V. Zabrouskov, C. C. Wu, and M. J. MacCoss, "Evaluating the performance of the astral mass analyzer for quantitative proteomics using data independent acquisition." Aug. 2023.
- [42] D. W. Koppenaal, C. J. Barinaga, M. B. Denton, R. P. Sperline, G. M. Hieftje, G. D. Schilling, F. J. Andrade, and J. H. Barnes, 4th, "MS detectors," *Anal. Chem.*, vol. 77, pp. 418A–427A, Nov. 2005.
- [43] V. Gabelica, A. A. Shvartsburg, C. Afonso, P. Barran, J. L. P. Benesch, C. Bleiholder, M. T. Bowers, A. Bilbao, M. F. Bush, J. L. Campbell, I. D. G. Campuzano, T. Causon, B. H. Clowers, C. S. Creaser, E. De Pauw, J. Far, F. Fernandez-Lima, J. C. Fjeldsted, K. Giles, M. Groessl, C. J. Hogan, Jr, S. Hann, H. I. Kim, R. T. Kurulugama, J. C. May, J. A. McLean, K. Pagel, K. Richardson, M. E. Ridgeway, F. Rosu, F. Sobott, K. Thalassinou, S. J. Valentine, and T. Wytenbach, "Recommendations for reporting ion mobility mass spectrometry measurements," *Mass Spectrom. Rev.*, vol. 38, pp. 291–320, May 2019.
- [44] F. W. Karasek, "Plasma chromatography," *Anal. Chem.*, vol. 46, pp. 710A–720A, July 1974.
- [45] A. B. Kanu, P. Dwivedi, M. Tam, L. Matz, and H. H. Hill, Jr, "Ion mobility-mass spectrometry," *J. Mass Spectrom.*, vol. 43, pp. 1–22, Jan. 2008.
- [46] A. Marchand, S. Livet, F. Rosu, and V. Gabelica, "Drift tube ion mobility: How to reconstruct collision cross section distributions from arrival time distributions?," *Anal. Chem.*, vol. 89, pp. 12674–12681, Dec. 2017.
- [47] A. D. Rolland, L. S. Biberic, and J. S. Prell, "Investigation of Charge-State-Dependent compaction of protein ions with native ion Mobility-Mass spectrometry and theory," *J. Am. Soc. Mass Spectrom.*, vol. 33, pp. 369–381, Feb. 2022.
- [48] A. Q. Stiving, B. J. Jones, J. Ujma, K. Giles, and V. H. Wysocki, "Collision cross sections of Charge-Reduced proteins and protein complexes: A database for collision cross section calibration," *Anal. Chem.*, vol. 92, pp. 4475–4483, Mar. 2020.
- [49] S. D. Pringle, K. Giles, J. L. Wildgoose, J. P. Williams, S. E. Slade, K. Thalassinou, R. H. Bateman, M. T. Bowers, and J. H. Scrivens, "An investigation of the mobility separation of some peptide and protein ions using a new hybrid quadrupole/travelling wave IMS/oa-ToF instrument," *Int. J. Mass Spectrom.*, vol. 261, pp. 1–12, Mar. 2007.

- [50] K. Giles, S. D. Pringle, K. R. Worthington, D. Little, J. L. Wildgoose, and R. H. Bateman, "Applications of a travelling wave-based radio-frequency-only stacked ring ion guide," *Rapid Commun. Mass Spectrom.*, vol. 18, no. 20, pp. 2401–2414, 2004.
- [51] D. P. Smith, T. W. Knapman, I. Campuzano, R. W. Malham, J. T. Berryman, S. E. Radford, and A. E. Ashcroft, "Deciphering drift time measurements from travelling wave ion mobility spectrometry-mass spectrometry studies," *Eur. J. Mass Spectrom.*, vol. 15, no. 2, pp. 113–130, 2009.
- [52] A. A. Shvartsburg and R. D. Smith, "Fundamentals of traveling wave ion mobility spectrometry," *Anal. Chem.*, vol. 80, no. 24, pp. 9689–9699, 2008.
- [53] M. F. Bush, Z. Hall, K. Giles, J. Hoyes, C. V. Robinson, and B. T. Ruotolo, "Collision cross sections of proteins and their complexes: A calibration framework and database for Gas-Phase structural biology," *Anal. Chem.*, vol. 82, pp. 9557–9565, Nov. 2010.
- [54] K. Giles, J. Ujma, J. Wildgoose, S. Pringle, K. Richardson, D. Langridge, and M. Green, "A cyclic ion Mobility-Mass spectrometry system," *Anal. Chem.*, vol. 91, pp. 8564–8573, July 2019.
- [55] J. A. Harrison, A. Pruška, P. Bittner, A. Muck, D. A. Cooper-Shepherd, and R. Zenobi, "Advancing cyclic ion mobility mass spectrometry methods for studying biomolecules: Toward the conformational dynamics of mega dalton protein aggregates," *Anal. Chem.*, vol. 94, pp. 12435–12443, Sept. 2022.
- [56] C. Eldrid, J. Ujma, S. Kalfas, N. Tomczyk, K. Giles, M. Morris, and K. Thalassinou, "Gas phase stability of protein ions in a cyclic ion mobility spectrometry traveling wave device," *Anal. Chem.*, vol. 91, pp. 7554–7561, June 2019.
- [57] J. S. Brodbelt, "Ion activation methods for peptides and proteins," *Anal. Chem.*, vol. 88, pp. 30–51, Jan. 2016.
- [58] R. B. Cody, R. C. Burnier, and B. S. Freiser, "Collision-induced dissociation with fourier transform mass spectrometry," *Anal. Chem.*, vol. 54, pp. 96–101, Jan. 1982.
- [59] D. B. Wilburn, A. L. Richards, D. L. Swaney, and B. C. Searle, "CIDer: A statistical framework for interpreting differences in CID and HCD fragmentation," *J. Proteome Res.*, vol. 20, pp. 1951–1965, Apr. 2021.
- [60] K. O. Zhurov, L. Fornelli, M. D. Wodrich, Ü. A. Laskay, and Y. O. Tsybin, "Principles of electron capture and transfer dissociation mass spectrometry applied to peptide and protein structure analysis," *Chem. Soc. Rev.*, vol. 42, pp. 5014–5030, June 2013.
- [61] R. A. Zubarev, N. L. Kelleher, and F. W. McLafferty, "Electron capture dissociation of multiply charged protein cations. a nonergodic process," *J. Am. Chem. Soc.*, vol. 120, pp. 3265–3266, Apr. 1998.
- [62] J. Wiesner, T. Premisler, and A. Sickmann, "Application of electron transfer dissociation (ETD) for the analysis of posttranslational modifications," *Proteomics*, vol. 8, pp. 4466–4483, Nov. 2008.

- [63] Y. Xie, J. Zhang, S. Yin, and J. A. Loo, "Top-down ESI-ECD-FT-ICR mass spectrometry localizes noncovalent protein-ligand binding sites," *J. Am. Chem. Soc.*, vol. 128, pp. 14432–14433, Nov. 2006.
- [64] H. Li, Y. Sheng, W. McGee, M. Cammarata, D. Holden, and J. A. Loo, "Structural characterization of native proteins and protein complexes by electron ionization Dissociation-Mass spectrometry," *Anal. Chem.*, vol. 89, pp. 2731–2738, Mar. 2017.
- [65] B. Wei, C. Lantz, W. Liu, R. Viner, R. R. Ogorzalek Loo, I. D. G. Campuzano, and J. A. Loo, "Added value of internal fragments for Top-Down mass spectrometry of intact monoclonal antibodies and Antibody-Drug conjugates," *Anal. Chem.*, vol. 95, pp. 9347–9356, June 2023.
- [66] H. J. Cooper, K. Håkansson, and A. G. Marshall, "The role of electron capture dissociation in biomolecular analysis," *Mass Spectrom. Rev.*, vol. 24, no. 2, pp. 201–222, 2005.
- [67] R. A. Zubarev, "Electron-capture dissociation tandem mass spectrometry," *Curr. Opin. Biotechnol.*, vol. 15, pp. 12–16, Feb. 2004.
- [68] K. Jeacock, A. Chappard, K. J. Gallagher, C. L. Mackay, D. P. A. Kilgour, M. H. Horrocks, T. Kunath, and D. J. Clarke, "Determining the location of the α -Synuclein dimer interface using native Top-Down fragmentation and isotope Depletion-Mass spectrometry," *J. Am. Soc. Mass Spectrom.*, vol. 34, pp. 847–856, May 2023.
- [69] J. B. Shaw, D. A. Cooper-Shepherd, D. Hewitt, J. L. Wildgoose, J. S. Beckman, J. I. Langridge, and V. G. Voinov, "Enhanced Top-Down protein characterization with electron capture dissociation and cyclic ion mobility spectrometry," *Anal. Chem.*, vol. 94, pp. 3888–3896, Mar. 2022.
- [70] J. E. P. Syka, J. J. Coon, M. J. Schroeder, J. Shabanowitz, and D. F. Hunt, "Peptide and protein sequence analysis by electron transfer dissociation mass spectrometry," *Proc. Natl. Acad. Sci. U. S. A.*, vol. 101, pp. 9528–9533, June 2004.
- [71] C. K. Frese, H. Zhou, T. Taus, A. F. M. Altelaar, K. Mechtler, A. J. R. Heck, and S. Mohammed, "Unambiguous phosphosite localization using electron-transfer/higher-energy collision dissociation (EThcD)," *J. Proteome Res.*, vol. 12, pp. 1520–1525, Mar. 2013.
- [72] I. Ntai, R. D. LeDuc, R. T. Fellers, P. Erdmann-Gilmore, S. R. Davies, J. Rumsey, B. P. Early, P. M. Thomas, S. Li, P. D. Compton, M. J. C. Ellis, K. V. Ruggles, D. Fenyö, E. S. Boja, H. Rodriguez, R. R. Townsend, and N. L. Kelleher, "Integrated Bottom-Up and Top-Down proteomics of Patient-Derived breast tumor xenografts," *Mol. Cell. Proteomics*, vol. 15, pp. 45–56, Jan. 2016.
- [73] R. R. Julian, "The mechanism behind Top-Down UVPD experiments: Making sense of apparent contradictions," *J. Am. Soc. Mass Spectrom.*, vol. 28, pp. 1823–1826, Sept. 2017.
- [74] J. S. Brodbelt, "Photodissociation mass spectrometry: new tools for characterization of biological molecules," *Chem. Soc. Rev.*, vol. 43, pp. 2757–2783, Apr. 2014.
- [75] J. P. Reilly, "Ultraviolet photofragmentation of biomolecular ions," *Mass Spectrom. Rev.*, vol. 28, no. 3, pp. 425–447, 2009.

- [76] T. Ly and R. R. Julian, "Ultraviolet photodissociation: developments towards applications for mass-spectrometry-based proteomics," *Angew. Chem. Int. Ed Engl.*, vol. 48, no. 39, pp. 7130–7137, 2009.
- [77] L. J. Morrison and J. S. Brodbelt, "193 nm ultraviolet photodissociation mass spectrometry of tetrameric protein complexes provides insight into quaternary and secondary protein topology," *J. Am. Chem. Soc.*, vol. 138, pp. 10849–10859, Aug. 2016.
- [78] Y. V. Karpievitch, A. D. Polpitiya, G. A. Anderson, R. D. Smith, and A. R. Dabney, "Liquid chromatography mass Spectrometry-Based proteomics: Biological and technological aspects," *Ann. Appl. Stat.*, vol. 4, no. 4, pp. 1797–1823, 2010.
- [79] K. K. Unger, D. Kumar, M. Grün, G. Büchel, S. Lüdtke, T. Adam, K. Schumacher, and S. Renker, "Synthesis of spherical porous silicas in the micron and submicron size range: challenges and opportunities for miniaturized high-resolution chromatographic and electrokinetic separations," *J. Chromatogr. A*, vol. 892, pp. 47–55, Sept. 2000.
- [80] M. E. Swartz, "UPLC™: An introduction and review," *J. Liq. Chromatogr. Relat. Technol.*, vol. 28, pp. 1253–1263, Apr. 2005.
- [81] N. Wu, J. A. Lippert, and M. L. Lee, "Practical aspects of ultrahigh pressure capillary liquid chromatography," *J. Chromatogr. A*, vol. 911, pp. 1–12, Mar. 2001.
- [82] E. A. Livesay, K. Tang, B. K. Taylor, M. A. Buschbach, D. F. Hopkins, B. L. LaMarche, R. Zhao, Y. Shen, D. J. Orton, R. J. Moore, R. T. Kelly, H. R. Udseth, and R. D. Smith, "Fully automated four-column capillary LC-MS system for maximizing throughput in proteomic analyses," *Anal. Chem.*, vol. 80, pp. 294–302, Jan. 2008.
- [83] S. Guan, P. P. Taylor, Z. Han, M. F. Moran, and B. Ma, "Data Dependent-Independent acquisition (DDIA) proteomics," *J. Proteome Res.*, vol. 19, pp. 3230–3237, Aug. 2020.
- [84] K. W. Li, M. A. Gonzalez-Lozano, F. Koopmans, and A. B. Smit, "Recent developments in data independent acquisition (DIA) mass spectrometry: Application of quantitative analysis of the brain proteome," *Front. Mol. Neurosci.*, vol. 13, p. 564446, Dec. 2020.
- [85] L. Bichmann, S. Gupta, G. Rosenberger, L. Kuchenbecker, T. Sachsenberg, P. Ewels, O. Alka, J. Pfeuffer, O. Kohlbacher, and H. Röst, "DIAProteomics: A multifunctional data analysis pipeline for Data-Independent acquisition proteomics and peptidomics," *J. Proteome Res.*, vol. 20, pp. 3758–3766, July 2021.
- [86] D. C. Stahl, K. M. Swiderek, M. T. Davis, and T. D. Lee, "Data-controlled automation of liquid chromatography/tandem mass spectrometry analysis of peptide mixtures," *J. Am. Soc. Mass Spectrom.*, vol. 7, pp. 532–540, June 1996.
- [87] L. C. Gillet, P. Navarro, S. Tate, H. Röst, N. Selevsek, L. Reiter, R. Bonner, and R. Aebersold, "Targeted data extraction of the MS/MS spectra generated by data-independent acquisition: a new concept for consistent and accurate proteome analysis," *Mol. Cell. Proteomics*, vol. 11, p. O111.016717, June 2012.

- [88] A. N. Calabrese, B. Schiffrin, M. Watson, T. K. Karamanos, M. Walko, J. R. Humes, J. E. Horne, P. White, A. J. Wilson, A. C. Kalli, R. Tuma, A. E. Ashcroft, D. J. Brockwell, and S. E. Radford, “Inter-domain dynamics in the chaperone SurA and multi-site binding to its outer membrane protein clients,” *Nat. Commun.*, vol. 11, p. 2155, May 2020.
- [89] N. I. Brodie, K. I. Popov, E. V. Petrotchenko, N. V. Dokholyan, and C. H. Borchers, “Conformational ensemble of native α -synuclein in solution as determined by short-distance crosslinking constraint-guided discrete molecular dynamics simulations,” *PLoS Comput. Biol.*, vol. 15, no. 3, pp. e1006859–e1006859, 2019.
- [90] J. Zamel, J. Chen, S. Zaer, P. D. Harris, P. Drori, M. Lebediker, N. Kalisman, N. V. Dokholyan, and E. Lerner, “Structural and dynamic insights into α -synuclein dimer conformations,” *Structure*, vol. 31, pp. 411–423.e6, Apr. 2023.
- [91] M. C. S. Kit and I. Webb, “Surveying the conformational landscape of α -Synuclein using native crosslinking, ion Mobility-Mass spectrometry and ensemble modeling,” *ChemRxiv*, July 2023.
- [92] S. Lenz, L. R. Sinn, F. J. O’Reilly, L. Fischer, F. Wegner, and J. Rappsilber, “Reliable identification of protein-protein interactions by crosslinking mass spectrometry,” *Nat. Commun.*, vol. 12, p. 3564, June 2021.
- [93] L. Piersimoni, P. L. Kastritis, C. Arlt, and A. Sinz, “Cross-Linking mass spectrometry for investigating protein conformations and Protein-Protein Interactions-A method for all seasons,” *Chem. Rev.*, vol. 122, pp. 7500–7531, Apr. 2022.
- [94] J. Rappsilber, “The beginning of a beautiful friendship: cross-linking/mass spectrometry and modelling of proteins and multi-protein complexes,” *J. Struct. Biol.*, vol. 173, no. 3, pp. 530–540, 2011.
- [95] M. Schittmayer, K. Fritz, L. Liesinger, J. Griss, and R. Birner-Gruenberger, “Cleaning out the litterbox of proteomic scientists’ favorite pet: Optimized data analysis avoiding trypsin artifacts,” *J. Proteome Res.*, vol. 15, pp. 1222–1229, Apr. 2016.
- [96] E. Vandermarliere, M. Mueller, and L. Martens, “Getting intimate with trypsin, the leading protease in proteomics,” *Mass Spectrom. Rev.*, vol. 32, pp. 453–465, June 2013.
- [97] T. Dau, K. Gupta, I. Berger, and J. Rappsilber, “Sequential digestion with trypsin and elastase in Cross-Linking mass spectrometry,” *Anal. Chem.*, vol. 91, pp. 4472–4478, Apr. 2019.
- [98] T. Dau, G. Bartolomucci, and J. Rappsilber, “Proteomics using protease alternatives to trypsin benefits from sequential digestion with trypsin,” *Anal. Chem.*, vol. 92, pp. 9523–9527, July 2020.
- [99] L. Tsiatsiani and A. J. R. Heck, “Proteomics beyond trypsin,” *FEBS J.*, vol. 282, pp. 2612–2626, July 2015.
- [100] A. Sinz, “The advancement of chemical cross-linking and mass spectrometry for structural proteomics: from single proteins to protein interaction networks,” *Expert Rev. Proteomics*, vol. 11, pp. 733–743, Dec. 2014.

- [101] S. Mädler, M. Seitz, J. Robinson, and R. Zenobi, “Does chemical Cross-Linking with NHS esters reflect the chemical equilibrium of Protein–Protein noncovalent interactions in solution?,” *J. Am. Soc. Mass Spectrom.*, vol. 21, pp. 1775–1783, Oct. 2010.
- [102] D. Ubbiali, M. Fratini, L. Piersimoni, C. H. Ihling, M. Kipping, I. Heilmann, C. Iacobucci, and A. Sinz, “Direct observation of “elongated” conformational states in α -Synuclein upon Liquid-Liquid phase separation,” *Angew. Chem. Int. Ed Engl.*, vol. 61, p. e202205726, Nov. 2022.
- [103] A. Leitner, L. A. Joachimiak, P. Unverdorben, T. Walzthoeni, J. Frydman, F. Förster, and R. Aebersold, “Chemical cross-linking/mass spectrometry targeting acidic residues in proteins and protein complexes,” *Proc. Natl. Acad. Sci. U. S. A.*, vol. 111, pp. 9455–9460, July 2014.
- [104] A. Belsom and J. Rappsilber, “Anatomy of a crosslinker,” *Curr. Opin. Chem. Biol.*, vol. 60, pp. 39–46, Feb. 2021.
- [105] J. Mintseris and S. P. Gygi, “High-density chemical cross-linking for modeling protein interactions,” *Proc. Natl. Acad. Sci. U. S. A.*, vol. 117, pp. 93–102, Jan. 2020.
- [106] M. Barth and C. Schmidt, “Quantitative Cross-Linking of proteins and protein Complexes Proteinscomplexes,” in *Quantitative Methods in Proteomics* (K. Marcus, M. Eisenacher, and B. Sitek, eds.), pp. 385–400, New York, NY: Springer US, 2021.
- [107] R. F. Rivera-Santiago, S. Sriswasdi, S. L. Harper, and D. W. Speicher, “Probing structures of large protein complexes using zero-length cross-linking,” *Methods*, vol. 89, pp. 99–111, Nov. 2015.
- [108] N. I. Brodie, K. I. Popov, E. V. Petrotchenko, N. V. Dokholyan, and C. H. Borchers, “Solving protein structures using short-distance cross-linking constraints as a guide for discrete molecular dynamics simulations,” *Sci Adv*, vol. 3, p. e1700479, July 2017.
- [109] K. Lee and F. J. O’Reilly, “Cross-linking mass spectrometry for mapping protein complex topologies in situ,” *Essays Biochem.*, vol. 67, pp. 215–228, Mar. 2023.
- [110] W. Javed, D. Griffiths, and A. Politis, “Hydrogen/deuterium exchange-mass spectrometry of integral membrane proteins in native-like environments: current scenario and the way forward,” *Essays Biochem.*, vol. 67, pp. 187–200, Mar. 2023.
- [111] Z. Ahdash, E. Pyle, W. J. Allen, R. A. Corey, I. Collinson, and A. Politis, “HDX-MS reveals nucleotide-dependent, anti-correlated opening and closure of SecA and SecY channels of the bacterial translocon,” *Elife*, vol. 8, July 2019.
- [112] P. M. Scrosati, V. Yin, and L. Konermann, “Hydrogen/Deuterium exchange measurements may provide an incomplete view of protein dynamics: a case study on cytochrome c,” *Anal. Chem.*, vol. 93, pp. 14121–14129, Oct. 2021.
- [113] Y. Haidar and L. Konermann, “Effects of Hydrogen/Deuterium exchange on protein stability in solution and in the gas phase,” *J. Am. Soc. Mass Spectrom.*, vol. 34, pp. 1447–1458, July 2023.

- [114] A. D. Stephens, M. Zacharopoulou, R. Moons, G. Fusco, N. Seetaloo, A. Chiki, P. J. Woodhams, I. Mela, H. A. Lashuel, J. J. Phillips, A. De Simone, F. Sobott, and G. S. K. Schierle, “Extent of n-terminus exposure of monomeric alpha-synuclein determines its aggregation propensity,” *Nat. Commun.*, vol. 11, p. 2820, June 2020.
- [115] M. Kish, S. Subramanian, V. Smith, N. Lethbridge, L. Cole, F. Vollmer, N. J. Bond, and J. J. Phillips, “Allosteric regulation of glycogen phosphorylase by Order/Disorder transition of the 250’ and 280s loops,” *Biochemistry*, vol. 62, pp. 1360–1368, Apr. 2023.
- [116] N. Seetaloo, M. Zacharopoulou, A. D. Stephens, G. S. Kaminski Schierle, and J. J. Phillips, “Millisecond Hydrogen/Deuterium-Exchange mass spectrometry approach to correlate local structure and aggregation in α -Synuclein,” *Anal. Chem.*, vol. 94, pp. 16711–16719, Dec. 2022.
- [117] J. Li, H. Wei, S. R. Krystek, Jr, D. Bond, T. M. Brender, D. Cohen, J. Feiner, N. Hamacher, J. Harshman, R. Y. C. Huang, S. H. Julien, Z. Lin, K. Moore, L. Mueller, C. Noriega, P. Sejwal, P. Sheppard, B. Stevens, G. Chen, A. A. Tymiak, M. L. Gross, and L. A. Schneeweis, “Mapping the energetic epitope of an Antibody/Interleukin-23 interaction with Hydrogen/Deuterium exchange, fast photochemical oxidation of proteins mass spectrometry, and alanine shave mutagenesis,” *Anal. Chem.*, vol. 89, no. 4, pp. 2250–2258, 2017.
- [118] K. Przygońska, J. Poznański, U. H. Mizarz, K. D. Rand, and M. Dadlez, “Side-chain moieties from the n-terminal region of A β are involved in an oligomer-stabilizing network of interactions,” *PLoS One*, vol. 13, no. 8, p. e0201761, 2018.
- [119] L. Konermann, J. Pan, and Y.-H. Liu, “Hydrogen exchange mass spectrometry for studying protein structure and dynamics,” *Chem. Soc. Rev.*, vol. 40, pp. 1224–1234, Mar. 2011.
- [120] G. R. Masson, J. E. Burke, N. G. Ahn, G. S. Anand, C. Borchers, S. Brier, G. M. Bou-Assaf, J. R. Engen, S. W. Englander, J. Faber, R. Garlish, P. R. Griffin, M. L. Gross, M. Guttman, Y. Hamuro, A. J. R. Heck, D. Houde, R. E. Iacob, T. J. D. Jørgensen, I. A. Kaltashov, J. P. Klinman, L. Konermann, P. Man, L. Mayne, B. D. Pascal, D. Reichmann, M. Skehel, J. Snijder, T. S. Strutzenberg, E. S. Underbakke, C. Wagner, T. E. Wales, B. T. Walters, D. D. Weis, D. J. Wilson, P. L. Wintrode, Z. Zhang, J. Zheng, D. C. Schriemer, and K. D. Rand, “Recommendations for performing, interpreting and reporting hydrogen deuterium exchange mass spectrometry (HDX-MS) experiments,” *Nat. Methods*, vol. 16, pp. 595–602, July 2019.
- [121] E. I. James, T. A. Murphree, C. Vorauer, J. R. Engen, and M. Guttman, “Advances in Hydrogen/Deuterium exchange mass spectrometry and the pursuit of challenging biological systems,” *Chem. Rev.*, vol. 122, pp. 7562–7623, Apr. 2022.
- [122] I. Kheterpal, K. D. Cook, and R. Wetzel, “Hydrogen/Deuterium exchange mass spectrometry analysis of protein aggregates,” in *Methods in Enzymology*, vol. 413, pp. 140–166, Academic Press, Jan. 2006.
- [123] M. Noda, K. Ishii, M. Yamauchi, H. Oyama, T. Tadokoro, K. Maenaka, T. Torisu, and S. Uchiyama, “Identification of IgG1 aggregation initiation region by hydrogen deuterium mass spectrometry,” *J. Pharm. Sci.*, vol. 108, pp. 2323–2333, July 2019.

- [124] C. M. Dobson, A. Šali, and M. Karplus, "Protein folding: A perspective from theory and experiment," *Angew. Chem. Int. Ed Engl.*, vol. 37, pp. 868–893, Apr. 1998.
- [125] L. Pauling and R. B. Corey, "The pleated sheet, a new layer configuration of polypeptide chains," *Proc. Natl. Acad. Sci. U. S. A.*, vol. 37, pp. 251–256, May 1951.
- [126] L. Pauling and R. B. Corey, "Atomic coordinates and structure factors for two helical configurations of polypeptide chains," *Proc. Natl. Acad. Sci. U. S. A.*, vol. 37, pp. 235–240, May 1951.
- [127] T. Pascher, J. P. Chesick, J. R. Winkler, and H. B. Gray, "Protein folding triggered by electron transfer," *Science*, vol. 271, pp. 1558–1560, Mar. 1996.
- [128] R. Aurora, T. P. Creamer, R. Srinivasan, and G. D. Rose, "Local interactions in protein folding: lessons from the alpha-helix," *J. Biol. Chem.*, vol. 272, pp. 1413–1416, Jan. 1997.
- [129] K. A. Dill and H. S. Chan, "From levinthal to pathways to funnels," *Nat. Struct. Biol.*, vol. 4, pp. 10–19, Jan. 1997.
- [130] C. B. Anfinsen and H. A. Scheraga, "Experimental and theoretical aspects of protein folding," in *Advances in Protein Chemistry* (C. B. Anfinsen, J. T. Edsall, and F. M. Richards, eds.), vol. 29, pp. 205–300, Academic Press, Jan. 1975.
- [131] R. L. Baldwin, "Matching speed and stability." <http://dx.doi.org/10.1038/369183a0>, May 1994. Accessed: 2023-11-8.
- [132] R. M. Ballew, J. Sabelko, and M. Gruebele, "Observation of distinct nanosecond and microsecond protein folding events," *Nat. Struct. Biol.*, vol. 3, pp. 923–926, Nov. 1996.
- [133] R. L. Baldwin, "The nature of protein folding pathways: the classical versus the new view," *J. Biomol. NMR*, vol. 5, pp. 103–109, Feb. 1995.
- [134] M. C. Shastry and H. Roder, "Evidence for barrier-limited protein folding kinetics on the microsecond time scale," *Nat. Struct. Biol.*, vol. 5, pp. 385–392, May 1998.
- [135] K. A. Dill, "Polymer principles and protein folding," *Protein Sci.*, vol. 8, pp. 1166–1180, June 1999.
- [136] Y. Cordeiro, B. Macedo, J. L. Silva, and M. P. B. Gomes, "Pathological implications of nucleic acid interactions with proteins associated with neurodegenerative diseases," *Biophys. Rev.*, vol. 6, pp. 97–110, Mar. 2014.
- [137] K. F. Winklhofer, J. Tatzelt, and C. Haass, "The two faces of protein misfolding: gain- and loss-of-function in neurodegenerative diseases," *EMBO J.*, vol. 27, pp. 336–349, Jan. 2008.
- [138] R. W. Carrell and D. A. Lomas, "Conformational disease," *Lancet*, vol. 350, pp. 134–138, July 1997.
- [139] C. M. Dobson, "Protein-misfolding diseases: Getting out of shape." <http://dx.doi.org/10.1038/418729a>, Aug. 2002. Accessed: 2023-11-8.

- [140] C. M. Dobson, "Protein folding and misfolding," *Nature*, vol. 426, pp. 884–890, Dec. 2003.
- [141] F. Chiti and C. M. Dobson, "Protein misfolding, functional amyloid, and human disease," *Annu. Rev. Biochem.*, vol. 75, pp. 333–366, June 2006.
- [142] M. Maiti, M. Rao, and S. Sastry, "Competition between folding and aggregation in a model for protein solutions," *Eur. Phys. J. E Soft Matter*, vol. 32, pp. 217–221, June 2010.
- [143] C. M. Dobson, "Principles of protein folding, misfolding and aggregation," *Semin. Cell Dev. Biol.*, vol. 15, pp. 3–16, Feb. 2004.
- [144] D. Otzen and R. Riek, "Functional amyloids," *Cold Spring Harb. Perspect. Biol.*, vol. 11, Dec. 2019.
- [145] W. T. Astbury, S. Dickinson, and K. Bailey, "The x-ray interpretation of denaturation and the structure of the seed globulins," *Biochem. J*, vol. 29, pp. 2351–2360.1, Oct. 1935.
- [146] M. B. Pepys, "Pathogenesis, diagnosis and treatment of systemic amyloidosis," *Philos. Trans. R. Soc. Lond. B Biol. Sci.*, vol. 356, pp. 203–10; discussion 210–1, Feb. 2001.
- [147] J. F. Smith, T. P. J. Knowles, C. M. Dobson, C. E. Macphee, and M. E. Welland, "Characterization of the nanoscale properties of individual amyloid fibrils," *Proc. Natl. Acad. Sci. U. S. A.*, vol. 103, pp. 15806–15811, Oct. 2006.
- [148] H. L. Krystal, D. A. Ross, and A. P. Mecca, "Amyloid: From starch to finish," *Biol. Psychiatry*, vol. 87, pp. e23–e24, May 2020.
- [149] R. A. Kyle, "Amyloidosis: a convoluted story," *Br. J. Haematol.*, vol. 114, pp. 529–538, Sept. 2001.
- [150] A. I. P. Taylor and R. A. Staniforth, "General principles underpinning amyloid structure," *Front. Neurosci.*, vol. 16, p. 878869, June 2022.
- [151] P. Kazman, M.-T. Vielberg, M. D. Pulido Cendales, L. Hunziger, B. Weber, U. Hegenbart, M. Zacharias, R. Köhler, S. Schönland, M. Groll, and J. Buchner, "Fatal amyloid formation in a patient's antibody light chain is caused by a single point mutation," *Elife*, vol. 9, Mar. 2020.
- [152] R. M. Absmeier, G. J. Rottenaicher, H. L. Svilenov, P. Kazman, and J. Buchner, "Antibodies gone bad - the molecular mechanism of light chain amyloidosis," *FEBS J.*, vol. 290, pp. 1398–1419, Mar. 2023.
- [153] L. M. Blancas-Mejia, P. Misra, C. J. Dick, S. A. Cooper, K. R. Redhage, M. R. Bergman, T. L. Jordan, K. Maar, and M. Ramirez-Alvarado, "Immunoglobulin light chain amyloid aggregation," *Chem. Commun.*, vol. 54, pp. 10664–10674, Sept. 2018.

- [154] A. Soragni, S. Yousefi, C. Stoeckle, A. B. Soriaga, M. R. Sawaya, E. Kozlowski, I. Schmid, S. Radonjic-Hoesli, S. Boutet, G. J. Williams, M. Messerschmidt, M. M. Seibert, D. Cascio, N. A. Zatsopin, M. Burghammer, C. Riek, J.-P. Colletier, R. Riek, D. S. Eisenberg, and H.-U. Simon, "Toxicity of eosinophil MBP is repressed by intracellular crystallization and promoted by extracellular aggregation," *Mol. Cell*, vol. 57, pp. 1011–1021, Mar. 2015.
- [155] R. R. Boyer, S. S. Sumner, R. C. Williams, M. D. Pierson, D. L. Popham, and K. E. Kniel, "Influence of curli expression by *Escherichia coli* 0157:h7 on the cell's overall hydrophobicity, charge, and ability to attach to lettuce," *J. Food Prot.*, vol. 70, pp. 1339–1345, June 2007.
- [156] M. G. Iadanza, M. P. Jackson, E. W. Hewitt, N. A. Ranson, and S. E. Radford, "A new era for understanding amyloid structures and disease," *Nat. Rev. Mol. Cell Biol.*, vol. 19, pp. 755–773, Dec. 2018.
- [157] F. Chiti and C. M. Dobson, "Protein misfolding, amyloid formation, and human disease: A summary of progress over the last decade," *Annu. Rev. Biochem.*, vol. 86, pp. 27–68, June 2017.
- [158] J. D. Sipe, M. D. Benson, J. N. Buxbaum, S.-I. Ikeda, G. Merlini, M. J. M. Saraiva, and P. Westermark, "Amyloid fibril proteins and amyloidosis: chemical identification and clinical classification international society of amyloidosis 2016 nomenclature guidelines," *Amyloid*, vol. 23, pp. 209–213, Dec. 2016.
- [159] M. P. Hughes, L. Goldschmidt, and D. S. Eisenberg, "Prevalence and species distribution of the low-complexity, amyloid-like, reversible, kinked segment structural motif in amyloid-like fibrils," *J. Biol. Chem.*, vol. 297, p. 101194, Oct. 2021.
- [160] S. M. Cascarina, M. R. Elder, and E. D. Ross, "Atypical structural tendencies among low-complexity domains in the protein data bank proteome," *PLoS Comput. Biol.*, vol. 16, p. e1007487, Jan. 2020.
- [161] T. M. Franzmann and S. Alberti, "Prion-like low-complexity sequences: Key regulators of protein solubility and phase behavior," *J. Biol. Chem.*, vol. 294, pp. 7128–7136, May 2019.
- [162] R. Kisilevsky, "Review: amyloidogenesis-unquestioned answers and unanswered questions," *J. Struct. Biol.*, vol. 130, pp. 99–108, June 2000.
- [163] R. Khurana, C. Coleman, C. Ionescu-Zanetti, S. A. Carter, V. Krishna, R. K. Grover, R. Roy, and S. Singh, "Mechanism of thioflavin T binding to amyloid fibrils," *J. Struct. Biol.*, vol. 151, pp. 229–238, Sept. 2005.
- [164] S. Linse and T. Knowles, "Amyloids and protein aggregation," *Chem. Sci.*, vol. 14, pp. 6491–6492, June 2023.
- [165] R. N. Rambaran and L. C. Serpell, "Amyloid fibrils: abnormal protein assembly," *Prion*, vol. 2, pp. 112–117, July 2008.
- [166] W.-F. Xue, S. W. Homans, and S. E. Radford, "Systematic analysis of nucleation-dependent polymerization reveals new insights into the mechanism of amyloid self-assembly," *Proc. Natl. Acad. Sci. U. S. A.*, vol. 105, pp. 8926–8931, July 2008.

- [167] M. Bokor and Á. Tantos, “Protein-Protein Connections-Oligomer, amyloid and protein Complex-By wide line 1H NMR,” *Biomolecules*, vol. 11, May 2021.
- [168] J. Santos, J. Cuellar, I. Pallarès, E. J. Byrd, A. Lends, F. Moro, M. B. Abdul-Shukoor, J. Pujols, L. Velasco-Carneros, F. Sobott, D. E. Otzen, A. N. Calabrese, A. Muga, J. S. Pedersen, A. Loquet, J. M. Valpuesta, S. E. Radford, and S. Ventura, “The structural architecture of an α -synuclein toxic oligomer.” Feb. 2023.
- [169] K. A. Conway, S.-J. Lee, J.-C. Rochet, T. T. Ding, R. E. Williamson, and P. T. Lansbury, “Acceleration of oligomerization, not fibrillization, is a shared property of both α -synuclein mutations linked to early-onset parkinson’s disease: Implications for pathogenesis and therapy,” *Proceedings of the National Academy of Sciences*, vol. 97, no. 2, pp. 571–576, 2000.
- [170] K. M. Danzer, D. Haasen, A. R. Karow, S. Moussaud, M. Habeck, A. Giese, H. Kretschmar, B. Hengerer, and M. Kostka, “Different species of alpha-synuclein oligomers induce calcium influx and seeding,” *J. Neurosci.*, vol. 27, no. 34, pp. 9220–9232, 2007.
- [171] N. Cremades, S. I. A. Cohen, E. Deas, A. Y. Abramov, A. Y. Chen, A. Orte, M. Sandal, R. W. Clarke, P. Dunne, F. A. Aprile, C. W. Bertocini, N. W. Wood, T. P. J. Knowles, C. M. Dobson, and D. Klenerman, “Direct observation of the interconversion of normal and toxic forms of α -synuclein,” *Cell*, vol. 149, pp. 1048–1059, May 2012.
- [172] G. Fusco, S. W. Chen, P. T. F. Williamson, R. Cascella, M. Perni, J. A. Jarvis, C. Cecchi, M. Vendruscolo, F. Chiti, N. Cremades, L. Ying, C. M. Dobson, and A. De Simone, “Structural basis of membrane disruption and cellular toxicity by α -synuclein oligomers,” *Science*, vol. 358, pp. 1440–1443, Dec. 2017.
- [173] S. R. Durell, R. Kaye, and H. R. Guy, “The amyloid concentric β -barrel hypothesis: Models of amyloid beta 42 oligomers and annular protofibrils,” *Proteins*, vol. 90, pp. 1190–1209, May 2022.
- [174] M. Serra-Batiste, M. Ninot-Pedrosa, M. Bayoumi, M. Gairí, G. Maglia, and N. Carulla, “A β 42 assembles into specific β -barrel pore-forming oligomers in membrane-mimicking environments,” *Proc. Natl. Acad. Sci. U. S. A.*, vol. 113, pp. 10866–10871, Sept. 2016.
- [175] Y. Sun, X. Ge, Y. Xing, B. Wang, and F. Ding, “ β -barrel oligomers as common intermediates of peptides Self-Assembling into Cross- β aggregates,” *Sci. Rep.*, vol. 8, p. 10353, July 2018.
- [176] N. Österlund, R. Moons, L. L. Ilag, F. Sobott, and A. Gräslund, “Native ion Mobility-Mass spectrometry reveals the formation of β -Barrel shaped Amyloid- β hexamers in a Membrane-Mimicking environment,” *J. Am. Chem. Soc.*, vol. 141, pp. 10440–10450, July 2019.
- [177] M. Biancalana, K. Makabe, A. Koide, and S. Koide, “Molecular mechanism of thioflavin-t binding to the surface of beta-rich peptide self-assemblies,” *J. Mol. Biol.*, vol. 385, pp. 1052–1063, Jan. 2009.

- [178] M. Groenning, L. Olsen, M. van de Weert, J. M. Flink, S. Frokjaer, and F. S. Jørgensen, "Study on the binding of thioflavin T to beta-sheet-rich and non-beta-sheet cavities," *J. Struct. Biol.*, vol. 158, pp. 358–369, June 2007.
- [179] R. Riek, "The Three-Dimensional structures of amyloids," *Cold Spring Harb. Perspect. Biol.*, vol. 9, Feb. 2017.
- [180] E. Gazit, "A possible role for pi-stacking in the self-assembly of amyloid fibrils," *FASEB J.*, vol. 16, pp. 77–83, Jan. 2002.
- [181] L. C. Serpell, "Alzheimer's amyloid fibrils: structure and assembly," *Biochimica et Biophysica Acta (BBA) - Molecular Basis of Disease*, vol. 1502, pp. 16–30, July 2000.
- [182] G. Meisl, J. B. Kirkegaard, P. Arosio, T. C. T. Michaels, M. Vendruscolo, C. M. Dobson, S. Linse, and T. P. J. Knowles, "Molecular mechanisms of protein aggregation from global fitting of kinetic models," *Nat. Protoc.*, vol. 11, pp. 252–272, Feb. 2016.
- [183] A. Binolfi, R. M. Rasia, C. W. Bertocini, M. Ceolin, M. Zweckstetter, C. Griesinger, T. M. Jovin, and C. O. Fernández, "Interaction of α -Synuclein with divalent metal ions reveals key differences: A link between structure, binding specificity and fibrillation enhancement," *J. Am. Chem. Soc.*, vol. 128, pp. 9893–9901, Aug. 2006.
- [184] R. J. Mason, A. R. Paskins, C. F. Dalton, and D. P. Smith, "Copper binding and subsequent aggregation of α -Synuclein are modulated by N-Terminal acetylation and ablated by the H50Q missense mutation," *Biochemistry*, vol. 55, pp. 4737–4741, Aug. 2016.
- [185] L. Khemtemourian, F. Antoniciello, B. R. Sahoo, M. Decossas, S. Lecomte, and A. Ramamoorthy, "Investigation of the effects of two major secretory granules components, insulin and zinc, on human-IAPP amyloid aggregation and membrane damage," *Chem. Phys. Lipids*, vol. 237, p. 105083, July 2021.
- [186] J. R. Brender, K. Hartman, R. P. R. Nanga, N. Popovych, R. de la Salud Bea, S. Vivekanandan, E. N. G. Marsh, and A. Ramamoorthy, "Role of zinc in human islet amyloid polypeptide aggregation," *J. Am. Chem. Soc.*, vol. 132, pp. 8973–8983, July 2010.
- [187] B. Ward, K. Walker, and C. Exley, "Copper(II) inhibits the formation of amylin amyloid in vitro," *J. Inorg. Biochem.*, vol. 102, pp. 371–375, Feb. 2008.
- [188] B. Caughey, G. S. Baron, B. Chesebro, and M. Jeffrey, "Getting a grip on prions: oligomers, amyloids, and pathological membrane interactions," *Annu. Rev. Biochem.*, vol. 78, pp. 177–204, 2009.
- [189] G. Yoo, Y.-K. Shin, and N. K. Lee, "The role of α -Synuclein in SNARE-mediated synaptic vesicle fusion," *J. Mol. Biol.*, vol. 435, p. 167775, Jan. 2023.
- [190] D. Ruzafa, Y. S. Hernandez-Gomez, G. Bisello, K. Broersen, B. Morel, and F. Conejero-Lara, "The influence of n-terminal acetylation on micelle-induced conformational changes and aggregation of α -Synuclein," *PLoS One*, vol. 12, p. e0178576, May 2017.

- [191] M. Bucciantini, S. Rigacci, and M. Stefani, "Amyloid aggregation: Role of biological membranes and the Aggregate-Membrane system," *J. Phys. Chem. Lett.*, vol. 5, pp. 517–527, Feb. 2014.
- [192] G. A. P. de Oliveira, Y. Cordeiro, J. L. Silva, and T. C. R. G. Vieira, "Liquid-liquid phase transitions and amyloid aggregation in proteins related to cancer and neurodegenerative diseases," *Adv. Protein Chem. Struct. Biol.*, vol. 118, pp. 289–331, Sept. 2019.
- [193] J. D. Camino, P. Gracia, and N. Cremades, "The role of water in the primary nucleation of protein amyloid aggregation," *Biophys. Chem.*, vol. 269, p. 106520, Feb. 2021.
- [194] A. Ahmad, V. N. Uversky, and R. H. Khan, "Aberrant liquid-liquid phase separation and amyloid aggregation of proteins related to neurodegenerative diseases," *Int. J. Biol. Macromol.*, vol. 220, pp. 703–720, Nov. 2022.
- [195] M. Li, Y. Fan, Q. Li, X. Wang, L. Zhao, and M. Zhu, "Liquid-Liquid phase separation promotes protein aggregation and its implications in ferroptosis in parkinson's disease dementia," *Oxid. Med. Cell. Longev.*, vol. 2022, p. 7165387, Oct. 2022.
- [196] S. F. Banani, H. O. Lee, A. A. Hyman, and M. K. Rosen, "Biomolecular condensates: organizers of cellular biochemistry," *Nat. Rev. Mol. Cell Biol.*, vol. 18, pp. 285–298, May 2017.
- [197] A. S. Lyon, W. B. Peeples, and M. K. Rosen, "A framework for understanding the functions of biomolecular condensates across scales," *Nat. Rev. Mol. Cell Biol.*, vol. 22, pp. 215–235, Mar. 2021.
- [198] X. Niu, L. Zhang, Y. Wu, Z. Zong, B. Wang, J. Liu, L. Zhang, and F. Zhou, "Biomolecular condensates: Formation mechanisms, biological functions, and therapeutic targets," *MedComm (2020)*, vol. 4, p. e223, Apr. 2023.
- [199] N. Lorén, J. Hagman, J. K. Jonasson, H. Deschout, D. Bernin, F. Cella-Zanacchi, A. Diaspro, J. G. McNally, M. Ameloot, N. Smisdom, M. Nydén, A.-M. Hermansson, M. Rudemo, and K. Braeckmans, "Fluorescence recovery after photobleaching in material and life sciences: putting theory into practice," *Q. Rev. Biophys.*, vol. 48, pp. 323–387, Aug. 2015.
- [200] F. Muzzopappa, J. Hummert, M. Anfossi, S. A. Tashev, D.-P. Herten, and F. Erdel, "Detecting and quantifying liquid-liquid phase separation in living cells by model-free calibrated half-bleaching," *Nat. Commun.*, vol. 13, p. 7787, Dec. 2022.
- [201] S. Ray, N. Singh, K. Patel, G. Krishnamoorthy, and S. K. Maji, "FRAP and FRET investigation of α -Synuclein fibrillization via Liquid-Liquid phase separation in vitro and in HeLa cells," *Methods Mol. Biol.*, vol. 2551, pp. 395–423, 2023.
- [202] L. Pytowski, C. F. Lee, A. C. Foley, D. J. Vaux, and L. Jean, "Liquid-liquid phase separation of type II diabetes-associated IAPP initiates hydrogelation and aggregation," *Proc. Natl. Acad. Sci. U. S. A.*, vol. 117, pp. 12050–12061, June 2020.
- [203] A. E. Conicella, G. H. Zerze, J. Mittal, and N. L. Fawzi, "ALS mutations disrupt phase separation mediated by α -Helical structure in the TDP-43 Low-Complexity C-Terminal domain," *Structure*, vol. 24, pp. 1537–1549, Sept. 2016.

- [204] S. Ray, N. Singh, R. Kumar, K. Patel, S. Pandey, D. Datta, J. Mahato, R. Panigrahi, A. Navalkar, S. Mehra, L. Gadhe, D. Chatterjee, A. S. Sawner, S. Maiti, S. Bhatia, J. A. Gerez, A. Chowdhury, A. Kumar, R. Padinhateeri, R. Riek, G. Krishnamoorthy, and S. K. Maji, “ α -Synuclein aggregation nucleates through liquid–liquid phase separation,” *Nat. Chem.*, vol. 12, pp. 705–716, Aug. 2020.
- [205] M. C. Hardenberg, T. Sinnige, S. Casford, S. T. Dada, C. Poudel, E. A. Robinson, M. Fuxreiter, C. F. Kaminski, G. S. Kaminski Schierle, E. A. A. Nollen, C. M. Dobson, and M. Vendruscolo, “Observation of an α -synuclein liquid droplet state and its maturation into lewy body-like assemblies,” *J. Mol. Cell Biol.*, vol. 13, pp. 282–294, Aug. 2021.
- [206] M. D. Tuttle, G. Comellas, A. J. Nieuwkoop, D. J. Covell, D. A. Berthold, K. D. Kloepper, J. M. Courtney, J. K. Kim, A. M. Barclay, A. Kendall, W. Wan, G. Stubbs, C. D. Schwieters, V. M. Y. Lee, J. M. George, and C. M. Rienstra, “Solid-state NMR structure of a pathogenic fibril of full-length human α -synuclein,” *Nat. Struct. Mol. Biol.*, vol. 23, pp. 409–415, May 2016.
- [207] X. Yang, B. Wang, C. L. Hoop, J. K. Williams, and J. Baum, “NMR unveils an n-terminal interaction interface on acetylated- α -synuclein monomers for recruitment to fibrils,” *Proc. Natl. Acad. Sci. U. S. A.*, vol. 118, May 2021.
- [208] R. Guerrero-Ferreira, N. M. Taylor, A.-A. Arteni, P. Kumari, D. Mona, P. Ringler, M. Britschgi, M. E. Lauer, A. Makky, J. Verasdonck, R. Riek, R. Melki, B. H. Meier, A. Böckmann, L. Bousset, and H. Stahlberg, “Two new polymorphic structures of human full-length alpha-synuclein fibrils solved by cryo-electron microscopy,” *Elife*, vol. 8, Dec. 2019.
- [209] R. Guerrero-Ferreira, N. M. Taylor, D. Mona, P. Ringler, M. E. Lauer, R. Riek, M. Britschgi, and H. Stahlberg, “Cryo-EM structure of alpha-synuclein fibrils,” *Elife*, vol. 7, p. e36402, 2018.
- [210] Y. Yang, Y. Shi, M. Schweighauser, X. Zhang, A. Kotecha, A. G. Murzin, H. J. Garringer, P. W. Cullinane, Y. Saito, T. Foroud, T. T. Warner, K. Hasegawa, R. Vidal, S. Murayama, T. Revesz, B. Ghetti, M. Hasegawa, T. Lashley, S. H. W. Scheres, and M. Goedert, “Structures of α -synuclein filaments from human brains with lewy pathology,” *Nature*, vol. 610, pp. 791–795, Oct. 2022.
- [211] B. Li, P. Ge, K. A. Murray, P. Sheth, M. Zhang, G. Nair, M. R. Sawaya, W. S. Shin, D. R. Boyer, S. Ye, D. S. Eisenberg, Z. H. Zhou, and L. Jiang, “Cryo-EM of full-length α -synuclein reveals fibril polymorphs with a common structural kernel,” *Nat. Commun.*, vol. 9, p. 3609, Sept. 2018.
- [212] W.-F. Xue, S. W. Homans, and S. E. Radford, “Amyloid fibril length distribution quantified by atomic force microscopy single-particle image analysis,” *Protein Eng. Des. Sel.*, vol. 22, pp. 489–496, Aug. 2009.
- [213] “Amyloid atlas 2023.” <https://people.mbi.ucla.edu/sawaya/amyloidatlas/>. Accessed: 2023-9-12.
- [214] M. Sunde, L. C. Serpell, M. Bartlam, P. E. Fraser, M. B. Pepys, and C. C. Blake, “Common core structure of amyloid fibrils by synchrotron x-ray diffraction,” *J. Mol. Biol.*, vol. 273, pp. 729–739, Oct. 1997.

- [215] J. W. Kelly, "Alternative conformations of amyloidogenic proteins govern their behavior," *Curr. Opin. Struct. Biol.*, vol. 6, pp. 11–17, Feb. 1996.
- [216] N. Salinas, E. Tayeb-Fligelman, M. D. Sammito, D. Bloch, R. Jelinek, D. Noy, I. Usón, and M. Landau, "The amphibian antimicrobial peptide uperin 3.5 is a cross- α /cross- β chameleon functional amyloid," *Proc. Natl. Acad. Sci. U. S. A.*, vol. 118, Jan. 2021.
- [217] B. C. Creekmore, Y.-W. Chang, and E. B. Lee, "The Cryo-EM effect: Structural biology of neurodegenerative disease aggregates," *J. Neuropathol. Exp. Neurol.*, vol. 80, pp. 514–529, June 2021.
- [218] L. D. Aubrey, B. J. F. Blakeman, L. Lutter, C. J. Serpell, M. F. Tuite, L. C. Serpell, and W.-F. Xue, "Quantification of amyloid fibril polymorphism by nanomorphometry reveals the individuality of filament assembly," *Commun Chem*, vol. 3, p. 125, Sept. 2020.
- [219] J. D. Harper, S. S. Wong, C. M. Lieber, and P. T. Lansbury, "Observation of metastable abeta amyloid protofibrils by atomic force microscopy," *Chem. Biol.*, vol. 4, pp. 119–125, Feb. 1997.
- [220] L. Gremer, D. Schölzel, C. Schenk, E. Reinartz, J. Labahn, R. B. G. Ravelli, M. Tusche, C. Lopez-Iglesias, W. Hoyer, H. Heise, D. Willbold, and G. F. Schröder, "Fibril structure of amyloid- β (1-42) by cryo-electron microscopy," *Science*, vol. 358, pp. 116–119, Oct. 2017.
- [221] Y. Yang, D. Arseni, W. Zhang, M. Huang, S. Lövestam, M. Schweighauser, A. Kotecha, A. G. Murzin, S. Y. Peak-Chew, J. Macdonald, I. Lavenir, H. J. Garringer, E. Gelpi, K. L. Newell, G. G. Kovacs, R. Vidal, B. Ghetti, B. Ryskeldi-Falcon, S. H. W. Scheres, and M. Goedert, "Cryo-EM structures of amyloid- β 42 filaments from human brains," *Science*, vol. 375, pp. 167–172, Jan. 2022.
- [222] S. H. Scheres, W. Zhang, B. Falcon, and M. Goedert, "Cryo-EM structures of tau filaments," *Curr. Opin. Struct. Biol.*, vol. 64, pp. 17–25, Oct. 2020.
- [223] A. W. P. Fitzpatrick, B. Falcon, S. He, A. G. Murzin, G. Murshudov, H. J. Garringer, R. A. Crowther, B. Ghetti, M. Goedert, and S. H. W. Scheres, "Cryo-EM structures of tau filaments from alzheimer's disease," *Nature*, vol. 547, pp. 185–190, July 2017.
- [224] M. Schweighauser, D. Arseni, M. Bacioglu, M. Huang, S. Lövestam, Y. Shi, Y. Yang, W. Zhang, A. Kotecha, H. J. Garringer, R. Vidal, G. I. Hallinan, K. L. Newell, A. Tarutani, S. Murayama, M. Miyazaki, Y. Saito, M. Yoshida, K. Hasegawa, T. Lashley, T. Revesz, G. G. Kovacs, J. van Swieten, M. Takao, M. Hasegawa, B. Ghetti, M. G. Spillantini, B. Ryskeldi-Falcon, A. G. Murzin, M. Goedert, and S. H. W. Scheres, "Age-dependent formation of TMEM106B amyloid filaments in human brains," *Nature*, vol. 605, pp. 310–314, May 2022.
- [225] C. Röder, T. Kupreichyk, L. Gremer, L. U. Schäfer, K. R. Pothula, R. B. G. Ravelli, D. Willbold, W. Hoyer, and G. F. Schröder, "Cryo-EM structure of islet amyloid polypeptide fibrils reveals similarities with amyloid- β fibrils," *Nat. Struct. Mol. Biol.*, vol. 27, pp. 660–667, July 2020.

- [226] M. Schweighauser, Y. Shi, A. Tarutani, F. Kametani, A. G. Murzin, B. Ghetti, T. Matsubara, T. Tomita, T. Ando, K. Hasegawa, S. Murayama, M. Yoshida, M. Hasegawa, S. H. W. Scheres, and M. Goedert, “Structures of α -synuclein filaments from multiple system atrophy,” *Nature*, vol. 585, pp. 464–469, Sept. 2020.
- [227] Y. Li, C. Zhao, F. Luo, Z. Liu, X. Gui, Z. Luo, X. Zhang, D. Li, C. Liu, and X. Li, “Amyloid fibril structure of α -synuclein determined by cryo-electron microscopy,” *Cell Res.*, vol. 28, pp. 897–903, Sept. 2018.
- [228] Y. Sun, S. Hou, K. Zhao, H. Long, Z. Liu, J. Gao, Y. Zhang, X.-D. Su, D. Li, and C. Liu, “Cryo-EM structure of full-length α -synuclein amyloid fibril with parkinson’s disease familial A53T mutation,” *Cell Res.*, vol. 30, pp. 360–362, Apr. 2020.
- [229] E. Chatani, K. Yuzu, Y. Ohhashi, and Y. Goto, “Current understanding of the structure, stability and dynamic properties of amyloid fibrils,” *Int. J. Mol. Sci.*, vol. 22, Apr. 2021.
- [230] A. Espargaró, M. A. Busquets, J. Estelrich, and R. Sabate, “Key points concerning amyloid infectivity and Prion-Like neuronal invasion,” *Front. Mol. Neurosci.*, vol. 9, p. 29, Apr. 2016.
- [231] P. Chien, J. S. Weissman, and A. H. DePace, “Emerging principles of conformation-based prion inheritance,” *Annu. Rev. Biochem.*, vol. 73, pp. 617–656, 2004.
- [232] D. Vilette, J. Courte, J. M. Peyrin, L. Coudert, L. Schaeffer, O. Andréoletti, and P. Leblanc, “Cellular mechanisms responsible for cell-to-cell spreading of prions,” *Cell. Mol. Life Sci.*, vol. 75, pp. 2557–2574, July 2018.
- [233] C. Robertson, S. A. Booth, D. R. Beniac, M. B. Coulthart, T. F. Booth, and A. McNicol, “Cellular prion protein is released on exosomes from activated platelets,” *Blood*, vol. 107, pp. 3907–3911, May 2006.
- [234] C.-Y. King and R. Diaz-Avalos, “Protein-only transmission of three yeast prion strains,” *Nature*, vol. 428, pp. 319–323, Mar. 2004.
- [235] C. Weissmann, M. Enari, P.-C. Klöhn, D. Rossi, and E. Flechsig, “Transmission of prions,” *Proc. Natl. Acad. Sci. U. S. A.*, vol. 99 Suppl 4, pp. 16378–16383, Dec. 2002.
- [236] M. Prinz, F. Montrasio, M. A. Klein, P. Schwarz, J. Priller, B. Odermatt, K. Pfeffer, and A. Aguzzi, “Lymph nodal prion replication and neuroinvasion in mice devoid of follicular dendritic cells,” *Proc. Natl. Acad. Sci. U. S. A.*, vol. 99, pp. 919–924, Jan. 2002.
- [237] Z. Jaunmuktane, S. Mead, M. Ellis, J. D. F. Wadsworth, A. J. Nicoll, J. Kenny, F. Launchbury, J. Linehan, A. Richard-Loendt, A. S. Walker, P. Rudge, J. Collinge, and S. Brandner, “Evidence for human transmission of amyloid- β pathology and cerebral amyloid angiopathy,” *Nature*, vol. 525, pp. 247–250, Sept. 2015.
- [238] F. Clavaguera, H. Akatsu, G. Fraser, R. A. Crowther, S. Frank, J. Hench, A. Probst, D. T. Winkler, J. Reichwald, M. Staufenbiel, B. Ghetti, M. Goedert, and M. Tolnay, “Brain homogenates from human tauopathies induce tau inclusions in mouse brain,” *Proc. Natl. Acad. Sci. U. S. A.*, vol. 110, pp. 9535–9540, June 2013.

- [239] S. Nath, L. Agholme, F. R. Kurudenkandy, B. Granseth, J. Marcusson, and M. Hallbeck, "Spreading of neurodegenerative pathology via neuron-to-neuron transmission of β -amyloid," *J. Neurosci.*, vol. 32, pp. 8767–8777, June 2012.
- [240] M. Chen and D. E. Mor, "Gut-to-Brain α -Synuclein transmission in parkinson's disease: Evidence for prion-like mechanisms," *Int. J. Mol. Sci.*, vol. 24, Apr. 2023.
- [241] P. Desplats, H.-J. Lee, E.-J. Bae, C. Patrick, E. Rockenstein, L. Crews, B. Spencer, E. Masliah, and S.-J. Lee, "Inclusion formation and neuronal cell death through neuron-to-neuron transmission of α -synuclein," *Proceedings of the National Academy of Sciences*, vol. 106, no. 31, pp. 13010–13015, 2009.
- [242] E. Schaeffer, A. Kluge, M. Böttner, F. Zunke, F. Cossais, D. Berg, and P. Arnold, "Alpha synuclein connects the Gut-Brain axis in parkinson's disease patients - a view on clinical aspects, cellular pathology and analytical methodology," *Front Cell Dev Biol*, vol. 8, p. 573696, Sept. 2020.
- [243] Q. Lei, T. Wu, J. Wu, X. Hu, Y. Guan, Y. Wang, J. Yan, and G. Shi, "Roles of α -synuclein in gastrointestinal microbiome dysbiosis-related parkinson's disease progression (review)," *Mol. Med. Rep.*, vol. 24, Oct. 2021.
- [244] S. Paillusson, T. Clairembault, M. Biraud, M. Neunlist, and P. Derkinderen, "Activity-dependent secretion of alpha-synuclein by enteric neurons," *J. Neurochem.*, vol. 125, pp. 512–517, May 2013.
- [245] G. Beck, Y. Hori, Y. Hayashi, E. Morii, T. Takehara, and H. Mochizuki, "Detection of phosphorylated Alpha-Synuclein in the muscularis propria of the gastrointestinal tract is a sensitive predictor for parkinson's disease," *Parkinson's Disease*, vol. 2020, Sept. 2020.
- [246] C. Challis, A. Hori, T. R. Sampson, B. B. Yoo, R. C. Challis, A. M. Hamilton, S. K. Mazmanian, L. A. Volpicelli-Daley, and V. Gradinaru, "Gut-seeded α -synuclein fibrils promote gut dysfunction and brain pathology specifically in aged mice," *Nat. Neurosci.*, vol. 23, pp. 327–336, Mar. 2020.
- [247] Y. Cheng, Q. Tong, Y. Yuan, X. Song, W. Jiang, Y. Wang, W. Li, Y. Li, and K. Zhang, " α -Synuclein induces prodromal symptoms of parkinson's disease via activating TLR2/MyD88/NF- κ B pathway in schwann cells of vagus nerve in a rat model," *J. Neuroinflammation*, vol. 20, p. 36, Feb. 2023.
- [248] D. Jeremic, L. Jiménez-Díaz, and J. D. Navarro-López, "Past, present and future of therapeutic strategies against amyloid- β peptides in alzheimer's disease: a systematic review," *Ageing Res. Rev.*, vol. 72, p. 101496, Dec. 2021.
- [249] S. Cerri, L. Mus, and F. Blandini, "Parkinson's disease in women and men: What's the difference?," *J. Parkinsons. Dis.*, vol. 9, no. 3, pp. 501–515, 2019.
- [250] R. M. Meade, D. P. Fairlie, and J. M. Mason, "Alpha-synuclein structure and parkinson's disease – lessons and emerging principles," *Mol. Neurodegener.*, vol. 14, p. 29, July 2019.
- [251] J. Parkinson, "An essay on the shaking palsy," *J. Neuropsychiatry Clin. Neurosci.*, vol. 14, pp. 223–236, May 2002.

- [252] B. Holdorff, "Friedrich heinrich lewy (1885–1950) and his work," *J. Hist. Neurosci.*, vol. 11, pp. 19–28, Mar. 2002.
- [253] M. G. Spillantini, M. L. Schmidt, V. M. Lee, J. Q. Trojanowski, R. Jakes, and M. Goedert, "Alpha-synuclein in lewy bodies," *Nature*, vol. 388, pp. 839–840, Aug. 1997.
- [254] M. H. Polymeropoulos, C. Lavedan, E. Leroy, S. E. Ide, A. Dehejia, A. Dutra, B. Pike, H. Root, J. Rubenstein, R. Boyer, E. S. Stenroos, S. Chandrasekharappa, A. Athanassiadou, T. Papapetropoulos, W. G. Johnson, A. M. Lazzarini, R. C. Duvoisin, G. Di Iorio, L. I. Golbe, and R. L. Nussbaum, "Mutation in the alpha-synuclein gene identified in families with parkinson's disease," *Science*, vol. 276, pp. 2045–2047, June 1997.
- [255] L. I. Golbe, G. Di Iorio, V. Bonavita, D. C. Miller, and R. C. Duvoisin, "A large kindred with autosomal dominant parkinson's disease," *Ann. Neurol.*, vol. 27, pp. 276–282, Mar. 1990.
- [256] M. H. Polymeropoulos, J. J. Higgins, L. I. Golbe, W. G. Johnson, S. E. Ide, G. Di Iorio, G. Sanges, E. S. Stenroos, L. T. Pho, A. A. Schaffer, A. M. Lazzarini, R. L. Nussbaum, and R. C. Duvoisin, "Mapping of a gene for parkinson's disease to chromosome 4q21-q23," *Science*, vol. 274, pp. 1197–1199, Nov. 1996.
- [257] D. E. Mor, S. E. Ugras, M. J. Daniels, and H. Ischiropoulos, "Dynamic structural flexibility of α -synuclein," *Neurobiol. Dis.*, vol. 88, pp. 66–74, Apr. 2016.
- [258] U. Dettmer, A. J. Newman, V. E. von Saucken, T. Bartels, and D. Selkoe, "KTKEGV repeat motifs are key mediators of normal α -synuclein tetramerization: Their mutation causes excess monomers and neurotoxicity," *Proc. Natl. Acad. Sci. U. S. A.*, vol. 112, pp. 9596–9601, Aug. 2015.
- [259] K. Vamvaca, M. J. Volles, and P. T. Lansbury, Jr, "The first n-terminal amino acids of alpha-synuclein are essential for alpha-helical structure formation in vitro and membrane binding in yeast," *J. Mol. Biol.*, vol. 389, pp. 413–424, June 2009.
- [260] T. Bartels, L. S. Ahlstrom, A. Leftin, F. Kamp, C. Haass, M. F. Brown, and K. Beyer, "The n-terminus of the intrinsically disordered protein α -synuclein triggers membrane binding and helix folding," *Biophys. J.*, vol. 99, pp. 2116–2124, Oct. 2010.
- [261] T. S. Ulmer, A. Bax, N. B. Cole, and R. L. Nussbaum, "Structure and dynamics of micelle-bound human α -Synuclein*," *J. Biol. Chem.*, vol. 280, pp. 9595–9603, Mar. 2005.
- [262] E. R. Georgieva, T. F. Ramlall, P. P. Borbat, J. H. Freed, and D. Eliezer, "Membrane-Bound α -Synuclein forms an extended helix: Long-Distance pulsed ESR measurements using vesicles, bicelles, and rodlike micelles," *J. Am. Chem. Soc.*, vol. 130, pp. 12856–12857, Oct. 2008.
- [263] H. M. Sanders, M. M. Kostelic, C. K. Zak, and M. T. Marty, "Lipids and EGCG affect α -Synuclein association and disruption of nanodiscs," *Biochemistry*, vol. 61, pp. 1014–1021, June 2022.
- [264] P. J. Barrett and J. Timothy Greenamyre, "Post-translational modification of α -synuclein in parkinson's disease," *Brain Res.*, vol. 1628, pp. 247–253, Dec. 2015.

- [265] J. Zhang, X. Li, and J.-D. Li, “The roles of post-translational modifications on α -Synuclein in the pathogenesis of parkinson’s diseases,” *Front. Neurosci.*, vol. 13, p. 381, Apr. 2019.
- [266] N. d. O. Manzanza, L. Sedlackova, and R. N. Kalaria, “Alpha-Synuclein post-translational modifications: Implications for pathogenesis of lewy body disorders,” *Front. Aging Neurosci.*, vol. 13, p. 690293, June 2021.
- [267] A. S. Maltsev, J. Ying, and A. Bax, “Impact of N-Terminal acetylation of α -Synuclein on its random coil and lipid binding properties,” *Biochemistry*, vol. 51, pp. 5004–5013, June 2012.
- [268] A. Iyer, S. J. Roeters, N. Schilderink, B. Hommersom, R. M. A. Heeren, S. Woutersen, M. M. A. E. Claessens, and V. Subramaniam, “The impact of n-terminal acetylation of α -Synuclein on phospholipid membrane binding and fibril structure,” *J. Biol. Chem.*, vol. 291, pp. 21110–21122, Sept. 2016.
- [269] M. Runfola, A. De Simone, M. Vendruscolo, C. M. Dobson, and G. Fusco, “The n-terminal acetylation of α -Synuclein changes the affinity for lipid membranes but not the structural properties of the bound state,” *Sci. Rep.*, vol. 10, p. 204, Jan. 2020.
- [270] R. Bell and M. Vendruscolo, “Modulation of the interactions between α -Synuclein and lipid membranes by post-translational modifications,” *Front. Neurol.*, vol. 12, p. 661117, July 2021.
- [271] A. Iyer, A. Sidhu, and V. Subramaniam, “How important is the n-terminal acetylation of alpha-synuclein for its function and aggregation into amyloids?,” *Front. Neurosci.*, vol. 16, p. 1003997, Nov. 2022.
- [272] K. Daida, S. Shimonaka, K. Shiba-Fukushima, J. Ogata, H. Yoshino, A. Okuzumi, T. Hatano, Y. Motoi, T. Hirunagi, M. Katsuno, H. Shindou, M. Funayama, K. Nishioka, N. Hattori, and Y. Imai, “ α -Synuclein V15A variant in familial parkinson’s disease exhibits a weaker Lipid-Binding property,” *Mov. Disord.*, vol. 37, pp. 2075–2085, Oct. 2022.
- [273] M. Robotta, J. Cattani, J. C. Martins, V. Subramaniam, and M. Drescher, “Alpha-Synuclein disease mutations are structurally defective and locally affect membrane binding,” *J. Am. Chem. Soc.*, vol. 139, pp. 4254–4257, Mar. 2017.
- [274] J. J. Zarranz, J. Alegre, J. C. Gómez-Esteban, E. Lezcano, R. Ros, I. Ampuero, L. Vidal, J. Hoenicka, O. Rodriguez, B. Atarés, V. Llorens, E. Gomez Tortosa, T. del Ser, D. G. Muñoz, and J. G. de Yébenes, “The new mutation, E46K, of alpha-synuclein causes parkinson and lewy body dementia,” *Ann. Neurol.*, vol. 55, pp. 164–173, Feb. 2004.
- [275] D. Ghosh, M. Mondal, G. M. Mohite, P. K. Singh, P. Ranjan, A. Anoop, S. Ghosh, N. N. Jha, A. Kumar, and S. K. Maji, “The parkinson’s disease-associated H50Q mutation accelerates α -Synuclein aggregation in vitro,” *Biochemistry*, vol. 52, pp. 6925–6927, Oct. 2013.
- [276] N. J. Rutherford, B. D. Moore, T. E. Golde, and B. I. Giasson, “Divergent effects of the H50Q and G51D SNCA mutations on the aggregation of α -synuclein,” *J. Neurochem.*, vol. 131, pp. 859–867, Dec. 2014.

- [277] M. Bisaglia, A. Trolino, M. Bellanda, E. Bergantino, L. Bubacco, and S. Mammi, "Structure and topology of the non-amyloid-beta component fragment of human alpha-synuclein bound to micelles: implications for the aggregation process," *Protein Sci.*, vol. 15, pp. 1408–1416, June 2006.
- [278] H.-T. Li, H.-N. Du, L. Tang, J. Hu, and H.-Y. Hu, "Structural transformation and aggregation of human alpha-synuclein in trifluoroethanol: non-amyloid component sequence is essential and beta-sheet formation is prerequisite to aggregation," *Biopolymers*, vol. 64, pp. 221–226, Aug. 2002.
- [279] J. Gallardo, C. Escalona-Noguero, and B. Sot, "Role of α -Synuclein regions in nucleation and elongation of amyloid fiber assembly," *ACS Chem. Neurosci.*, vol. 11, pp. 872–879, Mar. 2020.
- [280] B. A. Hijaz and L. A. Volpicelli-Daley, "Initiation and propagation of α -synuclein aggregation in the nervous system," *Mol. Neurodegener.*, vol. 15, p. 19, Mar. 2020.
- [281] T. Srivastava, R. Raj, A. Dubey, D. Kumar, R. K. Chaturvedi, S. K. Sharma, and S. Priya, "Fast kinetics of environmentally induced α -synuclein aggregation mediated by structural alteration in NAC region and result in structure dependent cytotoxicity," *Sci. Rep.*, vol. 10, p. 18412, Oct. 2020.
- [282] V. N. Uversky, J. Li, and A. L. Fink, "Metal-triggered structural transformations, aggregation, and fibrillation of human α -Synuclein: A POSSIBLE MOLECULAR LINK BETWEEN PARKINSON'S DISEASE AND HEAVY METAL EXPOSURE," *J. Biol. Chem.*, vol. 276, pp. 44284–44296, Nov. 2001.
- [283] E. Illes-Toth, C. F. Dalton, and D. P. Smith, "Binding of dopamine to Alpha-Synuclein is mediated by specific conformational states," *J. Am. Soc. Mass Spectrom.*, vol. 24, pp. 1346–1354, Sept. 2013.
- [284] Y. Wang, M. Shi, K. A. Chung, C. P. Zabetian, J. B. Leverenz, D. Berg, K. Srujijes, J. Q. Trojanowski, V. M.-Y. Lee, A. D. Siderowf, H. Hurtig, I. Litvan, M. C. Schiess, E. R. Peskind, M. Masuda, M. Hasegawa, X. Lin, C. Pan, D. Galasko, D. S. Goldstein, P. H. Jensen, H. Yang, K. C. Cain, and J. Zhang, "Phosphorylated α -synuclein in parkinson's disease," *Sci. Transl. Med.*, vol. 4, p. 121ra20, Feb. 2012.
- [285] S. Arawaka, H. Sato, A. Sasaki, S. Koyama, and T. Kato, "Mechanisms underlying extensive ser129-phosphorylation in α -synuclein aggregates," *Acta Neuropathol Commun*, vol. 5, p. 48, June 2017.
- [286] A. Canerina-Amaro, D. Pereda, M. Diaz, D. Rodriguez-Barreto, V. Casañas-Sánchez, M. Heffer, P. Garcia-Esparcia, I. Ferrer, R. Puertas-Avendaño, and R. Marin, "Differential aggregation and phosphorylation of alpha synuclein in membrane compartments associated with parkinson disease," *Front. Neurosci.*, vol. 13, p. 382, Apr. 2019.
- [287] M. Okochi, J. Walter, A. Koyama, S. Nakajo, M. Baba, T. Iwatsubo, L. Meijer, P. J. Kahle, and C. Haass, "Constitutive phosphorylation of the parkinson's disease associated α -Synuclein*," *J. Biol. Chem.*, vol. 275, pp. 390–397, Jan. 2000.
- [288] I. Kawahata, D. I. Finkelstein, and K. Fukunaga, "Pathogenic impact of α -Synuclein phosphorylation and its kinases in α -Synucleinopathies," *Int. J. Mol. Sci.*, vol. 23, June 2022.

- [289] C. Kontaxi and R. H. Edwards, "Synuclein phosphorylation: pathogenic or physiologic?," *NPJ Parkinsons Dis*, vol. 9, p. 47, Mar. 2023.
- [290] A. E. Dorn, E. de Bruyn, G. Rossetti, C. Fernandez, T. F. Outeiro, J. B. Schulz, and P. Carloni, "Impact of phosphorylation on alpha-synuclein structural determinants." Mar. 2023.
- [291] H. Fujiwara, M. Hasegawa, N. Dohmae, A. Kawashima, E. Masliah, M. S. Goldberg, J. Shen, K. Takio, and T. Iwatsubo, "alpha-synuclein is phosphorylated in synucleinopathy lesions," *Nat. Cell Biol.*, vol. 4, pp. 160–164, Feb. 2002.
- [292] J. P. Anderson, D. E. Walker, J. M. Goldstein, R. de Laat, K. Banducci, R. J. Caccavello, R. Barbour, J. Huang, K. Kling, M. Lee, L. Diep, P. S. Keim, X. Shen, T. Chataway, M. G. Schlossmacher, P. Seubert, D. Schenk, S. Sinha, W. P. Gai, and T. J. Chilcote, "Phosphorylation of ser-129 is the dominant pathological modification of α -Synuclein in familial and sporadic lewy body disease*," *J. Biol. Chem.*, vol. 281, pp. 29739–29752, Oct. 2006.
- [293] K. E. Paleologou, A. Oueslati, G. Shakked, C. C. Rospigliosi, H.-Y. Kim, G. R. Lamberto, C. O. Fernandez, A. Schmid, F. Chegini, W. P. Gai, D. Chiappe, M. Morniatte, B. L. Schneider, P. Aebischer, D. Eliezer, M. Zweckstetter, E. Masliah, and H. A. Lashuel, "Phosphorylation at S87 is enhanced in synucleinopathies, inhibits alpha-synuclein oligomerization, and influences synuclein-membrane interactions," *J. Neurosci.*, vol. 30, pp. 3184–3198, Mar. 2010.
- [294] K. Wakabayashi, K. Tanji, F. Mori, and H. Takahashi, "The lewy body in parkinson's disease: molecules implicated in the formation and degradation of alpha-synuclein aggregates," *Neuropathology*, vol. 27, pp. 494–506, Oct. 2007.
- [295] A.-L. Mahul-Mellier, J. Bartscher, N. Maharjan, L. Weerens, M. Croisier, F. Kuttler, M. Leleu, G. W. Knott, and H. A. Lashuel, "The process of lewy body formation, rather than simply α -synuclein fibrillization, is one of the major drivers of neurodegeneration," *Proc. Natl. Acad. Sci. U. S. A.*, vol. 117, pp. 4971–4982, Mar. 2020.
- [296] M. Baba, S. Nakajo, P. H. Tu, T. Tomita, K. Nakaya, V. M. Lee, J. Q. Trojanowski, and T. Iwatsubo, "Aggregation of alpha-synuclein in lewy bodies of sporadic parkinson's disease and dementia with lewy bodies," *Am. J. Pathol.*, vol. 152, pp. 879–884, Apr. 1998.
- [297] R. A. Crowther, R. Jakes, M. G. Spillantini, and M. Goedert, "Synthetic filaments assembled from c-terminally truncated alpha-synuclein," *FEBS Lett.*, vol. 436, pp. 309–312, Oct. 1998.
- [298] W. Li, N. West, E. Colla, O. Pletnikova, J. C. Troncoso, L. Marsh, T. M. Dawson, P. Jäkälä, T. Hartmann, D. L. Price, and M. K. Lee, "Aggregation promoting c-terminal truncation of α -synuclein is a normal cellular process and is enhanced by the familial parkinson's disease-linked mutations," *Proceedings of the National Academy of Sciences*, vol. 102, pp. 2162–2167, Feb. 2005.
- [299] C.-W. Liu, B. I. Giasson, K. A. Lewis, V. M. Lee, G. N. Demartino, and P. J. Thomas, "A precipitating role for truncated alpha-synuclein and the proteasome in alpha-synuclein aggregation: implications for pathogenesis of parkinson disease," *J. Biol. Chem.*, vol. 280, pp. 22670–22678, June 2005.

- [300] Z. A. Sorrentino and B. I. Giasson, “The emerging role of α -synuclein truncation in aggregation and disease,” *J. Biol. Chem.*, vol. 295, pp. 10224–10244, July 2020.
- [301] K. M. Danzer, L. R. Kranich, W. P. Ruf, O. Cagsal-Getkin, A. R. Winslow, L. Zhu, C. R. Vanderburg, and P. J. McLean, “Exosomal cell-to-cell transmission of alpha synuclein oligomers,” *Mol. Neurodegener.*, vol. 7, p. 42, Aug. 2012.
- [302] L. Stefanis, “ α -Synuclein in parkinson’s disease,” *Cold Spring Harb. Perspect. Med.*, vol. 2, p. a009399, Feb. 2012.
- [303] J. T. Bendor, T. P. Logan, and R. H. Edwards, “The function of α -synuclein,” *Neuron*, vol. 79, pp. 1044–1066, Sept. 2013.
- [304] J. Burré, “The synaptic function of α -Synuclein,” *J. Parkinsons. Dis.*, vol. 5, no. 4, pp. 699–713, 2015.
- [305] L. D. Bernal-Conde, R. Ramos-Acevedo, M. A. Reyes-Hernández, A. J. Balbuena-Olvera, I. D. Morales-Moreno, R. Argüero-Sánchez, B. Schüle, and M. Guerra-Crespo, “Alpha-Synuclein physiology and pathology: A perspective on cellular structures and organelles,” *Front. Neurosci.*, vol. 13, p. 1399, 2019.
- [306] P. Calabresi, G. Di Lazzaro, G. Marino, F. Campanelli, and V. Ghiglieri, “Advances in understanding the function of alpha-synuclein: implications for parkinson’s disease,” *Brain*, vol. 146, pp. 3587–3597, Sept. 2023.
- [307] J. Varkey, J. M. Isas, N. Mizuno, M. B. Jensen, V. K. Bhatia, C. C. Jao, J. Petrlava, J. C. Voss, D. G. Stamou, A. C. Steven, and R. Langen, “Membrane curvature induction and tubulation are common features of synucleins and apolipoproteins,” *J. Biol. Chem.*, vol. 285, pp. 32486–32493, Oct. 2010.
- [308] E. R. Middleton and E. Rhoades, “Effects of curvature and composition on α -synuclein binding to lipid vesicles,” *Biophys. J.*, vol. 99, pp. 2279–2288, Oct. 2010.
- [309] H. Cui, E. Lyman, and G. A. Voth, “Mechanism of membrane curvature sensing by amphipathic helix containing proteins,” *Biophys. J.*, vol. 100, pp. 1271–1279, Mar. 2011.
- [310] M. Giménez-Andrés, A. Čopič, and B. Antonny, “The many faces of amphipathic helices,” *Biomolecules*, vol. 8, July 2018.
- [311] M. A. Zhukovsky, A. Filograna, A. Luini, D. Corda, and C. Valente, “Protein amphipathic helix insertion: A mechanism to induce membrane fission,” *Front Cell Dev Biol*, vol. 7, p. 291, Dec. 2019.
- [312] C. W. Sauvola and J. T. Littleton, “SNARE regulatory proteins in synaptic vesicle fusion and recycling,” *Front. Mol. Neurosci.*, vol. 14, p. 733138, Aug. 2021.
- [313] J. Burré, M. Sharma, T. Tsetsenis, V. Buchman, M. R. Etherton, and T. C. Südhof, “Alpha-synuclein promotes SNARE-complex assembly in vivo and in vitro,” *Science*, vol. 329, pp. 1663–1667, Sept. 2010.
- [314] F. Darios, V. Ruipérez, I. López, J. Villanueva, L. M. Gutierrez, and B. Davletov, “Alpha-synuclein sequesters arachidonic acid to modulate SNARE-mediated exocytosis,” *EMBO Rep.*, vol. 11, pp. 528–533, July 2010.

- [315] K. J. Vargas, S. Makani, T. Davis, C. H. Westphal, P. E. Castillo, and S. S. Chandra, "Synucleins regulate the kinetics of synaptic vesicle endocytosis," *J. Neurosci.*, vol. 34, pp. 9364–9376, July 2014.
- [316] L. Barba, F. Paolini Paoletti, G. Bellomo, L. Gaetani, S. Halbgebauer, P. Oeckl, M. Otto, and L. Parnetti, "Alpha and beta synucleins: From pathophysiology to clinical application as biomarkers," *Mov. Disord.*, vol. 37, pp. 669–683, Apr. 2022.
- [317] A. A. Alabi and R. W. Tsien, "Perspectives on kiss-and-run: role in exocytosis, endocytosis, and neurotransmission," *Annu. Rev. Physiol.*, vol. 75, pp. 393–422, 2013.
- [318] B. Granseth, B. Odermatt, S. J. Royle, and L. Lagnado, "Clathrin-mediated endocytosis is the dominant mechanism of vesicle retrieval at hippocampal synapses," *Neuron*, vol. 51, pp. 773–786, Sept. 2006.
- [319] K. J. Vargas, P. L. Colosi, E. Girardi, J.-M. Park, L. E. Harmon, and S. S. Chandra, " α -Synuclein colocalizes with AP180 and affects the size of clathrin lattices," *J. Biol. Chem.*, vol. 299, p. 105091, July 2023.
- [320] G. Fusco, A. De Simone, T. Gopinath, V. Vostrikov, M. Vendruscolo, C. M. Dobson, and G. Veglia, "Direct observation of the three regions in α -synuclein that determine its membrane-bound behaviour," *Nat. Commun.*, vol. 5, p. 3827, May 2014.
- [321] J. Lautenschläger, A. D. Stephens, G. Fusco, F. Ströhl, N. Curry, M. Zacharopoulou, C. H. Michel, R. Laine, N. Nespovityaya, M. Fantham, D. Pinotsi, W. Zago, P. Fraser, A. Tandon, P. St George-Hyslop, E. Rees, J. J. Phillips, A. De Simone, C. F. Kaminski, and G. S. K. Schierle, "C-terminal calcium binding of α -synuclein modulates synaptic vesicle interaction," *Nat. Commun.*, vol. 9, p. 712, Feb. 2018.
- [322] S. W. Chen, S. Drakulic, E. Deas, M. Ouberai, F. A. Aprile, R. Arranz, S. Ness, C. Roodveldt, T. Williams, E. J. De-Genst, D. Klenerman, N. W. Wood, T. P. J. Knowles, C. Alfonso, G. Rivas, A. Y. Abramov, J. M. Valpuesta, C. M. Dobson, and N. Cremades, "Structural characterization of toxic oligomers that are kinetically trapped during α -synuclein fibril formation," *Proc. Natl. Acad. Sci. U. S. A.*, vol. 112, pp. E1994–2003, Apr. 2015.
- [323] P. Rizek, N. Kumar, and M. S. Jog, "An update on the diagnosis and treatment of parkinson disease," *CMAJ*, vol. 188, pp. 1157–1165, Nov. 2016.
- [324] Z. Jia, H. Zhu, B. R. Misra, Y. Li, and H. P. Misra, "Dopamine as a potent inducer of cellular glutathione and NAD(P)H:quinone oxidoreductase 1 in PC12 neuronal cells: a potential adaptive mechanism for dopaminergic neuroprotection," *Neurochem. Res.*, vol. 33, pp. 2197–2205, Nov. 2008.
- [325] J. Dorszewska, M. Prendecki, M. Lianeri, and W. Kozubski, "Molecular effects of l-dopa therapy in parkinson's disease," *Curr. Genomics*, vol. 15, pp. 11–17, Feb. 2014.
- [326] T. Nagatsua and M. Sawadab, "L-dopa therapy for parkinson's disease: past, present, and future," *Parkinsonism Relat. Disord.*, vol. 15 Suppl 1, pp. S3–8, Jan. 2009.
- [327] H. A. Shill and M. Stacy, "Update on ropinirole in the treatment of parkinson's disease," *Neuropsychiatr. Dis. Treat.*, vol. 5, pp. 33–36, Apr. 2009.

- [328] D. Robakis and S. Fahn, "Defining the role of the monoamine Oxidase-B inhibitors for parkinson's disease," *CNS Drugs*, vol. 29, pp. 433–441, June 2015.
- [329] P. A. Chromiec, Z. K. Urbaś, M. Jacko, and J. J. Kaczor, "The proper diet and regular physical activity slow down the development of parkinson disease," *Aging Dis.*, vol. 12, pp. 1605–1623, Oct. 2021.
- [330] A. Loquet, N. El Mammeri, J. Stanek, M. Berbon, B. Bardiaux, G. Pintacuda, and B. Habenstein, "3D structure determination of amyloid fibrils using solid-state NMR spectroscopy," *Methods*, vol. 138–139, pp. 26–38, Apr. 2018.
- [331] A. Savastano, G. Jaipuria, L. Andreas, E. Mandelkow, and M. Zweckstetter, "Solid-state NMR investigation of the involvement of the P2 region in tau amyloid fibrils," *Sci. Rep.*, vol. 10, p. 21210, Dec. 2020.
- [332] A. T. Petkova, Y. Ishii, J. J. Balbach, O. N. Antzutkin, R. D. Leapman, F. Delaglio, and R. Tycko, "A structural model for alzheimer's β -amyloid fibrils based on experimental constraints from solid state NMR," *Proceedings of the National Academy of Sciences*, vol. 99, no. 26, pp. 16742–16747, 2002.
- [333] A. L. Grønnemose, E. C. Østerlund, D. E. Otzen, and T. J. D. Jørgensen, "EGCG has dual and opposing effects on the n-terminal region of self-associating α -synuclein oligomers," *J. Mol. Biol.*, vol. 434, p. 167855, Dec. 2022.
- [334] J. Bieschke, J. Russ, R. P. Friedrich, D. E. Ehrnhoefer, H. Wobst, K. Neugebauer, and E. E. Wanker, "EGCG remodels mature α -synuclein and amyloid- β fibrils and reduces cellular toxicity," *Proceedings of the National Academy of Sciences*, vol. 107, no. 17, pp. 7710–7715, 2010.
- [335] H. A. Lashuel, B. M. Petre, J. Wall, M. Simon, R. J. Nowak, T. Walz, and P. T. Lansbury, Jr, "Alpha-synuclein, especially the parkinson's disease-associated mutants, forms pore-like annular and tubular protofibrils," *J. Mol. Biol.*, vol. 322, pp. 1089–1102, Oct. 2002.
- [336] S.-Y. Ow and D. E. Dunstan, "A brief overview of amyloids and alzheimer's disease," *Protein Sci.*, vol. 23, pp. 1315–1331, Oct. 2014.
- [337] K. Ono and T. Watanabe-Nakayama, "Aggregation and structure of amyloid β -protein," *Neurochem. Int.*, vol. 151, p. 105208, Dec. 2021.
- [338] K. S. Li, D. L. Rempel, and M. L. Gross, "Conformational-Sensitive fast photochemical oxidation of proteins and mass spectrometry characterize amyloid beta 1–42 aggregation," *J. Am. Chem. Soc.*, vol. 138, pp. 12090–12098, Sept. 2016.
- [339] M. Landureau, V. Redeker, T. Bellande, S. Eyquem, and R. Melki, "The differential solvent exposure of n-terminal residues provides "fingerprints" of alpha-synuclein fibrillar polymorphs," *J. Biol. Chem.*, vol. 296, Jan. 2021.
- [340] W. F. Vranken, W. Boucher, T. J. Stevens, R. H. Fogh, A. Pajon, M. Llinas, E. L. Ulrich, J. L. Markley, J. Ionides, and E. D. Laue, "The CCPN data model for NMR spectroscopy: development of a software pipeline," *Proteins*, vol. 59, pp. 687–696, June 2005.

- [341] M. P. Williamson, "Using chemical shift perturbation to characterise ligand binding," *Prog. Nucl. Magn. Reson. Spectrosc.*, vol. 73, pp. 1–16, Aug. 2013.
- [342] K. R. Durbin, M. T. Robey, L. N. Voong, R. T. Fellers, C. A. Lutomski, T. J. El-Baba, C. V. Robinson, and N. L. Kelleher, "ProSight native: Defining protein complex composition from native Top-Down mass spectrometry data," *J. Proteome Res.*, vol. 22, pp. 2660–2668, Aug. 2023.
- [343] A. M. Lau, J. Claesen, K. Hansen, and A. Politis, "Deuterios 2.0: peptide-level significance testing of data from hydrogen deuterium exchange mass spectrometry," *Bioinformatics*, vol. 37, pp. 270–272, Apr. 2021.
- [344] W. S. Davidson, A. Jonas, D. F. Clayton, and J. M. George, "Stabilization of α -Synuclein secondary structure upon binding to synthetic membranes *," *J. Biol. Chem.*, vol. 273, no. 16, pp. 9443–9449, 1998.
- [345] J. Chen, S. Zaer, P. Drori, J. Zamel, K. Joron, N. Kalisman, E. Lerner, and N. V. Dokholyan, "The structural heterogeneity of α -synuclein is governed by several distinct subpopulations with interconversion times slower than milliseconds," *Structure*, vol. 29, pp. 1048–1064.e6, Sept. 2021.
- [346] R. Nelson, M. R. Sawaya, M. Balbirnie, A. Ø. Madsen, C. Riek, R. Grothe, and D. Eisenberg, "Structure of the cross- β spine of amyloid-like fibrils," *Nature*, vol. 435, pp. 773–778, June 2005.
- [347] M. R. Sawaya, S. Sambashivan, R. Nelson, M. I. Ivanova, S. A. Sievers, M. I. Apostol, M. J. Thompson, M. Balbirnie, J. J. W. Wiltzius, H. T. McFarlane, A. Ø. Madsen, C. Riek, and D. Eisenberg, "Atomic structures of amyloid cross- β spines reveal varied steric zippers," *Nature*, vol. 447, pp. 453–457, May 2007.
- [348] M. S. Celej, R. Sarroukh, E. Goormaghtigh, G. D. Fidelio, J.-M. Ruyschaert, and V. Raussens, "Toxic prefibrillar α -synuclein amyloid oligomers adopt a distinctive antiparallel β -sheet structure," *Biochem. J.*, vol. 443, no. 3, pp. 719–726, 2012.
- [349] E. E. Cawood, T. K. Karamanos, A. J. Wilson, and S. E. Radford, "Visualizing and trapping transient oligomers in amyloid assembly pathways," *Biophys. Chem.*, vol. 268, p. 106505, Jan. 2021.
- [350] C. P. A. Doherty, S. M. Ulamec, R. Maya-Martinez, S. C. Good, J. Makepeace, G. N. Khan, P. van Oosten-Hawle, S. E. Radford, and D. J. Brockwell, "A short motif in the n-terminal region of α -synuclein is critical for both aggregation and function," *Nat. Struct. Mol. Biol.*, vol. 27, pp. 249–259, Mar. 2020.
- [351] A. J. Trexler and E. Rhoades, "N-terminal acetylation is critical for forming α -helical oligomer of α -synuclein," *Protein Sci.*, vol. 21, pp. 601–605, May 2012.
- [352] A. Öhrfelt, H. Zetterberg, K. Andersson, R. Persson, D. Secic, G. Brinkmalm, A. Wallin, E. Mulugeta, P. T. Francis, E. Vanmechelen, D. Aarsland, C. Ballard, K. Blennow, and A. Westman-Brinkmalm, "Identification of novel α -Synuclein isoforms in human brain tissue by using an online NanoLC-ESI-FTICR-MS method," *Neurochem. Res.*, vol. 36, pp. 2029–2042, Nov. 2011.

- [353] S. Sadiq, Z. Ghazala, A. Chowdhury, and D. Büsselberg, “Metal toxicity at the synapse: Presynaptic, postsynaptic, and Long-Term effects,” *J. Toxicol.*, vol. 2012, p. 132671, Jan. 2012.
- [354] M. P. Mattson, “Calcium and neurodegeneration,” *Aging Cell*, vol. 6, pp. 337–350, June 2007.
- [355] A. E. Finefrock, A. I. Bush, and P. M. Doraiswamy, “Current status of metals as therapeutic targets in alzheimer’s disease,” *J. Am. Geriatr. Soc.*, vol. 51, pp. 1143–1148, Aug. 2003.
- [356] M. Bisaglia, I. Tessari, S. Mammi, and L. Bubacco, “Interaction between α -Synuclein and metal ions, still looking for a role in the pathogenesis of parkinson’s disease,” *Neuromolecular Med.*, vol. 11, pp. 239–251, Dec. 2009.
- [357] A. Carija, F. Pinheiro, J. Pujols, I. C. Brás, D. F. Lázaro, C. Santambrogio, R. Grandori, T. F. Outeiro, S. Navarro, and S. Ventura, “Biasing the native α -synuclein conformational ensemble towards compact states abolishes aggregation and neurotoxicity,” *Redox Biol*, vol. 22, p. 101135, Apr. 2019.
- [358] P. Wongkongkathep, J. Y. Han, T. S. Choi, S. Yin, H. I. Kim, and J. A. Loo, “Native Top-Down mass spectrometry and ion mobility MS for characterizing the cobalt and manganese metal binding of α -Synuclein protein,” *J. Am. Soc. Mass Spectrom.*, vol. 29, no. 9, pp. 1870–1880, 2018.
- [359] D. R. Brown, “Metal binding to alpha-synuclein peptides and its contribution to toxicity,” *Biochem. Biophys. Res. Commun.*, vol. 380, pp. 377–381, Mar. 2009.
- [360] H. LeVine, “Thioflavine T interaction with amyloid β -sheet structures,” *Amyloid*, vol. 2, pp. 1–6, Jan. 1995.
- [361] C. Xue, T. Y. Lin, D. Chang, and Z. Guo, “Thioflavin T as an amyloid dye: fibril quantification, optimal concentration and effect on aggregation,” *Royal Society Open Science*, vol. 4, no. 1, p. 160696.
- [362] R. Grandori, C. Santambrogio, S. Brocca, G. Invernizzi, and M. Lotti, “Electrospray-ionization mass spectrometry as a tool for fast screening of protein structural properties,” *Biotechnol. J.*, vol. 4, pp. 73–87, Jan. 2009.
- [363] C. Santambrogio, A. Natalello, S. Brocca, E. Ponzini, and R. Grandori, “Conformational characterization and classification of intrinsically disordered proteins by native mass spectrometry and Charge-State distribution analysis,” *Proteomics*, vol. 19, p. e1800060, Mar. 2019.
- [364] S. L. Bernstein, D. Liu, T. Wyttenbach, M. T. Bowers, J. C. Lee, H. B. Gray, and J. R. Winkler, “ α -Synuclein: Stable compact and extended monomeric structures and ph dependence of dimer formation,” *J. Am. Soc. Mass Spectrom.*, vol. 15, pp. 1435–1443, Oct. 2004.
- [365] C. Wang, C. Zhao, D. Li, Z. Tian, Y. Lai, J. Diao, and C. Liu, “Versatile structures of α -Synuclein,” *Front. Mol. Neurosci.*, vol. 9, June 2016.

- [366] A. D. Stephens, M. Zacharopoulou, and G. S. Kaminski Schierle, “The cellular environment affects monomeric α -Synuclein structure,” *Trends Biochem. Sci.*, vol. 44, pp. 453–466, May 2019.
- [367] A. S. Phillips, A. F. Gomes, J. M. D. Kalapothakis, J. E. Gillam, J. Gasparavicius, F. C. Gozzo, T. Kunath, C. MacPhee, and P. E. Barran, “Conformational dynamics of α -synuclein: insights from mass spectrometry,” *Analyst*, vol. 140, no. 9, pp. 3070–3081, 2015.
- [368] C. J. Krusemark, B. L. Frey, P. J. Belshaw, and L. M. Smith, “Modifying the charge state distribution of proteins in electrospray ionization mass spectrometry by chemical derivatization,” *J. Am. Soc. Mass Spectrom.*, vol. 20, pp. 1617–1625, Sept. 2009.
- [369] A. C. Susa, Z. Xia, H. Y. H. Tang, J. A. Tainer, and E. R. Williams, “Charging of proteins in native mass spectrometry,” *J. Am. Soc. Mass Spectrom.*, vol. 28, pp. 332–340, Feb. 2017.
- [370] Q. Duez, F. Chirot, R. Liénard, T. Josse, C. Choi, O. Coulembier, P. Dugourd, J. Cornil, P. Gerbaux, and J. De Winter, “Polymers for traveling wave ion mobility spectrometry calibration,” *J. Am. Soc. Mass Spectrom.*, vol. 28, pp. 2483–2491, Nov. 2017.
- [371] C. Laphorn, F. Pullen, and B. Z. Chowdhry, “Ion mobility spectrometry-mass spectrometry (IMS-MS) of small molecules: separating and assigning structures to ions,” *Mass Spectrom. Rev.*, vol. 32, no. 1, pp. 43–71, 2013.
- [372] B. Gardner, B. V. Dieriks, S. Cameron, L. H. S. Mendis, C. Turner, R. L. M. Faull, and M. A. Curtis, “Metal concentrations and distributions in the human olfactory bulb in parkinson’s disease,” *Sci. Rep.*, vol. 7, p. 10454, Sept. 2017.
- [373] L. Kang, G. M. Moriarty, L. A. Woods, A. E. Ashcroft, S. E. Radford, and J. Baum, “N-terminal acetylation of α -synuclein induces increased transient helical propensity and decreased aggregation rates in the intrinsically disordered monomer,” *Protein Sci.*, vol. 21, pp. 911–917, July 2012.
- [374] J. Everett, J. F. Collingwood, V. Tjendana-Tjhin, J. Brooks, F. Lermyte, G. Plascencia-Villa, I. Hands-Portman, J. Dobson, G. Perry, and N. D. Telling, “Nanoscale synchrotron x-ray speciation of iron and calcium compounds in amyloid plaque cores from alzheimer’s disease subjects,” *Nanoscale*, vol. 10, pp. 11782–11796, July 2018.
- [375] S. M. Dixit, D. A. Polasky, and B. T. Ruotolo, “Collision induced unfolding of isolated proteins in the gas phase: past, present, and future,” *Curr. Opin. Chem. Biol.*, vol. 42, pp. 93–100, Feb. 2018.
- [376] V. V. Gadkari, C. R. Ramírez, D. D. Vallejo, R. T. Kurulugama, J. C. Fjeldsted, and B. T. Ruotolo, “Enhanced collision induced unfolding and electron capture dissociation of native-like protein ions,” *Anal. Chem.*, vol. 92, pp. 15489–15496, Dec. 2020.

- [377] G. van Schaick, E. Domínguez-Vega, J. Castel, M. Wuhrer, O. Hernandez-Alba, and S. Cianféroni, "Online Collision-Induced unfolding of therapeutic monoclonal antibody Glyco-Variants through direct hyphenation of cation exchange chromatography with native ion Mobility-Mass spectrometry," *Anal. Chem.*, vol. 95, pp. 3932–3939, Feb. 2023.
- [378] N. B. Borotto, K. E. Osho, T. K. Richards, and K. A. Graham, "Collision-Induced unfolding of native-like protein ions within a trapped ion mobility spectrometry device," *J. Am. Soc. Mass Spectrom.*, vol. 33, pp. 83–89, Jan. 2022.
- [379] M. Ferreón Allan Chris, Y. Gambin, A. Lemke Edward, and A. Deniz Ashok, "Interplay of α -synuclein binding and conformational switching probed by single-molecule fluorescence," *Proceedings of the National Academy of Sciences*, vol. 106, pp. 5645–5650, Apr. 2009.
- [380] S. M. Ulamec, R. Maya-Martinez, E. J. Byrd, K. M. Dewison, Y. Xu, L. F. Willis, F. Sobott, G. R. Heath, P. van Oosten Hawle, V. L. Buchman, S. E. Radford, and D. J. Brockwell, "Single residue modulators of amyloid formation in the n-terminal p1-region of α -synuclein," *Nat. Commun.*, vol. 13, p. 4986, Aug. 2022.
- [381] L. M. Young, J. C. Saunders, R. A. Mahood, C. H. Revill, R. J. Foster, L.-H. Tu, D. P. Raleigh, S. E. Radford, and A. E. Ashcroft, "Screening and classifying small-molecule inhibitors of amyloid formation using ion mobility spectrometry–mass spectrometry," *Nat. Chem.*, vol. 7, pp. 73–81, Jan. 2015.
- [382] K. Levitan, D. Chereau, S. I. A. Cohen, T. P. J. Knowles, C. M. Dobson, A. L. Fink, J. P. Anderson, J. M. Goldstein, and G. L. Millhauser, "Conserved C-Terminal charge exerts a profound influence on the aggregation rate of α -Synuclein," *J. Mol. Biol.*, vol. 411, pp. 329–333, Aug. 2011.
- [383] A. Farzadfard, J. N. Pedersen, G. Meisl, A. K. Somavarapu, P. Alam, L. Goksøyr, M. A. Nielsen, A. F. Sander, T. P. J. Knowles, J. S. Pedersen, and D. E. Otzen, "The c-terminal tail of α -synuclein protects against aggregate replication but is critical for oligomerization," *Communications Biology*, vol. 5, p. 123, Feb. 2022.
- [384] C.-W. Liu, B. I. Giasson, K. A. Lewis, V. M. Lee, G. N. DeMartino, and P. J. Thomas, "A precipitating role for truncated α -Synuclein and the proteasome in α -Synuclein aggregation: IMPLICATIONS FOR PATHOGENESIS OF PARKINSON DISEASE*," *J. Biol. Chem.*, vol. 280, pp. 22670–22678, June 2005.
- [385] A. J. Mishizen-Eberz, E. H. Norris, B. I. Giasson, R. Hodara, H. Ischiropoulos, V. M. Y. Lee, J. Q. Trojanowski, and D. R. Lynch, "Cleavage of α -Synuclein by calpain: Potential role in degradation of fibrillized and nitrated species of α -Synuclein," *Biochemistry*, vol. 44, pp. 7818–7829, May 2005.
- [386] M. C. Bennett, J. F. Bishop, Y. Leng, P. B. Chock, T. N. Chase, and M. M. Mouradian, "Degradation of α -Synuclein by proteasome *," *J. Biol. Chem.*, vol. 274, no. 48, pp. 33855–33858, 1999.
- [387] K. K. K. Chung, V. L. Dawson, and T. M. Dawson, "The role of the ubiquitin-proteasomal pathway in parkinson's disease and other neurodegenerative disorders," *Trends Neurosci.*, vol. 24, pp. S7–S14, Nov. 2001.

- [388] H.-J. Lee, F. Khoshaghideh, S. Patel, and S.-J. Lee, "Clearance of α -Synuclein oligomeric intermediates via the lysosomal degradation pathway," *J. Neurosci.*, vol. 24, no. 8, pp. 1888–1896, 2004.
- [389] B. A. Bahr and J. Bendiske, "The neuropathogenic contributions of lysosomal dysfunction," *J. Neurochem.*, vol. 83, pp. 481–489, Nov. 2002.
- [390] S. J. Kim, J. Y. Sung, J. W. Um, N. Hattori, Y. Mizuno, K. Tanaka, S. R. Paik, J. Kim, and K. C. Chung, "Parkin cleaves intracellular α -Synuclein inclusions via the activation of calpain *," *J. Biol. Chem.*, vol. 278, no. 43, pp. 41890–41899, 2003.
- [391] A. J. Mishizen-Eberz, R. P. Guttman, B. I. Giasson, G. A. Day, Iii, R. Hodara, H. Ischiropoulos, V. M. Y. Lee, J. Q. Trojanowski, and D. R. Lynch, "Distinct cleavage patterns of normal and pathologic forms of α -synuclein by calpain I in vitro," *J. Neurochem.*, vol. 86, pp. 836–847, Aug. 2003.
- [392] W. Hoyer, D. Cherny, V. Subramaniam, and T. M. Jovin, "Impact of the acidic C-Terminal region comprising amino acids 109-140 on α -Synuclein aggregation in vitro," *Biochemistry*, vol. 43, pp. 16233–16242, Dec. 2004.
- [393] L. C. Serpell, J. Berriman, R. Jakes, M. Goedert, and R. A. Crowther, "Fiber diffraction of synthetic α -synuclein filaments shows amyloid-like cross- β conformation," *Proceedings of the National Academy of Sciences*, vol. 97, pp. 4897–4902, Apr. 2000.
- [394] M. C. Miotto, A. Binolfi, M. Zweckstetter, C. Griesinger, and C. O. Fernández, "Bioinorganic chemistry of synucleinopathies: deciphering the binding features of met motifs and his-50 in AS-Cu(I) interactions," *J. Inorg. Biochem.*, vol. 141, pp. 208–211, Dec. 2014.
- [395] S. J. Wood, J. Wypych, S. Steavenson, J.-C. Louis, M. Citron, and A. L. Biere, " α -Synuclein fibrillogenesis is nucleation-dependent: IMPLICATIONS FOR THE PATHOGENESIS OF PARKINSON'S DISEASE," *J. Biol. Chem.*, vol. 274, pp. 19509–19512, July 1999.
- [396] Y. A. Kyriukha, K. Afitska, A. S. Kurochka, S. Sachan, M. Galkin, D. A. Yushchenko, and V. V. Shvadchak, " α -Synuclein dimers as potent inhibitors of fibrillization," *J. Med. Chem.*, vol. 62, pp. 10342–10351, Nov. 2019.
- [397] J. Y. Han, T. S. Choi, and H. I. Kim, "Molecular role of Ca^{2+} and hard divalent metal cations on accelerated fibrillation and interfibrillar aggregation of α -Synuclein," *Sci. Rep.*, vol. 8, p. 1895, Jan. 2018.
- [398] C. Bich, S. Baer, M. C. Jecklin, and R. Zenobi, "Probing the hydrophobic effect of noncovalent complexes by mass spectrometry," *J. Am. Soc. Mass Spectrom.*, vol. 21, pp. 286–289, Feb. 2010.
- [399] D. Stuchfield and P. Barran, "Unique insights to intrinsically disordered proteins provided by ion mobility mass spectrometry," *Curr. Opin. Chem. Biol.*, vol. 42, pp. 177–185, Feb. 2018.

- [400] B. M. Burmann, J. A. Gerez, I. Matečko-Burmann, S. Campioni, P. Kumari, D. Ghosh, A. Mazur, E. E. Aspholm, D. Šulskis, M. Wawrzyniuk, T. Bock, A. Schmidt, S. G. D. Rüdiger, R. Riek, and S. Hiller, “Regulation of α -synuclein by chaperones in mammalian cells,” *Nature*, Dec. 2019.
- [401] J. Tao, A. Berthet, Y. R. Citron, P. L. Tsiolaki, R. Stanley, J. E. Gestwicki, D. A. Agard, and L. McConlogue, “Hsp70 chaperone blocks α -synuclein oligomer formation via a novel engagement mechanism,” *J. Biol. Chem.*, vol. 296, p. 100613, Mar. 2021.
- [402] R. M. Rasia, C. W. Bertoncini, D. Marsh, W. Hoyer, D. Cherny, M. Zweckstetter, C. Griesinger, T. M. Jovin, and C. O. Fernández, “Structural characterization of copper(II) binding to alpha-synuclein: Insights into the bioinorganic chemistry of parkinson’s disease,” *Proc. Natl. Acad. Sci. U. S. A.*, vol. 102, pp. 4294–4299, Mar. 2005.
- [403] T. Wyttenbach, M. Grabenauer, K. Thalassinou, J. H. Scrivens, and M. T. Bowers, “The effect of calcium ions and peptide ligands on the relative stabilities of the calmodulin dumbbell and compact structures,” *J. Phys. Chem. B*, vol. 114, pp. 437–447, Jan. 2010.
- [404] M. C. McCord and E. Aizenman, “The role of intracellular zinc release in aging, oxidative stress, and alzheimer’s disease,” *Front. Aging Neurosci.*, vol. 6, p. 77, Apr. 2014.
- [405] E. Aizenman, A. K. Stout, K. A. Hartnett, K. E. Dineley, B. McLaughlin, and I. J. Reynolds, “Induction of neuronal apoptosis by thiol oxidation: putative role of intracellular zinc release,” *J. Neurochem.*, vol. 75, pp. 1878–1888, Nov. 2000.
- [406] M. Perni, C. Galvagnion, A. Maltsev, G. Meisl, M. B. D. Müller, P. K. Challa, J. B. Kirkegaard, P. Flagmeier, S. I. A. Cohen, R. Cascella, S. W. Chen, R. Limbocker, P. Sormanni, G. T. Heller, F. A. Aprile, N. Cremades, C. Cecchi, F. Chiti, E. A. A. Nollen, T. P. J. Knowles, M. Vendruscolo, A. Bax, M. Zaslouff, and C. M. Dobson, “A natural product inhibits the initiation of α -synuclein aggregation and suppresses its toxicity,” *Proc. Natl. Acad. Sci. U. S. A.*, vol. 114, pp. E1009–E1017, Feb. 2017.
- [407] A. F. M. Gavriilidou, F. P. Holding, J. E. Coyle, and R. Zenobi, “Application of native ESI-MS to characterize interactions between compounds derived from Fragment-Based discovery campaigns and two pharmaceutically relevant proteins,” *SLAS Discov*, vol. 23, pp. 951–959, Oct. 2018.
- [408] G. T. H. Nguyen, T. N. Tran, M. N. Podgorski, S. G. Bell, C. T. Supuran, and W. A. Donald, “Nanoscale ion emitters in native mass spectrometry for measuring Ligand-Protein binding affinities,” *ACS Cent Sci*, vol. 5, pp. 308–318, Feb. 2019.
- [409] H. S. Jayasekera, F. A. Mohona, M. Ewbank, and M. T. Marty, “Simultaneous native mass spectrometry analysis of single and double mutants to probe lipid binding to membrane proteins.” Sept. 2023.
- [410] K. Ishii, M. Noda, and S. Uchiyama, “Mass spectrometric analysis of protein-ligand interactions,” *Biophys Physicobiol*, vol. 13, pp. 87–95, July 2016.

- [411] T. M. Allison, P. Barran, J. L. P. Benesch, S. Cianferani, M. T. Degiacomi, V. Gabelica, R. Grandori, E. G. Marklund, T. Menneteau, L. G. Migas, A. Politis, M. Sharon, F. Sobott, and K. Thalassinos, “Software requirements for the analysis and interpretation of native ion mobility mass spectrometry data,” *Anal. Chem.*, vol. 92, pp. 10881–10890, Aug. 2020.
- [412] M. T. Marty, A. J. Baldwin, E. G. Marklund, G. K. A. Hochberg, J. L. P. Benesch, and C. V. Robinson, “Bayesian deconvolution of mass and ion mobility spectra: from binary interactions to polydisperse ensembles,” *Anal. Chem.*, vol. 87, pp. 4370–4376, Apr. 2015.
- [413] M. Gonzalez-Garcia, G. Fusco, and A. De Simone, “Metal interactions of α -synuclein probed by NMR amide-proton exchange,” *Front Chem*, vol. 11, p. 1167766, May 2023.
- [414] R. Moons, R. van der Wekken-de Bruijne, S. Maudsley, F. Lemièrè, A.-M. Lambeir, and F. Sobott, “Effects of detergent on α -Synuclein structure. a native MS-Ion mobility study,” *Int. J. Mol. Sci.*, vol. 21, Oct. 2020.
- [415] R. Moons, A. Konijnenberg, C. Mensch, R. Van Elzen, C. Johannessen, S. Maudsley, A.-M. Lambeir, and F. Sobott, “Metal ions shape α -synuclein,” *Sci. Rep.*, vol. 10, p. 16293, Oct. 2020.
- [416] S. J. Allen, R. M. Eaton, and M. F. Bush, “Structural dynamics of Native-Like ions in the gas phase: Results from tandem ion mobility of cytochrome c,” *Anal. Chem.*, vol. 89, pp. 7527–7534, July 2017.
- [417] C. Eldrid, A. Ben-Younis, J. Ujma, H. Britt, T. Cragolini, S. Kalfas, D. Cooper-Shepherd, N. Tomczyk, K. Giles, M. Morris, R. Akter, D. Raleigh, and K. Thalassinos, “Cyclic ion Mobility-Collision activation experiments elucidate protein behavior in the gas phase,” *J. Am. Soc. Mass Spectrom.*, vol. 32, pp. 1545–1552, June 2021.
- [418] T. Meyer, V. Gabelica, H. Grubmüller, and M. Orozco, “Proteins in the gas phase,” *Wiley Interdiscip. Rev. Comput. Mol. Sci.*, vol. 3, pp. 408–425, July 2013.
- [419] R. Beveridge and A. N. Calabrese, “Structural proteomics methods to interrogate the conformations and dynamics of intrinsically disordered proteins,” *Front Chem*, vol. 9, p. 603639, Mar. 2021.
- [420] D. Chen and L. A. Joachimiak, “Cross-Linking mass spectrometry analysis of metastable compact structures in intrinsically disordered proteins,” in *Protein Aggregation: Methods and Protocols* (A. S. Cieplak, ed.), pp. 189–201, New York, NY: Springer US, 2023.
- [421] A. Binolfi, G. R. Lamberto, R. Duran, L. Quintanar, C. W. Bertocini, J. M. Souza, C. Cerveñansky, M. Zweckstetter, C. Griesinger, and C. O. Fernández, “Site-specific interactions of Cu(II) with alpha and beta-synuclein: bridging the molecular gap between metal binding and aggregation,” *J. Am. Chem. Soc.*, vol. 130, pp. 11801–11812, Sept. 2008.
- [422] A. Binolfi, A. A. Valiente-Gabioud, R. Duran, M. Zweckstetter, C. Griesinger, and C. O. Fernandez, “Exploring the structural details of Cu(I) binding to α -synuclein by NMR spectroscopy,” *J. Am. Chem. Soc.*, vol. 133, pp. 194–196, Jan. 2011.

- [423] A. A. Valiente-Gabioud, V. Torres-Monserrat, L. Molina-Rubino, A. Binolfi, C. Griesinger, and C. O. Fernández, “Structural basis behind the interaction of zn^{2+} with the protein α -synuclein and the A β peptide: a comparative analysis,” *J. Inorg. Biochem.*, vol. 117, pp. 334–341, Dec. 2012.
- [424] M. C. Miotto, A. A. Valiente-Gabioud, G. Rossetti, M. Zweckstetter, P. Carloni, P. Selenko, C. Griesinger, A. Binolfi, and C. O. Fernández, “Copper binding to the n-terminally acetylated, naturally occurring form of alpha-synuclein induces local helical folding,” *J. Am. Chem. Soc.*, vol. 137, pp. 6444–6447, May 2015.
- [425] A. Villar-Piqué, G. Rossetti, S. Ventura, P. Carloni, C. O. Fernández, and T. F. Outeiro, “Copper(II) and the pathological H50Q α -synuclein mutant: Environment meets genetics,” *Commun. Integr. Biol.*, vol. 10, p. e1270484, Feb. 2017.
- [426] A. Binolfi, E. E. Rodriguez, D. Valensin, N. D’Amelio, E. Ippoliti, G. Obal, R. Duran, A. Magistrato, O. Pritsch, M. Zweckstetter, G. Valensin, P. Carloni, L. Quintanar, C. Griesinger, and C. O. Fernández, “Bioinorganic chemistry of parkinson’s disease: structural determinants for the copper-mediated amyloid formation of alpha-synuclein,” *Inorg. Chem.*, vol. 49, pp. 10668–10679, Nov. 2010.
- [427] R. Llinás, M. Sugimori, and R. B. Silver, “Microdomains of high calcium concentration in a presynaptic terminal,” *Science*, vol. 256, pp. 677–679, May 1992.
- [428] R. Schneggenburger and E. Neher, “Intracellular calcium dependence of transmitter release rates at a fast central synapse,” *Nature*, vol. 406, pp. 889–893, Aug. 2000.
- [429] D. S. Chorev, L. A. Baker, D. Wu, V. Beilsten-Edmands, S. L. Rouse, T. Zeev-Ben-Mordehai, C. Jiko, F. Samsudin, C. Gerle, S. Khalid, A. G. Stewart, S. J. Matthews, K. Grünwald, and C. V. Robinson, “Protein assemblies ejected directly from native membranes yield complexes for mass spectrometry,” *Science*, vol. 362, pp. 829–834, Nov. 2018.
- [430] A. Panda, F. Giska, A. L. Duncan, A. J. Welch, C. Brown, R. McAllister, P. Hariharan, J. N. D. Goder, J. Coleman, S. Ramakrishnan, F. Pincet, L. Guan, S. Krishnakumar, J. E. Rothman, and K. Gupta, “Direct determination of oligomeric organization of integral membrane proteins and lipids from intact customizable bilayer,” *Nat. Methods*, vol. 20, pp. 891–897, June 2023.
- [431] A. T. Iavarone, K. Paech, and E. R. Williams, “Effects of charge state and cationizing agent on the electron capture dissociation of a peptide,” *Anal. Chem.*, vol. 76, pp. 2231–2238, Apr. 2004.
- [432] J. J. Commodore and C. J. Cassady, “Effects of acidic peptide size and sequence on trivalent praseodymium adduction and electron transfer dissociation mass spectrometry,” *J. Mass Spectrom.*, vol. 52, pp. 218–229, Apr. 2017.
- [433] M. A. Zenaidee, B. Wei, C. Lantz, H. T. Wu, T. R. Lambeth, J. K. Diedrich, R. R. Ogorzalek Loo, R. R. Julian, and J. A. Loo, “Internal fragments generated from different Top-Down mass spectrometry fragmentation methods extend protein sequence coverage,” *J. Am. Soc. Mass Spectrom.*, vol. 32, pp. 1752–1758, July 2021.

- [434] N. D. Schmitt, J. M. Berger, J. B. Conway, and J. N. Agar, "Increasing Top-Down mass spectrometry sequence coverage by an order of magnitude through optimized internal fragment generation and assignment," *Anal. Chem.*, vol. 93, pp. 6355–6362, Apr. 2021.
- [435] F. Lermyte, M. K. Łacki, D. Valkenborg, A. Gambin, and F. Sobott, "Conformational space and stability of ETD charge reduction products of ubiquitin," *J. Am. Soc. Mass Spectrom.*, vol. 28, pp. 69–76, Jan. 2017.
- [436] B. Wei, M. A. Zenaidee, C. Lantz, R. R. Ogorzalek Loo, and J. A. Loo, "Towards understanding the formation of internal fragments generated by collisionally activated dissociation for top-down mass spectrometry," *Anal. Chim. Acta*, vol. 1194, p. 339400, Feb. 2022.
- [437] M. Girod, Z. Sanader, M. Vojkovic, R. Antoine, L. MacAleese, J. Lemoine, V. Bonacic-Koutecky, and P. Dugourd, "UV photodissociation of proline-containing peptide ions: insights from molecular dynamics," *J. Am. Soc. Mass Spectrom.*, vol. 26, pp. 432–443, Mar. 2015.
- [438] S. J. Blanksby and G. B. Ellison, "Bond dissociation energies of organic molecules," *Acc. Chem. Res.*, vol. 36, pp. 255–263, Apr. 2003.
- [439] S. Warnke, G. von Helden, and K. Pagel, "Analyzing the higher order structure of proteins with conformer-selective ultraviolet photodissociation," *Proteomics*, vol. 15, pp. 2804–2812, Aug. 2015.
- [440] L. J. Morrison and J. S. Brodbelt, "Charge site assignment in native proteins by ultraviolet photodissociation (UVPD) mass spectrometry," *Analyst*, vol. 141, pp. 166–176, Jan. 2016.
- [441] J. S. Brodbelt, L. J. Morrison, and I. Santos, "Ultraviolet photodissociation mass spectrometry for analysis of biological molecules," *Chem. Rev.*, vol. 120, pp. 3328–3380, Apr. 2020.
- [442] B. Alies, A. Conte-Daban, S. Sayen, F. Collin, I. Kieffer, E. Guillon, P. Faller, and C. Hureau, "Zinc(II) binding site to the Amyloid- β peptide: Insights from spectroscopic studies with a wide series of modified peptides," *Inorg. Chem.*, vol. 55, pp. 10499–10509, Oct. 2016.
- [443] T. Ha, T. Enderle, D. F. Ogletree, D. S. Chemla, P. R. Selvin, and S. Weiss, "Probing the interaction between two single molecules: fluorescence resonance energy transfer between a single donor and a single acceptor," *Proc. Natl. Acad. Sci. U. S. A.*, vol. 93, pp. 6264–6268, June 1996.
- [444] E. Lerner, T. Cordes, A. Ingargiola, Y. Alhadid, S. Chung, X. Michalet, and S. Weiss, "Toward dynamic structural biology: Two decades of single-molecule Förster resonance energy transfer," *Science*, vol. 359, Jan. 2018.
- [445] J. Hendrix and D. C. Lamb, "Chapter nine - pulsed interleaved excitation: Principles and applications," in *Methods in Enzymology* (S. Y. Tetin, ed.), vol. 518, pp. 205–243, Academic Press, Jan. 2013.

- [446] N. K. Lee, A. N. Kapanidis, Y. Wang, X. Michalet, J. Mukhopadhyay, R. H. Ebricht, and S. Weiss, "Accurate FRET measurements within single diffusing biomolecules using alternating-laser excitation," *Biophys. J.*, vol. 88, pp. 2939–2953, Apr. 2005.
- [447] A. Barth, O. Opanasyuk, T.-O. Peulen, S. Felekyan, S. Kalinin, H. Sanabria, and C. A. M. Seidel, "Unraveling multi-state molecular dynamics in single-molecule FRET experiments. i. theory of FRET-lines," *J. Chem. Phys.*, vol. 156, p. 141501, Apr. 2022.
- [448] B. Schuler, "Perspective: Chain dynamics of unfolded and intrinsically disordered proteins from nanosecond fluorescence correlation spectroscopy combined with single-molecule FRET," *J. Chem. Phys.*, vol. 149, p. 010901, July 2018.
- [449] A. M. Vergnano, N. Rebola, L. P. Savtchenko, P. S. Pinheiro, M. Casado, B. L. Kieffer, D. A. Rusakov, C. Mulle, and P. Paoletti, "Zinc dynamics and action at excitatory synapses," *Neuron*, vol. 82, pp. 1101–1114, June 2014.
- [450] B. Winner, R. Jappelli, S. K. Maji, P. A. Desplats, L. Boyer, S. Aigner, C. Hetzer, T. Loher, M. Vilar, S. Campioni, C. Tzitzilonis, A. Soragni, S. Jessberger, H. Mira, A. Consiglio, E. Pham, E. Masliah, F. H. Gage, and R. Riek, "In vivo demonstration that alpha-synuclein oligomers are toxic," *Proceedings of the National Academy of Sciences*, vol. 108, no. 10, pp. 4194–4199, 2011.
- [451] J. M. Froula, M. Castellana-Cruz, N. M. Anabtawi, J. D. Camino, S. W. Chen, D. R. Thrasher, J. Freire, A. A. Yazdi, S. Fleming, C. M. Dobson, J. R. Kumita, N. Cremades, and L. A. Volpicelli-Daley, "Defining α -synuclein species responsible for parkinson's disease phenotypes in mice," *J. Biol. Chem.*, vol. 294, pp. 10392–10406, July 2019.
- [452] C. Mehlin, C. M. Headley, and S. J. Klebanoff, "An inflammatory polypeptide complex from staphylococcus epidermidis: isolation and characterization," *J. Exp. Med.*, vol. 189, pp. 907–918, Mar. 1999.
- [453] M. Otto, "Phenol-soluble modulins," *Int. J. Med. Microbiol.*, vol. 304, pp. 164–169, Mar. 2014.
- [454] R. Wang, K. R. Braughton, D. Kretschmer, T.-H. L. Bach, S. Y. Queck, M. Li, A. D. Kennedy, D. W. Dorward, S. J. Klebanoff, A. Peschel, F. R. DeLeo, and M. Otto, "Identification of novel cytolytic peptides as key virulence determinants for community-associated MRSA," *Nat. Med.*, vol. 13, pp. 1510–1514, Dec. 2007.
- [455] G. Y. C. Cheung, H.-S. Joo, S. S. Chatterjee, and M. Otto, "Phenol-soluble modulins—critical determinants of staphylococcal virulence," *FEMS Microbiol. Rev.*, vol. 38, pp. 698–719, July 2014.
- [456] Y. Zheng, H.-S. Joo, V. Nair, K. Y. Le, and M. Otto, "Do amyloid structures formed by staphylococcus aureus phenol-soluble modulins have a biological function?," *Int. J. Med. Microbiol.*, vol. 308, pp. 675–682, Aug. 2018.
- [457] P. Marinelli, I. Pallares, S. Navarro, and S. Ventura, "Dissecting the contribution of staphylococcus aureus α -phenol-soluble modulins to biofilm amyloid structure," *Sci. Rep.*, vol. 6, p. 34552, Oct. 2016.

- [458] M. Zaman and M. Andreassen, “Cross-talk between individual phenol-soluble modulins in staphylococcus aureus biofilm enables rapid and efficient amyloid formation,” *Elife*, vol. 9, Dec. 2020.
- [459] E. Tayeb-Fligelman, N. Salinas, O. Tabachnikov, and M. Landau, “Staphylococcus aureus PSM α 3 Cross- α fibril polymorphism and determinants of cytotoxicity,” *Structure*, vol. 28, pp. 301–313.e6, Mar. 2020.
- [460] Ü. Akbey and M. Andreassen, “Functional amyloids from bacterial biofilms - structural properties and interaction partners,” *Chem. Sci.*, vol. 13, pp. 6457–6477, June 2022.
- [461] M. Laabei, W. D. Jamieson, Y. Yang, J. van den Elsen, and A. T. A. Jenkins, “Investigating the lytic activity and structural properties of staphylococcus aureus phenol soluble modulin (PSM) peptide toxins,” *Biochim. Biophys. Acta*, vol. 1838, pp. 3153–3161, Dec. 2014.
- [462] K. M. Towle, C. T. Lohans, M. Miskolzie, J. Z. Acedo, M. J. van Belkum, and J. C. Vederas, “Solution structures of Phenol-Soluble modulins α 1, α 3, and β 2, virulence factors from staphylococcus aureus,” *Biochemistry*, vol. 55, pp. 4798–4806, Aug. 2016.
- [463] E. Tayeb-Fligelman, O. Tabachnikov, A. Moshe, O. Goldshmidt-Tran, M. R. Sawaya, N. Coquelle, J.-P. Colletier, and M. Landau, “The cytotoxic *Staphylococcus aureus* PSM α 3 reveals a cross- α amyloid-like fibril,” *Science*, vol. 355, pp. 831–833, Feb. 2017.
- [464] J. Santos, P. Gracia, S. Navarro, S. Peña-Díaz, J. Pujols, N. Cremades, I. Pallarès, and S. Ventura, “ α -Helical peptidic scaffolds to target α -synuclein toxic species with nanomolar affinity,” *Nat. Commun.*, vol. 12, p. 3752, June 2021.
- [465] V. Vinciauskaite and G. R. Masson, “Fundamentals of HDX-MS,” *Essays Biochem.*, vol. 67, pp. 301–314, Mar. 2023.
- [466] E. A. Hodge, M. A. Benhaim, and K. K. Lee, “Bridging protein structure, dynamics, and function using hydrogen/deuterium-exchange mass spectrometry,” *Protein Sci.*, vol. n/a, Nov. 2019.
- [467] Y. Li, C. Zhao, F. Luo, Z. Liu, X. Gui, Z. Luo, X. Zhang, D. Li, C. Liu, and X. Li, “Amyloid fibril structure of α -synuclein determined by cryo-electron microscopy,” *Cell Res.*, vol. 28, no. 9, pp. 897–903, 2018.
- [468] C. K. Xu, M. Castellana-Cruz, S. W. Chen, Z. Du, G. Meisl, A. Levin, B. Mannini, L. S. Itzhaki, T. P. J. Knowles, C. M. Dobson, N. Cremades, and J. R. Kumita, “The pathological G51D mutation in Alpha-Synuclein oligomers confers distinct structural attributes and cellular toxicity,” *Molecules*, vol. 27, Feb. 2022.
- [469] G. Fusco, T. Pape, A. D. Stephens, P. Mahou, A. R. Costa, C. F. Kaminski, G. S. Kaminski Schierle, M. Vendruscolo, G. Veglia, C. M. Dobson, and A. De Simone, “Structural basis of synaptic vesicle assembly promoted by α -synuclein,” *Nat. Commun.*, vol. 7, p. 12563, Sept. 2016.

- [470] E. D. B. Foley, M. S. Kushwah, G. Young, and P. Kukura, “Mass photometry enables label-free tracking and mass measurement of single proteins on lipid bilayers,” *Nat. Methods*, vol. 18, pp. 1247–1252, Oct. 2021.
- [471] S. Ray, T. O. Mason, L. Boyens-Thiele, A. Farzadfard, J. A. Larsen, R. K. Norrild, N. Jahnke, and A. K. Buell, “Mass photometric detection and quantification of nanoscale α -synuclein phase separation,” *Nat. Chem.*, vol. 15, pp. 1306–1316, Sept. 2023.
- [472] G. Young, N. Hundt, D. Cole, A. Fineberg, J. Andrecka, A. Tyler, A. Olerinyova, A. Ansari, E. G. Marklund, M. P. Collier, S. A. Chandler, O. Tkachenko, J. Allen, M. Crispin, N. Billington, Y. Takagi, J. R. Sellers, C. Eichmann, P. Selenko, L. Frey, R. Riek, M. R. Galpin, W. B. Struwe, J. L. P. Benesch, and P. Kukura, “Quantitative mass imaging of single biological macromolecules,” *Science*, vol. 360, pp. 423–427, Apr. 2018.
- [473] D. Wu and G. Piszczek, “Standard protocol for mass photometry experiments,” *Eur. Biophys. J.*, vol. 50, pp. 403–409, May 2021.
- [474] Z. Ou, J. Pan, S. Tang, D. Duan, D. Yu, H. Nong, and Z. Wang, “Global trends in the incidence, prevalence, and years lived with disability of parkinson’s disease in 204 Countries/Territories from 1990 to 2019,” *Front Public Health*, vol. 9, p. 776847, Dec. 2021.
- [475] H. A. Lashuel, C. R. Overk, A. Oueslati, and E. Masliah, “The many faces of α -synuclein: from structure and toxicity to therapeutic target,” *Nat. Rev. Neurosci.*, vol. 14, pp. 38–48, Jan. 2013.
- [476] T. Bartels, J. G. Choi, and D. J. Selkoe, “ α -Synuclein occurs physiologically as a helically folded tetramer that resists aggregation,” *Nature*, vol. 477, pp. 107–110, Aug. 2011.
- [477] L. Xu, S. Bhattacharya, and D. Thompson, “On the ubiquity of helical α -synuclein tetramers,” *Phys. Chem. Chem. Phys.*, vol. 21, pp. 12036–12043, June 2019.
- [478] W. Wang, I. Perovic, J. Chittuluru, A. Kaganovich, L. T. T. Nguyen, J. Liao, J. R. Auclair, D. Johnson, A. Landner, A. K. Simorellis, S. Ju, M. R. Cookson, F. J. Asturias, J. N. Agar, B. N. Webb, C. Kang, D. Ringe, G. A. Petsko, T. C. Pochapsky, and Q. Q. Hoang, “A soluble α -synuclein construct forms a dynamic tetramer,” *Proc. Natl. Acad. Sci. U. S. A.*, vol. 108, pp. 17797–17802, Oct. 2011.
- [479] U. Dettmer, A. J. Newman, F. Soldner, E. S. Luth, N. C. Kim, V. E. von Saucken, J. B. Sanderson, R. Jaenisch, T. Bartels, and D. Selkoe, “Parkinson-causing α -synuclein missense mutations shift native tetramers to monomers as a mechanism for disease initiation,” *Nat. Commun.*, vol. 6, p. 7314, June 2015.
- [480] S. N. Jackson, S. Dutta, and A. S. Woods, “The use of ECD/ETD to identify the site of electrostatic interaction in noncovalent complexes,” *J. Am. Soc. Mass Spectrom.*, vol. 20, pp. 176–179, Feb. 2009.

Appendix A

Appendix

A.1 Appendix A: Related information for Chapter 3

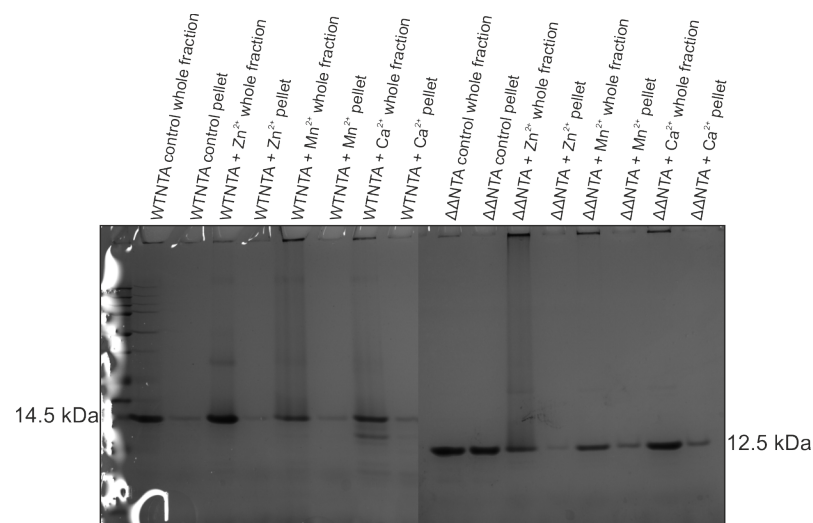


Figure. A.1 SDS-PAGE showing fibril yields of WT, $\Delta P1$, $\Delta P2$ and $\Delta\Delta\alpha SNTA$. SDS-PAGE analysis comparing pelleted and non-pelleted ThT end points with and without metal ions. Amyloid assembly was carried out using 100 μM $\alpha SNTA$, with or without 2.5 mM zinc, manganese or calcium acetate, at 37°C, 600 rpm containing one Teflon polyball (1/8" diameter; Polysciences Europe, Eppelheim, Germany) per each well of sample.

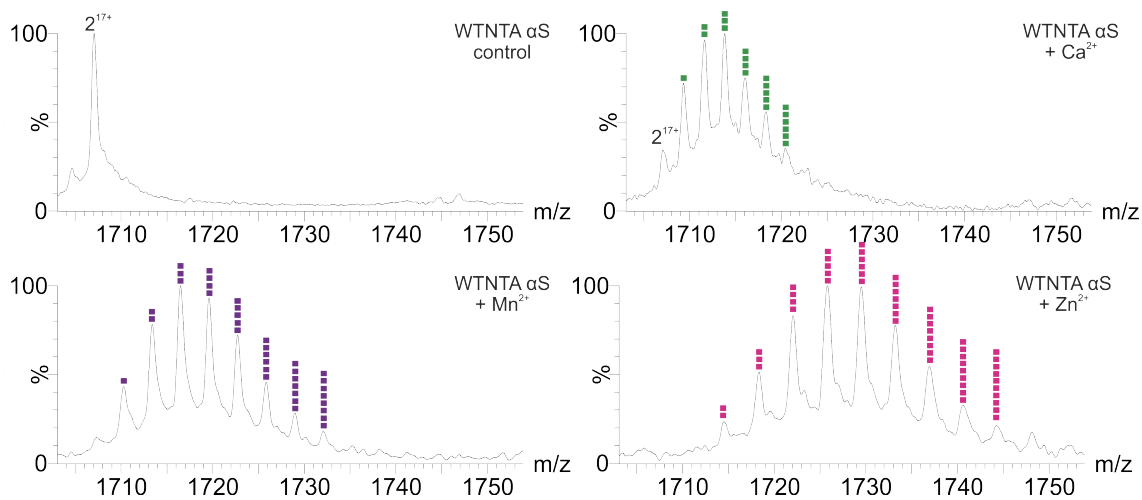


Figure. A.2 Native nESI-MS identifies binding of metal ions to WT α SNTA 17+ dimer. 20 μ M protein in 20 mM ammonium acetate, pH 7.5 and the concentration of metal acetate was 500 μ M for a ratio of 1:25 (protein:ion). Zn^{2+} binding is represented by pink squares, Mn^{2+} by purple and Ca^{2+} by green.

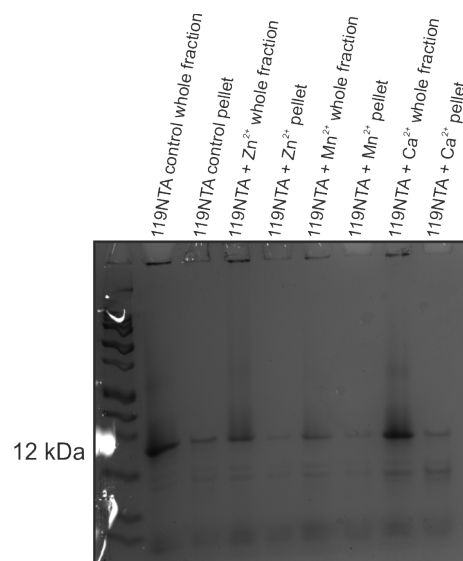


Figure. A.3 SDS-PAGE showing fibril yields of of 119 α SNTA. SDS-PAGE analysis comparing pelleted and non-pelleted ThT end points with and without metal ions. Amyloid assembly was carried out using 100 μ M α SNTA, with or without 2.5 mM Zn^{2+} , Mn^{2+} or Ca^{2+} acetate, at 37°C, 600 rpm containing one Teflon polyball (1/8" diameter; Polysciences Europe) per each sample.

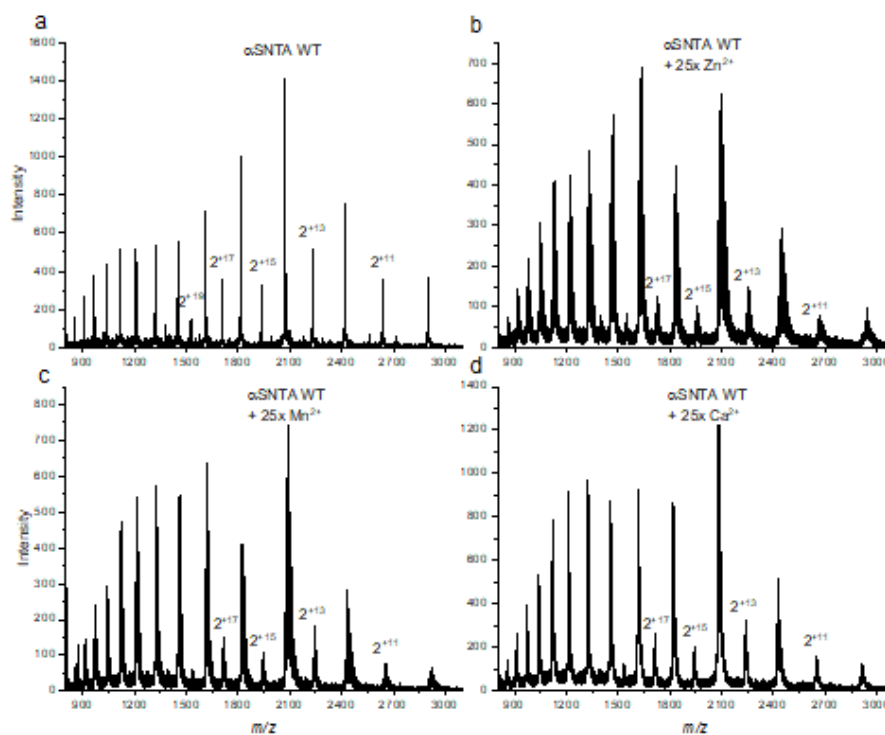


Figure. A.4 Native nESI-MS of (a) WT α SNTA, (b) WT α SNTA with 25-fold excess of Zn^{2+} , (c) WT α SNTA with 25-fold excess of Mn^{2+} and (d) WT α SNTA with 25-fold excess of Ca^{2+} . 2 = dimer with the charge state in superscript. Proteins were analysed at 20 μ M, in 20 mM ammonium acetate pH 7.5.

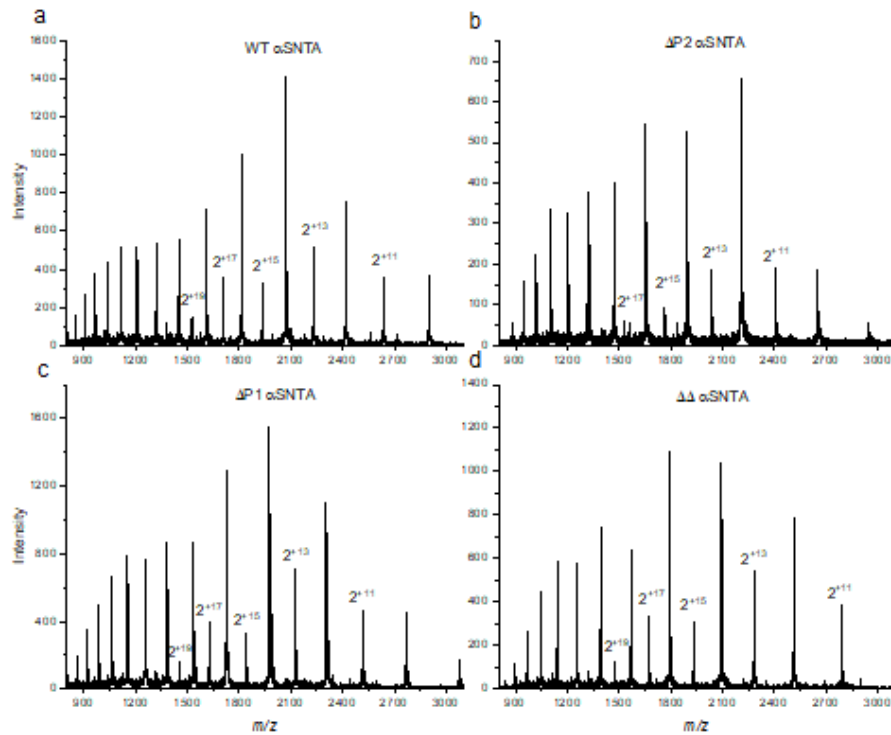


Figure. A.5 Native nESI-MS of (a) WT α SNTA, (b) $\Delta P2$ α SNTA, (c) $\Delta P1$ α SNTA and (d) $\Delta\Delta$ α SNTA. 2 = dimer with the charge state in superscript. Proteins were analysed at 20 μ M, in 20 mM ammonium acetate pH 7.5.

A.2 Appendix B: Related information for Chapter 4

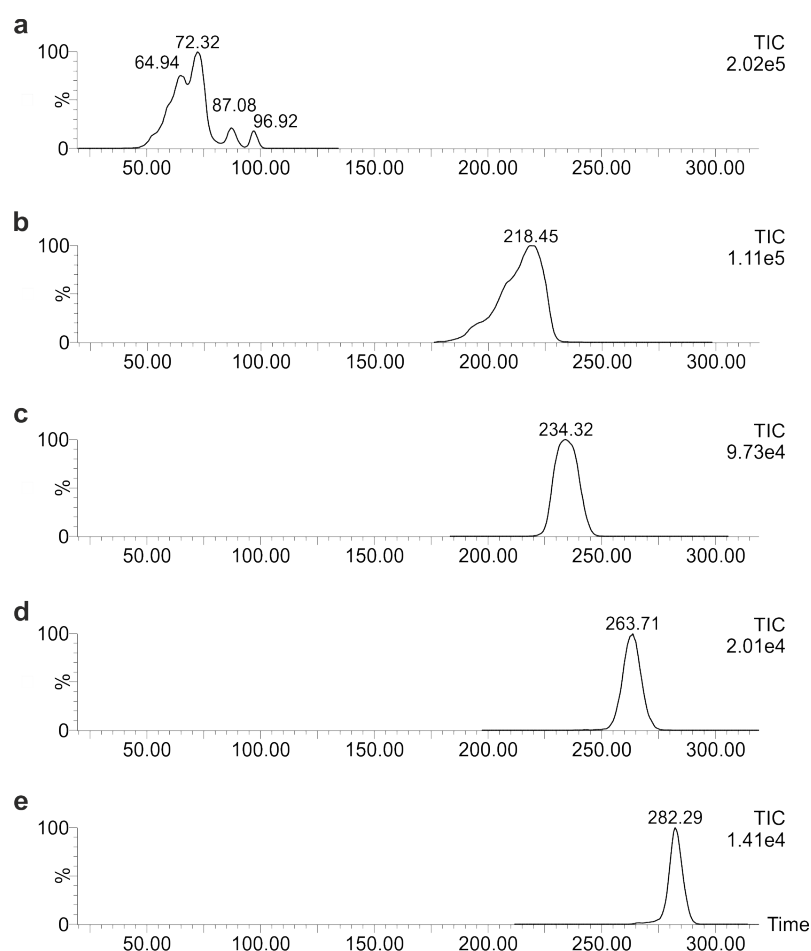


Figure. A.6 cIM-MS of the 8+ charge state for WT α SNTA with total ion counts. 20 μ M α SNTA was analysed in 20 mM ammonium acetate, pH 7.5. ATDs were extracted using MassLynx 4.1. Data were acquired with Dr Dale Cooper-Shepherd at Waters Corporation.

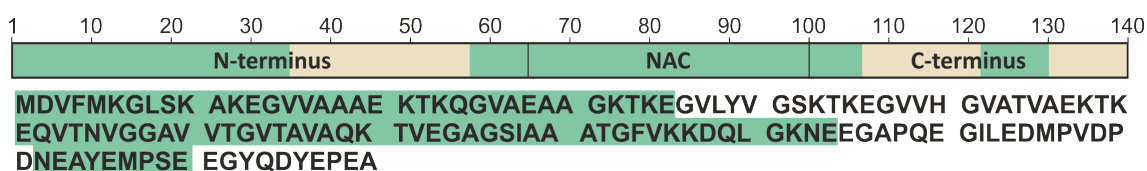


Figure. A.7 Cross-linking sequence coverage. Analysed using ProteomeDiscoverer, XlinkX node. Sequence coverage was 65.71%.

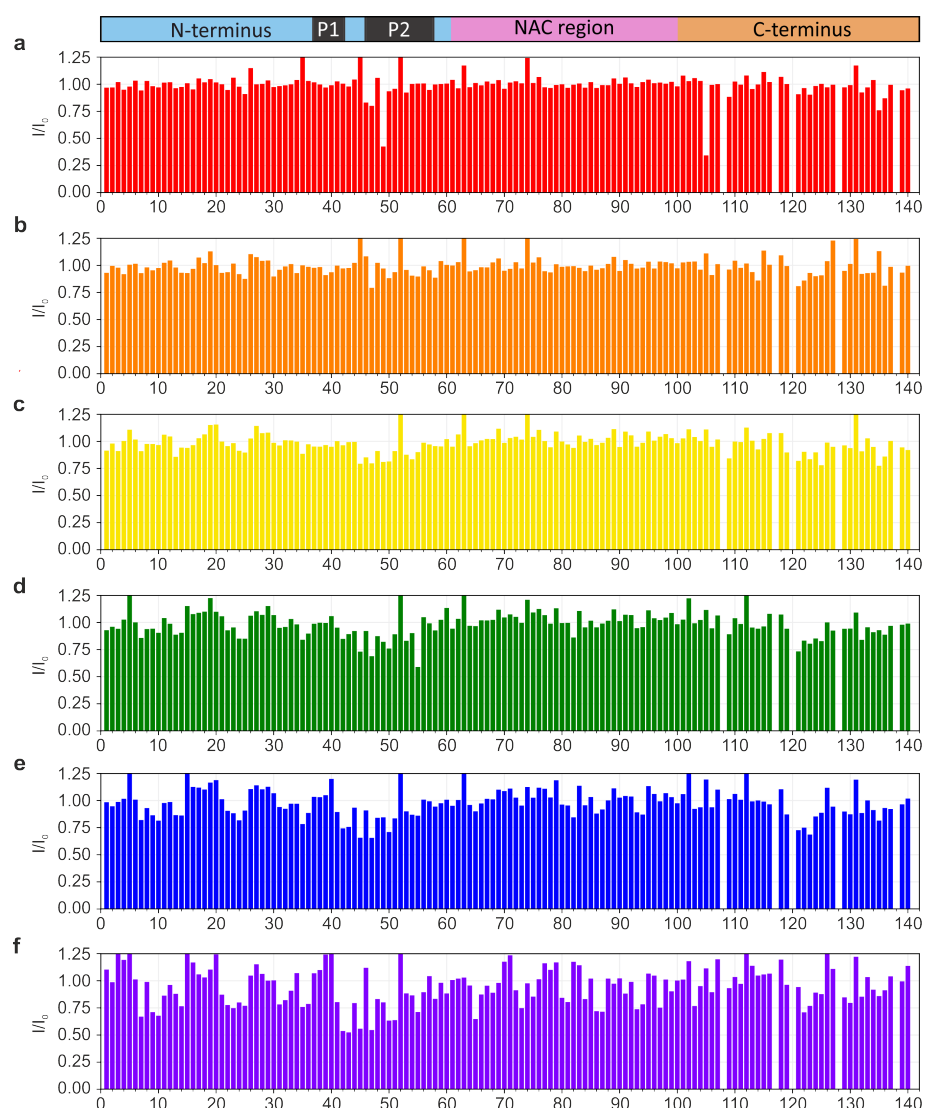


Figure. A.8 Intensity change expressed as a ratio of the resonances of α SNTA in the presence of (I) and the absence of (I_0) of Zn^{2+} . The concentrations used of Zn^{2+} were (a) 100 μ M (red), (b) 250 μ M (orange), (c) 500 μ M (yellow), (d) 1 mM μ M (green), (e) 1.5 mM (blue) and (f) 2.5 mM (purple). Residues at 0.00 are missing assignments. Spectra were acquired at 25°C in 20 mM ammonium acetate, pH 7.5, 100 μ M α SNTA. Spectra were acquired and analysed by Dr Ben Rowlinson the University of Leeds.

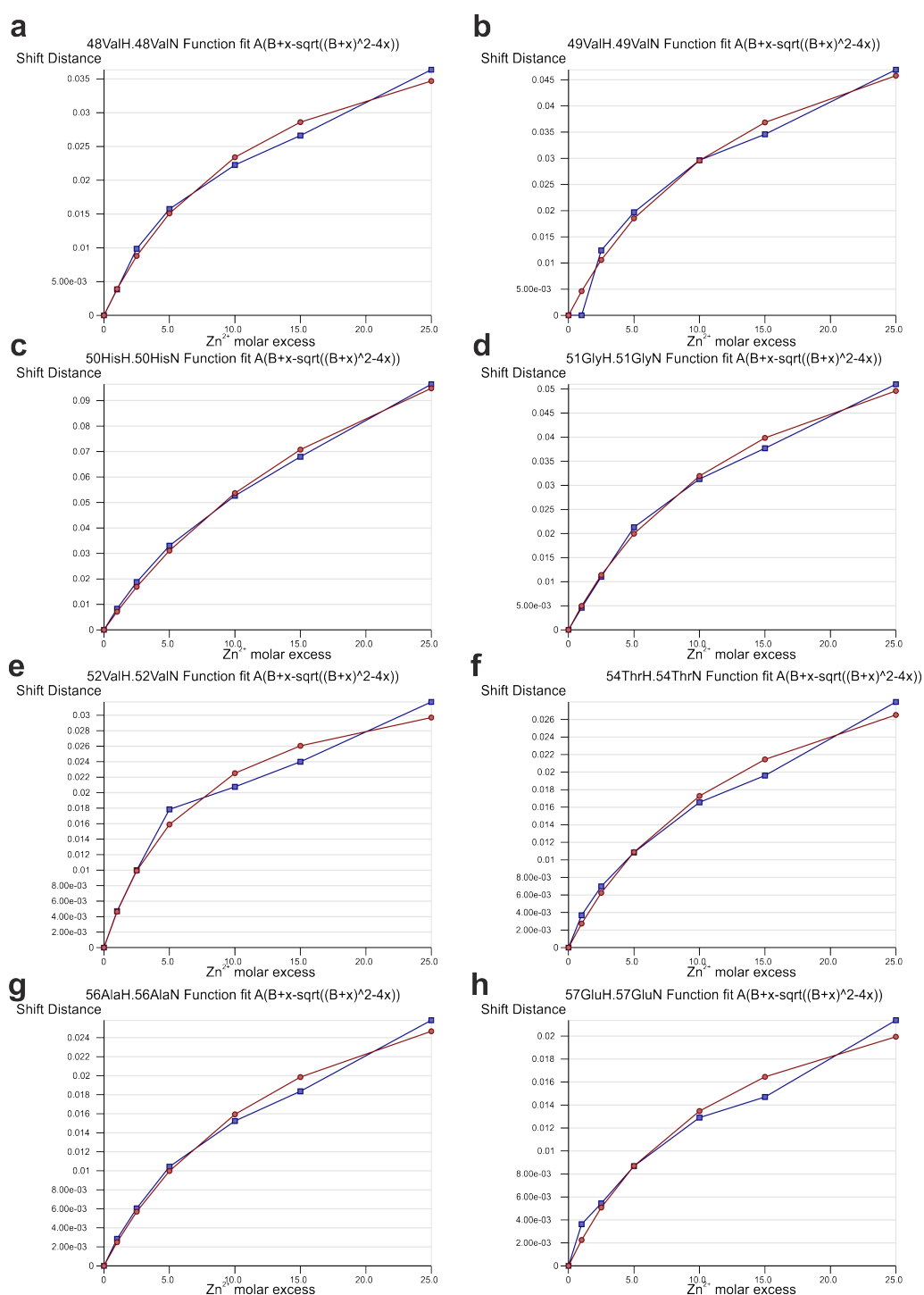


Figure. A.9 Calculation of the K_D of Zn^{2+} binding to different αS residues by NMR. Residue (a) 48, (b) 49, (c) 50, (d) 51, (e) 52, (f) 54, (g) 56, (h) 57. The red line is the fit and the blue line is the raw data. Shift distance is measured in ppm. Data were acquired and processed by Dr Ben Rowlinson the University of Leeds.

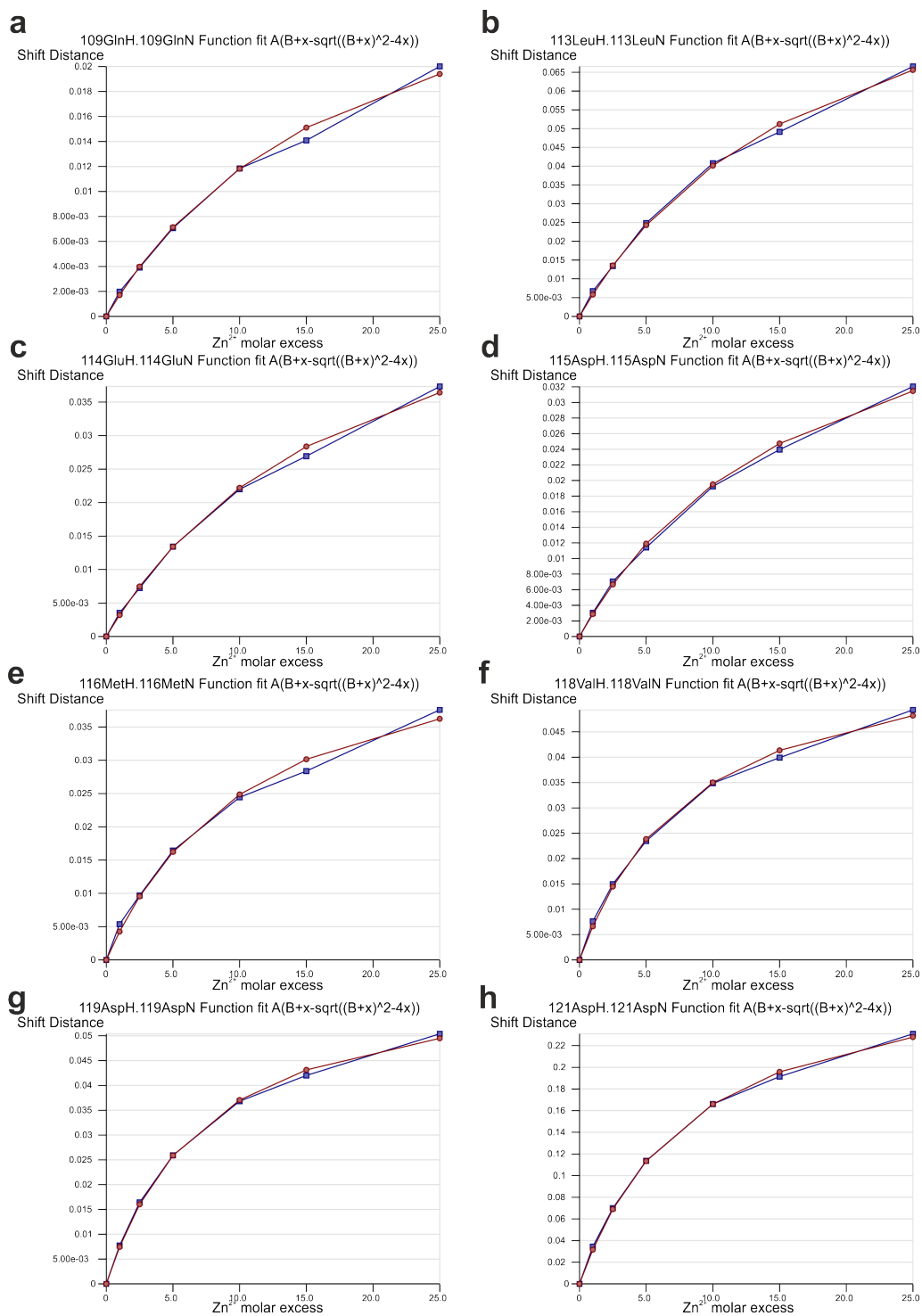


Figure. A.10 Calculation of the K_D of Zn^{2+} binding to different αS residues by NMR. Residue (a) 109, (b) 113, (c) 114, (d) 115, (e) 116, (f) 118, (g) 119, (h) 121. The red line is the fit and the blue line is the raw data. Shift distance is measured in ppm. Data were acquired and processed by Dr Ben Rowlinson the University of Leeds.

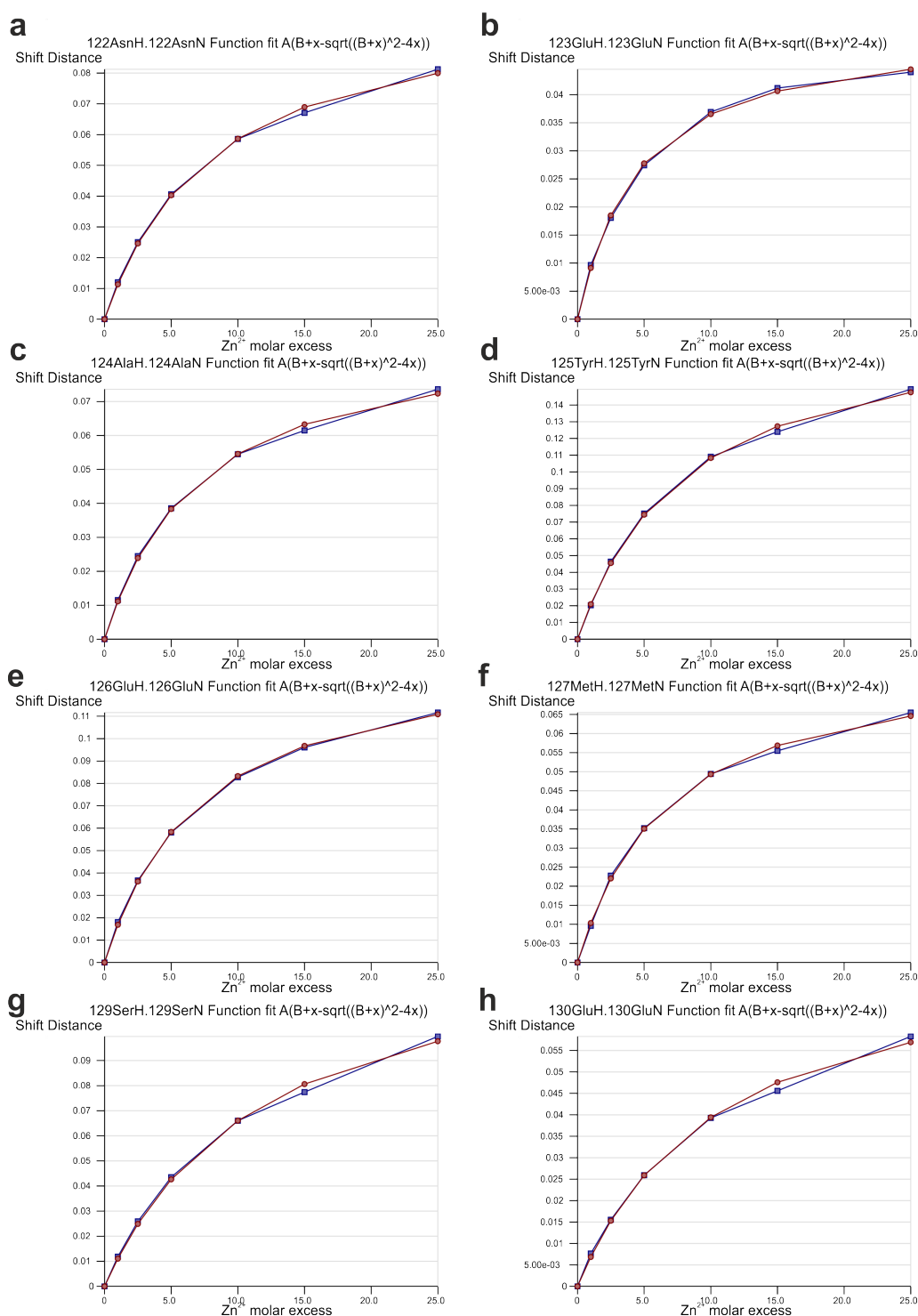


Figure. A.11 Calculation of the K_D of Zn^{2+} binding to different αS residues by NMR. Residue (a) 122, (b) 123, (c) 124, (d) 125, (e) 126, (f) 127, (g) 129, (h) 130. The red line is the fit and the blue line is the raw data. Shift distance is measured in ppm. Data were acquired and processed by Dr Ben Rowlinson the University of Leeds.

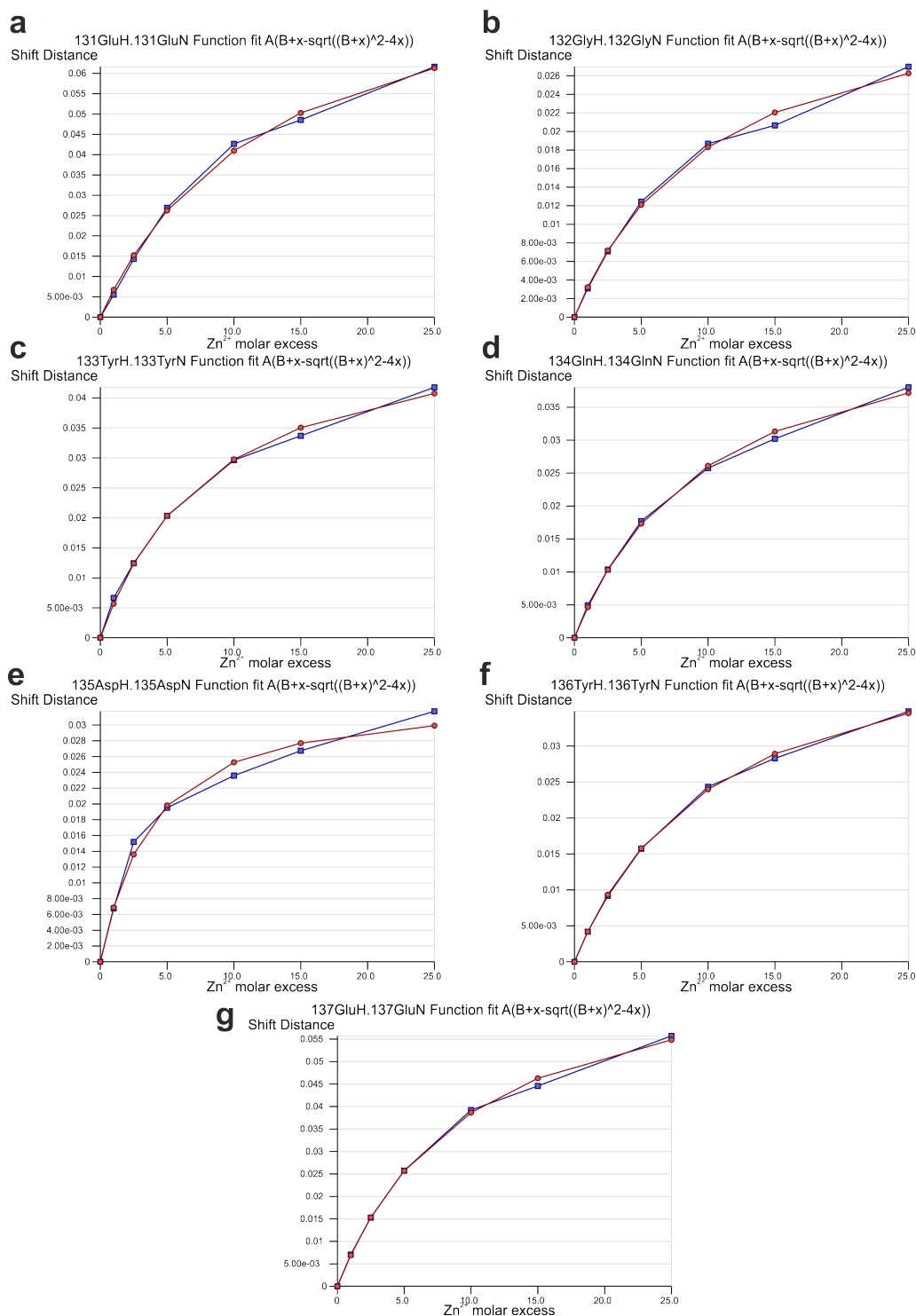


Figure. A.12 Calculation of the K_D of Zn^{2+} binding to different αS residues by NMR. Residue (a) 131, (b) 132, (c) 133, (d) 134, (e) 135, (f) 136, (g) 137. The red line is the fit and the blue line is the raw data. Shift distance is measured in ppm. Data were acquired and processed by Dr Ben Rowlinson the University of Leeds.

Table A.1 Fragment ions detected for ETD of denatured 12+ charge state of α SNTA processed using ProSight Native, Proteinaceous. Score is the isotopic fit score.

Name	Theoretical Mass	ppm Error	Charge	Mono. m/z	S/N	Intensity	Score
C6	810.38	-5.31	1	811.38	275.1	2076861	0.64
C9	1067.51	-5.22	1	1068.52	88.8	868714	0.56
C11	1266.65	-5.19	1	1267.65	55.7	691364	0.56
C17	1849.98	-4.96	2	926	12.3	181267	0.64
C18	1921.02	-5.04	2	961.52	7.5	117309	0.79
C20	2121.1	-5.33	3	708.04	12.7	173470	0.77
C21	2249.19	-5.27	2	1125.6	8.6	153929	0.75
C22	2350.24	-5.17	3	784.42	26.9	380985	0.72
C22	2350.24	-5.37	2	1176.13	12.4	225227	0.79
C23	2478.33	-5.28	3	827.12	59.7	863987	0.74
C23	2478.33	-5.34	2	1240.17	13.6	261694	0.82
C24	2606.39	-4.77	3	869.8	76.9	1153604	0.77
C24	2606.39	-4.57	2	1304.2	33.5	648509	0.77
C25	2663.41	-4.64	3	888.81	3.7	63714	0.69
C25	2663.41	-5.47	2	1332.71	4.4	113598	0.65
C27	2833.52	-5.48	3	945.51	121.8	1967895	0.85
C27	2833.52	-6.56	2	1417.77	5.7	153106	0.67
C28	2962.56	-5.47	4	741.65	6.7	108278	0.83
C28	2962.56	-5.57	3	988.53	41	701674	0.78
C30	3104.64	-5.52	4	777.17	4.4	76867	0.86
C30	3104.64	-6.1	3	1035.89	13.2	249204	0.6
C32	3289.75	-5.18	4	823.45	5.9	107752	0.8
C32	3289.75	-4.86	3	1097.59	35	689909	0.81
C33	3390.8	-5.38	4	848.71	9.7	177998	0.77
C33	3390.8	-5.45	3	1131.27	36.6	751972	0.66
C34	3518.9	-4.86	4	880.73	13	240883	0.8
C34	3518.9	-5.34	3	1173.97	4.6	117911	0.51
C35	3647.94	-5.11	4	912.99	49	901288	0.81
C35	3647.94	-5.11	3	1216.99	26.7	591080	0.69
C36	3704.96	-4.88	3	1235.99	3.7	106597	0.76
C37	3804.03	-5.57	5	761.81	3.3	63315	0.58
C37	3804.03	-5.37	4	952.01	26.4	503602	0.85
C37	3804.03	-4.81	3	1269.02	19.4	456954	0.76
C38	3917.11	-5.57	5	784.43	6.1	113927	0.63
C38	3917.11	-5.37	4	980.29	128.9	2465476	0.9
C38	3917.11	-4.79	3	1306.71	45.1	1055528	0.78
C39	4080.18	-4.89	5	817.04	6.5	125336	0.79
C39	4080.18	-5.5	4	1021.05	31.7	641675	0.71
C39	4080.18	-6.92	3	1361.07	6.2	185889	0.73
C41	4236.27	-5.22	5	848.26	8.7	169550	0.69
C42	4323.3	-5.02	5	865.67	6.8	137105	0.68
C42	4323.3	-5.4	4	1081.83	4.7	116534	0.52
C43	4451.39	-5.02	5	891.29	10.1	207053	0.52
C43	4451.39	-5.29	4	1113.86	20.8	468839	0.85

Continued on next page

Continued from previous page

Name	Theoretical Mass	ppm Error	Charge	Mono. m/z	S/N	Intensity	Score
C44	4552.44	-5.06	5	911.5	13	270194	0.85
C44	4552.44	-5.31	4	1139.12	16.7	393327	0.75
C46	4809.58	-5.26	6	802.6	4.8	102701	0.79
C46	4809.58	-5.35	5	962.92	152.7	3236524	0.91
C46	4809.58	-5.15	4	1203.4	103.9	2507275	0.92
Z43	4810.99	9.22	4	1203.76	27	669719	0.59
C47	4866.6	-5.45	5	974.33	17.1	380272	0.63
C49	5064.74	-5.42	6	845.13	6.3	139920	0.62
C49	5064.74	-5.56	5	1013.95	4.1	109149	0.55
C50	5201.79	-5.08	6	867.97	37.7	806492	0.88
C50	5201.79	-5.59	5	1041.37	38.6	900688	0.88
C52	5357.88	-5.07	6	893.99	9.8	222156	0.8
C52	5357.88	-4.49	5	1072.58	3.1	92925	0.54
C53	5428.92	-5.22	6	905.83	16	358037	0.84
C53	5428.92	-4.87	5	1086.79	10	256932	0.51
C54	5529.97	-4.88	6	922.67	13.5	309061	0.76
C55	5629.04	-5.74	7	805.16	3.8	88094	0.76
C55	5629.04	-4.99	6	939.18	42.8	963537	0.87
C55	5629.04	-5.36	5	1126.81	10.2	272985	0.63
C56	5700.07	-5.15	5	1141.02	3.2	103697	0.6
C57	5829.12	-4.4	7	833.74	3.1	76215	0.63
C57	5829.12	-5.23	6	972.53	38.1	883627	0.92
C57	5829.12	-6.13	5	1166.83	15.9	428464	0.76
C58	5957.21	-5.23	7	852.04	5.1	120208	0.85
C58	5957.21	-5.44	6	993.88	19.1	461051	0.85
C59	6058.26	-5.02	7	866.47	5.8	139607	0.76
C59	6058.26	-5.18	6	1010.72	17.9	441759	0.8
C59	6058.26	-5.7	5	1212.66	6.4	201569	0.72
C60	6186.35	-5.78	8	774.3	5.6	130199	0.61
C60	6186.35	-5.05	7	884.77	55.8	1276614	0.94
C60	6186.35	-5.59	6	1032.07	23.1	580309	0.86
C60	6186.35	-4.67	5	1238.28	3.4	126685	0.7
C61	6315.4	-4.83	7	903.21	83.2	1940110	0.9
C61	6315.4	-5.35	6	1053.57	90.9	2277233	0.94
C61	6315.4	-5.02	5	1264.09	15.8	477325	0.78
C62	6443.46	-5.1	7	921.5	35.8	861281	0.88
C62	6443.46	-5.01	6	1074.92	13.4	364703	0.8
C63	6542.52	-4.84	7	935.65	34.6	848456	0.92
C63	6542.52	-5.37	6	1091.43	39.9	1060231	0.9
C64	6643.57	-5.42	7	950.09	25.3	637631	0.91
C64	6643.57	-5.32	6	1108.27	23	633994	0.85
C64	6643.57	-5.28	5	1329.72	4.8	190232	0.64
C65	6757.62	-5.48	7	966.38	6.9	188401	0.69
C66	6856.68	-5.59	7	980.53	7.3	200709	0.77
C66	6856.68	-5.05	6	1143.79	6.4	202616	0.74
Z65	6896.15	-5.61	4	1725.05	25.7	1015260	0.82
C67	6913.7	-5.41	7	988.68	9	246597	0.64
C68	6970.73	-5.04	8	872.35	4.3	114818	0.66

Continued on next page

Continued from previous page

Name	Theoretical Mass	ppm Error	Charge	Mono. m/z	S/N	Intensity	Score
C68	6970.73	-5.46	7	996.83	20.5	541347	0.83
C68	6970.73	-5.21	6	1162.8	8.1	255702	0.75
C69	7041.76	-5.26	7	1006.97	4.5	134143	0.68
C72	7340.95	-5.51	7	1049.71	5.4	166184	0.76
Z72	7523.51	-5.66	4	1881.89	7.7	367529	0.83
C75	7598.09	-5.53	8	950.77	22.4	589732	0.74
C75	7598.09	-5.17	7	1086.45	45.9	1282707	0.9
C75	7598.09	-5.06	6	1267.35	21	677295	0.89
Z76	7850.67	-3.96	4	1963.67	22.8	995796	0.73
Z77	7951.71	-4.93	5	1591.35	22.4	894308	0.6
Z77	7951.71	-4.87	4	1988.94	35.1	1517503	0.78
Z79	8178.84	-4.84	5	1636.78	29.6	1211903	0.84
Z81	8435.98	-5.28	5	1688.2	10.3	485256	0.8
Z82	8537.03	-5.48	5	1708.41	13.5	626149	0.74
Z83	8665.12	-5.46	5	1734.03	24.1	1061623	0.79
Z84	8794.16	-4.39	5	1759.84	6.5	340042	0.75
Z85	8865.2	-5.2	5	1774.05	27.6	1222848	0.88
Z87	9065.32	-5.64	5	1814.07	13.4	636940	0.54
Z90	9292.44	-5.79	6	1549.75	13.7	604234	0.54
Z90	9292.44	-5.35	5	1859.5	38.6	1736789	0.83
Z93	9627.64	-4.16	7	1376.38	3.7	194350	0.55
Z93	9627.64	-5.64	5	1926.54	6.6	367216	0.8
Z94	9684.66	-4.79	7	1384.53	14.3	582128	0.87
Z94	9684.66	-5.21	6	1615.12	100.3	4200580	0.95
Z94	9684.66	-4.46	5	1937.94	68.6	3158461	0.84
Z96	9941.8	-5.42	6	1657.97	12.3	607060	0.66
Z97	10042.85	-4.99	6	1674.81	13.4	657379	0.79
Z101	10414.06	-4.92	7	1488.73	13.5	615014	0.54
Z101	10414.06	-5.54	6	1736.68	10.9	566705	0.6
Z102	10577.13	-5.21	8	1323.15	6.8	305919	0.52
Z102	10577.13	-4.99	7	1512.03	48.9	2072567	0.88
Z102	10577.13	-5.97	6	1763.86	48.7	2278801	0.73
Z103	10690.21	-4.98	7	1528.18	15	693875	0.77
Z103	10690.21	-5.7	6	1782.71	8.9	483215	0.76
Z104	10789.28	-6.02	7	1542.33	7.3	379357	0.64
Z105	10846.3	-4.22	7	1550.48	21.7	986189	0.78
Z106	10975.34	-3.78	7	1568.91	12.6	615100	0.77
Z107	11103.44	-4.76	8	1388.94	6.2	307615	0.6
Z107	11103.44	-4.45	7	1587.21	19.9	940153	0.77
Z107	11103.44	-4.9	6	1851.58	5.5	334257	0.61
Z108	11204.48	-5.39	8	1401.57	9.7	446948	0.81
Z108	11204.48	-5.01	6	1868.42	5	316383	0.69
Z109	11332.58	-3.85	7	1619.95	13.6	686742	0.78
Z110	11389.6	-3.29	8	1424.71	12.3	563711	0.55
Z110	11389.6	-5.85	7	1628.09	15.7	784962	0.54
Z112	11531.68	-5.29	7	1648.39	21	1041445	0.78
Z112	11531.68	-4.12	6	1922.95	6.8	412351	0.54
Z113	11660.72	-5.37	8	1458.6	28.6	1264865	0.79

Continued on next page

Continued from previous page

Name	Theoretical Mass	ppm Error	Charge	Mono. m/z	S/N	Intensity	Score
Z113	11660.72	-5.21	7	1666.82	29.3	1441089	0.87
Z113	11660.72	-4.34	6	1944.46	8	471428	0.66
Z116	11887.85	-4.6	8	1486.99	29.3	1337414	0.89
Z116	11887.85	-5.86	7	1699.27	24.6	1253259	0.86
Z117	12015.9	-3.89	8	1503	20.2	957929	0.92
Z117	12015.9	-5.5	7	1717.56	15.3	817284	0.84
Z118	12144	-5.62	9	1350.34	3.8	214812	0.71
Z118	12144	-4.14	8	1519.01	15.9	778559	0.83
Z118	12144	-5.38	7	1735.86	8.1	476090	0.68
Z119	12245.05	-5.17	8	1531.64	11.6	593250	0.83
Z119	12245.05	-5.11	7	1750.3	7.5	447062	0.76
Z120	12373.14	-3.58	8	1547.65	8.1	443319	0.78
Z122	12573.22	-1.56	9	1398.03	5.7	305373	0.73
Z123	12644.26	-2.56	9	1405.92	10.1	493543	0.68
Z123	12644.26	-3.79	8	1581.54	8	449490	0.6
Z124	12715.3	-3.12	9	1413.82	9.1	454459	0.67
Z127	12970.45	-4.84	10	1298.05	5.9	293338	0.53
Z128	13099.5	-4.46	9	1456.51	6.6	364459	0.56
Z129	13227.59	-4.55	10	1323.77	19.1	844186	0.83
Z129	13227.59	-5.17	8	1654.46	10	579797	0.77
Z130	13298.63	-3.58	10	1330.87	7.9	390919	0.72
Z130	13298.63	-2.26	9	1478.63	8.6	462674	0.75
Z131	13426.72	-4.08	10	1343.68	26	1156086	0.92
Z131	13426.72	-4.5	9	1492.87	34.3	1638583	0.93
Z131	13426.72	-4.61	8	1679.35	15.8	877174	0.79
Z132	13513.76	-3.67	10	1352.38	5.9	317523	0.63
Z132	13513.76	-3.49	9	1502.54	7.6	430260	0.56
Z133	13626.84	-5.08	10	1363.69	9.6	481377	0.82
Z133	13626.84	-2.89	9	1515.1	14.2	745896	0.71
Z133	13626.84	-5.84	8	1704.36	6.4	418452	0.65
Z134	13683.86	-4.69	10	1369.39	56.4	2505313	0.94
Z134	13683.86	-4.6	9	1521.44	76.1	3648798	0.92
Z134	13683.86	-4.47	7	1955.84	10	625253	0.56
Z135	13811.96	0.63	10	1382.2	4.8	279974	0.74
Z136	13943	-3.5	10	1395.31	4.5	271685	0.63
Z137	14090.06	-6.19	10	1410.01	5	298778	0.58
Z138	14189.13	-6.1	11	1290.93	7.3	365762	0.53
Z138	14189.13	-6.57	9	1577.58	5.8	370520	0.54
C138	14292.17	-6.78	11	1300.3	5.2	284195	0.56
C138	14292.17	-7.43	10	1430.22	7.7	429292	0.58
Z139	14304.16	-4.37	11	1301.39	28.7	1277383	0.85
Z139	14304.16	-4.71	10	1431.42	32.8	1568017	0.89
Z139	14304.16	-4.34	9	1590.36	25.2	1336844	0.74
Z139	14304.16	-5.74	8	1789.03	6.6	440671	0.75
C139	14421.21	-6.29	12	1202.77	28.6	1205887	0.81
C139	14421.21	-5.38	11	1312.03	89.8	3930268	0.84
C139	14421.21	-4.93	10	1443.13	111.2	5225351	0.87
C139	14421.21	-4.49	9	1603.36	80.8	4159726	0.83

Continued on next page

Continued from previous page

Name	Theoretical Mass	ppm Error	Charge	Mono. m/z	S/N	Intensity	Score
C139	14421.21	-5.31	8	1803.66	28.7	1632599	0.84

Table A.2 Fragment ions detected for ETD of native 12+ charge state of α SNTA processed using ProSight Native, Proteinaceous. Score is the isotopic fit score.

Name	Theoretical Mass	ppm Error	Charge	Mono. m/z	S/N	Intensity	Score
C11	1266.65	-1.72	1	1267.65	11	53890	0.55
C21	2249.19	-2.1	3	750.74	5.4	30916	0.5
C22	2350.24	-1.46	3	784.42	4.9	28817	0.6
C22	2350.24	-2.48	2	1176.13	5.1	37754	0.79
C23	2478.33	-1.58	3	827.12	7.5	44191	0.81
C23	2478.33	-2.39	2	1240.17	7.8	57802	0.74
C24	2606.39	-1.22	3	869.8	13.2	77553	0.69
C24	2606.39	-1.79	2	1304.2	22.3	156802	0.7
C27	2833.52	-1.82	3	945.51	20.2	124633	0.75
C28	2962.56	-1.82	3	988.53	6.2	43055	0.85
C32	3289.75	-2.07	3	1097.59	6.6	52996	0.71
C33	3390.8	-1.82	3	1131.27	8.6	69712	0.7
C35	3647.94	-1.82	4	912.99	7.9	58469	0.76
C35	3647.94	-1.51	3	1216.99	10.2	87410	0.61
C37	3804.03	-2.14	3	1269.02	8.8	80471	0.8
C38	3917.11	-1.8	4	980.29	23.7	171418	0.85
C38	3917.11	-1.96	3	1306.71	26.9	227636	0.73
C39	4080.18	-2.05	4	1021.05	6.7	54358	0.62
C41	4236.27	-1.93	5	848.26	3.1	26195	0.71
C43	4451.39	-1.86	4	1113.86	4.6	43766	0.9
C44	4552.44	-2.2	4	1139.12	6	56234	0.53
C46	4809.58	-1.9	5	962.92	29.4	235280	0.88
C46	4809.58	-1.93	4	1203.4	49.7	432070	0.9
C50	5201.79	-1.99	6	867.97	7.8	67330	0.81
C50	5201.79	-1.67	5	1041.37	10.3	93395	0.82
C55	5629.04	-1.96	6	939.18	8.8	78124	0.76
C57	5829.12	-1.77	6	972.53	8.6	78636	0.81
C57	5829.12	-3.44	5	1166.83	5.8	63237	0.79
C58	5957.21	-2.03	6	993.88	4.1	42081	0.73
C59	6058.26	-1.6	6	1010.72	3.4	36600	0.62
C60	6186.35	-1.86	7	884.77	13	116029	0.8
C60	6186.35	-1.99	6	1032.07	9	86991	0.82
C61	6315.4	-1.92	7	903.21	15.7	141315	0.88
C61	6315.4	-1.82	6	1053.57	21.6	202779	0.95
C61	6315.4	-1.68	5	1264.09	8.9	102524	0.8
C62	6443.46	-2.05	7	921.5	7.2	69756	0.85
C62	6443.46	-1.89	6	1074.92	4.1	46895	0.8
C63	6542.52	-1.64	7	935.65	8.2	80086	0.85
C63	6542.52	-1.9	6	1091.43	11.2	114291	0.9

Continued on next page

Continued from previous page

Name	Theoretical Mass	ppm Error	Charge	Mono. m/z	S/N	Intensity	Score
C64	6643.57	-1.6	7	950.09	5.2	53663	0.82
C64	6643.57	-1.84	6	1108.27	6	67754	0.79
C68	6970.73	-1.75	7	996.83	4.8	52734	0.71
C68	6970.73	-1.87	6	1162.8	3.1	42312	0.52
C75	7598.09	-1.56	8	950.77	4.9	53097	0.61
C75	7598.09	-1.72	7	1086.45	11.4	122856	0.85
C75	7598.09	-1.61	6	1267.35	11.4	138403	0.83
C131	13439.84	-7.52	9	1494.32	13.5	249932	0.55
C138	14292.17	-3.53	10	1430.22	7.5	149948	0.53
C139	14421.21	-3.46	12	1202.77	17.4	269558	0.78
C139	14421.21	-2.71	11	1312.03	82.8	1278822	0.83
C139	14421.21	-2.53	10	1443.13	151.3	2458767	0.85
C139	14421.21	-2.68	9	1603.36	83.7	1472416	0.84
C139	14421.21	-3.64	8	1803.66	53	998271	0.82
Z14	1627.61	6.07	15	109.51	3	1676	0.8
Z94	9684.66	-1.2	7	1384.53	9.3	142735	0.81
Z108	11204.48	-1.06	8	1401.57	4.9	94620	0.55
Z109	11332.58	-0.91	8	1417.58	7.6	133391	0.57
Z113	11660.72	-1.52	8	1458.6	9.9	171239	0.72
Z116	11887.85	-0.3	8	1486.99	10.2	182288	0.84
Z124	12715.3	4.89	9	1413.82	8.7	156153	0.53
Z129	13227.59	-0.11	10	1323.77	8	140281	0.67
Z130	13298.63	1.7	9	1478.63	6.9	138728	0.71
Z131	13426.72	0.2	10	1343.68	8.4	151261	0.76
Z131	13426.72	-0.63	9	1492.87	17.4	304545	0.87
Z133	13626.84	0.04	10	1363.69	3.9	87520	0.71
Z134	13683.86	-1.71	10	1369.39	14.9	254281	0.9
Z134	13683.86	-0.91	9	1521.44	3.9	95906	0.7
Z138	14189.13	-3.34	10	1419.92	7.5	148907	0.75
Z139	14304.16	-1.3	11	1301.39	14	233501	0.74
Z139	14304.16	-0.94	10	1431.42	24.4	415412	0.82
Z139	14304.16	-2.02	9	1590.36	9.4	194196	0.72
Z139	14304.16	-3.04	8	1789.03	4.5	118502	0.59

A.3 Appendix C: Related information for Chapter 5

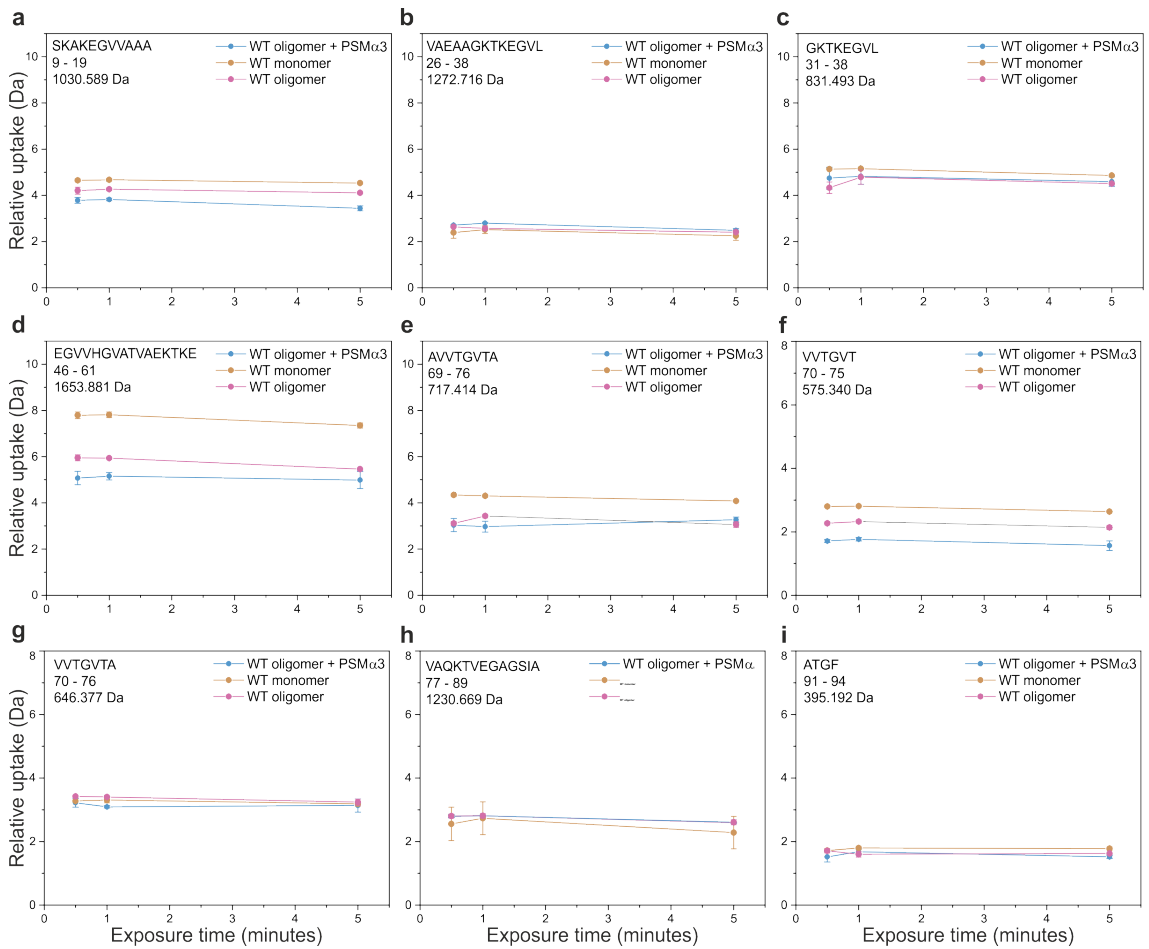


Figure. A.13 Uptake plots for the N-terminal and NAC regions of α S monomers, WT oligomers and WT oligomer + PSM α 3 by HDX. Peptides (a) 9-19, (b) 26-38, (c) 31-38, (d) 46-61, (e) 69-76, (f) 70-75, (g) 70-76, (h) 77-89, (i) 91-94. Data were generated using Deuterios and the plots were generated using Origin.

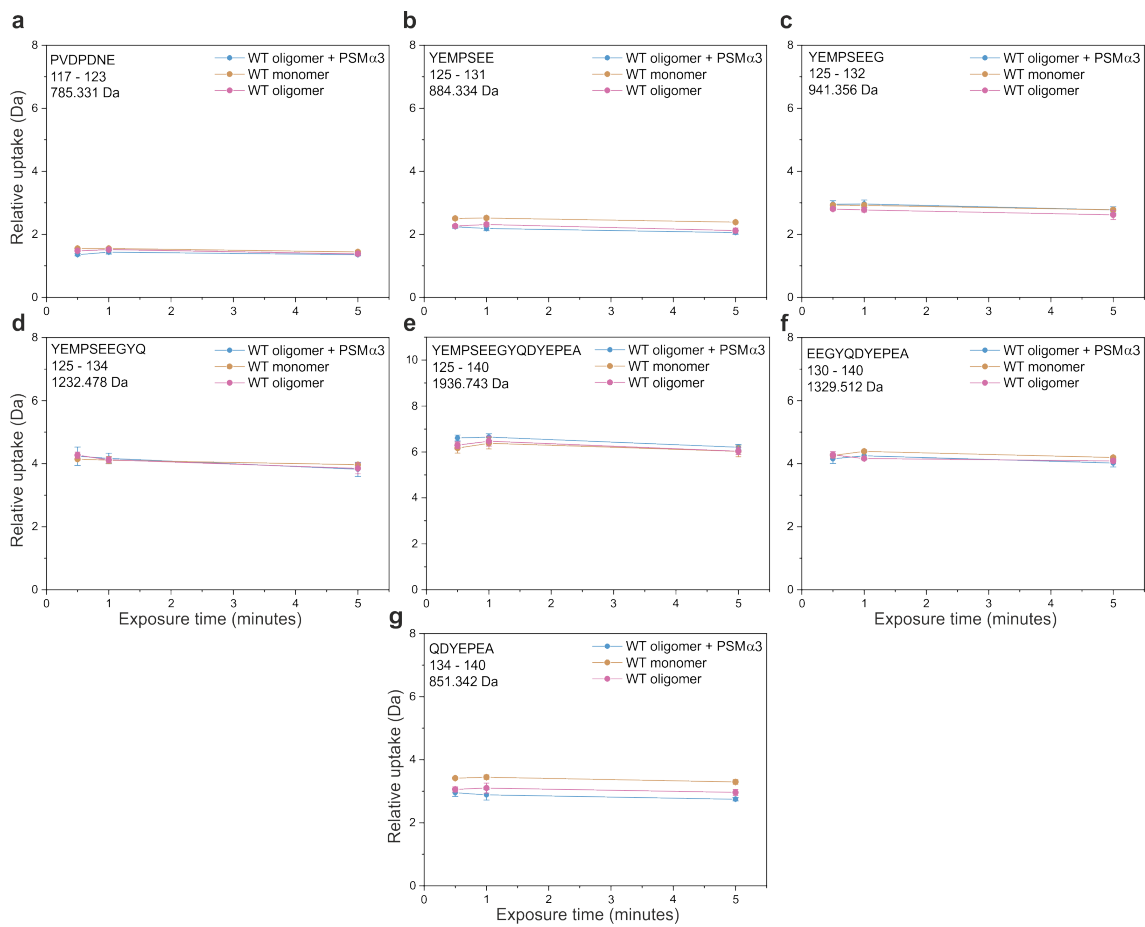


Figure. A.14 Uptake plots for the C-terminal region of α S monomers, WT oligomers and WT oligomer + PSM α 3 by HDX. Peptides (a) 117-123, (b) 125-131, (c) 125-132, (d) 125-134, (e) 125-140, (f) 130-140, (g) 134-140. Data were generated using Deuterios and the plots were generated using Origin.

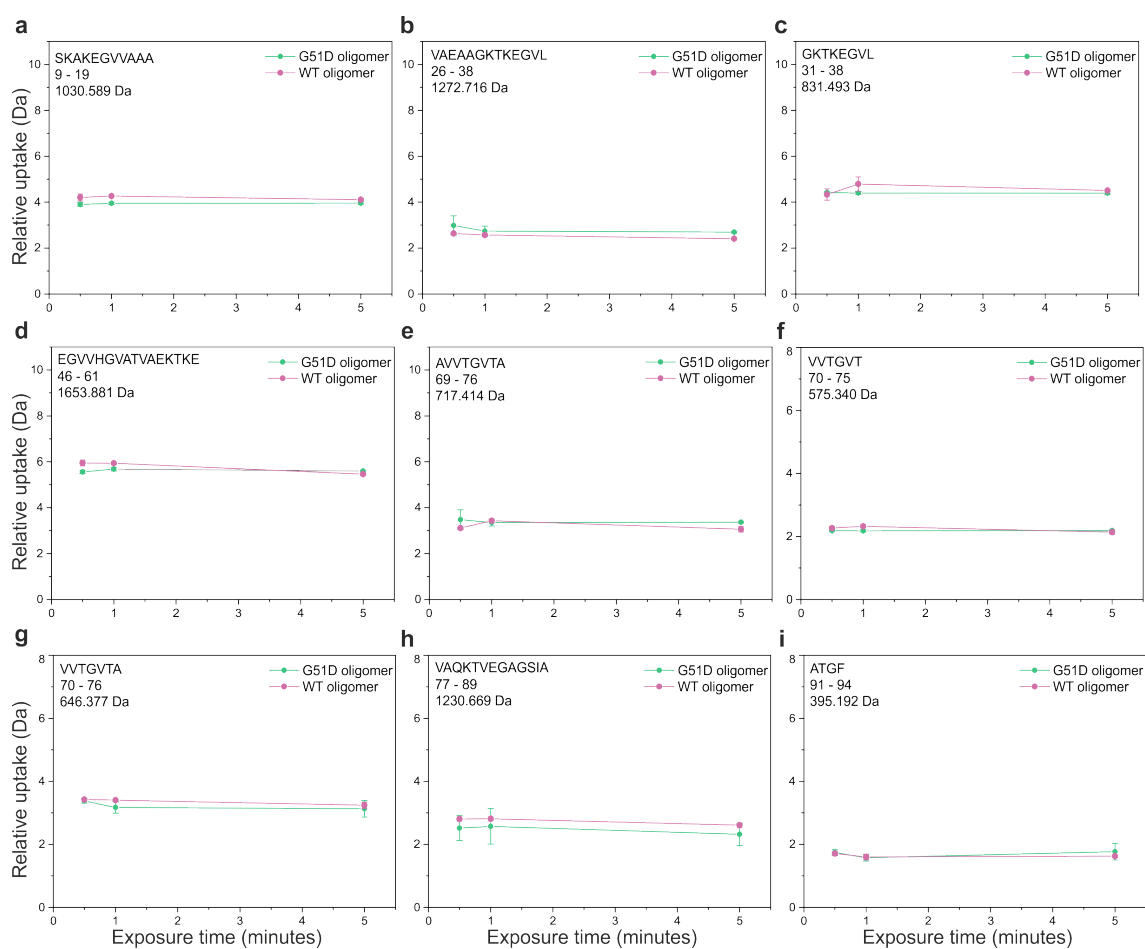


Figure. A.15 Uptake plots for the N-terminal and NAC regions of G51D α S oligomers and WT oligomers by HDX. Peptides (a) 9-19, (b) 26-38, (c) 31-38, (d) 46-61, (e) 69-76, (f) 70-75, (g) 70-76, (h) 77-89, (i) 91-94. Data were generated using Deuterios and the plots were generated using Origin.

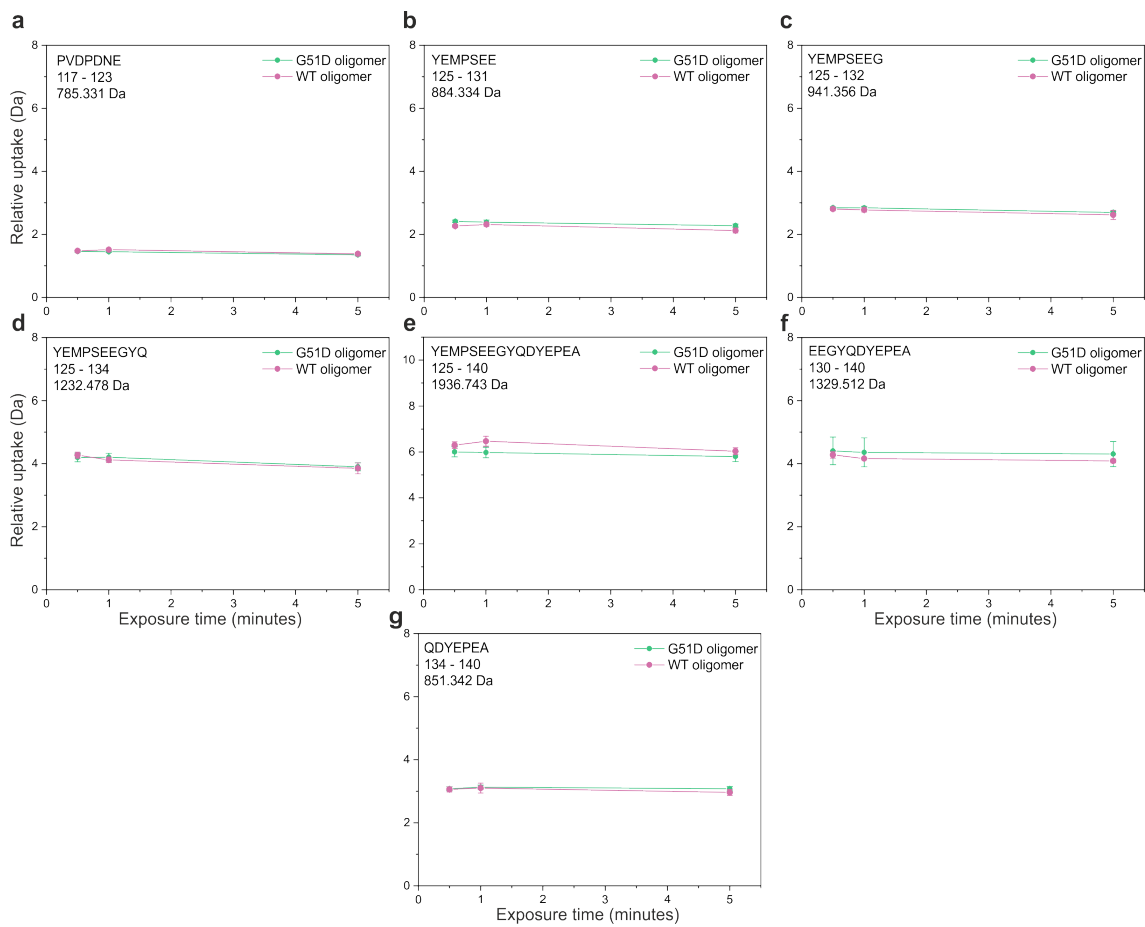


Figure. A.16 Uptake plots for the C-terminal region of α S monomers, WT oligomers and WT oligomer + PSM α 3 by HDX. Peptides (a) 117-123, (b) 125-131, (c) 125-132, (d) 125-134, (e) 125-140, (f) 130-140, (g) 134-140. Data were generated using Deuterios and the plots were generated using Origin.

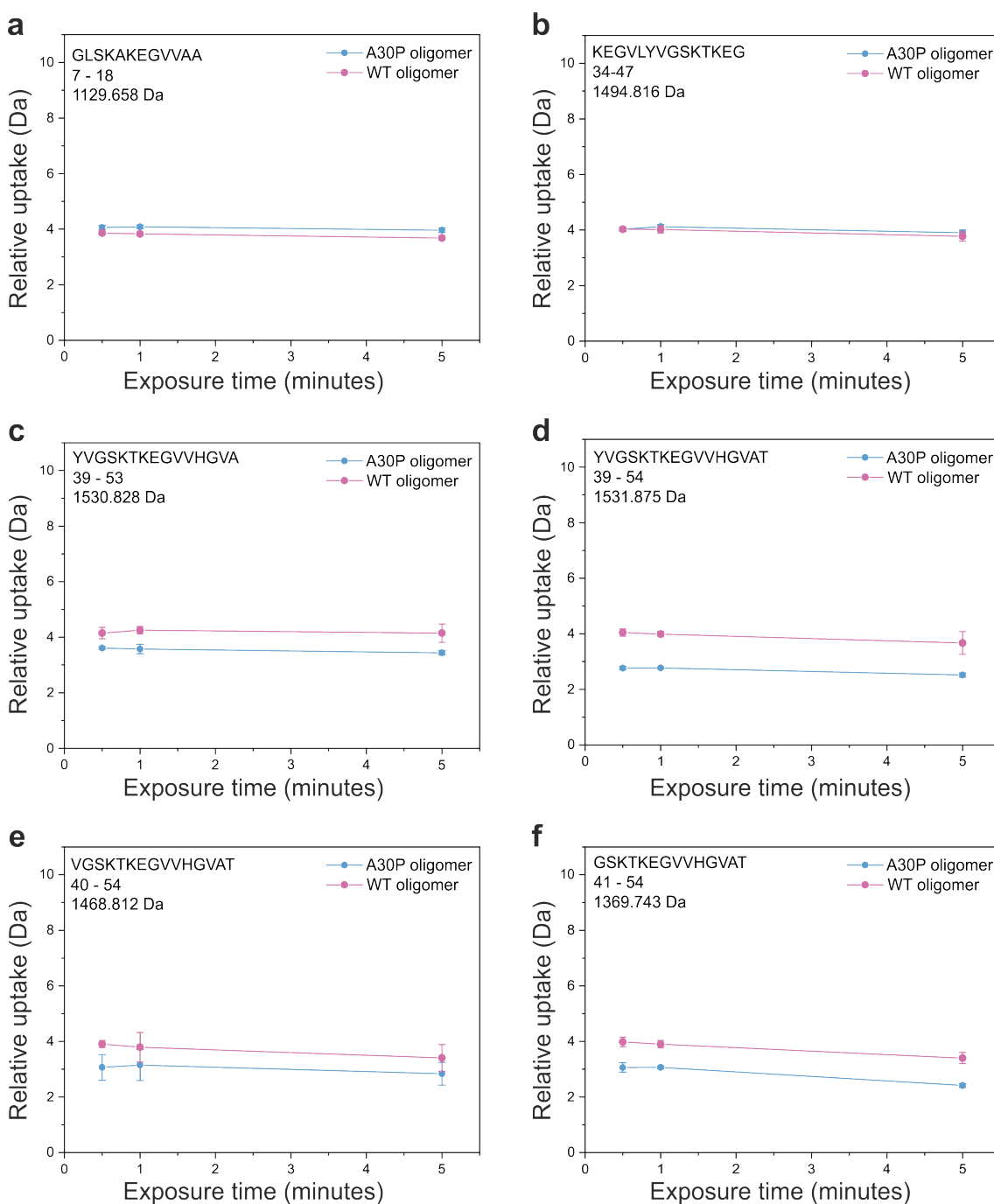


Figure. A.17 Uptake plots of A30P α S oligomers and WT oligomers by HDX. Peptides (a) 7-18, (b) 34-47, (c) 39-53, (d) 39-54, (e) 40-54, (f) 41-54. Data were generated using Deuterios and the plots were generated using Origin.

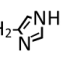
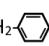
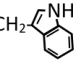
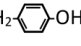
Name	Abbreviation	Side chain group	Properties	Average mass (Da)
Alanine	Ala (A)	CH ₃	Hydrophobic	89.09
Arginine	Arg (R)	-CH ₂ -CH ₂ -CH ₂ - NH-C=N ⁺ H ₂ NH ₂	Positive charge	174.20
Asparagine	Asn (N)	-CH ₂ -C=O NH ₂	Polar (uncharged)	132.12
Aspartic acid	Asp (D)	-CH ₂ -C(=O)OH O ⁻	Negative charge	133.10
Cysteine	Cys (C)	-CH ₂ -SH	Sulphur containing	121.16
Glutamine	Gln (Q)	-CH ₂ -CH ₂ -C=O NH ₂	Polar (uncharged)	146.15
Glutamic acid	Glu (E)	-CH ₂ -CH ₂ -C(=O)OH O ⁻	Negative charge	147.13
Glycine	Gly (G)	-H	Small	75.07
Histidine	His (H)	-CH ₂ - 	Positive charge	155.16
Isoleucine	Ile (I)	-CH(CH ₃)-CH ₂ -CH ₃	Hydrophobic	131.18
Leucine	Leu (L)	-CH ₂ -CH(CH ₃) ₂	Hydrophobic	131.18
Lysine	Lys (K)	-CH ₂ -CH ₂ -CH ₂ - CH ₂ -N ⁺ H ₃	Positive charge	146.19
Methionine	Met (M)	-CH ₂ -CH ₂ -S-CH ₃	Hydrophobic, sulphur containing	149.21
Phenylalanine	Phe (f)	-CH ₂ - 	Hydrophobic	165.19
Proline	Pro (P)		Uncharged	115.13
Serine	Ser (S)	-CH ₂ -OH	Polar (uncharged)	105.09
Threonine	Thr (T)	-CH(CH ₃)- OH	Polar (uncharged)	119.12
Tryptophan	Trp (W)	-CH ₂ - 	Hydrophobic	204.23
Tyrosine	Tyr (Y)	-CH ₂ - 	Hydrophobic	181.19
Valine	Val (V)	-CH(CH ₃) ₂	Hydrophobic	117.15

Figure. A.18 Amino acids summary.